Experimental Investigation of Heat Exchange between Thermal Mass and Room Environments

Dipl.-Ing. (FH) Stefan Hudjetz MSc

Gosheim, December 2012

This thesis is submitted to
De Montfort University, Leicester,
in partial fulfilment of the requirements
for the degree of Doctor of Philosophy.

The research was conducted in cooperation with
Biberach University of Applied Sciences, Germany.

To my parents,
Heinrich and Hilde Hudjetz.

Abstract

The different technologies of passive cooling concepts have to rely on a good thermal coupling between a building's thermal mass and indoor air. In many cases, the ceiling is the only surface remaining for a good coupling. Further research is necessary to investigate discrepancies between existing correlations. Therefore, the overall aim of the work described in this thesis is the investigation of heat transfer at a heated ceiling in an experimental chamber.

Acoustic baffles obstruct the surface of the ceiling and impede heat transfer. However, there is nearly no published data about the effect of such baffles on heat transfer. Available results from simulations should be verified with an experimental investigation. Consequently, one of the primary aims of this work was to experimentally determine the influence of such acoustic baffles. A suitable experimental chamber has been built at Biberach University of Applied Sciences. The thesis describes the experimental chamber, the experimental programme as well as results from five different test series.

With a value of $\pm 0.1\,\mathrm{W\,m^{-2}\,K^{-1}}$ for larger temperature differences, uncertainty in resulting convective heat transfer coefficients for natural convection is comparable to that of results from an existing recent experimental work often recommended for use. Additionally, total heat transfer (by convection and radiation) results are presented. Results are given for natural, forced and mixed convection conditions at an unobstructed heated ceiling. Furthermore, results for acoustic baffles in both an unventilated and a ventilated chamber are shown. Natural convection results show a very good agreement with existing correlations. Under mixed convection conditions, convective heat transfer at an unobstructed ceiling decreases to the limiting case described by natural convection. Installation of acoustic baffles leads to a reduction in total heat transfer (convection and radiation) between 20 % and 30 % when compared to the case of an unobstructed ceiling.

Acknowledgement

This work was funded to a large extent by the German Federal Ministry of Education and Research through the *Arbeitsgemeinschaft industrieller Forschungsvereinigungen (AiF e.V.)* under the research grant number 1749A04.

I would like to thank my supervisors Dr. Simon Rees (De Montfort University), Prof. Dr. Malcolm Cook (Loughborough University) and Prof. Dr.-Ing. Roland Koenigsdorff (Biberach University of Applied Sciences) for their support, guidance and attention to detail throughout this work. Furthermore, I would like to thank Prof. Dr. Peter Pfrommer and Dr. Tobias Zitzmann from Coburg University of Applied Sciences for enlightening discussions and their CFD results of an office room with acoustic baffles.

Thanks must go to Dipl.-Ing. (FH) Tobias Stuhlenmiller MEng for his support. Moreover, I would like to thank Dipl.-Ing. (FH) Michael Bachseitz MSc. His assistance was invaluable—particularly after I had left Biberach. Thanks is also due to all of the staff at Biberach UAS who helped me in so many different ways.

I am grateful to Manuela and Georg Riekert and their sons Michael and Sven for their advice and assistance with the construction of the heating and cooling plates and the opportunity to use their workshop and tools.

Furthermore, I would like to thank my uncle, Herbert Krämer, for his help with the construction of the experimental chamber. Thanks must also go to my sister, Claudia Hudjetz, for her moral support.

It is difficult to find words which adequately express my gratefulness towards my mother, Hilde Hudjetz, for always encouraging me to pursue a scientific career, and towards my father, Heinrich Hudjetz, whose unfailing support and constant interest in my research played, without doubt, a fundamental role in the completion of this work.

Contents

List of Figures

List of Tables

1 Introduction

1.1 Background

In recent years, concern about global warming, greenhouse effect and climate change has risen. The Intergovernmental Panel on Climate Change states that "most of the observed increase in global average temperatures since the mid-20th century is *very likely* due to the observed increase in anthropogenic greenhouse gas concentrations" (IPCC, 2007).

According to Pérez-Lombard et al. (2008), buildings contribute up to 40 % of total energy use in developed countries and heating, ventilation and air conditioning (HVAC) systems account "... for almost half the energy consumed in buildings".

In Germany, past national standards and regulations dealing with energy demand of buildings (WSVO95; EnEV2002) mainly focused on new, residential buildings and there primarily on reduction of heating demand. With the EU directive on the energy performance of buildings (EPBD2003) and the national implementation of this directive in Germany (DIN V 18599:2007-02), regulations have been extended and total energy demand for heating, cooling, ventilation, hot water and lighting has been taken into consideration. Furthermore, both residential and non-residential buildings are treated with this new directive.

Besides reduction of a building's energy consumption for heating, additional demands were already made in the past by (DIN 4108-2:2003-07) to ensure thermal comfort in summer. According to this standard, indoor air temperature should not exceed 25 °C to 27 °C on more than 10 % of the time of occupancy.

However, legal practice in Germany went further than the requirements from (DIN 4108-2:2003-07). (OLG Rostock, 2000) and (LG Bielefeld, 2003) acknowledged the

tenants' right that indoor air temperature normally should not exceed 26 °C. The landlord has to take necessary measures to meet these demands. Therefore, both judgements reinforce German Workplace Regulations (ASR6) which state that

1. for ambient temperatures below 32 °C, indoor air temperature should not exceed 26 °C, and
2. for ambient temperatures above 32 °C, indoor air temperature should be at least 6 K below ambient temperature.

Thus, the question whether indoor environments must be provided with a cooling possibility in particular cases, has become a relevant topic in building design.

Passive cooling concepts—also referred to as low energy cooling concepts—offer a possibility to achieve comfortable indoor environments without making use of energy consuming active cooling devices. A multitude of different low energy cooling technologies has been examined by the International Energy Agency (IEA, 1995). Pfafferott (2003) reports that nowadays, more and more clients demand such passive cooling concepts from their building design team.

One approach which is often pursued in such concepts is night-time ventilation. In this case, the building is flushed with cold air during the night to cool down—or "discharge"—its thermal mass. Ventilation can either be provided mechanically or naturally using for example window openings, wind towers or atria (Liddament, 1996). The next day, the building's thermal mass can be "charged" again with occurring solar or internal heat gains. A presentation of naturally ventilated modern practice examples is given by Cook (1998).

Another approach is the use of thermally activated building systems or thermoactive building systems (TABS) as they are also called by some authors such as Pfafferott and Kalz (2007). With such a concept, tubes are embedded into a building's thermal mass. Temperature of the mass is then controlled by circulating a working fluid—mostly water—through these tubes. Depending on the supply temperature, such a system can be used for either heating or cooling of the slab. This approach has become very popular in Germany in recent years. Koenigsdorff (2003) states that up to one third of new, non-residential buildings in Germany are equipped with TABS.

Both approaches have in common that they make use of a building's thermal mass by storing occurring heat gains during day-time and discharging the slab at night-time. Therefore, presented low energy cooling concepts have to rely on a good thermal coupling between a building's mass and indoor air. However, thermal coupling is often limited by interior design. Elevated floors and floor coverings offer additional thermal resistances but are often necessary for providing electricity or information and communications technology (ICT) to workplaces. Internal walls are mostly light-weight constructions which can easily be removed to ensure maximum flexibility for the tenants and thus offer virtually no opportunity to store thermal energy. Hence, the ceiling often is the only surface remaining for a good coupling between indoor air and thermal mass, and Pfafferott et al. (2005) state the need for further research on heat transfer at the ceiling for passive cooling concepts using both night-time ventilation and TABS.

Yet, even ceilings of modern buildings are sometimes obstructed either by (partial) suspended ceilings or by acoustic baffles which can become mandatory as additional sound absorbing surface. Besides for improvement of acoustics, suspended ceilings are also used to provide "static cooling" in the form of chilled ceiling panels—often in combination with other HVAC components. Rees (1998) investigated the combined use of chilled ceiling systems and displacement ventilation. While a noticeable body of research has been devoted to chilled ceilings, there still is nearly no published data about the effect of acoustic baffles on heat transfer at the ceiling. Design guidelines for such baffles predominantly still follow aesthetic or acoustic reasons (Uygun, 2007) and are not based on experimentally verified results. This circumstance increases the already identified need for further research on this topic even more.

Therefore, an experimental programme for investigation of heat transfer at the ceiling both with and without acoustic baffles is regarded as necessary to overcome these shortcomings. The objectives and approach defined for carrying out such a programme within this work are presented in the next section.

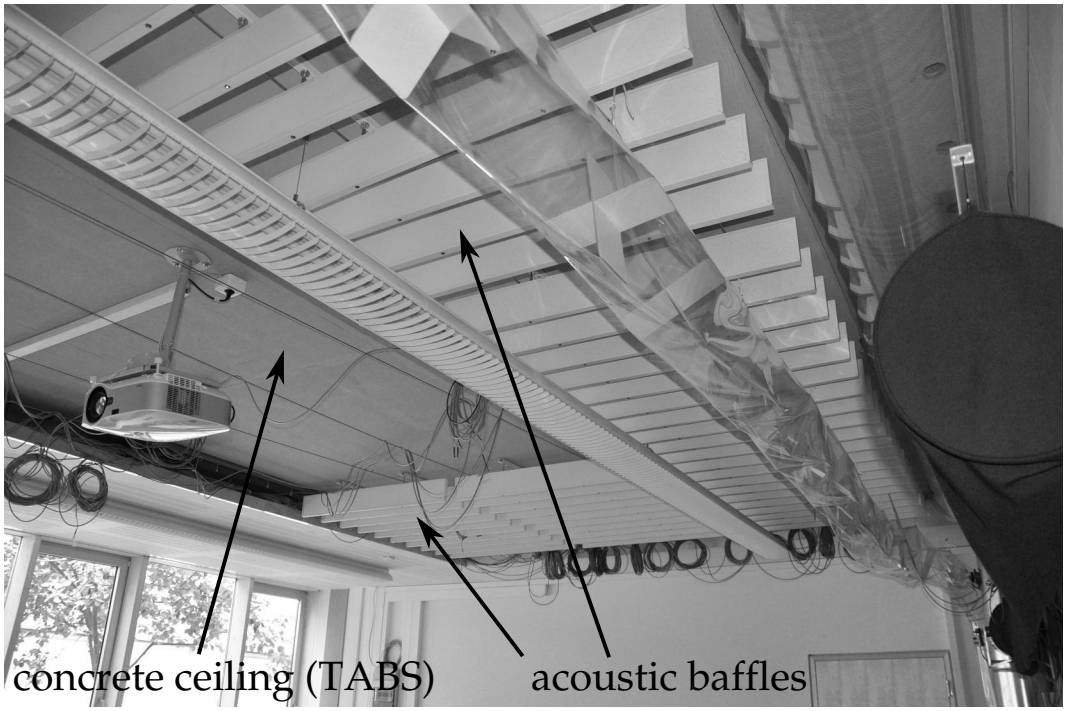

Figure 1.1: Photo of a classroom with acoustic baffles at the ceiling.

1.2 Objectives and Approach

Overall aim of the experimental programme is the investigation of heat transfer at the ceiling for arrangements both with and without acoustic baffles. This was done by

- constructing a suitable experimental chamber at Biberach University of Applied Sciences,
- installing the associated instrumentation,
- conducting experiments with a range of heat transfer rates and flow conditions, both with and without baffles, (The different test series will be presented below.)
- deriving correlations for these different boundary conditions and experimental arrangements.

Prior to the construction of the experimental chamber, a literature review has been carried out to identify publications relevant to this project and to find out more about facilities and setups used by other researchers in their work. Furthermore, existing heat transfer correlations were sought.

The following test series were carried out:

- Heat source at an unobstructed ceiling with an unventilated chamber. Objective of this arrangement was to investigate natural convection below the heat source. The results of these tests serve as a base case to which other conditions can be compared.
- Heat source at an unobstructed ceiling with a chamber ventilated via a modified air inlet opening at high level. This arrangement was used to investigate forced convection.
- Heat source at an unobstructed ceiling with a ventilated chamber. Air was supplied with the regular high-level inlet in the rear wall. This test series was used to investigate the effect of ventilation on heat transfer below the ceiling and to study mixed convection.
- Heat source at the ceiling with acoustic baffles installed below. Again, the chamber was unventilated. Objective of this test series was to investigate the influence of acoustic baffles on natural convection below the heat source.
- Heat source at the ceiling with acoustic baffles installed below and with ventilation. This arrangement was used to investigate the effect of acoustic baffles in the ventilated case.

A further aim was that the derived correlations could be implemented into programmes for dynamic thermal simulation of buildings such as TRNSYS. Thus, the results can be used for a better design of buildings with low energy cooling concepts like TABS or night-time ventilation. The outcomes of the experimental test series with acoustic baffles can be used for a design which is not only based on acoustic considerations but also on thermal engineering.

1.3 Overview of the Thesis

The main text of the thesis document is divided into 7 chapters. Chapter 2 is concerned with the literature relevant to investigation of heat transfer at the ceiling. Previously published experimental studies as well as known correlations are discussed. In chapter 3, the experimental chamber built for this work and the associated measurement systems are shown. Furthermore, the experimental design for investigation of heat transfer both with and without acoustic baffles is presented. A detailed error analysis which quantifies the different sources of error as well as the final uncertainty in the experimental results obtained is given in chapter 4. Chapter 5 deals with modelling of radiant heat transfer as radiation significantly contributes to overall heat transfer and thus must be determined accurately. Subsequently, experimental results are presented in chapter 6. The chapter starts with experimental results for an unventilated chamber with a hot plate at the ceiling. No acoustic baffles are installed for this initial test series. Results are compared to correlations known from literature. Next, the influence of ventilation on heat transfer near the ceiling is examined. Furthermore, results from experiments with acoustic baffles are presented and discussed. The main text ends with chapter 7 where conclusions and recommendations for further work are given.

Further details of the experiments and the chamber are given in a number of appendices. Appendix A contains a comprehensive list of sensors installed in the experimental chamber together with additional sketches indicating sensor positions. Further information on uncertainty, a collection of equations necessary for error analysis as well as a table with values of Student's t can be found in appendix B while dimensionless numbers are treated in appendix C. Additional experimental results—such as temperature gradient plots—which are supplementary to those in the main text of this document are presented in appendix D. In appendix E, photos of the experimental chamber from different stages of construction are shown. Last, appendix F contains photos of the additional experimental arrangement which was necessary to determine the emissivity of the surface of the hot plate.

2 Literature Review

2.1 Introduction

The literature review had several aims. These were to

- confirm the already stated need for further research in the field of heat transfer at the ceiling,
- learn more about the experimental methods applied by other scientists,
- identify the most important existing correlations for convective heat transfer at a heated ceiling,
- investigate discrepancies between these correlations,
- find out in which ways total heat transfer by both radiation and convection has been described so far,
- explore the current state of research on the special topic of reduction of heat transfer due to acoustic baffles.

The literature is not presented here as a sequence of different researchers' works but grouped into different topics. First, there is a very brief section about heat transfer by conduction as conduction is needed for quantifying the heat losses of the experimental chamber. Second, radiant heat transfer is treated in section 2.3 on page 9. Radiation contributes significantly to heat exchange inside the chamber. In this section, it will be shown that existing, simplified ways of expressing thermal radiation with a radiant heat transfer coefficient h_{rad} cannot be used with this work. The necessary detailed calculation of radiant heat transfer is treated separately in chapter 5 on page 124. Third, a detailed presentation of convection is given in section 2.4 on page 13. This section of the chapter starts with an

overview how convection is described, a discussion of characteristic length and possible choices for reference temperature in section 2.4.1 on page 13. Subsequently, convection is treated separately for natural convection (section 2.4.2 on page 20), forced convection (section 2.4.3 on page 34) and mixed convection (section 2.4.4 on page 40). Then, existing correlations for total heat transfer by both convection and radiation are presented in section 2.5 on page 54. Finally, the influence of acoustic baffles on heat transfer is reviewed in section 2.6 on page 58. The chapter closes with a summary of the most important outcomes of the literature review.

2.2 Conduction

Conduction, as it will be shown in chapter 3, plays a minor role in the planned experimental investigation of convective heat transfer in a well-insulated chamber—a fact which has also been observed by others such as Goldstein and Novoselac (2010). In the test chamber experiments considered here, conduction can be regarded as steady-state and one-dimensional. Steady-state conduction through a multilayer construction can be expressed as

$$\dot{q}_{\text{cond}} = \left(\sum_{i=1}^{n} \frac{d_i}{\lambda_i} \right)^{-1} \cdot \left(\vartheta_{\text{surf,in}} - \vartheta_{\text{surf,out}} \right) \tag{2.1}$$

where

$\dot{q}_{\text{cond}}$ is the conductive heat flux in $\mathrm{W\,m^{-2}}$,
d_i is the thickness of each material i in m,
λ_i is the conductivity of each material i in $\mathrm{W\,m^{-1}\,K^{-1}}$,
$\vartheta_{\text{surf,in}}$ is the inner surface temperature of the construction in °C, and
$\vartheta_{\text{surf,out}}$ is the outer surface temperature of the construction in °C.

The temperatures at the inner and outer surface of the ceiling of the facility are measured. Thus, the temperature difference $\vartheta_{\text{surf,in}} - \vartheta_{\text{surf,out}}$ is known. Thickness d of each material i of the ceiling is also known. Furthermore, conductivity λ of the

test chamber materials has been taken from the data sheets provided by the manufacturers. In chapter 4, uncertainties in these values, δd and $\delta\lambda$, are analysed to make sure that any variation in material properties and thus in conductive loss is taken into consideration together with uncertainties in temperature measurement when calculating the resulting uncertainty in convective heat transfer coefficients. With known temperature difference and known material properties, conduction can be easily calculated for each experiment.

2.3 Radiation

At temperatures above absolute zero, all substances continuously absorb or emit electromagnetic radiation by raising or lowering their level of internal energy. The wavelengths of emission can range from cosmic waves to radio waves and depend on the temperature of the emitting material. For thermal radiation, wavelengths range between 1×10^{-7} m and 1×10^{-3} m (ultraviolet, visible, near infrared and far infrared). The spectrum of electromagnetic radiation is for example shown by Modest (2003) or by Siegel and Howell (2002).

The nature of radiative heat transfer is different from heat transfer by conduction or convection. The latter two are coupled to the presence of a medium (a solid or a fluid). Thermal radiation can travel over large distances and also in vacuum as it is transferred by electromagnetic waves and is thus not coupled to a medium. Furthermore, radiant energy transfer between two bodies is proportional to the difference in their absolute temperatures raised to the fourth power whereas conduction or convection are linearly related to temperature difference for most applications (Modest, 2003). Moreover, the geometric situation at hand must be taken into consideration in a detailed calculation of radiant heat transfer between multiple surfaces the way it occurs within an experimental chamber as the one used in this work. For this purpose, so called *view factors* are used.

One could say that an accurate treatment of radiation is more intricate than the previously shown calculation of conduction. Therefore, an analytical solution for radiant heat transfer within in an enclosure as well as a way for a detailed modelling of radiation using the software RadTherm will be presented separately in

chapter 5. In this chapter, existing possibilities for a simplified way of calculating thermal radiation are presented. Furthermore, how other researchers dealt with radiation in their experimental work is discussed.

Due to the aforementioned complexity and since radiation contributes significantly to indoor heat transfer, some researchers tried to minimize radiant heat transfer as much as possible in their experiments either by using materials with a low emissivity (Awbi and Hatton, 1999) or by actively heating or cooling the surfaces of their experimental facility so that near isothermal conditions are achieved (Min et al., 1956; Spitler et al., 1991a). Furthermore, it is common practice to simplify the calculation of radiant heat transfer in the field of engineering. In such a simplified calculation, radiation from a surface with temperature ϑ_{surf} is described in the same way that convection is described. Hence, a linear relationship between ϑ_{surf} and a reference temperature ϑ_{ref} is assumed and room geometry is neglected. Only one variable is used for summarizing all parameters influencing radiant heat transfer. This variable is called radiant heat transfer coefficient h_{rad} and can be used to calculate radiant heat flux as

$$\dot{q}_{rad} = h_{rad} \left(\vartheta_{surf} - \vartheta_{ref} \right) \tag{2.2}$$

where

$\dot{q}_{rad}$ is the radiant heat flux in $\mathrm{W\,m^{-2}}$,
h_{rad} is the radiant heat transfer coefficient in $\mathrm{W\,m^{-2}\,K^{-1}}$,
ϑ_{surf} is the temperature of the surface under investigation in °C, and
ϑ_{ref} is the chosen reference temperature in °C.

Different suggestions for reference temperature ϑ_{ref} and for appropriate values of radiant heat transfer coefficient h_{rad} can be found in the literature.

Causone et al. (2009) investigated heat transfer between a radiant ceiling and room. A test chamber was used to carry out experiments with both a heated ceiling and a cooled ceiling. Experimental results are presented in form of convective heat transfer coefficients, radiant heat transfer coefficients and total heat transfer coefficients. Radiant heat transfer coefficients are shown here while convective heat transfer and total heat transfer results will be presented separately in sections 2.4.2

and 2.5 respectively. The authors point out that choice of a proper reference temperature is important when calculating heat transfer coefficients. For the calculation of radiant heat transfer coefficients the average unheated surface temperature (AUST) is used. This AUST is the result of a detailed calculation using view factors between the surfaces. Alternatively, an area-weighted average temperature could be used instead of the AUST. However, the view factor method is considered to be more precise. Temperature differences between the radiant ceiling and the AUST range from 6 K to 13 K in their results. Experiments with a heated ceiling lead to the same values for radiant heat transfer coefficients as experiments with a cooled ceiling. The resulting radiant heat transfer coefficient is given as approximately $5.6\,\mathrm{W\,m^{-2}\,K^{-1}}$. Causone et al. (2009) state that h_{rad} can be regarded as constant for the temperature range occurring in their experimental setup as well as for any low temperature heating or high temperature cooling system in general. However, the authors warn that this is not true for high temperature radiant heating systems or for situations with a high temperature heat source.

Glück (2007) also calculates radiant heat flux as shown in equation (2.2) and uses the average radiant temperature of the enclosing surfaces $\vartheta_{\mathrm{encl}}$ which form the half space above the surface of interest as reference temperature. For calculation of radiant heat transfer coefficient h_{rad}, equation (2.3) is used.

$$h_{\mathrm{rad}} = \varepsilon_{\mathrm{surf,encl}} \cdot \sigma \cdot b \tag{2.3}$$

where

h_{rad} is the radiant heat transfer coefficient in $\mathrm{W\,m^{-2}\,K^{-1}}$,
$\varepsilon_{\mathrm{surf,encl}}$ is the resulting emissivity,
σ is the Stefan–Boltzmann constant in $\mathrm{W\,m^{-2}\,K^{-4}}$, and
b is the temperature factor in $\mathrm{K^3}$.

Glück (2007) dispenses with a detailed modelling of room geometry and simplifies the calculation of $\varepsilon_{\mathrm{surf,encl}}$. Therefore, the resulting emissivity is calculated as

$$\varepsilon_{\mathrm{surf,encl}} = \varepsilon_{\mathrm{surf}} \cdot \varepsilon_{\mathrm{encl}} \tag{2.4}$$

where

ε_{surf} is the emissivity of the thermo-active surface under investigation, and
ε_{encl} is the emissivity of the remaining enclosing surfaces of the room.

The temperature factor b is used for the necessary linearization of radiant heat transfer so that it can be described by h_{rad} as given in equation (2.2). Therefore,

$$b = \frac{T_{surf}^4 - T_{encl}^4}{T_{surf} - T_{encl}}. \tag{2.5}$$

Glück (2007) gives two examples for appropriate values of the temperature factor b. The first example is a chilled ceiling with $\vartheta_{ceil} \approx 15\,^{\circ}\mathrm{C}$ and $\vartheta_{encl} \approx 26\,^{\circ}\mathrm{C}$. The second example is a floor heating system with $\vartheta_{floor} \approx 28\,^{\circ}\mathrm{C}$ and $\vartheta_{encl} \approx 18\,^{\circ}\mathrm{C}$. In both cases, $b \approx 1.03 \times 10^8\,\mathrm{K}^3$. Hence, Glück (2007) concludes that radiant heat transfer coefficient can be treated as a constant value of $h_{rad} \approx 5.1\,\mathrm{W\,m^{-2}\,K^{-1}}$ when using a standard emissivity for typical building materials of 0.93 in such situations.

Both chilled ceiling and floor heating fall into the group of low temperature heating or high temperature cooling systems mentioned by Causone et al. (2009). Thus, two different values are suggested by two different scientists for one and the same application. Glück (2007) suggests a constant value of $5.1\,\mathrm{W\,m^{-2}\,K^{-1}}$ for radiant heat transfer coefficient while Causone et al. (2009) suggest a constant value of $5.6\,\mathrm{W\,m^{-2}\,K^{-1}}$. These different constant values already lead to a 9 % deviation in calculated radiant heat flux.

From figure 2.1 it must be deduced that the warning of Causone et al. (2009) is true and that the simplification of using a constant value for h_{rad} is not appropriate for the experiments considered in this work. The figure shows the resulting temperature factor b from equation (2.5) for different combinations of temperature of the thermo-active surface ϑ_{surf} and temperature of the remaining enclosing surfaces ϑ_{encl}. For low values of heat output of a hot plate, both temperature values will be around $20\,^{\circ}\mathrm{C}$. Thus, $b \approx 1.0 \times 10^8\,\mathrm{K}^3$. With increasing heat output of the hot plate, both ϑ_{surf} and ϑ_{encl} will also rise. In this case, temperature factor b might reach values of up to approximately $1.25 \times 10^8\,\mathrm{K}^3$ depending on the temperatures occurring during the experiment.

Hence, neither the simplified constant value of $b \approx 1.03 \times 10^8\,\mathrm{K}^3$ and $h_{rad} \approx 5.1\,\mathrm{W\,m^{-2}\,K^{-1}}$ used by Glück (2007) nor the constant value for h_{rad} suggested by

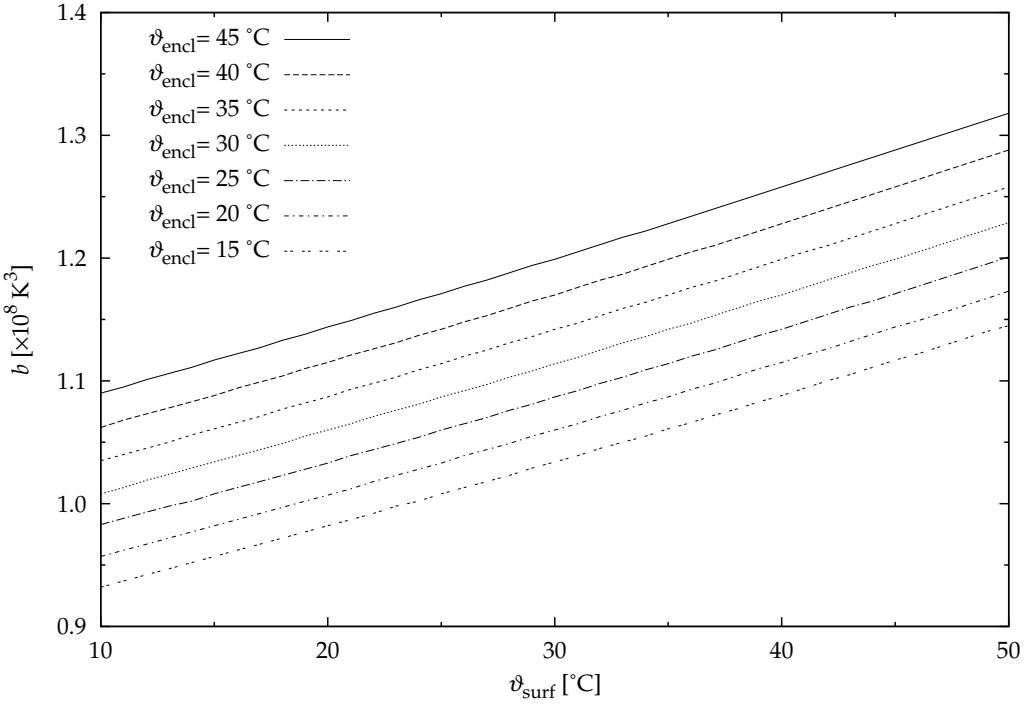

Figure 2.1: Temperature factor b (based on a figure presented by Glück (2007)).

Causone et al. (2009) is applicable to this work. Due to the linear correlation between b and h_{rad}, the error in h_{rad} is as much as 25 %. As a consequence, a detailed calculation of radiant heat transfer in the experimental chamber is necessary for each experiment. The result of this detailed calculation can then be used to calculate a radiant heat transfer coefficient for each situation. Calculation of radiative heat rates in the experimental chamber is treated in detail in chapter 5.

2.4 Convection

2.4.1 General Remarks

Convective heat flux can be written as

$$\dot{q}_c = h_c \left(\vartheta_{surf} - \vartheta_{ref} \right) \tag{2.6}$$

where

$\dot{q}_c$ is the convective heat flux in $W\,m^{-2}$,
h_c is the convective heat transfer coefficient in $W\,m^{-2}\,K^{-1}$,
ϑ_{surf} is the surface temperature in °C, and
ϑ_{ref} is the reference temperature of the fluid in °C.

The convective heat transfer coefficient (CHTC) depends on several parameters such as

- velocity and flow regime of the fluid,
- temperature of surface and fluid,
- fluid properties such as viscosity, density or conductivity, as well as
- size and geometry of the surface.

Thus, the CHTC is a function of all of these parameters and can be written as

$$h_c = h_c\left(U, \vartheta, \nu, \rho, \lambda, \text{geometry}, ...\right). \tag{2.7}$$

Due to this complexity, CHTCs are often determined experimentally and results are expressed in dimensionless form. If the motion of the fluid is due to buoyant forces, one talks about natural convection. Convection is considered to be forced if the motion of the fluid is externally generated—for example with a fan or a pump. If both natural and forced components are present, it is called mixed convection.

In general, correlations for natural convection are often given in the dimensionless form [1] of equation (2.8).

$$Nu = C\left(Gr\,Pr\right)^n = C\,Ra^n \tag{2.8}$$

where

Nu is the dimensionless Nusselt number,
C is an experimentally defined constant,

[1] A list of dimensionless numbers and their definitions can be found in the appendix.

Gr is the dimensionless Grashof number,
Pr is the dimensionless Prandtl number,
Ra is the dimensionless Rayleigh number, and
n is the exponent (typically $\frac{1}{4}$ for the laminar and $\frac{1}{3}$ for the turbulent regime).

The Nusselt number describes the ratio of convectively transferred heat to heat transfer due to conduction and is defined as

$$Nu = \frac{h_c L_c}{\lambda} \tag{2.9}$$

where

Nu is the dimensionless Nusselt number,
h_c is the convective heat transfer coefficient in $\mathrm{W\,m^{-2}\,K^{-1}}$,
L_c is the characteristic length in m (to be discussed below),
λ is the conductivity of the fluid in $\mathrm{W\,m^{-1}\,K^{-1}}$.

Another possible form of the function used for representing natural convection is

$$h_c = C \left(\frac{\vartheta_{surf} - \vartheta_{ref}}{L_c} \right)^n \tag{2.10}$$

where

h_c is the convective heat transfer coefficient in $\mathrm{W\,m^{-2}\,K^{-1}}$,
C is an experimentally defined constant,
ϑ_{surf} is the surface temperature in °C,
ϑ_{ref} is a reference temperature in °C,
L_c is a characteristic surface dimension in m, e.g. the surface height, and
n is the exponent.

Correlations for forced convection make use of the Reynolds number Re (also presented in more detail in appendix C) and are given in the form shown in equation (2.11).

$$Nu = C\,(Re\,Pr)^n \tag{2.11}$$

Different definitions can be found for the appropriate characteristic length L_c. Three different definitions have been presented by Glück (2007) for room surfaces:

$$L_{c_1} = \frac{L \cdot W}{2\,(L + W)} \tag{2.12}$$

$$L_{c_2} = \mathrm{MIN}\,(L, W) \tag{2.13}$$

$$L_{c_3} = \frac{1}{2}\,\mathrm{MIN}\,(L, W) \tag{2.14}$$

where in each definition

W is the width of the surface in m, and
L is the length of the surface in m.

Glück (2007) mentions that definition L_{c_1} is regarded as controversial for horizontal surfaces. L_{c_2} assumes that the air completely flows along the short edge of the surface. This assumption seems to be suitable for an air flow pattern with cross ventilation in cases where the long edge of the surface is parallel and close to a slot inlet. With L_{c_3}, buoyancy effects influence both edges of the surface and no further sources of air movement are present.

In another definition which is also often encountered and which is for example used by Alamdari and Hammond (1983) to name only one, characteristic length is defined as

$$L_{c_4} = D_h = \frac{4A_s}{P_s} \tag{2.15}$$

with D_h being the hydraulic diameter, A_s being the surface area and P_s being the surface perimeter.

Further examples (Glück, 1997) of characteristic length are

$$L_{c_5} = H \tag{2.16}$$

with H being the height of a vertical plate or cylinder, and

$$L_{c_6} = \frac{D}{4} \tag{2.17}$$

for a horizontal circular disk with D being the diameter of the disk.

Various further definitions of characteristic length can be found in the literature. However, from a practical point of view, no problems arise from these different definitions as long as authors mention which length is used in their work. Dimensionless numbers can namely be converted easily from one characteristic length to another if only characteristic length is changed and all other variables are assumed as known and constant—for example fluid properties or measured values from an experiment. A given Rayleigh number $Ra_{L_{c_x}}$ for a given characteristic length L_{c_x} can be converted so that it is valid for a different characteristic length L_{c_y} using equation (2.18).

$$Ra_{L_{c_y}} = Ra_{L_{c_x}} \left(\frac{L_{c_y}}{L_{c_x}} \right)^3 \tag{2.18}$$

The same applies to the Nusselt number. If Nu is calculated according to equation (2.8), a given Nusselt number $Nu_{L_{c_x}}$ for a given characteristic length L_{c_x} can be converted to be valid for a different characteristic length L_{c_y} with equation (2.19).

$$Nu_{L_{c_y}} = Nu_{L_{c_x}} \left(\frac{L_{c_y}}{L_{c_x}} \right)^{3n} \tag{2.19}$$

Another variable that can easily lead to misunderstandings and controversial discussions is the use of an appropriate reference temperature ϑ_{ref}. Different researchers choose different reference temperatures for the calculation of convective heat transfer coefficients as given in equation (2.10). The encountered variety is due to the fact that depending on the situation some choices might be more suitable than others. While one temperature might be a very good choice under specific boundary conditions—for example upstream temperature with forced convection—it could be a bad choice in another situation—for example upstream temperature if there is no clearly defined direction of air flow. As a consequence, there is no universal agreement about the "correct" choice of reference temperature.

A selection of possible reference temperatures is shown in figure 2.2 for two different situations which are characterized by two different air flow patterns. The sketch depicts convective heat transfer at the ceiling. Thus, the ceiling surface temperature is denoted with T_{surf}. The other temperatures shown could be used

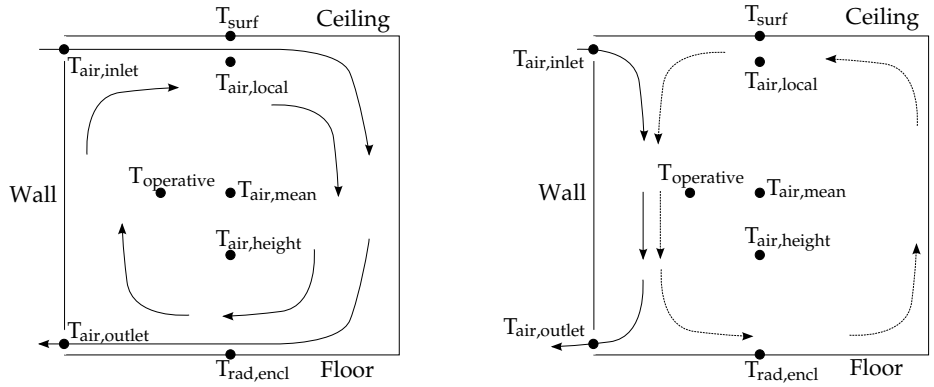

(a) Much air movement.

(b) Little air movement.

Figure 2.2: Two different air flow patterns in a room shown together with possible reference temperatures for calculation of convective heat transfer coefficients.

as a reference temperature T_{ref}. In figure 2.2a, a situation with much air movement is shown. It is assumed that zone air is well-stirred or fully mixed in such a case. On the other hand, there are situations with stably stratified conditions or where there is at least only little air movement. Such a situation is shown in figure 2.2b where the incoming air drops to the floor immediately.

The possible reference temperatures will be discussed in a general manner below. (Definitions used in particular published works will be cited later.)

- Inlet air temperature ($T_{\text{air,inlet}}$):
  Inlet air temperature might be a good choice if there is ventilation and a large ventilative flow rate. In buildings with TABS, mechanical ventilation is often running only during day-time to provide the necessary hygienic air change. At night, ventilation is turned off and heat stored in the thermal slab is extracted using a hydronic system embedded in the slab. Hence, inlet air temperature is not regarded as a good choice for reference temperature if heat transfer in buildings which rely solely or primarily on TABS is investigated.
- Outlet air temperature ($T_{\text{air,outlet}}$):
  Spitler et al. (1991a) state that in their experimental investigation of convec-

tive heat transfer with large ventilative flow rates outlet air temperature led to the smallest uncertainties in the resulting convective heat transfer coefficients. If the zone air is considered to be well-stirred and fully mixed, all air in the zone—including the return air—has the same temperature. Thus, it is comprehensible that Spitler et al. (1991a) use return air temperature as reference temperature as it is easily measurable. However, return air temperature might be a less ideal choice for small flow rates as the reference temperature might not contain enough information about the heat transfer processes occurring in the room (see figure 2.2b). Furthermore, the restrictions noted above for inlet air temperature also hold for outlet air temperature with regard to buildings with TABS.

- Mean air temperature ($T_{\text{air,mean}}$):
  In most building simulation programs, information on zone air temperature is provided for one air node which represents mean air temperature of the zone. Thus, mean air temperature is often used as reference temperature in such programs and is regarded as suitable if the correlation shall be implemented in such tools.

- Local air temperature ($T_{\text{air,local}}$):
  Local air temperature has also been used as reference temperature by several researchers such as Spitler et al. (1991a) and also Awbi and Hatton (1999). The latter used air temperature at a distance of 10 cm from the surface under investigation in some of their experiments.

- Air temperature at a specific height ($T_{\text{air,height}}$):
  Air temperature at a specific height—for example at a height of 1.1 m above the floor—is another possibility. This approach has been used by Min et al. (1956) who chose a height of 1.52 m which corresponded to the air temperature at the centre of the room. Awbi and Hatton (1999) also used air temperature at the centre of the room in case of a heated ceiling.

- Operative room temperature ($T_{\text{operative}}$):
  Operative room temperature has been used as a reference temperature for characterizing total heat transfer (not convection alone) as will be shown in section 2.5. In such a case, it is often suggested as an appropriate choice.

- Radiant temperature of the enclosing surfaces (T_{rad}):
  Radiant temperature is normally not used as a reference temperature for describing convective heat transfer coefficients but is rather used for defining a radiant heat transfer coefficient h_{rad} as already shown in section 2.3. Furthermore, radiant temperature is used for calculation of operative room temperature described above. These relationships will also be highlighted later.

As long as a valid relationship between the temperature used as reference temperature and another temperature is known convective heat transfer coefficients can easily be converted from one reference temperature to another one. Thus, conversion of convective heat transfer coefficients can be done similar to the conversion of dimensionless numbers mentioned above. In chapter 6, the correlation by Awbi and Hatton (1999) has been converted from air temperature at the centre of the room as reference temperature to mean air temperature as reference temperature.

2.4.2 Natural convection

Glück (2007) provides an overview of convective heat transfer correlations for surfaces of TABS. Various geometric configurations are presented. For natural convection at a vertical wall, Glück (2007) proposes to use the equation according to Churchill and Chu which is also recommended for use by Elsner et al. (1993) and which is given as

$$Nu = \left[0.825 + 0.387\, Ra^{\frac{1}{6}} \left[1 + \left(\frac{0.492}{Pr} \right)^{\frac{9}{16}} \right]^{-\frac{8}{27}} \right]^2 . \tag{2.20}$$

Equation (2.20) is valid for $0.1 < Ra < 10^{12}$ and $0 < Pr < \infty$.

For horizontal surfaces, Glück (2007) suggests using the equations according to El-Riedy, Al Arabi and Churchill. These equations are dependent on the direction of heat flow. For a horizontal surface with heat flow upwards and in the turbulent flow regime,

$$Nu = 0.155\, Ra^{0.333}. \tag{2.21}$$

Glück (2007) states that equation (2.21) is valid for $Ra < 17 \times 10^4$ (for air) and $0 < Pr < \infty$. However, in a previous publication (Glück, 1997) the same author states that this equation is valid for $Ra > 4 \times 10^7$. No reason could be found for the discrepancy in the range of Rayleigh numbers. However, CIBSE (2007) suggests to use $Nu = 0.15\,Ra^{0.333}$ for $10^7 < Ra < 10^{11}$.

For a horizontal surface with heat flow downwards and laminar flow,

$$Nu = 0.485\,Ra^{0.2}. \tag{2.22}$$

For this equation an identical range for Ra is given by both Glück (2007) and Glück (1997). Equation (2.22) is valid for $3 \times 10^3 < Ra < 3 \times 10^{10}$ (for air) and $0 < Pr < \infty$.

Equations (2.20), (2.21) and (2.22) are plotted together in figure 2.3 for different values of characteristic length L_c. It can be seen that equation (2.21) (heated floor) delivers the highest values for the convective heat transfer coefficient h_c while the lowest values occur with a cooled floor and heated ceiling respectively (equation (2.22)).

Since L_c^3 is used for the calculation of Ra (q.v. appendix C) and since according to equation (2.21) $Nu \propto Ra^{0.333}$, the convective heat transfer coefficient at a horizontal surface with heat flow upwards is independent of L_c. Thus, the discussion about an appropriate choice for the characteristic length becomes irrelevant in this case. Applying the same thoughts to the equation for a horizontal surface with heat flow downwards, it can be concluded that $h_c \propto L_c^{-0.4}$. However, Glück (2007) states that convective heat transfer is hard to predict in this case as it strongly depends on the occurring air flow pattern.

Additionally, three further approximations for horizontal surfaces with heat flow downwards are given by Glück (1997):

$$h_c = 0.5\,\Delta\vartheta^{0.2} L_c^{-0.4} \tag{2.23}$$

for situations without air movement, where $\Delta\vartheta = \vartheta_{ceil} - \vartheta_\infty$ and ϑ_{ceil} is the average ceiling surface temperature and ϑ_∞ is the temperature of the undisturbed fluid.

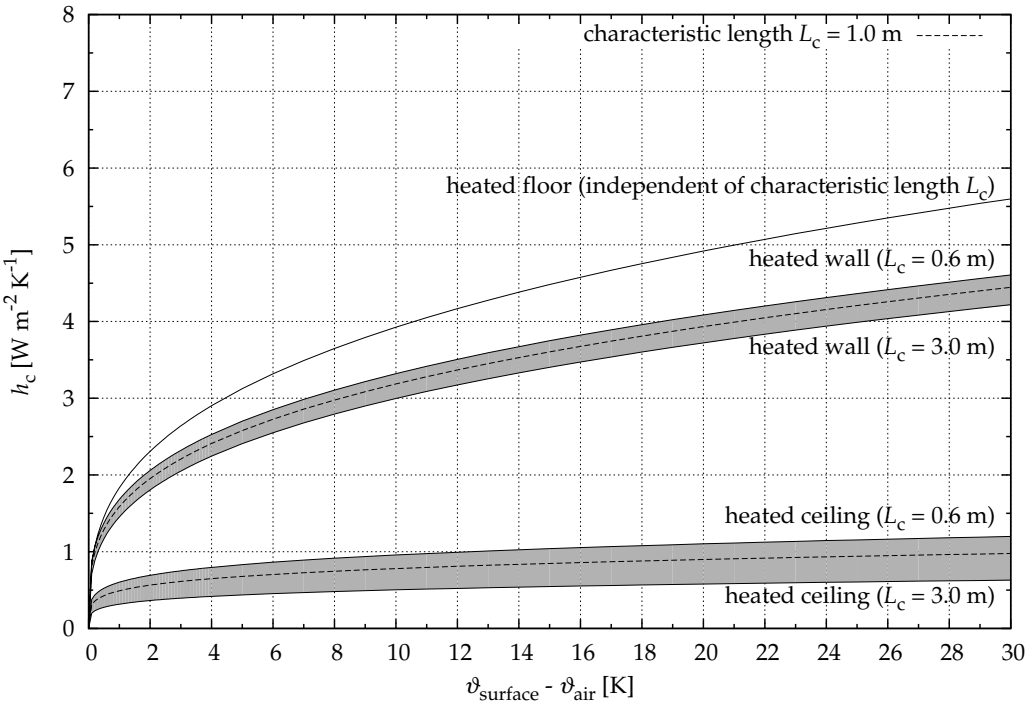

Figure 2.3: Natural convection heat transfer coefficients for different geometric configurations from equations (2.20), (2.21) and (2.22) (based on a figure presented by Glück (2007)).

For heating strips in halls, convective heat transfer coefficient can be expressed as

$$h_c = 1.08\,\Delta\vartheta^{0.31}. \tag{2.24}$$

It has been reported by the SEL (2012) that equation (2.24) is also used as default correlation in the simulation software TRNSYS for calculation of convective heat transfer coefficients at a heated ceiling if the routine for a detailed internal calculation of convective heat transfer coefficients is activated in the multizone building model type 56.

For heated surfaces with stably stratified air,

$$h_c \leq 0.54\Delta\vartheta^{0.31}. \tag{2.25}$$

Glück (2007) suggests to use equation (2.25) as an approximation which represents the upper range of natural convection and the lower range of mixed convection heat transfer coefficients for situations with a heated surface with heat flow downwards.

Khalifa (2001a) provides an extensive review on natural convective heat transfer coefficients obtained from isolated vertical and horizontal surfaces. The author emphasizes that application of the correlations to building geometries was of special interest for his work. He identified and presented 48 references which cover more than a century of research. The oldest publication cited by Khalifa (2001a) goes back to the year 1881. The most recent paper is the work of Al-Arabi and Sakr (1988) which covers the topic of heat transfer from inclined isothermal surfaces. Khalifa distinguishes between correlations for vertical surfaces and heated plates facing upwards (heated floor/cold roof) as well as heated plates facing downwards (heated roof/cold floor). Correlations are given either in the form of equation (2.8) or in the form of equation (2.10). The author mentions that more recent correlations report forms of the equation and values for the exponent n which are different from the older correlations. Discrepancies between resulting convective heat transfer coefficients for horizontal heated surfaces facing downward from these different correlations are up to a factor of 4.

In a subsequent paper, Khalifa (2001b) added correlations he found in literature for two-dimensional and three-dimensional enclosures. The study revealed that discrepancies for the case of a heated ceiling are further increased up to a factor of 8 when these correlations are also taken into consideration. Khalifa (2001b) points out that results were often obtained in small enclosures with water as the working fluid and that only very limited data is available for heat transfer coefficients at surfaces of real sized enclosures which are of interest for heat transfer in buildings.

The author presents nine correlations for natural convection at a heated plate facing downwards. Figure 2.4 shows a reproduction of the graph given by Khalifa (2001b). The oldest correlations which have been obtained in the 1920s and 1930s lead to the largest values for h_c. The only correlation from a three-dimensional study offers the lowest convection with values below $0.4\,\mathrm{W\,m^{-2}\,K^{-1}}$. More recent experimental investigations result in values for convective heat transfer coefficients between approximately $0.4\,\mathrm{W\,m^{-2}\,K^{-1}}$ for small temperature differences

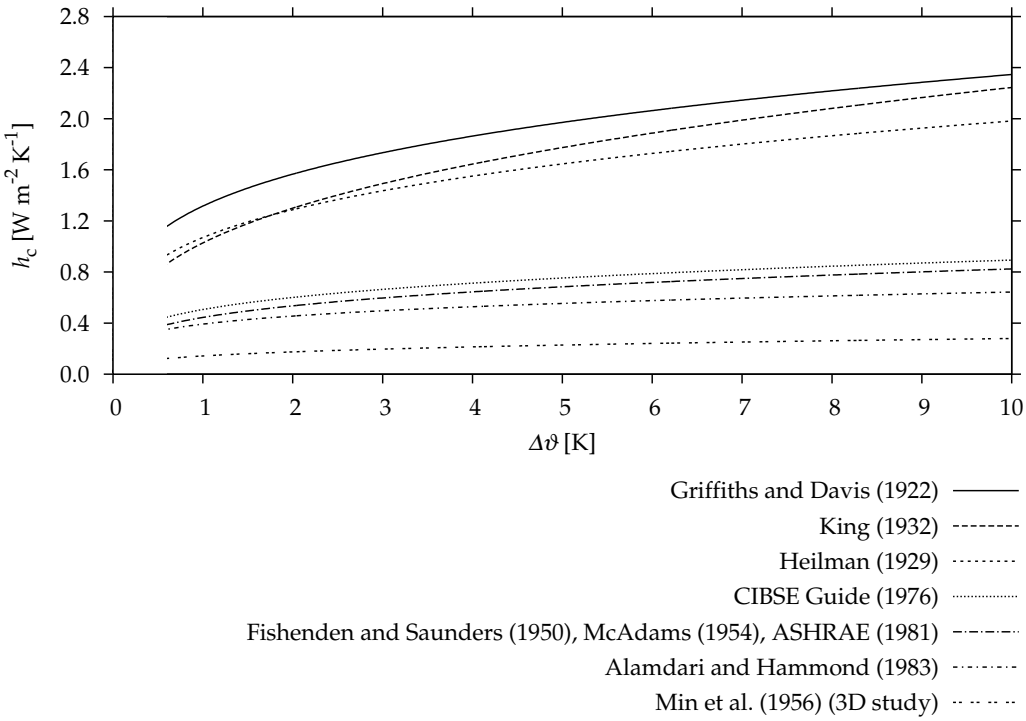

Figure 2.4: Existing correlations for natural convection heat transfer at a heated ceiling. (Reproduction of a figure from Khalifa (2001b).)

and 0.8 W m^{-2} K^{-1} for larger temperature differences.

McAdams (1954) and ASHRAE (1981) use the same correlation as the one given in the book by Fishenden and Saunders (1950).

Fishenden and Saunders (1950) present the following equation for $(Gr\,Pr)$ greater than 1×10^5:

$$Nu = C\,(Gr\,Pr)^{0.25} \tag{2.26}$$

For gases in the turbulent range, the authors suggest that

$$Nu = C'\,(Gr\,Pr)^{0.33} \tag{2.27}$$

where C and C' are constants which depend on the geometrical configuration and which are given in table 2.1 on page 25. The bottom row which is valid for

Table 2.1: Values of constants C and C' used in equations (2.26) and (2.27) from Fishenden and Saunders (1950).

	C	C'
1. horizontal or vertical cylinders (characteristic dimension: diameter)	0.47	0.10
2. vertical planes or vertical cylinders of large diameter (characteristic dimension: height)	0.56	0.12
3. horizontal planes facing upwards (characteristic dimension: side length)	0.54	0.14
4. horizontal planes facing downwards (characteristic dimension: side length)	0.25	$\frac{1}{3}$ slope not reached

warm horizontal surfaces facing downwards is relevant for this work. In this case, the turbulent range (equation (2.27) and constant C') is not even reached for the highest values of $(Gr\,Pr)$ investigated. Hence, equation (2.26) should be applied for $10^5 < (Gr\,Pr) < 10^{10}$.

Min et al. (1956) were the first to investigate natural convective heat transfer in a full-scale, unventilated enclosure. Both convection and radiation has been considered in their study. The surfaces of the enclosure were made of aluminium panels through which water could be circulated. All surfaces of the test cell were kept at an identical temperature during the experiments except for the surface under investigation—for example the ceiling—which was heated to a higher temperature with the panel. Tests were made under steady-state conditions. Min et al. (1956) obtained the convective component by subtracting radiation from the total exchange between the room surface and its environment. Ceiling panel temperature was varied between 32 °C and 66 °C. The AUST ranged from 4 °C to 21 °C. For the evaluation of experimental data, physical properties were taken at the arithmetic mean of the surface and room air temperature with room air temperature being measured at a height of 1.52 m at the centre of the room. The quotient of four times the surface area divided by the surface perimeter was used as characteristic length for the calculations. This expression is commonly known as hydraulic diameter or equivalent diameter. Min et al. (1956) found that convection from a heated ceiling is very small. Hence, slight errors in radiation lead to large er-

rors in the calculated values for convective heat transfer coefficients. This effect is also described by Goldstein and Novoselac (2010). According to Min et al. (1956), convection from a heated ceiling to the room can be described as

$$h_c = 0.2027 \frac{\Delta\vartheta^{0.25}}{D_h^{0.24}} \tag{2.28}$$

where

h_c is the convective heat transfer coefficient in $W\,m^{-2}\,K^{-1}$,
$\Delta\vartheta$ is the temperature difference in K, and
D_h is the hydraulic diameter in m.

The above equation was converted to fit the SI units system while imperial units were used in the original equation by Min et al. (1956). A dimensionless form of this result is given as

$$Nu = 0.071\,(Gr\,Pr)^{0.255}. \tag{2.29}$$

As the results for convection at a heated ceiling by Min et al. (1956) were considerably smaller than results from small horizontal plates facing downwards with free edges from previous investigations such as Heilman (1929), King (1932) or Fishenden and Saunders (1950) which are all shown together in figure 2.4, the authors conducted additional tests to verify the low values they obtained. They used a horizontal free-edged heated plate for these tests which was suspended from the ceiling of the chamber to the height of 1.52 m at the centre of the room. All enclosing surfaces of the room were kept at an identical, constant temperature below the temperature of the suspended plate. For the free-edged heated plate, results showed a good agreement with results from investigations conducted prior to the work of Min et al. (1956). An additional wooden frame around the suspended plate slightly decreased the convection component and attaching the plate directly to the ceiling lead to a further reduction in convective heat transfer. From these results, the authors concluded that their equation for convective heat transfer at the ceiling within a three-dimensional enclosure is applicable and that, due to the restriction of air currents at the ceiling of a room, convection rates within a three-dimensional enclosure are smaller than the ones obtained from free-edged plates.

According to Khalifa (2001a), CIBSE (1976) states that natural convection below an isolated horizontal surface can be described as

$$h_c = 0.64 \left(\frac{\vartheta_{surf} - \vartheta_{fluid}}{L_c} \right)^{0.25} \tag{2.30}$$

where

h_c is the convective heat transfer coefficient in $W\,m^{-2}\,K^{-1}$,
ϑ_{surf} is the surface temperature in °C,
ϑ_{fluid} is the fluid temperature in °C, and
L_c is the characteristic length in m.

More than 30 years later, this equation can still be found in CIBSE (2007, chapter 3.3.4.1, page 3-21). It is based on equation (2.31) which is also given in CIBSE (2007, chapter 3.2.1.1, page 3-5) and which states that

$$Nu = 0.27\, Ra^{0.25} \tag{2.31}$$

for $1 \times 10^5 < Ra < 1 \times 10^{11}$. All fluid properties are taken at the arithmetic mean of the surface temperature ϑ_{surf} and the free stream fluid temperature ϑ_{fluid} for the calculation. However, no recommendation could be found how ϑ_{fluid} should be measured in case of a heated ceiling. Attention must also be directed to using the correct characteristic length which in this case is defined as $\frac{A_s}{P_s}$ and not as $D_h = \frac{4A_s}{P_s}$ as in other publications. A_s is as usual the surface area and P_s its perimeter.

A discrepancy could be observed with the equations valid for the upper surface of a horizontal hot plate. According to CIBSE (2007), $Nu = 0.54\, Ra^{\frac{1}{4}}$ for $10^4 < Ra < 10^7$ and $Nu = 0.15\, Ra^{\frac{1}{3}}$ for $10^7 < Ra < 10^{11}$. Characteristic length is again given as $\frac{A_s}{P_s}$. The first of the above two correlations is the same as the one suggested by Fishenden and Saunders (1950) which has been given in equation (2.26). However, Fishenden and Saunders (1950) give the lower end of Ra numbers as 1×10^5 while it is 1×10^4 according to CIBSE (2007). For the turbulent range, constant C' in equation (2.27) is given as 0.14 by Fishenden and Saunders (1950) while CIBSE (2007) states that $C' = 0.15$. Another discrepancy is the suggested characteristic length. Fishenden and Saunders (1950) state that most results come

from experiments with square plates where side length of the surface is used as characteristic length. A mean value was taken as side length in case of rectangular surfaces by these authors. However, CIBSE (2007) uses $\frac{A_s}{P_s}$ as characteristic length. The definition used by Fishenden and Saunders (1950) leads to a characteristic length of a for a square plate with side length a while the other definition leads to a characteristic length of only $0.25a$ for the same square plate.

Alamdari and Hammond (1983) present "improved data correlations for buoyancy driven convection in rooms". The suggested correlations are based on existing correlations obtained from experiments with isolated plates and cover the full range of laminar, transitional and turbulent airflows. The frequently used mathematical model of Churchill and Usagi (1972) is used to combine these existing correlations into a new, improved correlation. For stably stratified conditions below a heated plate facing downwards, Alamdari and Hammond (1983) suggested calculating CHTC according to,

$$h_c = 0.6 \left(\frac{\Delta\vartheta}{L_c^2} \right)^{0.2} \tag{2.32}$$

where $\Delta\vartheta$ again is the temperature difference between surface and fluid and L_c is the hydraulic diameter which is defined as in equation (2.15) on page 16. The authors note that the proper choice of a characteristic length is subject of discussion and that there are different opinions as to the best choice.

Furthermore, Alamdari and Hammond (1983) give the following expression in non-dimensional form for stably stratified conditions below a horizontal heated surface:

$$Nu = 0.58\, Ra^{0.2} \tag{2.33}$$

This expression is valid for up to at least $Ra \approx 10^{11}$.

The correlations suggested by Alamdari and Hammond (1983) have some limitations:

1. The authors state that their data was obtained from experiments using isolated surfaces. Thus, it must be questioned in how far their correlation is applicable to airflow and heat transfer phenomena in rooms.
2. The authors note that their correlation applies to buoyancy-driven convection and thus to buildings that are naturally ventilated. Hence, it is question-

able whether their correlation can be applied in situations of a mechanically driven airflow.

Awbi (1998) compares results for natural convection heat transfer coefficients of a heated wall, floor and ceiling which have been calculated using Computational Fluid Dynamics (CFD) with experimental data from a test chamber and a small test box. The external dimensions of the test chamber are 4.0 m × 3.0 m × 2.5 m and it was divided into two inner compartments—a main compartment and a smaller cool compartment.

In their experimental programme, Awbi and Hatton (1999) investigated ten different arrangements, three of which deal with a heated ceiling:

1. Large plates at the ceiling of the test chamber.
2. Small plates at the ceiling of the small box.
3. Small plates at the ceiling of the test chamber at three different positions.

The first test series was conducted to find a correlation for a fully heated ceiling. The second test series was conducted to investigate scale effects. Natural convection heat transfer at a partially heated ceiling was determined in the last test series.

From additional CFD calculations, the authors found out that there is very little air movement and regarded conditions with a heated ceiling as stably stratified. As strong air temperature gradients occur inside the cabin for a heated ceiling, no suitable height for positioning a sensor which measures a reference temperature for the calculation of convective heat transfer coefficients could be found. Thus, air temperature at the centre of the cabin and at the centre of the small box was considered the most appropriate choice for reference temperature.

Awbi (1998) presents results for convective heat transfer coefficients in the general form of equation (2.10). Hydraulic diameter D_h is used as characteristic length. ΔT is the difference between the surface temperature T_surf and the reference temperature T_ref mentioned above. For the measurements with a heated ceiling,

$$h_\mathrm{c} = \frac{0.704}{D_\mathrm{h}^{0.601}} \left(\Delta T\right)^{0.133}. \tag{2.34}$$

The error in h_c is given as $\pm 0.1\,\mathrm{W\,m^{-2}\,K^{-1}}$ in this case.

Nusselt number is given as

$$Nu = 1.78\,(Gr)^{0.133} \tag{2.35}$$

and Grashof numbers range from 9×10^8 to 1×10^{11}.

Awbi (1998) concludes that equations like (2.34) which have been experimentally determined for room surfaces should be implemented into CFD or zonal air flow codes.

Equation (2.34) is also recommended for use with a heated ceiling by Novoselac et al. (2006) who validated existing correlations in a full-scale experimental facility for rooms with displacement ventilation. Their work is focused on the development of a new correlation for floor surfaces but a recommendation for ceilings is nevertheless given. However, Novoselac et al. (2006, chapter 5.4, page 172) state that all of their recommended correlations including equation (2.34) use local air temperature at a distance of 0.1 m of the surface as reference temperature. Awbi (1998, chapter 4.2, page 224) explicitly states that this is only true for his correlations valid for floor and wall and that reference temperature for the ceiling correlation given in equation (2.34) was taken to be the air temperature at the centre of the chamber—that is at a height of 1.15 m for the large chamber and at a height of 0.52 m for the small box.

For the fully heated ceiling in their environmental chamber, Awbi and Hatton (1999) confirm that convective heat transfer coefficient h_c is best described by equation (2.34) which has already been presented in identical form by Awbi (1998).

However, a more general dimensionless representation is given by Awbi and Hatton (1999) as

$$Nu = 2.376\,(Gr)^{0.133} \tag{2.36}$$

for the heated ceiling in the chamber.

Nusselt numbers calculated with equation (2.36) differ from the values calculated with equation (2.35) which has been given by Awbi (1998) although both Nu equations are presented for natural convection at a heated ceiling by the authors and

obviously come from the same experiments. Nusselt numbers calculated with equation (2.36) differ from the ones obtained from equation (2.35) by 33 % due to the different value for constant C while the equation for h_c is exactly the same in both publications. The reason for this discrepancy in the two Nu correlations could not be found as both analogously given equations for h_c are identical. In a subsequently published paper, Awbi and Hatton (2000) suggest again to use equation (2.35).

For the small plates at the partially heated ceiling of the environmental chamber, Awbi and Hatton (1999) suggest to describe convective heat transfer by

$$h_c = \frac{1.736}{D_h^{0.52}} \left(\Delta T\right)^{0.16} \tag{2.37}$$

and the dimensionless form is given as

$$Nu = 3.517 \left(Gr\right)^{0.16}. \tag{2.38}$$

Convection data for the small plates installed at the ceiling of the chamber increases more with temperature difference than the ceiling data obtained in the small box. The authors found out that there are no stably stratified conditions with the small plates at the ceiling of the chamber but that there is more mixing of air inside the chamber. Hence, convective heat transfer is increased in this case.

The CHTC correlation from Awbi and Hatton (1999) for a heated ceiling given by equation (2.34) reduces to

$$h_c = 0.76 \Delta\vartheta^{0.133} \tag{2.39}$$

for the geometry of the hot plate which is used for this work and installed in the new experimental chamber at Biberach University of Applied Sciences. For a partly heated ceiling, Awbi and Hatton (1999) suggest to use equation (2.37) which reduces to

$$h_c = 1.855 \Delta\vartheta^{0.16} \tag{2.40}$$

for the geometry of the hot plate installed in the new experimental chamber used in this work.

Glück (1997) cites from Michejew (1964) when presenting a correlation for natural

convection. The author warns that convective heat transfer coefficients may not be determined exactly with Michejew's correlation but he considers the given correlation to be a good choice for an early guess as long as no better correlation—for example from measurements—is known. This warning is most likely due to the fact that Glück (1997) started to develop a model suitable for calculation of heat transfer in indoor environments while Michejew (1964) used experimental results from a number of investigations with heated wires, ducts, plates and spheres. The correlation by Michejew (1964) is

for $Ra < 10^{-3}$:

$$Nu = 0.5 \tag{2.41a}$$

for $10^{-3} < Ra < 5 \times 10^{2}$:

$$Nu = 1.18\, Ra^{0.125} \tag{2.41b}$$

for $5 \times 10^{2} < Ra < 2 \times 10^{7}$:

$$Nu = 0.54\, Ra^{0.25} \tag{2.41c}$$

for $2 \times 10^{7} < Ra < 10^{13}$:

$$Nu = 0.135\, Ra^{0.333} \tag{2.41d}$$

Michejew (1964) states that above equations can also be applied for calculation of convective heat transfer at horizontal heated plates. In this case, the shorter edge of the plate should be used as characteristic length for calculation of Ra numbers. Furthermore, he suggests to increase Nu by 30 % for a heated plate facing upwards and to decrease the resulting Nusselt number by 30 % for a heated plate facing downwards.

Glück (1997) combined equations (2.41a) to (2.41d) into (2.42) to form a comprehensive correlation.

$$Nu = \left((0.5)^{20} + \left(1.18\, Ra^{0.125}\right)^{20} + \left(0.54\, Ra^{0.25}\right)^{20} + \left(0.135\, Ra^{0.333}\right)^{20} \right)^{0.05} \tag{2.42}$$

For the calculation of Rayleigh numbers in above equation, Glück (2007) states that Prandtl number and viscosity are taken at the average value of surface temperature and undisturbed fluid temperature. Characteristic length L_c depends on

the geometric situation at hand: For a vertical plate or duct, the height of the body shall be used. For a horizontal rectangular plate, L_c shall be taken as short edge of the plate. Finally, the diameter is recommended as characteristic length for a horizontal duct or a sphere.

Fohanno and Polidori (2006) developed a theoretical expression for natural convection at a uniformly heated, vertical interior building surface and compared their expression with the correlation suggested by Alamdari and Hammond (1983). The authors note that this correlation has been, and still is often used in building simulations although it is based on outcomes from experiments with isolated plates, and indicate that applicability of such expressions for the purpose of building simulation must be investigated further. One solution could be comparisons with data obtained from experiments which have been carried out using full-scale enclosures instead of isolated plates. However, Fohanno and Polidori (2006) state that such data is still scarce. Thus, the need for further research using a full-scale experimental test facility is once more stated. Among the limited data available, results by Awbi and Hatton (1999) are mentioned by the authors. The expression of Fohanno and Polidori (2006) for the vertical surface showed a slightly better agreement with the results of Awbi and Hatton (1999) than the correlation by Alamdari and Hammond (1983) did. Hence, it would be interesting to see if a correlation more suitable than that of Alamdari and Hammond (1983) can be found for the case of a heated ceiling.

Causone et al. (2009) investigated heat transfer between a radiant ceiling and room. A test chamber was used to carry out experiments with both a heated ceiling and a cooled ceiling. Experimental results are presented in form of convective heat transfer coefficients, radiant heat transfer coefficients and total heat transfer coefficients. Total heat transfer results will be presented separately in section 2.5. Radiant heat transfer coefficients have already been shown in section 2.3. Only minor deviations in resulting convection coefficients could be observed due to the different reference temperatures. As a consequence, no recommendation as to which reference temperature is regarded as the best for the calculation of convective heat transfer coefficients was made.

Their experimental programme consisted of sets of measurements with both cooling and heating conditions. As interest of the present work lies on heated ceilings,

only the experimental results with heating conditions are presented.

Resulting convective heat transfer coefficients from these nine tests with a heated radiant ceiling did not exceed a value of 0.6 $W\,m^{-2}\,K^{-1}$. The reported average value is 0.3 $W\,m^{-2}\,K^{-1}$. The authors suggest that the correlations by Awbi and Hatton should be used for calculation of convective heat transfer coefficients.

2.4.3 Forced convection

Forced convection is not the focus of this work but is primarily referred to in the analysis of mixed convection experiments. With forced convection, the situation is similarly intricate as with natural convection. Several correlations which can be used to describe forced convection could be identified. A number of these correlations make use of a different reference temperature but otherwise use a nearly identical expression. Furthermore, different researchers present the same correlation but provide a different range in which the correlation is regarded as valid.

Michejew (1964) summarized the results of experimental work on forced convection of Jürges (1924), Frank (1929), Petuchov et al. (1954) and Shukauskas (1955) [2]. These authors used flat plates of different shapes, different temperature ranges as well as different working fluids for their experiments. Air was used in most experiments but some were done with water and some with transformer oil. Michejew (1964) presented all of these results in dimensionless form. Upstream temperature of the fluid was used as reference temperature and length of the plate in direction of the flow was used as characteristic length for the calculation. According to Michejew (1964), results of each researcher can be described by the one following common equation:

$$Nu = 0.037\,Re^{0.8} Pr_{\mathrm{ref}}^{0.43} \left(\frac{Pr_{\mathrm{ref}}}{Pr_{\mathrm{w}}}\right)^{0.25} \tag{2.43}$$

Pr_{ref} is the Prandtl number calculated at reference temperature while Pr_{w} is the Prandtl number calculated at wall temperature. Equation (2.43) is regarded as

[2] Only the summary of results given by Michejew (1964) has been analysed closer since it showed a very good agreement between the outcomes of different researchers. The original citations have not been read since all information relevant for this work could be found in the summary.

valid for a turbulent flow with $Re > 1 \times 10^5$. The very same equation is also recommended for use by Elsner et al. (1993) for a purely turbulent flow. However, a value of $Re_{\text{critical}} = 3.5 \times 10^5$ is recommended as typical by Elsner et al. (1993) for the critical Reynolds number where the flow regime changes from laminar to turbulent flow for forced convection along a flat plate. Elsner et al. (1993) further state that above equation is only valid for $0.6 \leq Pr \leq 100$ while no such restriction on Prandtl number could be found in Michejew's text. These authors also mention that the quotient of Prandtl numbers at the end of equation (2.43) can be omitted in cases where a gas is used as working fluid since the quotient has a value close to unity in this case. For air, equation (2.43) can be simplified to

$$Nu = 0.032\, Re^{0.8} \tag{2.44}$$

according to Michejew (1964).

For laminar flow with $Re < 1 \times 10^5$,

$$Nu = 0.664\, Re^{0.5} Pr_{\text{ref}}^{0.43} \left(\frac{Pr_{\text{ref}}}{Pr_{\text{w}}} \right)^{0.25}. \tag{2.45}$$

Elsner et al. (1993) suggest that forced convection along flat plates or walls with a purely laminar flow and constant wall temperature can be described according to,

$$Nu = 0.664\, Re^{\frac{1}{2}} Pr_{\text{ref}}^{\frac{1}{3}} \left(\frac{Pr_{\text{ref}}}{Pr_{\text{w}}} \right)^{0.25}. \tag{2.46}$$

Again, the quotient of Prandtl numbers at the end of the equation can be omitted in cases where a gas is used as working fluid. It can be seen that Elsner et al. (1993) use an exponent of $\frac{1}{3}$ with Pr while Michejew (1964) uses a value of 0.43. Obviously, the discrepancy in Re_{critical} described above for the turbulent case also exists in the laminar case. Furthermore, Elsner et al. (1993) state that reference temperature for calculation of fluid properties in the laminar case is the mean value of fluid temperature and temperature of the plate whereas Michejew (1964) also uses the undisturbed (upstream) temperature of the fluid alone as reference temperature in the laminar case. Moreover, Elsner et al. (1993) again specifies a range of applicable Prandtl numbers of $0.1 \leq Pr \leq 10^3$.

Michejew (1964) simplifies equation (2.45) for laminar flow with air as working fluid so that,

$$Nu = 0.57\, Re^{0.5}. \tag{2.47}$$

Fishenden and Saunders (1950) also present correlations for forced convection due to a flow over a plane surface. For this purpose, they sum up the results from Colburn (1942), Jakob and Dow (1946), and Fage and Faulkner (1931) as well as results from an unpublished work done at the Imperial College of Science and Technology, London. The length of the plate in the direction of flow is used as characteristic length and the mean film temperature as reference temperature for calculation of fluid properties like conductivity or viscosity. The critical Reynolds number Re_{critical} is given as 2×10^4. For the turbulent region,

$$Nu = 0.036\, Re^{0.8} Pr^{0.33}. \tag{2.48}$$

For air and other gases with similar Prandtl number, Fishenden and Saunders (1950) suggest to simplify above expression and use equation (2.44) which is also recommended in identical form by Michejew (1964).

For laminar flow, Fishenden and Saunders (1950) suggest,

$$Nu = 0.66\, Re^{0.5} Pr^{0.33} \tag{2.49}$$

which is identical to equation (2.46) if only the first two digits are taken into consideration and if the quotient of Prandtl numbers at the end of the equation is neglected.

For gases, Fishenden and Saunders (1950) suggest to further simplify the correlation and use

$$Nu = 0.6\, Re^{0.5}. \tag{2.50}$$

Re_{critical} as well as the corresponding critical velocity for two different lengths of a plate are summarized in table 2.2.

Glück (2007) investigated convective heat transfer at surfaces of TABS. For describing forced convection, Glück (2007) suggests to use the equation given by

Table 2.2: Critical Reynolds number used by different authors for distinction between laminar and turbulent forced convection correlations and the corresponding critical velocity for plates of two different lengths.

Author	Re_{critical}	corresponding U_{critical}	
		for $L = 1\,\text{m}$	for $L = 10\,\text{m}$
	[-]	$[\text{m}\,\text{s}^{-1}]$	$[\text{m}\,\text{s}^{-1}]$
Fishenden and Saunders (1950)	2.0×10^4	0.30	0.03
Michejew (1964)	1.0×10^5	1.52	0.15
Elsner et al. (1993)	3.5×10^5	5.31	0.53

Pohlhausen, Krouzhiline, Petukhov, Popov, Gnielinski, Krischer, Kast which is also given in the form $Nu = Nu\,(Re\,Pr)$. This correlation is regarded as an appropriate approximation of Nusselt number for both a laminar and a turbulent flow regime. It can be used with plates in arbitrary positions which are subject to a flow and has the form,

$$Nu = \left[0.441\,Re\,Pr^{0.667} + \frac{Re^{1.6}\,Pr^2}{\left[27.027 + 66.027\,Re^{-0.1}\left(Pr^{0.667} - 1\right)\right]^2} \right]^{0.5} \tag{2.51}$$

Equation (2.51) is valid for $10 < Re < 10^7$ and $0.6 < Pr < 2000$. The characteristic length L_c is the length of the plate (in direction of the flow) and velocity should be measured in the undisturbed environment—that is upstream of the plate. The reference temperature is taken as the arithmetic mean value of air temperature at the upstream edge of the plate and air temperature at the downstream edge. For convenience, Glück (2007) suggests that solely air temperature at the upstream edge of the plate could be used as reference temperature. Fluid properties are calculated at the reference temperature.

Figure 2.5 shows convective heat transfer coefficients calculated with equation (2.51) for the case of forced convection and two different characteristic lengths (1 m and 10 m) of a heated plate already used in table 2.2. Velocity U ranges between $0.1\,\text{m}\,\text{s}^{-1}$ and $1.0\,\text{m}\,\text{s}^{-1}$. For the short length of the plate shown in figure 2.5a, significantly larger values for h_c are obtained than for the longer plate shown in figure 2.5b. As can be expected, the correlations valid for laminar flow

yield smaller values than those for turbulent flow in both cases. Furthermore, the approximation of Glück (2007) given in equation (2.51) leads to the largest values for convective heat transfer coefficients. However, the discrepancy between this equation and the correlation for turbulent flow by Fishenden and Saunders (1950) diminishes with increasing plate length. The discrepancy between values for h_c obtained with equation (2.46) given by Elsner et al. (1993) for laminar flow and values for h_c from equation (2.45) suggested by Michejew (1964) is caused by aforementioned differences and can be considered marginal in both cases. Yet, for the longer plate with a length of 10 m the influence of the different values for $Re_{critical}$ can clearly be seen.

Both the equation for laminar and the equation for turbulent flow suggested by Elsner et al. (1993) are plotted in figure 2.5b. At $U = 0.53\,m\,s^{-1}$, a sharp change from laminar to turbulent is visible. The turbulent equation of Elsner et al. (1993) then follows the equation of Fishenden and Saunders (1950) for turbulent flow which covers the whole range from $0.1\,m\,s^{-1}$ to $1.0\,m\,s^{-1}$ due to the fact that Fishenden and Saunders (1950) suggest the smallest value for $Re_{critical}$. On the other hand, the laminar equation of Michejew (1964) leads to nearly identical values as the laminar equation of Elsner et al. (1993) but the critical Reynolds number is already reached with a much smaller velocity. Thus, the laminar equation of Michejew (1964) could only be used up to $U = 0.15\,m\,s^{-1}$ before the point of transition is reached and the turbulent equation should be used. This turbulent equation of Michejew (1964) is not displayed in the figure since the author uses the same equation as the one given by Elsner et al. (1993) which again is shown in figure 2.5b.

It can be concluded that already a small discrepancy in a single parameter such as the range which is regarded as valid for applying a correlation can lead to large discrepancies in the resulting values for convective heat transfer coefficient even if an otherwise identical expression is used for the calculation. Furthermore, it can be concluded that forced convection heat transfer is significantly larger than natural convection at a heated ceiling even for relatively small values of velocity by comparing the values shown in figure 2.5 to the values for natural convection shown in figure 2.4 on page 24. It will be shown in chapter 6 that a very good agreement between the experimental results and values from the correlation of Glück (2007) given in equation (2.51) can be achieved.

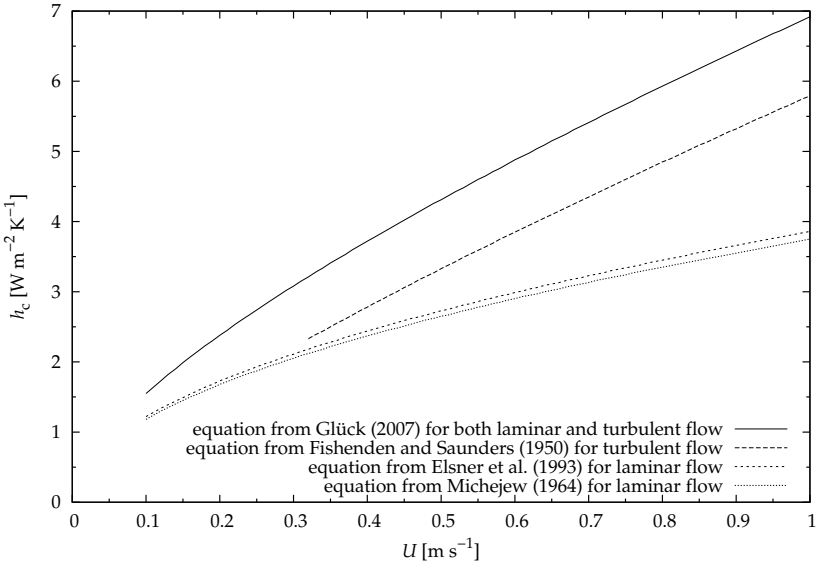

(a) Characteristic length of 1 m.

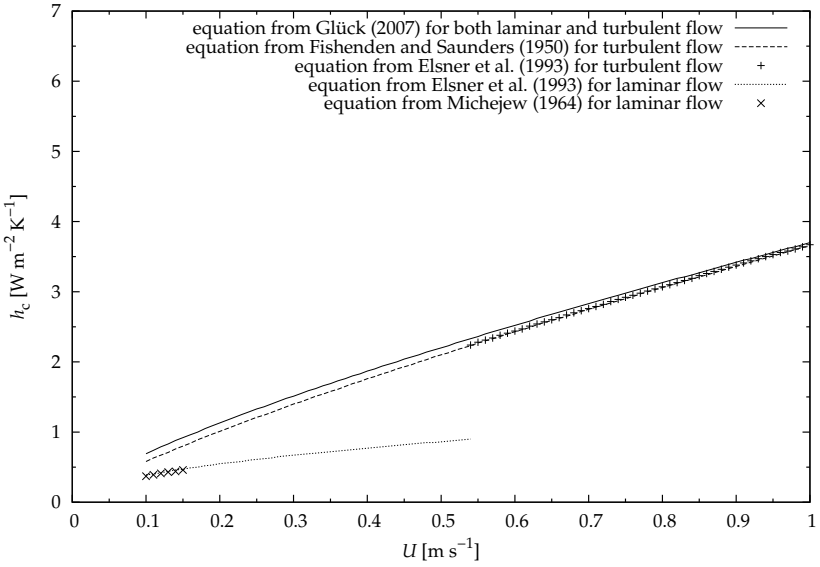

(b) Characteristic length of 10 m.

Figure 2.5: Convective heat transfer coefficients for two plates of different characteristic length from existing forced convection correlations with $\vartheta_{\text{plate}} = 30\,^{\circ}\text{C}$, $\vartheta_{\text{air,upstream}} = 20\,^{\circ}\text{C}$ and $\vartheta_{\text{air,mean}} = 25\,^{\circ}\text{C}$.

2.4.4 Mixed convection

In addition to their outcomes for natural convection which have already been presented in section 2.4.2, Awbi and Hatton (2000) also present results for mixed convection from heated room surfaces. They used their environmental chamber for experiments. The heated surface in the chamber was partially covered by an air jet which was created with a fan box with an adjustable nozzle which contains a variable speed fan. Due to this fan box, air movement in the experimental facility was increased and mixed convection results were yielded. Awbi and Hatton (2000) investigated mixed convection at walls, floor and ceiling. For the ceiling results, the increase in convective heat transfer was much greater than for floor or walls when compared to natural convection.

Figure 2.6 shows sketches of the different fan configurations used by Awbi and Hatton (2000). The wireframe sketch represents the chamber. The fan box is drawn in dark grey. The wall indicated by the light grey surface is the wall adjacent to the cool compartment already mentioned in section 2.4.2.

Awbi and Hatton (2000) present their results for mixed convection as a combination of natural and forced convection using their natural convection correlations from previous publications shown in equations (2.34) and (2.35). Their work demonstrated that for a small jet velocity at the nozzle ($U \to 0$), mixed convection can be described by natural convection alone and, for a high jet velocity and a small heat flow rate, convection can be described by forced convection alone.

For expression of mixed convection, Awbi and Hatton (2000) use the following equation which was earlier used by Neiswanger et al. (1987) in their investigation of mixed convection in a rectangular enclosure with water as working fluid:

$$h^{3.2}_{\mathrm{c,mixed}} = h^{3.2}_{\mathrm{c,natural}} + h^{3.2}_{\mathrm{c,forced}} \tag{2.52}$$

where

$h_{\mathrm{c,mixed}}$ is the CHTC for mixed convection in $\mathrm{W\,m^{-2}\,K^{-1}}$,
$h_{\mathrm{c,natural}}$ is the CHTC for natural convection in $\mathrm{W\,m^{-2}\,K^{-1}}$,
$h_{\mathrm{c,forced}}$ is the CHTC for forced convection in $\mathrm{W\,m^{-2}\,K^{-1}}$.

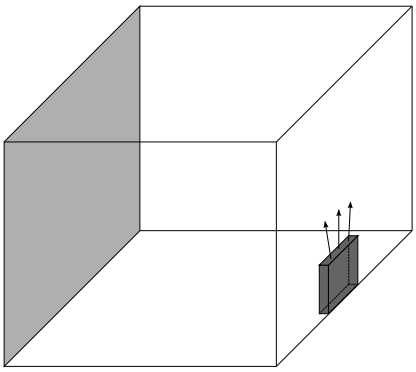

(a) Fan configuration 1 for impinging jet test.

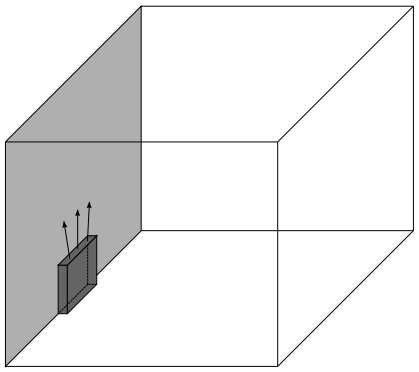

(b) Fan configuration 2 for impinging jet test.

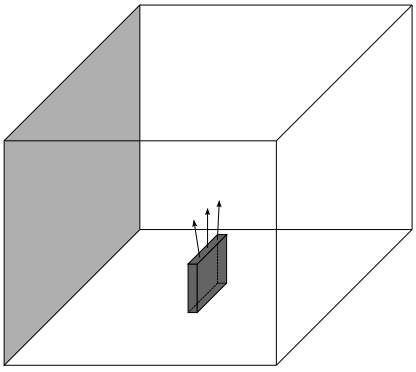

(c) Fan configuration 3 for impinging jet test.

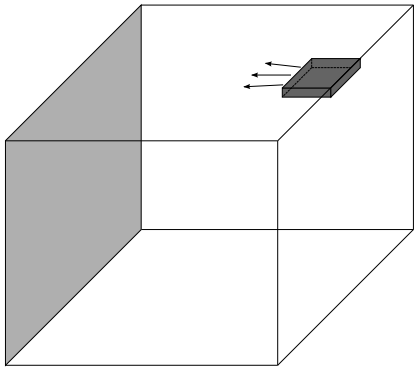

(d) Fan configuration 4 for wall jet test.

Figure 2.6: Position of the fan box in experiments of Awbi and Hatton (2000). (Summary of multiple figures given by Awbi and Hatton (2000).)

Rewriting equation (2.52) and introducing Γ leads to the following expression:

$$\frac{h_{\text{c,mixed}}}{h_{\text{c,natural}}} = \left(1 + \Gamma^{3.2}\right)^{\frac{1}{3.2}} \tag{2.53}$$

where Γ is defined as

$$\Gamma = \frac{h_{\text{c,forced}}}{h_{\text{c,natural}}}. \tag{2.54}$$

Initially, tests with a jet impinging onto a heated ceiling were conducted. In a subsequent, more extensive test series a wall jet was used to simulate mechanical ventilation.

Awbi and Hatton (2000) found out from their experiments that Γ can be written as

$$\Gamma = \left(3.45\,(W)^{0.074}\,\frac{U^{0.772}}{\Delta T^{0.133}}\right) \tag{2.55}$$

where

W is the width of the nozzle opening in m,
U is the velocity at the nozzle opening in $\mathrm{m\,s^{-1}}$, and
ΔT is the surface-to-air temperature difference in K.

By combining the previous equation with equation (2.54) and equation (2.34) which describes natural convection heat transfer, Awbi and Hatton (2000) express forced convection heat transfer coefficient $h_{\text{c,forced}}$ as

$$h_{\text{c,forced}} = 1.35\,(W)^{0.074}\,U^{0.772}. \tag{2.56}$$

Another representation of their results for the heated ceiling is given as

$$\left(\frac{h_{\text{c,mixed}}}{h_{\text{c,natural}}}\right)^{3.2} = 1 + \left(3.45\,(W)^{0.074}\,\frac{U^{0.772}}{\Delta T^{0.133}}\right)^{3.2}. \tag{2.57}$$

Spitler et al. (1991b) presented a full-scale experimental facility which was designed to investigate interior heat transfer in buildings. Primary design objective was the study of convective heat transfer coefficients for a wide range of flow

conditions including both forced and natural convection. The cabin was equipped with a ventilation system which is capable of supplying air with air change rates between $2\,h^{-1}$ and $100\,h^{-1}$. Flow rate is determined by measuring the pressure drop across flow nozzles. The uncertainty in the measured flow rate is given as $\pm 2\,\%$ by the authors. Air can be supplied either via a radial diffuser in the ceiling or via a side wall inlet at medium height in the east side wall. Larger inlet velocities are achieved with the ceiling inlet due to its smaller effective inlet area. The inlet opening which is not used during an experiment is capped. Return air leaves the cabin via an outlet opening at low level in the west side wall.

The surfaces of the facility are divided into 53 heated panels whose surface temperatures are monitored with a least two thermocouples and whose surface temperatures can be individually controlled by a microcomputer which switches panel power on and off.

Due to the individually controllable temperatures of these panels, near isothermal conditions could be achieved and radiant heat transfer inside the experimental facility was minimized.

Spitler et al. (1991b) report that there is no obvious choice for the reference temperature necessary to calculate convective heat transfer coefficients. A detailed discussion of appropriate reference temperatures can be found in Spitler et al. (1991a) where resulting convective heat transfer coefficients for high ventilative flow rates are presented. In aforesaid paper, the authors give a typical uncertainty for convective heat transfer coefficient at a vertical panel of approximately $\pm 3.5\,W\,m^{-2}\,K^{-1}$ using the return air as reference temperature. In the latter publication, a standard error of $0.6\,W\,m^{-2}\,K^{-1}$ is given for convective heat transfer coefficient at the ceiling with a side wall inlet.

Spitler et al. (1991a) investigated flow rates ranging from 15 to 100 air changes per hour (ac/h). The lower value is regarded as the high end of typical air change rates for an occupied office building by the the authors. Experiments included parametric tests with five different flow rates and varied inlet temperature (16 °C, 21 °C, 26 °C). Both inlet locations (ceiling and side wall) were used. Additionally, inlet area was reduced to investigate the effect of jet momentum. Interior room surfaces were at 30 °C for all tests. These boundary conditions meant that:

- All interior surfaces were actively kept at the same temperature. Thus, radiant heat exchange within the facility was minimized.
- There was no heat source installed to achieve a temperature higher than the surface temperature of 30 °C.
- Three different inlet air temperatures were used in the tests. Each inlet air temperature was below the surface temperature of the room. Hence, air temperature at an arbitrary position inside the cabin was limited to $\vartheta_{\text{air,inlet}} \leq \vartheta_{\text{air}} \leq \vartheta_{\text{surface}}$.
- Maximum achievable temperature difference between the surface under investigation and air was 4 K, 9 K or 14 K depending on the boundary conditions of the experimental test.
- The ceiling correlations are valid for (cooler) air under a heated ceiling.
- For the very high ventilative flow rates, air temperature inside the facility might tend to be best described by the well-stirred model.
- For the lower flow rates investigated—especially in combination with the side wall inlet at medium height—effects of stratification might have an influence on results.

The authors present plots of ventilative cooling rates (in W) for different experimental boundary conditions. Among these are the tests with reduced inlet area (33 %, 67 % and 100 % opening area). There is an approximately linear relationship between ventilative cooling rate and air change rate. For a constant volumetric flow rate, the 33 % opening leads to velocities which are three times as high as the ones obtained with the 100 % opening. Hence, the ventilative cooling rate increases with decreasing inlet area. However, at the low end of observed air change rates—that is 15 ac/h—all three opening areas lead to comparable results for ventilative cooling rate. The authors conclude that the effects of jet velocity, momentum and energy become small compared with the effects of buoyancy at low flow rates. Flow visualizations confirmed that in this case the jet was "pouring" into the room and "falling" to the floor.

Spitler et al. (1991a) investigated what temperature is the most appropriate choice for reference temperature in the calculation of convective heat transfer coefficients

by producing four different heat transfer coefficients for four different reference temperatures. These temperatures were:

- Room outlet or return air temperature:
  This temperature was measured by six thermocouples in the outlet duct.
- Bulk air temperature:
  Bulk air temperature is the average value of 896 air temperature measurements using a movable trolley.
- Air temperature adjacent to a surface:
  For this temperature, the values from measurement points where the trolley is closest to the surface under investigation are averaged.
- Local air temperature as a factor of height:
  Here, in a first step temperatures of each horizontal plane of the measurement grid are averaged. Then, temperatures of the horizontal planes adjacent to the panel under investigation are averaged to obtain the reference temperature in this case.

Due to the approximately linear relationship between convective heat transfer coefficients calculated with return air temperature as reference temperature and volumetric flow rate, the authors conclude that outlet temperature is the most appropriate reference temperature. They do not use bulk air temperature as they could observe that there is an increasing deviation between bulk air and outlet air for decreasing flow rates. This deviation is due to the fact that thermal stratification increases with decreasing flow rates. Thermal stratification increases the bulk air temperature but has only a small effect on return air temperature. The higher bulk air temperature leads to a small temperature difference between surface and reference temperature and thus to larger values for h_c. Furthermore, the authors state that the use of outlet temperature as reference temperature lead to the smallest experimental uncertainty in their study. Hence, outlet temperature was used by Spitler et al. (1991a) to calculate convective heat transfer coefficients.

Values for h_c were obtained for different setups. Among these setups, the following two are of interest for this work:

- ceiling with ceiling inlet, and

- ceiling with side wall inlet.

For correlating the convective heat transfer coefficients, a number of characteristic parameters are used by the authors. These characteristic parameters are:

1. Inlet velocity U_0 which is given as

$$U_0 = \frac{\dot{V}}{A_{\text{inlet}}} \tag{2.58}$$

where

U_0 is the inlet velocity in $\mathrm{m\,s^{-1}}$,
$\dot{V}$ is the volumetric flow rate in $\mathrm{m^3\,s^{-1}}$, and
A_{inlet} is the face of the inlet in $\mathrm{m^2}$.

2. Archimedes number Ar which is given as

$$Ar = \frac{\beta\, g\, L_c\, \Delta T_0}{U^2} \tag{2.59}$$

where

Ar is the dimensionless Archimedes number,
β is the coefficient of thermal expansion in $\mathrm{K^{-1}}$,
g is the acceleration due to earth's gravity in $\mathrm{m\,s^{-2}}$,
L_c is a characteristic length in m,
ΔT_0 is the temperature difference between room inlet and outlet in K, and
U is the fluid velocity in $\mathrm{m\,s^{-1}}$.

The authors state that different values for characteristic length and fluid velocity are used by different researchers. In their study, characteristic length was the maximum possible throw of the jet and inlet velocity was used as fluid velocity.

3. Jet Momentum is given as the jet momentum flux into the room $\dot{M}$ which can be written as

$$\dot{M} = \dot{m} \cdot U_0 \tag{2.60}$$

where

$\dot{M}$ is the jet momentum flux in $\mathrm{kg\,m\,s^{-2}}$,
$\dot{m}$ is the mass flow rate in $\mathrm{kg\,s^{-1}}$, and
U_0 is the velocity of the supply air jet in $\mathrm{m\,s^{-1}}$.

A dimensionless representation of the jet momentum is given as the jet momentum number J which can be expressed as

$$J = \frac{\dot{V}\,U_0}{g \cdot V_{\mathrm{room}}}. \tag{2.61}$$

The authors explicitly state that this dimensionless form has been given in a publication by other researchers. No justification for this method of non-dimensionalization other than it is possible is given. They further state that the influence of room volume V_{room} on J could not be investigated and therefore the limits on room size which give accurate results with above equation are not known.

4. Jet energy flux into the room $\dot{E}$ is given as

$$\dot{E} = \dot{m} \cdot U_0^2. \tag{2.62}$$

Spitler et al. (1991a) found out that in their case convective heat transfer coefficients were linearly related to bulk air velocity. However, increased scatter in CHTC was observed for the ceiling with a side wall inlet due to effects of stratification at larger Ar numbers. For this reason, the authors only used data from tests with $Ar < 0.3$—that is the forced convection component becomes more dominant—to obtain a correlation with only one parameter. As they found out that bulk air velocity correlates very well to jet momentum, they chose to give a correlation for CHTC in the form

$$h_{\mathrm{c}} = 0.6 + 59.4 J^{0.5} \tag{2.63}$$

for the ceiling with the side wall inlet and

$$h_{\mathrm{c}} = 11.4 + 209.7 J^{0.5} \tag{2.64}$$

for the ceiling with ceiling inlet. Equation (2.63) is valid for $0.001 < J < 0.03$. The limits for equation (2.64) are given as $0.002 < J < 0.011$ and $Ar < 0.3$. A number of

15 data points was used to obtain the first equation, only 12 data points were used for the second one since the authors had to exclude some data points as already mentioned above.

Archimedes number must be analysed very carefully as different definitions exist. One definition is the one given above in equation (2.59) which is used by Spitler et al. (1991a) and many others. From another definition which is for example used by Lakatos et al. (2008) and Aghajani et al. (2005), Archimedes number can be written as

$$Ar = \frac{\rho\, g\, \Delta\rho\, L_c^3}{\nu^2}. \tag{2.65}$$

Furthermore, Artmann et al. (2010) uses a modified Ar' which does not include a characteristic length and which is no longer dimensionless but has dimensions $\mathrm{K\,s^2\,m^{-6}}$. According to van der Maas (1992), Archimedes number is used in ventilation engineering to characterize non-isothermal jet behaviour. In the field of heat transfer, this value is called Richardson number instead of Archimedes number.

Huhn (2007) uses Richardson number Ri to describe the thermal stratification in hot water storage tanks during charging and discharging processes of the tank. The Richardson number describes whether a process is rather dominated by forced convection or by natural convection. For $Ri << 1$, forced convection dominates. For $Ri >> 1$, natural convection dominates. In between, convective heat transfer can be described by mixed convection. Thus, Richardson number is identical to the definition of Ar given in equation (2.59) and can be written as

$$Ri = \frac{g\beta L_c\,(\vartheta_1 - \vartheta_2)}{U^2} = \frac{Gr}{Re^2}. \tag{2.66}$$

The minimum air change rate which is necessary to achieve the minimum value for the range of J mentioned above in the experimental chamber at Biberach University of Applied Sciences can be calculated by combining equations (2.61) and (2.58) and inserting the geometric data. The air change rate n_J which is necessary to achieve a certain jet momentum number is

$$n_J = \sqrt{\frac{J\, A_{\mathrm{inlet}}\, g}{V_{\mathrm{room}}}}. \tag{2.67}$$

An air change rate of $35\,h^{-1}$ would need to be used to achieve a minimum jet momentum number of 0.001 for the correlation for the side wall inlet given in equation (2.63). An even higher air change rate of $49\,h^{-1}$ would need to be reached for the correlation with the ceiling inlet given in equation (2.64).

As such high flow rates might only be achieved with special ventilative cooling strategies, it must be questioned if the results of Spitler et al. (1991a) can be regarded as representative and applicable for the majority of buildings which might only use simple night-time ventilation strategies like single-sided ventilation via openings in the façade. Such a simple strategy leads to significantly smaller values for air change rates and buildings with TABS do not have to use ventilation at all to discharge the thermal slab but benefit from embedded hydronic systems.

Beausoleil-Morrison (2000, 2001, 2002) states that the field of building simulation has evolved noticeably since its early days. However, he states that one topic which still needs further attention is convective heat transfer at internal building surfaces. He developed an adaptive control algorithm for calculation of convective heat transfer coefficients at internal surfaces which has been implemented within the ESP-r simulation program. His algorithm is based on 28 convection coefficient correlations known from literature. Furthermore, he suggests a new method for modelling mixed convection within mechanically ventilated rooms. This new method is also based on published results from previous works. Depending on the flow regime, an appropriate set of equations is chosen from the pool of implemented correlations for each surface. Beausoleil-Morrison classified indoor air flow into five categories A to E:

A is a convective regime driven by buoyant forces due to different surface-to-air temperature differences—for example caused by chilled ceiling panels or heated walls.

B is a convective regime driven by buoyant forces due to a heating device—for example a radiator—located in a room.

C is a convective regime driven by mechanical forces with an air handling system delivering supply air through various types of diffusers.

D is a convective regime driven by mechanical forces without intentional supply or extract of air from the room.

E is a convective regime driven by mixed flow—that is a combination of both mechanical and buoyant forces.

For further information such as details about a category or a more detailed description of the adaptive control algorithm the reader is referred to the original sources. Here, only the mixed flow convective regime will be investigated closer.

The mixed convection model is based on the correlations of Alamdari and Hammond (1983) and of Fisher (1995). The Alamdari and Hammond correlation for buoyancy-driven convection has already been presented above. The Fisher correlations come from experiments within the same mechanically ventilated test chamber that had already been used by Spitler et al. (1991a). These correlations can be divided into three groups (Beausoleil-Morrison, 2001):

- isothermal rooms with ceiling jets emanating from radial ceiling diffusers,
- non-isothermal rooms with ceiling jets emanating from radial ceiling diffusers,
- isothermal rooms with free horizontal jets emanating from wall air supplies.

Due to the nature of the experiments, the isothermal correlation can only be applied to situations with negligible buoyancy effects which are governed by a mechanically driven jet. Beausoleil-Morrison (2001) also regards the non-isothermal correlation as not generally applicable to mixed flow conditions.

Hence, one can summarize that the Alamdari and Hammond correlations can be used to calculate convection caused by buoyant forces while the Fisher correlation can be used to calculate convection caused by a jet ignoring buoyant forces. As a result, the new mixed convection model by Beausoleil-Morrison (2001) combines these two correlations using the blending method of Churchill and Usagi (1972) as the two correlations are considered as asymptotic solutions for the mixed flow case.

Thus, the following two equations are given:

$$h_{\mathrm{c,mixed,assisting}} = \left(\left(h_{\mathrm{c,forced}}\right)^a + \left(h_{\mathrm{c,buoyant}}\right)^a \right)^{\frac{1}{a}} \tag{2.68}$$

$$h_{\mathrm{c,mixed,opposing}} = \left| \left(h_{\mathrm{c,forced}}\right)^a - \left(h_{\mathrm{c,buoyant}}\right)^a \right|^{\frac{1}{a}} \tag{2.69}$$

where $h_{\mathrm{c,forced}}$ and $h_{\mathrm{c,buoyant}}$ are the CHTCs from the two correlations and a is the blending coefficient which is set to 3. Equation (2.68) is valid for situations when both effects are significant and enhance heat transfer. When buoyant convection and forced convection oppose and thus reduce convective heat transfer, equation (2.69) should be used instead.

Beausoleil-Morrison (2001) suggests calculating convective heat transfer coefficient for mixed convection at the ceiling as

$$h_{\mathrm{c,mixed}} = \left(\left\{ \left[1.4 \left(\frac{\Delta\vartheta}{D_{\mathrm{h}}} \right)^{\frac{1}{4}} \right]^6 + \left[1.63 \Delta\vartheta^{\frac{1}{3}} \right]^6 \right\}^{3\cdot\frac{1}{6}} + \left\{ f_{\mathrm{scale}} \cdot \left(-0.166 + 0.484 n^{0.8} \right) \right\}^3 \right)^{\frac{1}{3}} \tag{2.70a}$$

in case of a buoyant situation and as

$$h_{\mathrm{c,mixed}} = \left(\left\{ 0.6 \left(\frac{\Delta\vartheta}{D_{\mathrm{h}}^2} \right)^{\frac{1}{5}} \right\}^3 + \left\{ f_{\mathrm{scale}} \cdot \left(-0.166 + 0.484 n^{0.8} \right) \right\}^3 \right)^{\frac{1}{3}} \tag{2.70b}$$

for stably stratified conditions.

In equations (2.70a) and (2.70b),

$$f_{\mathrm{scale}} = \frac{\vartheta_{\mathrm{surf}} - \vartheta_{\mathrm{diffuser}}}{\Delta\vartheta}. \tag{2.71}$$

Furthermore,

$h_{\mathrm{c,mixed}}$ is the CHTC for mixed convection in $\mathrm{W\,m^{-2}\,K^{-1}}$,
$\Delta\vartheta$ is the absolute value of the surface-to-air temperature difference in K,
D_{h} is the hydraulic diameter in m as shown in equation (2.15), and
n is the number of room air changes in $\mathrm{h^{-1}}$.

Glück (1997) also describes mixed convection as a combination of natural and forced convection and states that according to Churchill, mixed convection can be expressed as

$$Nu_{\text{mixed}} = \sqrt[3]{Nu_{\text{forced}}^3 + Nu_{\text{natural}}^3} \tag{2.72}$$

and

$$h_{\text{c,mixed}} = \sqrt[3]{h_{\text{c,forced}}^3 + h_{\text{c,natural}}^3} \tag{2.73}$$

respectively, if forced air movement and buoyancy act in the same direction.

For opposing directions,

$$Nu_{\text{mixed}} = \sqrt[3]{\left|Nu_{\text{forced}}^3 - Nu_{\text{natural}}^3\right|} \tag{2.74}$$

and

$$h_{\text{c,mixed}} = \sqrt[3]{\left|h_{\text{c,forced}}^3 - h_{\text{c,natural}}^3\right|} \tag{2.75}$$

respectively. These correlations are also valid if the driving forces act perpendicular to each other.

A simple approximation for CHTC at a horizontal surface with heat flow downwards from Glück (2007) is

$$h_{\text{c}} = 0.54 \left|\vartheta - \vartheta_{\text{air}}\right|^{0.31}. \tag{2.76}$$

In figure 2.7, the mixed convection correlations noted above are compared using boundary conditions of the experimental chamber at Biberach University of Applied Sciences. The correlation of Beausoleil-Morrison (2001) from equation (2.70a) delivers the largest values for h_{c} of up to nearly $5\,\text{W}\,\text{m}^{-2}\,\text{K}^{-1}$. With his correlation for the stably stratified situation from equation (2.70b), values slightly above $3\,\text{W}\,\text{m}^{-2}\,\text{K}^{-1}$ are reached. The approach suggested by Glück (1997) delivers values slightly below $3\,\text{W}\,\text{m}^{-2}\,\text{K}^{-1}$ if L_{c} is set to 0.6 m and a velocity U of $0.2\,\text{m}\,\text{s}^{-1}$ is used. For a higher velocity of $0.3\,\text{m}\,\text{s}^{-1}$, convective heat transfer coefficients from the correlation of Glück (1997) are between the values from the two correlations recommended by Beausoleil-Morrison (2001).

The correlation of Spitler et al. (1991a) for a heated ceiling with a side wall inlet from equation (2.63) leads to smaller values for h_{c} than any of the previously mentioned correlations although an air change rate of $35\,\text{h}^{-1}$ has been used to

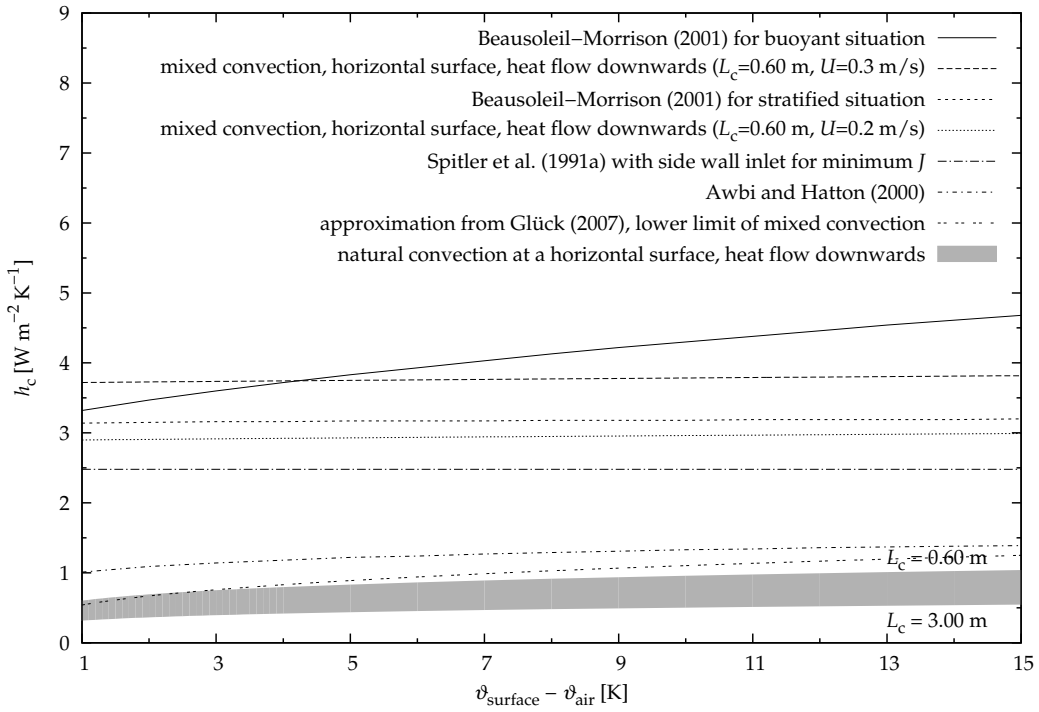

Figure 2.7: Convective heat transfer coefficients from different existing mixed convection correlations.

achieve the minimum jet momentum number provided by the authors while a significantly lower air change rate of only $11\,h^{-1}$ or a velocity of either $0.2\,m\,s^{-1}$ or $0.3\,m\,s^{-1}$ has been used with the other equations. The suggestion of Awbi and Hatton (2000) leads to values for CHTC between $1.0\,W\,m^{-2}\,K^{-1}$ and $1.5\,W\,m^{-2}\,K^{-1}$ for the shown range of $\Delta\vartheta$. Even smaller values are only obtained if the simple approximation of Glück (1997) from equation (2.76) is used which is regarded as the lower limit of mixed convection and the upper end of natural convection. For comparison, natural convection is indicated by the grey band at the bottom of the graph which has been drawn for two different characteristic lengths of 0.6 m and 3.0 m.

2.5 Total heat transfer

Causone et al. (2009) determined total heat transfer coefficients for a radiant ceiling in an experimental facility. They state that a reference temperature for calculation of total heat transfer coefficients has not been clearly defined yet. While air temperature at a specified height was used to calculate convective heat transfer coefficients and AUST was used to calculate radiant heat transfer coefficients (both shown in previous sections), operative room temperature is recommended as the most appropriate reference temperature for calculation of total heat transfer coefficients by the authors. For the practitioners in the field of building services engineering, this is a convenient solution as operative room temperature must for example also be used in calculation of the design heat load according to DIN EN 12831:2003-08. Furthermore, operative room temperature is also used in thermal comfort analysis according to DIN EN ISO 7730:2006-05. A definition of operative room temperature according to DIN EN ISO 7730:1995-09 is given as

$$\vartheta_{\text{operative}} = a\,\vartheta_{\text{air}} + (1-a)\,\vartheta_{\text{rad}} \tag{2.77a}$$

where

$\vartheta_{\text{operative}}$	is the operative room temperature in °C,
a	is a scaling factor that depends on air speed U,
ϑ_{air}	is the room air temperature in °C, and
ϑ_{rad}	is the radiant temperature of the room's enclosing surfaces in °C.

Scaling factor a depends on air speed U as specified below.

If $U < 0.2\,\text{m}\,\text{s}^{-1}$: $a = 0.5$
If $0.2\,\text{m}\,\text{s}^{-1} \leq U < 0.6\,\text{m}\,\text{s}^{-1}$: $a = 0.6$
If $0.6\,\text{m}\,\text{s}^{-1} \leq U < 1.0\,\text{m}\,\text{s}^{-1}$: $a = 0.7$

Glück (2006) mentions that for practical reasons above equation is often simplified to

$$\vartheta_{\text{operative}} = 0.5\,(\vartheta_{\text{air}} + \vartheta_{\text{rad}}) \tag{2.77b}$$

for situations where radiators or panel heating systems are present and to

$$\vartheta_{\text{operative}} = 0.6\,\vartheta_{\text{air}} + 0.4\,\vartheta_{\text{rad}} \tag{2.77c}$$

for situations where heating is provided via heated air.

Moreover, Glück (2006) suggests to use the following definition for a in future which takes into account the total heat transfer of a human body and could thus be used for an improved evaluation of thermal comfort criteria:

$$a = 0.48 + 0.04\,\dot{q}_{\text{total}} + 0.3\,U \tag{2.78}$$

where

a is the scaling factor for the calculation of operative room temperature,
$\dot{q}_{\text{total}}$ is the total heat transfer of a human body in $\mathrm{W\,m^{-2}}$, and
U is the air speed in $\mathrm{m\,s^{-1}}$.

DIN EN ISO 7730:1995-09 proposes that—besides the detailed calculation from equation (2.77a)—operative temperature can be calculated according to equation (2.77b) if the following two conditions are fulfilled:

- air velocities less than $0.2\,\mathrm{m\,s^{-1}}$, and
- difference between mean radiant and air temperature less than $4\,\mathrm{K}$.

Causone et al. (2009) use the term adjusted air temperature for the result of equation (2.77b). Furthermore, they found out that there are negligible differences in calculated total heat transfer coefficients as detailed operative temperature and adjusted air temperature had similar values in their experiments. As long as above criteria are met, adjusted air temperature can reliably be used as reference temperature for the calculation of total heat transfer coefficients.

The authors report a constant value of approximately $5.8\,\mathrm{W\,m^{-2}\,K^{-1}}$ for the total heat transfer coefficient from nine tests with a heated ceiling. For the chilled ceiling, total heat transfer coefficients are significantly larger with values around $13\,\mathrm{W\,m^{-2}\,K^{-1}}$ due to the more pronounced influence of convection.

Table 2.3: Values for C and n in equation (2.79) for different configurations.

geometric configuration	C	n
vertical surface	1.6	0.3
horizontal surface, heat flow upwards	2	0.31
horizontal surface, heat flow downwards	0.54	0.31

Glück (2007) presents correlations for convective heat transfer coefficients and also elaborates how radiant heat transfer could be described. He combines both expressions and defines a total heat transfer coefficient h_{total} as

$$h_{\text{total}} = C \ |\vartheta_{\text{surf}} - \vartheta_{\text{air}}|^n + 5.1 \, \frac{\vartheta_{\text{surf}} - \vartheta_{\text{encl}}}{\vartheta_{\text{surf}} - \vartheta_{\text{air}}} \tag{2.79}$$

The values for C and n in equation (2.79) depend on the geometric configuration at hand and are given in table 2.3.

The first term represents convection and, for a heated ceiling, is identical to h_{c} from equation (2.25). The second term represents the radiant component. As Glück (2007) suggests to use a constant value of $5.1\,\text{W}\,\text{m}^{-2}\,\text{K}^{-1}$ for h_{rad} and as h_{rad} is based on the radiant temperature of the room's enclosing surfaces T_{encl} as reference temperature, it is converted so that air temperature can also be used in the expression for radiation exchange.

The necessity that two temperatures in addition to the surface temperature must be used to calculate h_{total} and the fact that there is no uniform room air temperature but different values for air temperature which for example also depend on type and position of the installed heating and cooling system is regarded as a drawback by Glück (2007) since such information is not available to the building services engineer in most cases.

Thus, Glück (2007) also suggests to use operative room temperature as reference temperature in the calculation of total heat transfer coefficients. Since transferred heat must not change when a different reference temperature is used one can state that

$$\dot{q}_{\text{total}} = h_{\text{total}} \ (\vartheta_{\text{surf}} - \vartheta_{air}) = h^* \ \left(\vartheta_{\text{surf}} - \vartheta_{operative}\right). \tag{2.80}$$

Hence, h^* can be defined as

$$h^* = h_{\text{total}} \frac{\vartheta_{\text{surf}} - \vartheta_{air}}{\vartheta_{\text{surf}} - \vartheta_{operative}}. \tag{2.81}$$

The variable h^* is called heat transfer coefficient according to characteristic base curve (German: Wärmeübergangskoeffizient gemäß Basiskennlinie) and is already known from determination of the thermal output of floor heating systems given in DIN EN 1264-2:1997-11. For an implicit treatment of the thermal conditions in a room, Glück (2007) makes the following suggestions:

1. Operative temperature is the room temperature at the centre of the room at a height of 1.1 m. Radiant temperature and air temperature have approximately the same magnitude.

2. A vertical air temperature gradient $g_{\text{air},10}$ which is valid at $\vartheta_{\text{surf}} - \vartheta_{operative} = 10\,\text{K}$ is introduced. This vertical air temperature gradient can be used to calculate air temperature as a function of height H according to the following equation.

$$\vartheta_{\text{air}} = \vartheta_{\text{operative}} + g_{\text{air},10} \frac{\vartheta_{\text{surf}} - \vartheta_{\text{operative}}}{10\,\text{K}} (H - 1.1\,\text{m}) \tag{2.82}$$

3. A temperature correction $\delta\vartheta_{10}$ which takes into consideration that a temperature difference between the radiant temperature of the enclosing surfaces and operative room temperature might exist and which can be used to calculate the radiant temperature of the enclosing surfaces as shown in equation (2.83).

$$\vartheta_{\text{encl}} = \vartheta_{\text{operative}} - \delta\vartheta_{10} \frac{\vartheta_{\text{surf}} - \vartheta_{\text{operative}}}{10\,\text{K}} \tag{2.83}$$

Some values for vertical air temperature gradient $g_{\text{air},10}$ and temperature correction $\delta\vartheta_{10}$ are presented by Glück (2007). For further possible values of these two variables, the reader is referred to the report by Richter (2003) who investigated thermal comfort for a large number of different situations.

Finally, Glück (2007) calculates h^* as

$$h^* = C \left|\vartheta_{\text{surf}} - \vartheta_{\text{operative}}\right|^n \left(1 \pm \frac{g_{\text{air,10}}}{10\,\text{K}} (1.1\,\text{m} - H)\right)^{n+1} + 5.1 \left(1 + \frac{\delta\vartheta_{10}}{10\,\text{K}}\right) \quad (2.84)$$

where

C	is a constant given in table 2.3,
n	is an exponent given in table 2.3,
ϑ_{surf}	is the temperature of the surface under investigation in °C,
$\vartheta_{\text{operative}}$	is the operative room temperature in °C,
$g_{\text{air,10}}$	is the vertical air temperature gradient at $\vartheta_{\text{surf}} - \vartheta_{operative} = 10\,\text{K}$,
$\delta\vartheta_{10}$	is the radiant temperature correction at $\vartheta_{\text{surf}} - \vartheta_{operative} = 10\,\text{K}$, and
H	is the height above floor in m.

With parameters recommended by Glück (2007) for a heated ceiling, above equation can be simplified to

$$h^*_{\text{hori,down}} = 0.54 \left|\vartheta_{\text{surf}} - \vartheta_{\text{operative}}\right|^{0.31} \left(1 + 0.4\,\text{m}^{-1} (1.1\,\text{m} - H)\right)^{1.31} + 6.12 \quad (2.85)$$

Resulting values for the heat transfer coefficient according to characteristic base curve from equation (2.85) will be shown together with own experimental results in chapter 6.

2.6 Influence of Acoustic Baffles on Heat Transfer

In chapter 1, it has been shown that there often is a need for additional sound absorbing surfaces within a room. Acoustic baffles such as the ones shown in figure 1.1 on page 4 or in figures E.11 and E.12 in appendix E are one way to provide such sound absorbing surfaces. Furthermore, there is only limited data available about the effect of such acoustic baffles on heat transfer at the ceiling. Manufacturers have a demand for experimental evidence about the impact of baffles on heat transfer and need to improve installation guidelines. The little data that is already available will be presented below.

Beck (2008) states that in most buildings which rely on a TABS, the heat transfer between room air and thermal mass mostly takes place at the ceiling. As a result, unobstructed ceiling surfaces are desirable but compete with the need for sound absorbing surfaces. Consequently, acoustic elements which can be coupled with TABS have been developed in recent years. Beck (2008) mentions that there are several technical solutions and highlights two examples, namely

- acoustic elements which can be mounted directly to the ceiling, and
- acoustic elements which are suspended from the ceiling.

Using results from a thermographic camera, he shows that systems which are directly mounted to the ceiling impede heat transfer between ceiling and room air significantly. The surface temperature of the acoustic element is very close to room air temperature while a lower surface temperature (cooling case in summer) can be measured at the unobstructed ceiling. From the larger temperature difference between surface of the unobstructed ceiling and room air it can be concluded that heat transfer between room air and ceiling is more pronounced in the region where no acoustic elements are installed. Beck (2008) states that the influence of acoustic elements on heat transfer can be investigated experimentally and that reduction in heat transfer due to the installation of such elements typically ranges from 5 % to 40 % but could also be significantly larger in the worst case.

Publications based on experimental results about the effect on heat transfer of acoustic baffles such as the ones that are used in this work are not known to exist. In chapter 1, it has already been noted that even manufacturers' installation guidelines have been based on either aesthetic or at most on acoustic considerations but not on any sort of thermal engineering analysis.

Pfrommer and Zitzmann (2008) seem to be the first to investigate the effect of acoustic baffles on the thermal behaviour of an office room using dynamic long-term simulations with CFD. Their adaptive freeze-flow method FREEZECONT was used for these dynamic CFD simulations. The model of an office room is based on VDI 6020 Blatt 1 / Part 1 (2001) and VDI 2078 (1996). Length of the room is 5 m, its width is 3.5 m and its height 3 m.

Pfrommer and Zitzmann (2008) explicitly state that data about the effect of acoustic baffles on the thermal performance of a room are missing and that such knowl-

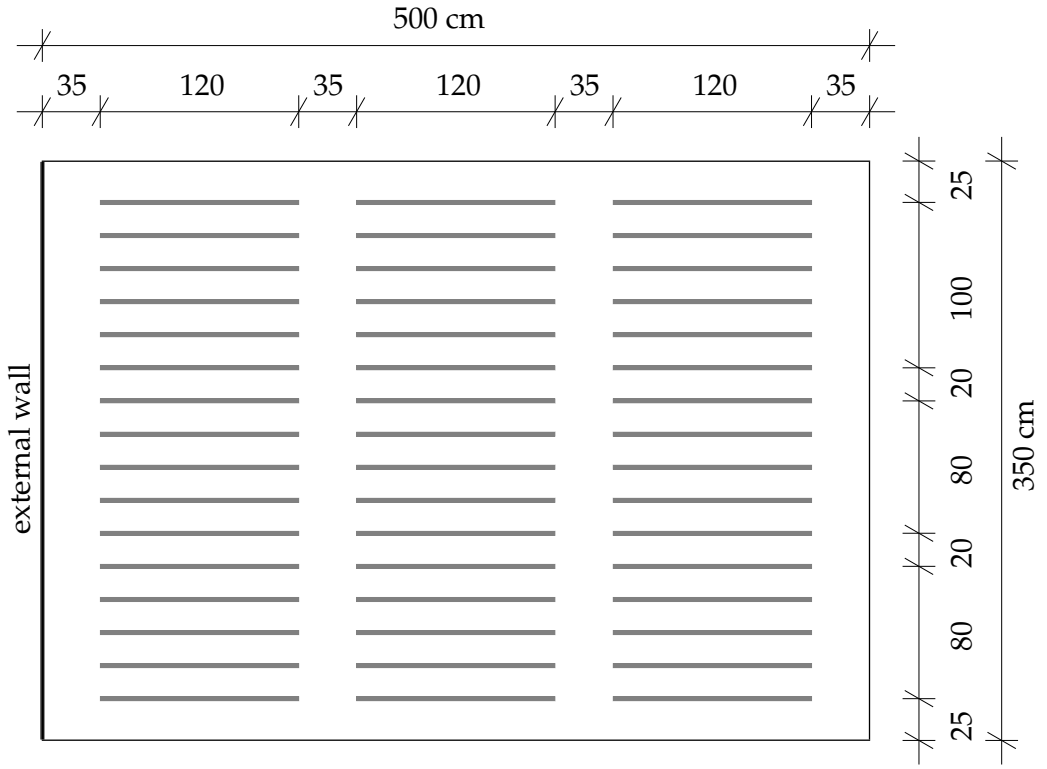

Figure 2.8: Plan showing the arrangement of acoustic baffles in the test room investigated by Pfrommer and Zitzmann (2008).

edge is crucial for manufacturers of such baffles. The authors modified their validated CFD model of an office room in cooperation with OWA Odenwald Faserplattenwerk GmbH (a manufacturer of acoustic baffles) and added 48 baffles with a height of 15 cm, a length of 120 cm and a thickness of 2.5 cm to the model. The baffles are divided into three groups of 16 baffles. The distance between baffle and ceiling is set to 7.5 cm. Emissivity of the baffles is 0.9. The acoustic elements are arranged perpendicular to the external façade. A sketch which shows the arrangement of the baffles can be found in figure 2.8.

Additionally to the setup in which the baffles where arranged perpendicular to the external façade, Pfrommer and Zitzmann (2008) investigated another setup with a parallel arrangement. They found out that a rotation of the baffles only has

negligible influence on the calculated results.

Three different simulations were conducted to investigate the influence of the acoustic baffles on heat transfer:

- eight hour charging process of the thermal slab (summer, daytime)
- eight hour discharging process of the thermal slab (summer, nighttime)
- six day simulation (single-sided ventilation, both with and without TABS)

For the summery daytime situation, initial room conditions were isothermal and the room was constantly heated with a heat source of 600 W positioned at the floor. Part of the heat load was removed by ventilation (0.7 ac/h) and the remaining heat was transferred to the ceiling via radiation and convection. As the baffles act like a heat shield, approximately 7 % less heat is stored in the ceiling compared to a simulation without baffles. The shielding effect is predominantly based on a reduction of convective heat transfer as there is nearly no change in radiant heat transfer to the ceiling.

For the summery nighttime situation, the initial room temperature was set to 30 °C. Cooling was provided by nighttime ventilation using a constant air change rate of 2 ac/h and a constant supply air temperature of 15 °C. According to the authors, heat is removed from the ceiling nearly completely via radiation. Heat transfer via convection only plays a minor role. In this case, the shielding effect of the baffles was quantified as approximately 10 % when compared to the no-baffle case.

Variations in air change rate did not lead to significant changes in the results. The authors conclude that the heat shield effect of the baffles does not depend on air change rate and that the effect is more pronounced in the nighttime situation.

In the six day simulation, the baffles were shown to reduce the average heat transfer from the ceiling by 14 %. Daytime charging of the slab was only reduced by 4 %. Pfrommer and Zitzmann (2008) conclude that the simulation results should be verified by an experimental investigation.

It appears that the investigation of Pfrommer and Zitzmann is the only publication available on this subject despite its importance to the design of passive cooling concepts. Most likely, larger engineering companies have some data and results

from in-house CFD calculations. However, such results are seldomly published as most companies will try to hold an advantage over their competitors. Thus, the influence of such acoustic baffles on heat transfer clearly needs further research and publicly available, experimentally verified results. The aim of this experimental programme has been to provide further insight into this topic and help to develop advanced installation guidelines for practitioners in the field of building services engineering.

2.7 Summary

The literature review has confirmed the need for further research in the field of heat transfer at the ceiling. Researchers have pursued a number of ways to obtain experimental correlations for convective heat transfer coefficients. Among these are, for example, experimental results from flat plates as well as from 3D enclosures. Some correlations are derived from experiments in cabins with isothermal surfaces while for others surfaces with a low emissivity were used to reduce radiation. There have also been differences in the heat sources used. In some experiments, heat was provided with electrically heated plates while hydronic elements were used in others. The common concept of all these experiments is that total heat transfer of the heated surface is measured. Then, conductive losses towards the back and radiation towards other surfaces are subtracted to obtain the convective part. The reported uncertainties in resulting convective heat transfer coefficients show that a great effort must be put in the experimental arrangement and conditions, and conditions should be controlled as much as possible or at least be stable avoiding large temperature swings—for example due to solar load.

Conduction only plays a minor role in a well insulated chamber and can simply be treated as one-dimensional, steady-state conduction through a multi-layer construction. For a detailed calculation of radiation, the view factor method is used. However, radiation is often simplified and linearized by introducing a radiant heat transfer coefficient h_{rad} so that radiation can be described in a similar way to convective heat transfer. A constant value has even been suggested for h_{rad}. However, it has been found out that the suggestions of different researchers lead to a variation of 9 % in calculated radiant heat flux. Furthermore, it can be shown that the

error in radiative transfer may be larger for this experimental investigation and the range of expected temperatures. Hence, a constant value for h_{rad} cannot be used within this work and a detailed calculation of radiation is necessary. This aspect is treated in detail in chapter 5.

Once radiation and conduction have been subtracted from total heat output of the heated surface, convective heat transfer can be found. Correlations for natural convection are given in the form of equation (2.8) or equation (2.10) while forced convection may be described by equation (2.11). Finally, mixed convection is a combination of both natural and forced convection and is thus expressed by combining the two parts using a blending function.

For the calculation of convection correlations, a characteristic length and a reference temperature are necessary. Different definitions of characteristic length can be found in the literature. From a practical point of view, no problems arise from these different definitions as long as authors state which definition is used in their work since values can be converted from one characteristic length to another. The same situation was found with regard to reference temperature ϑ_{ref}. A broad range of temperatures is used as reference temperature—for example some local air temperature or air temperature at the inlet or outlet opening as well as mean air temperature. Convective heat transfer coefficients can again be converted from one reference temperature to another as long as a valid relationship between these two reference temperatures is known.

Several correlations for natural convection at a heated ceiling could be found. Natural convection at a heated ceiling is significantly smaller than at a heated wall or floor. Discrepancies between CHTCs calculated with different correlations for a heated ceiling are a factor of eight. The equations by Awbi and Hatton (1999) are recommended by several other researchers as the most appropriate for natural convection in indoor environments.

Forced convection is similarly complex. Again, many experiments were done with flat plates. There are often only small discrepancies between two different correlations, for example, a different range of validity of the equation or a slightly different exponent. However, even such small differences can lead to large deviations in calculated CHTCs as illustrated in figure 2.5.

In figure 2.7, discrepancies between different correlations for mixed convection have been shown. Some correlations result in CHTC values which are approximately four times as large as the smallest values. The correlation suggested by Beausoleil-Morrison (2001) for a buoyant situation delivers the largest values while the simple approximation of Glück (2007) yields the smallest values.

Total heat transfer by both convection and radiation is described by the total heat transfer coefficient h_{total}. Operative room temperature is recommended as the most suitable reference temperature in this case. Causone et al. (2009) report a constant value of approximately $5.8\,\mathrm{W\,m^{-2}\,K^{-1}}$ for total heat transfer coefficients from nine tests with a heated ceiling. Glück (2007) goes a step further and suggests to use the heat transfer coefficient according to characteristic base curve h^* which is defined in DIN EN 1264-2:1997-11.

The literature review has also included the topic of the influence of acoustic baffles on heat transfer at the ceiling. Beck (2008) states that reduction in heat transfer at the ceiling due the installation of acoustic elements typically ranges from 5 % to 40 % but could also be significantly larger in the worst case.

Publications from an experimental work on the influence of acoustic baffles as the ones used in this work on heat transfer at the ceiling are not known to exist. Pfrommer and Zitzmann (2008) seem to be the first to investigate the effect of such acoustic baffles on the thermal behaviour of an office room using dynamic long-term simulations with CFD. They quantified the shielding effect of the baffles during the nightly discharging of a thermal slab as approximately 10 % to 14 % when compared to the no-baffle case. The authors conclude that these simulation results should be verified by an experimental investigation. Consequently, this has been one of the primary aims of the work reported in this thesis.

3 Experimental Method

3.1 Introduction

In chapters 1 and 2, it was shown that additional research on heat transfer is necessary for a good design of low energy cooling concepts which use technologies like night-time ventilation or TABS. Special emphasis must be put on heat transfer at the ceiling.

Therefore, an experimental programme for investigation of heat transfer at the ceiling has been developed. A new experimental chamber appropriate for carrying out this programme has been built as part of this work at Biberach University of Applied Sciences, Germany. Throughout the rest of this document, the terms "(experimental) chamber" and "(experimental) cabin" are used equivalently. In this chapter,

- the experimental design is explained,
- the experimental chamber and associated measurement systems are presented,
- the different experimental arrangements and boundary conditions are introduced.

The experimental design makes use of an electrically heated plate which forms part of the ceiling of the cabin and which is used as a heat source during the various test series.

The description of the chamber includes its location and size, sensor positions, used materials as well as associated systems—for example for ventilation of the cabin.

Measurement devices include systems for temperature measurement, equipment for measuring velocities inside the cabin as well as flow rate. Moreover, the power meter for measurements of the heat output of the electrically heated plate is presented. Thereafter, results from the calibration of the temperature measurement system are shown.

The following experimental test series will be introduced:

- Test series with an unobstructed heated ceiling
  - without ventilation for investigation of natural convection,
  - with ventilation and modified inlet opening for investigation of forced convection,
  - with ventilation and regular high-level slot inlet for investigation of mixed convection.
- Test series with acoustic baffles at the heated ceiling
  - without ventilation to investigate the effect of acoustic baffles on natural convection,
  - with ventilation and regular high-level slot inlet to investigate the effect of acoustic baffles on mixed convection.

3.2 Experimental Design

The aim of the experiments is to investigate heat transfer between an electrically heated plate at the ceiling and the indoor environment as this configuration can be compared to the conditions present when the thermal mass of a building is discharged—for example by flushing the room with ambient air during nighttime. The heat balance at the surface of the hot plate is sketched in figure 3.1. As all experiments are run until steady-state conditions are achieved, heat storage effects can be neglected. The surface under investigation is the surface of the electrically heated plate at the bottom of the shown cross section. This surface is subject to an incoming heat flux $\dot{q}_{\mathrm{el}}$. Since $\dot{q}_{\mathrm{el}}$ is a main experimental parameter, its magnitude must be determined as accurately as possible. As an electrically

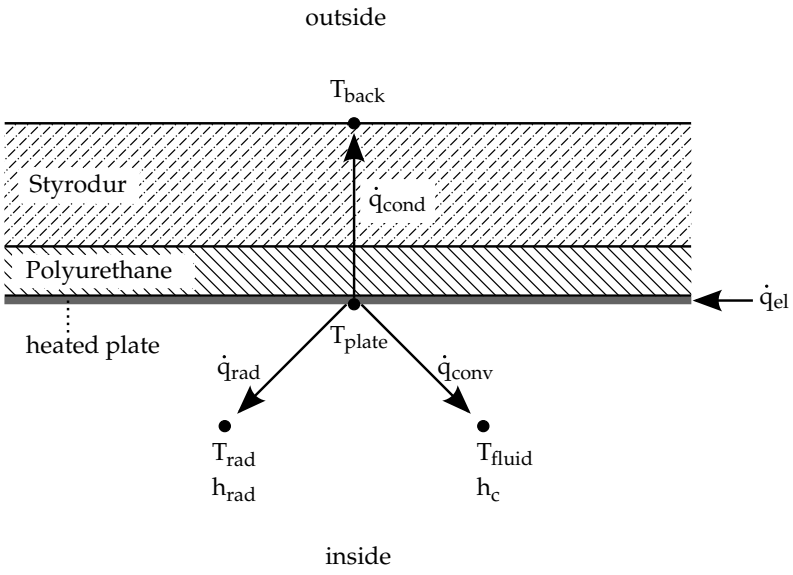

Figure 3.1: Heat exchange between a hot plate at the ceiling of the experimental chamber and the indoor environment.

heated plate is used in the experiments, heat input to the hot plate (and thus total heat output under steady state conditions) can be measured very precisely with a power meter.

Heat is transported away from the surface by three different phenomena. The first phenomenon is heat conduction $\dot{q}_{\text{cond}}$ through the fabric towards the outside. As the interest of this work is in heat transfer in indoor environments, conductive losses towards the back are undesired in the experiment. Thus, insulation materials (Styrodur and Polyurethane) are used for construction of the enclosing surfaces of the experimental chamber so that conduction is reduced as much as possible. Conductive losses can easily be calculated by inserting known properties of the used materials like their conductivities and thicknesses as well as the temperature difference between the inner surface T_{plate} and the temperature at the back T_{back} into equation (2.1) for one-dimensional conductive heat transfer which is described in chapter 2.

The second phenomenon is radiation exchange $\dot{q}_{\text{rad}}$ between the surface of the hot plate and the other enclosing surfaces of the cabin. Radiation transfer can be complex depending, for example, on geometry or the number of surfaces participating in radiant heat transfer. Hence, chapter 5 is solely devoted to radiant heat transfer and to the method used to determine its magnitude in the experiments. What must be known for a proper calculation of $\dot{q}_{\text{rad}}$ are the temperatures of the other participating surfaces. These temperatures must be measured in the experiment. Many authors—among them are Glück (2007) and Causone et al. (2009)—describe radiant heat transfer in terms of a radiant heat transfer coefficient h_{rad} and a (simplified) radiant temperature T_{rad} derived from the temperatures of the other enclosing surfaces. This is also explained in detail in chapter 2.

The third and last way by which the surface loses heat is by convection to the adjacent fluid. By subtracting conduction and radiation from the total heat output, the remaining convective heat flux $\dot{q}_{\text{conv}}$ can be calculated. Finally, convection can be described as shown in equation (3.1) by the convective heat transfer coefficient h_{c} which is obtained from dividing $\dot{q}_{\text{conv}}$ by the difference between the surface temperature T_{plate} and an appropriate reference temperature T_{ref}. A discussion about possible reference temperatures for describing convective heat transfer can be found in chapter 2. In the end, resulting convective heat transfer coefficients from the different test series can be compared to the base case—that is natural convection in an unventilated chamber without any obstacles at the ceiling—or to correlations presented in the literature review.

$$h_{\text{c}} = \frac{\dot{q}_{\text{conv}}}{T_{\text{plate}} - T_{\text{ref}}} = \frac{\dot{q}_{\text{el}} - \dot{q}_{\text{rad}} - \dot{q}_{\text{cond}}}{T_{\text{plate}} - T_{\text{ref}}} \tag{3.1}$$

3.3 The Experimental Chamber

The experimental chamber is situated in the building *Technikum* at Biberach University of Applied Sciences, Germany. It has been built inside an existing glass compartment which is located inside the *Labor für Gebäudesimulation G1.02*. Figure 3.2 shows a plan of the first floor of the *Technikum* with the laboratory room and the glass compartment. The glass compartment within which the experimental

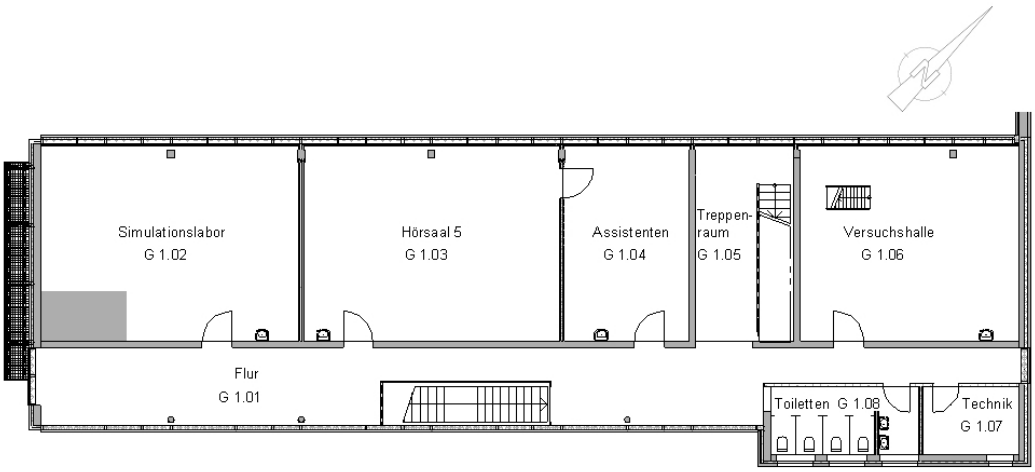

Figure 3.2: Floor plan of the building *Technikum* showing the first floor and the laboratory room G1.02. The glass compartment is indicated by the solid grey rectangle in the plan. (drawing based on: Koenigsdorff and Sedlak (2005))

chamber has been built is in that corner of the laboratory which is formed by the external wall facing southwest and the internal wall to the hallway. It is indicated by the solid grey rectangle in the plan.

Figure 3.3 shows the condition of the laboratory with the glass compartment prior to any construction work. Originally, the compartment was built as a test facility for interchangeable façade elements. In the photo, one can see the prototype of a double façade element with lowered blinds which remained in place and which is the only external wall of the chamber. The glass compartment is 3.53 m in length, 2.06 m in width, and 3.20 m in height (internal dimensions). The experimental chamber used for the work described here has been built inside this glass compartment. Hence, there were some restrictions on the maximum size of the new cabin. On the one hand, internal dimensions of the new cabin needed to be as large as possible so that its size resembled a small single cell office space, on the other hand the cabin could not exceed a certain size as it needed to be possible to carry out necessary construction and maintenance work or future modifications without damaging the existing structure. Hence, internal dimensions of the new

Figure 3.3: Photo of the laboratory showing the glass compartment before the construction of the experimental chamber started.

facility were set to a length of 2.34 m, a width of 1.65 m, and a height of 2.23 m. Although the internal width is limited, the new experimental chamber is still regarded as sufficiently wide due to the fact that the experimental design makes use of a slot air inlet opening which is used to provide supply air across the whole width of the cabin. Thus, a quasi-2D air flow pattern can be achieved inside the experimental chamber. A sequence of photos which document the evolution of the chamber can be found in appendix E.

The schematic shown in figure 3.4 provides an overview of the experimental chamber, the associated ventilation system and the hot plate which is used as a heat source inside the cabin. The aforementioned laboratory (room G1.02) is indicated by the outermost frame in this schematic. The cabin and the ventilation system are

built inside the glass compartment which is indicated by the second frame in the schematic. For ventilation, an inlet opening at high level and an outlet opening at low level are installed in the chamber. Supply air intake is in the glass compartment. The heat exchanger installed at the intake allows the temperature of the supply air to be manipulated. However, control of the supply air temperature is limited as there is no closed-loop control system with feedback from an air temperature sensor. The only way to achieve a certain rise or drop in supply air temperature is by controlling the bath temperature of the calibration thermostat bath to which the heat exchanger is connected to by a water circuit. As the duct system is not insulated, the rise or drop in inlet air temperature at the supply air inlet opening inside the cabin that can be achieved is limited but nonetheless measurable. Two parallel fans deliver the air from the intake to a supply air box. Figure E.9 on page 245 shows the return air box which has the same shape as the supply air box, so that it is possible to reverse the configuration of inlet and outlet openings in future experiments. This alternative configuration is documented in figure E.14 on page 250. The air box is connected to the slot inlet inside the experimental chamber via nine parallel ducts so that incoming air is distributed across the whole width of the experimental chamber. The slot inlet opening itself is covered with a metal grille. Return air leaves the cabin through the outlet opening and passes through an air box identical to the one installed in the supply duct. Having passed through the air box, return air is blown into the laboratory. At the very end of the return air duct, a rotating vane anemometer was installed for measuring the flow rate of the ventilation system. It is possible to achieve flow rates of up to nearly $160\,m^3\,h^{-1}$ which is equivalent to approximately 18 ac/h.

An *EB-Therm* sheet heating element which is embedded between two metal plates, is used as a heat source in the cabin. The element offers a purely resistive load (that is a power factor of unity). The front surface of the plate is sprayed with *OBI Classic Thermolack*. Its length is 1.65 m—equal to the internal width of the cabin—and its width amounts to 0.6 m which leads to a surface area of $0.99\,m^2$. More details on the heating element and the used lacquer can be found in section 4.5 where an experiment for determining the emissivity of the hot plate is presented. Emissivity was found out to be 0.84. Heat output of the element can reach up to $150\,W\,m^{-2}$. However, in most experiments it ranged between $15\,W\,m^{-2}$ and

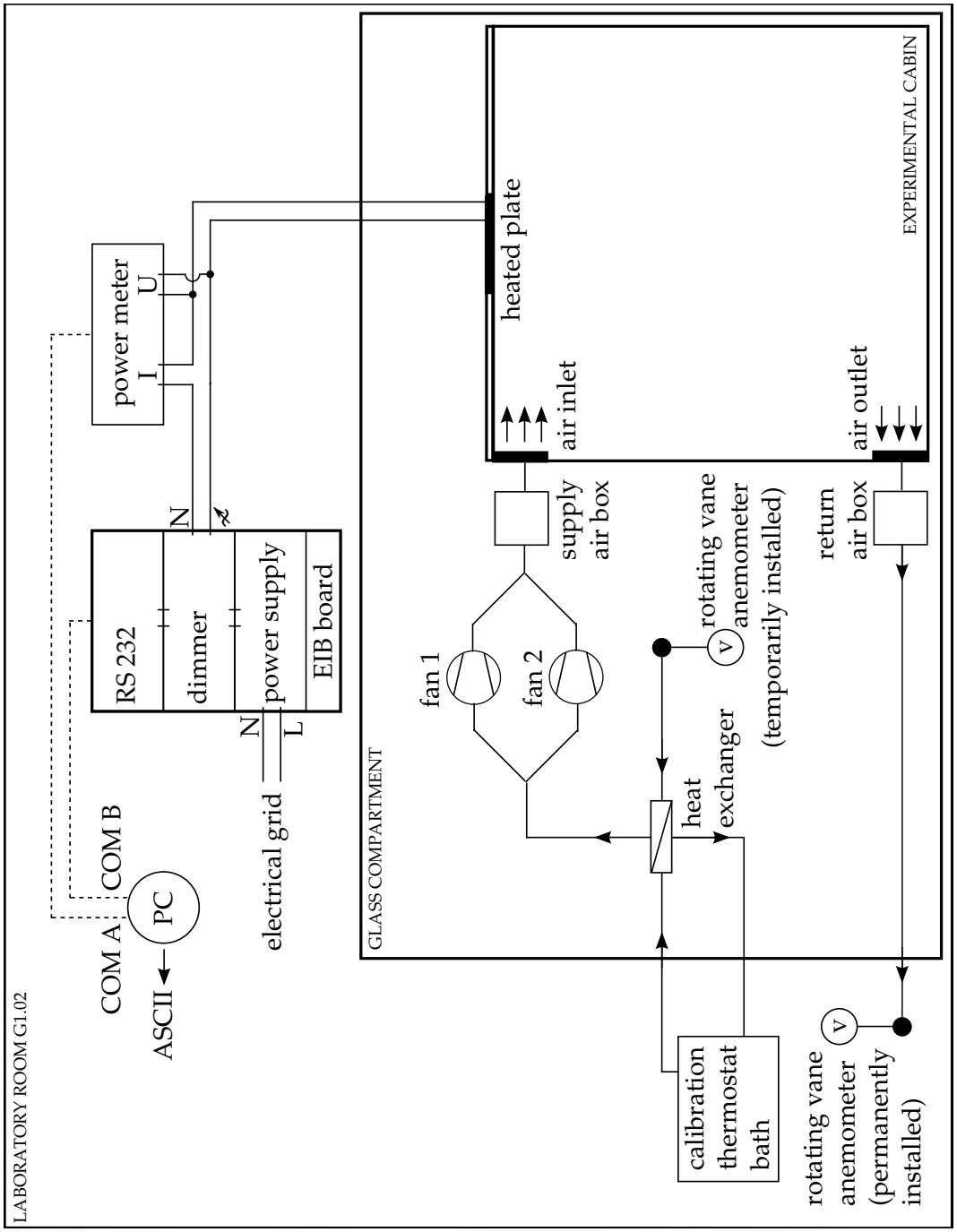

Figure 3.4: Schematic diagram showing the experimental chamber, the ventilation system as well as the hot plate and the instrumentation.

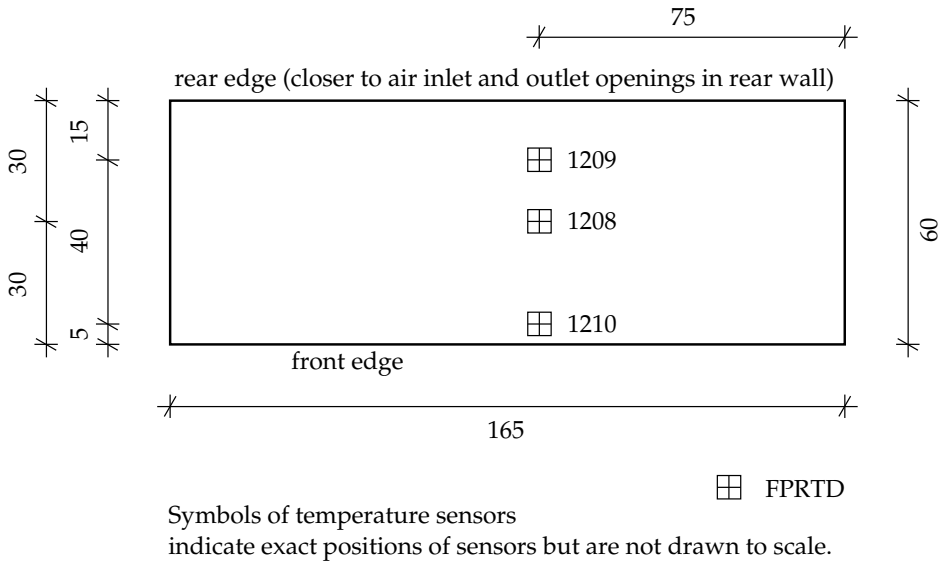

Figure 3.5: Hot plate and positions of the foil platinum resistance temperature detectors (FPRTD) used for measuring its front surface temperature.

100 W m^{-2} as heat fluxes in passive cooling applications—for example using a thermal slab activation—normally are much lower with achievable values of 30 W m^{-2} or 40 W m^{-2}. Surface temperature of the hot plate is measured with three foil temperature sensors which are attached to the front surface of the hot plate. The positions of the temperature sensors are shown in figure 3.5. More details on the temperature measurement system will be given in section 3.4.1 on page 77.

The hot plate is connected to a high-precision power meter described in the following section, and to an EIB board consisting of three elements:

1. a power supply unit which is connected to the electrical grid,
2. a controllable dimmer for adjusting heat output, and
3. a RS-232 interface which is used to connect the board to a computer.

The computer is used to adjust the dimmer to a desired setting at the beginning of an experiment. Thus, the heating element is supplied with a specific rate of electricity which is accurately measured with the power meter. The power meter

is connected to the same computer as the dimmer using a second serial port so that logged values can be stored in an ASCII file which is used for evaluating experiments.

Two types of insulation material have been used for the enclosing surfaces of the experimental chamber:

- *BASF Styrodur 3035 CS* insulation panels
  material : extruded polystyrene foam (XPS)
  conductivity : 0.035 $W\,m^{-1}\,K$ (*Wärmeleitgruppe* WLG 035)
  panel length : 1265 mm
  panel width : 615 mm
  panel thickness : 50 mm
  panel colour : green
  Subsequently, this material will be referred to as *Styrodur* or *Styrodur panel*.

- *KORFF Superwand DS* sandwich element insulation panels
  material : polyurethane core and aluminium clad paper cover
  conductivity : 0.025 $W\,m^{-1}\,K$ (*Wärmeleitgruppe* WLG 025)
  panel length : 1250 mm
  panel width : 800 mm
  panel thickness : 20 mm
  panel colour : white
  Subsequently, this material will be referred to as *PUR* or *PUR panel*.

All four walls have a total thickness of 7 cm and are constructed with one layer of Styrodur on the outside and one PUR panel on the inside. With a thickness of 14 cm, twice as much insulation material is used for floor and ceiling. Technical drawings showing the layer composition together with position of installed temperature sensors can be found in appendix A. The ceiling consists of two layers of PUR on the inside followed by two layers of Styrodur on the outside. The floor is composed of the same number of layers. However, layer composition differs from the ceiling insofar as materials alternate starting with one layer of PUR inside the cabin and ending with a layer of Styrodur. Floor insulation of the cabin is directly

attached to a wooden board of 21 mm thickness which serves as a ground plate, and which itself is laid out directly on the linoleum of the existing floor. Due to the construction chosen and the materials used, heat bridge and edge effects are negligibly small and do not have to be treated separately in the analysis of experiments.

Above the cabin, an additional layer of particle boards which carries the ventilation system has been suspended from the existing concrete ceiling using all-thread rods. The air gap between the particle boards and the top surface of the insulated ceiling of the cabin is approximately 15 cm.

The joints of all insulation panels which are visible inside the cabin are sealed with aluminium tape. Furthermore, all joints beneath the innermost layer of insulation are also sealed. Due to these two sealed layers of insulation, there is no detectable air leakage through the enclosing surfaces of the cabin. Measurements conducted after the completion of the experimental chamber which confirm its airtightness are presented below in section 3.4.3.

Figure 3.6 shows a plan of the cabin. The closable opening in the front wall which is the only way to enter the cabin is indicated by a dashed line. The electrically heated plate which serves as a heat source inside the experimental facility is mounted to the ceiling covering the whole width of the cabin. Inlet and outlet openings of the ventilation system also cover the whole width of the cabin and are both installed at the rear wall. The inlet opening is located at high level directly beneath the ceiling while the outlet opening is at low level directly above the floor. Thus, single-sided ventilation can be investigated. For measuring surface temperatures, chip platinum resistance temperature detectors (CPRTDs) and foil platinum resistance temperature detectors (FPRTDs) are used. Six sensors are installed at each wall at three different heights. Three sensors are used to measure ceiling temperature in the rear half of the cabin and three further sensors are intended for doing the same in the front half. Due to the limited total number of sensors, only five FPRTDs are installed on the floor. Detailed, dimensioned drawings showing the type of sensor, its exact position as well as the sensor's unique four digit identification number are given in appendix A. The first digit of the identification number indicates the data acquisition and switch unit (DAQ) and thus the file to which the value is saved. The second digit represents the device's

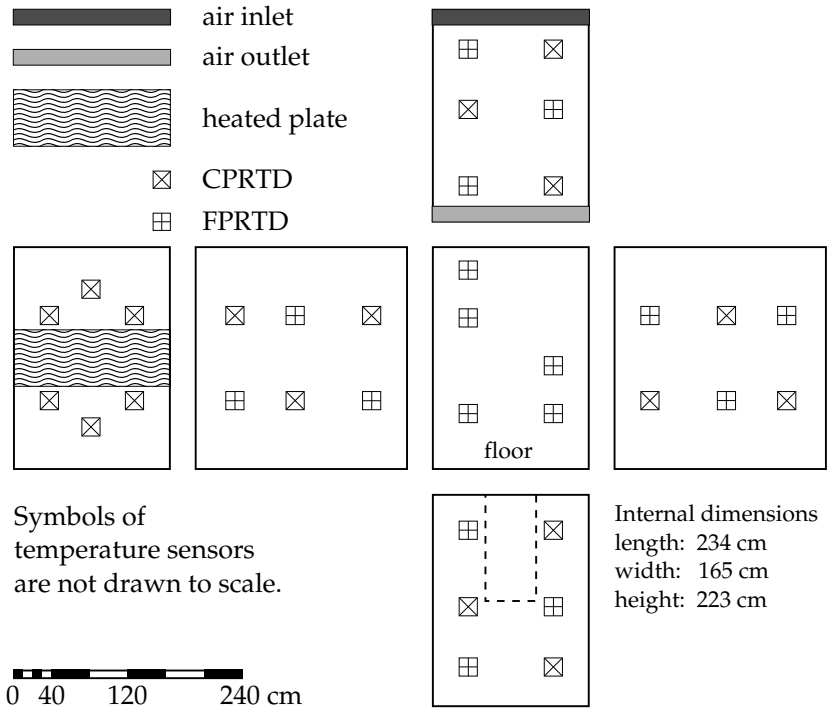

Figure 3.6: Plan of the cabin showing the heated plate, inlet and outlet openings of the ventilation system in the rear wall as well as positions of surface temperature sensors and the closable opening in the front wall.

plug-in module to which the sensor is connected. The associated data logging channel is expressed by the last two digits. More information on the temperature measurement system can be found in the following section.

Besides surface temperatures, indoor air temperatures are measured with a total of 18 chip sensors as shown in figure 3.7. Each sensor is installed in the symmetry plane at a width of $y = 82.5\,\text{cm}$. Sensors are installed in such a way that three temperature profiles are measured:

- one profile below the hot plate,
- one profile in the rear of the cabin close to the inlet and outlet openings,
- one profile in the front of the cabin.

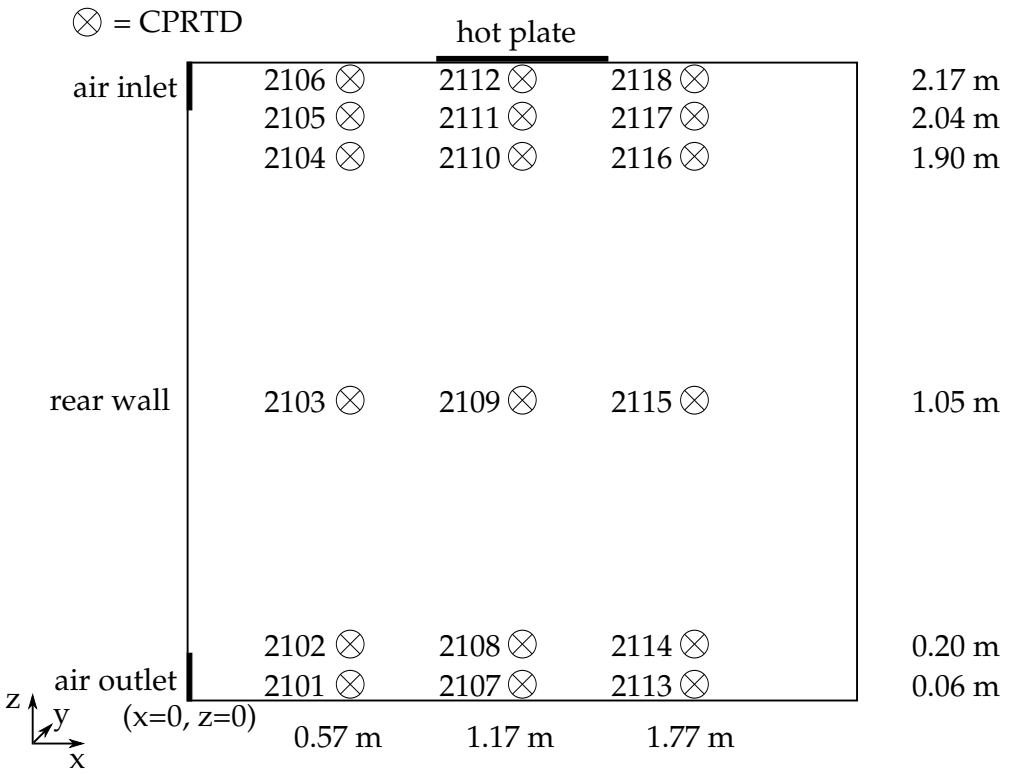

Figure 3.7: Section of the cabin showing positions of air temperature sensors and their ID numbers. Each sensor is placed in the symmetry plane at $y = 82.5\,\text{cm}$.

3.4 The Measurement Systems

3.4.1 Temperature Measurements

For measuring surface and air temperatures, a total of 85 platinum resistance thermometers (PRTs) have been permanently installed by the author of this work during the construction of the cabin. A further 27 PRTs have been added by a student towards the end of this work. Thus, at present time the number of sensors installed in the experimental chamber amounts to 112 PRTs.

Three types of PRTs have been installed:

1. *JUMO* Platinum Chip Temperature Sensors with Connection Wires, design: PCA/M, type: PCA 1.2003.1M, tolerance class: 1/3 DIN B. Throughout this work, always this type of sensor is meant when chip sensors (or CPRTDs) are referred to.
2. *JUMO* Platinum Foil Temperature Sensors, design: PF, type: PF 1.2150.1, tolerance class: DIN B. Throughout this work, always this type of sensor is meant when foil sensors (or FPRTDs) are referred to.
3. *JUMO* Screw-in RTD temperature probe for heat meter with connection cable for direct installation (type DS/DL),type: 902425/20, Pt500. Only two of these sensors have been already installed for an optional, future hydronic heating and cooling element.

A comprehensive table listing each installed sensor together with its labelling, calibration results and location in the cabin can be found in appendix A. Sensors 1101 up to 2211 in this table are the original 85 PRTs which have all been calibrated twice. The calibration process and its results are presented separately in section 3.5. Figure A.1 in appendix A on page 206 offers a graphical representation of the temperature measurement system and thus provides a good overview of the system. On the left hand side, aforementioned sensors are listed. Each sensor is connected in a four-wire configuration to a printed circuit board assembly (PCBA) which provides the RTDs with a constant electric current of 1 mA—the recommended value according to data sheet. PCBAs in turn are operated using 24 V DC from a laboratory power supply unit.

At the core of the installed temperature measurement system are two *Agilent 34970A* data acquisition/switch (DAQ) units. Each unit offers a three-slot card-cage for different switch and control plug-in modules. For measuring signals of the RTDs, six *Agilent 34901A* 20-channel-multiplexer cards are used.

19 temperature sensors are grouped together on one PCBA and from there connected to one module of the DAQ unit via a 40-pin ribbon cable. The 20th channel of the plug-in modules is reserved for monitoring electric current provided by the PCBA which leaves a maximum of 19 channels per slot for temperature measurement.

Using their RS-232 interfaces, both DAQ units are connected to a PC where measured temperatures are saved in two data files.

3.4.2 Velocity Measurements

For velocity measurements inside the cabin, up to eight *Ahlborn Almemo* omnidirectional thermoelectric flow sensors of type *FV A605 TA1O* with a symmetrical ball tip and with a protecting cage of ø110 mm are used. The flow sensors offer a measuring range from 0.01 m s^{-1} to 1.00 m s^{-1}. Only a limited number of experiments could be conducted where data from velocity measurements inside the experimental chamber is available since these sensors are used year-round on a regular basis in various other projects and for students' laboratory activities. Therefore, they could only be installed temporarily inside the experimental cabin. Nevertheless, it was possible to gain some velocity data for each experimental test series. Depending on the experimental arrangement and boundary conditions and the number of sensors available at that time, different positions were used for mounting the sensors. Figure 3.8 shows all possible positions from all investigated test series. The sensors were arranged in two rows—a left row L and a right row R—at different distances from the rear wall where the air inlet opening is located. Velocities were measured at least at the rear edge and front edge of the hot plate if the sensors were available. In each case, the distance between sensor and surface of the ceiling was 0.08 m. An explanation which position is actually used in which test series is given in section 3.6 where experimental arrangements are presented in detail.

The sensors were recalibrated by the manufacturer prior to the experiments. Calibration was carried out at 0.50 m s^{-1}, 0.75 m s^{-1} and 1.00 m s^{-1}. Uncertainty is given as 0.05 m s^{-1} for a velocity of up to 0.75 m s^{-1} and as 0.10 m s^{-1} for a velocity of 1.00 m s^{-1}.

During the experiments, flow sensors are connected to a mobile data logging device of type *Ahlborn Almemo 2590-9*.

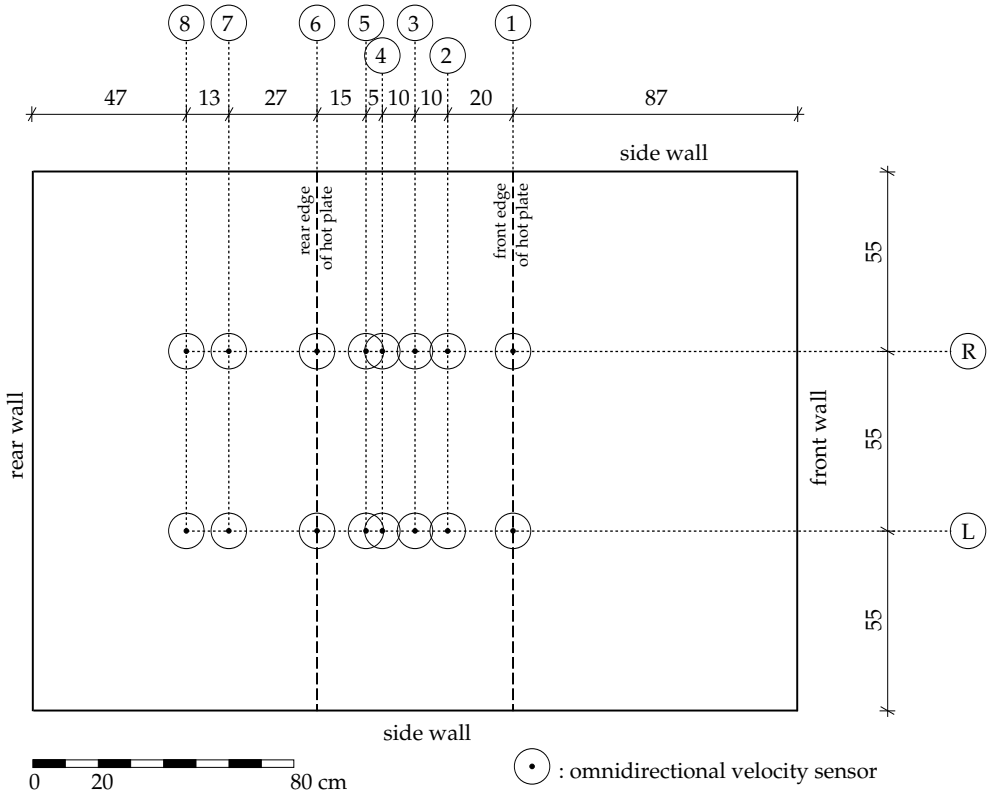

Figure 3.8: Plan with all mount positions used for the omnidirectional flow sensors. The distance between sensor and surface of the ceiling is eight centimetres for all positions.

3.4.3 Flow Rate Measurements

A calibrated *AIRFLOW LCA 501* rotating vane anemometer (RVA) with a 100 mm head and a built-in logger and data storage was used for system flow rate measurements. The RVA offers a measuring range of 0.25 m s^{-1} to 30 m s^{-1} with an accuracy of $\pm$1.0 % of reading $\pm$0.02 m s^{-1}.

As shown in figure 3.4 and previously mentioned, the instrument was permanently installed at the end of the return air duct with an aircone flow hood. A photograph showing the end of the return air duct, hood and instrument can be found in appendix E on page 249.

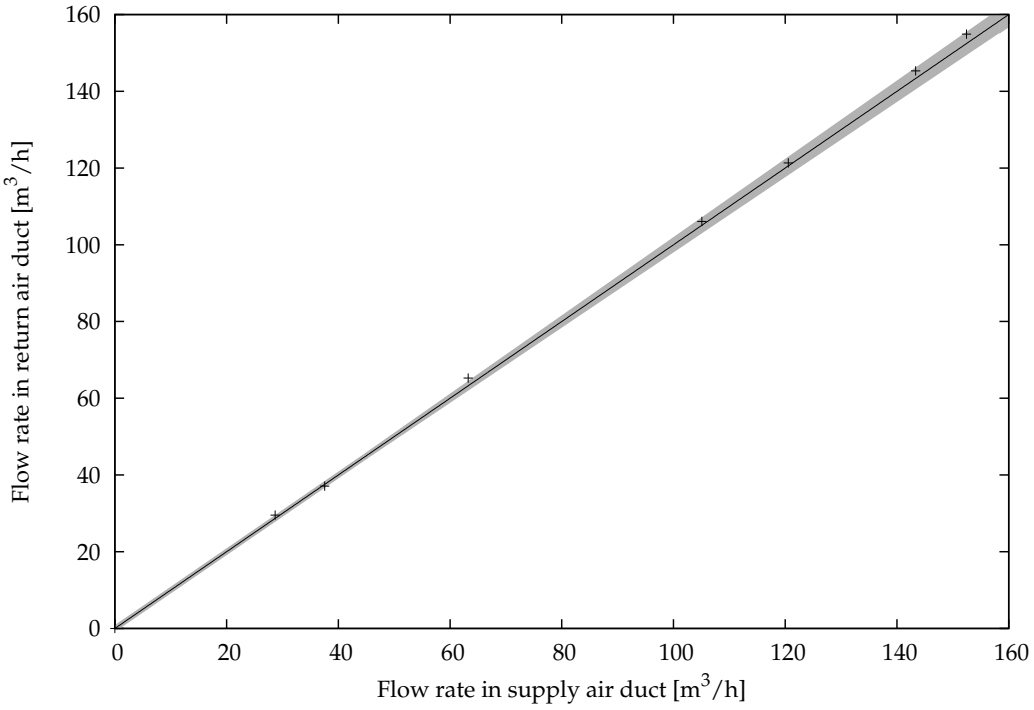

Figure 3.9: Flow rate measurements with a fully operational cabin for checking the airtightness of the cabin and the ventilation system. Uncertainty in measurement is indicated by the grey area around the $y = x$ line.

Temporarily, a second rotating vane anemometer of the same type was installed at the beginning of the supply air duct in the same manner as the one at the end of the return air duct. The fans were adjusted to different, arbitrarily chosen values between minimum and maximum possible flow rate. Then, flow rates were measured simultaneously at both ends of the duct system. Figure 3.9 shows that both flow rates were identical when taking into account the uncertainties in the measurements. Uncertainty in measurement is indicated by the grey area around the $y = x$ line. Furthermore, a tracer gas test made directly after the construction of the cabin showed that no decay in tracer gas concentration was observable over a period of several hours. It could be concluded from these results that there is no unwanted leakage, and that cabin and ventilation system can be regarded as airtight.

Table 3.1: Uncertainty in measurement of total heat output P of the electrically heated plate for different values of P.

P in W	δP in W	$\delta P/P$ in %
20	0.08	0.38
30	0.08	0.26
40	0.16	0.39
50	0.16	0.31
60	0.16	0.26
70	0.31	0.44
80	0.31	0.38
90	0.31	0.35
100	0.32	0.31
125	0.32	0.25
150	0.32	0.22

3.4.4 Power Measurements

For measuring heat output of the electrically heated plate, a *ZES LMG95* single-phase high-precision power meter was used. The device was installed as shown in figure 3.4. Values for electric current I, voltage U and power P are recorded in 30 s intervals and stored into an ASCII file which is later used for evaluation. Uncertainty in power measurement is given as $\delta P = \pm(0.015\%$ of reading $+$ 0.02% of range) by ZES (2007). Hence, a smaller range will lead to a smaller uncertainty for a specific heat output. Table 3.1 shows resulting uncertainties δP for different values of P. As $P = U \cdot I$, power range depends on the used measuring ranges for current and voltage. However, heat output can vary between 15 W and 150 W within a series of experiments and it is impossible to use the same ranges for measuring large and small values of heat output. As soon as a certain level of heat output has been reached the next higher measuring range must be used. This circumstance leads to the sudden increase in relative uncertainties which are given in the third column of table 3.1.

Finally, it can be noted that uncertainty does not exceed a value of 0.32 W for the highest heat output displayed and it never exceeds 0.5 % for any given value of heat output. Thus, power measurement can be regarded as very precise.

3.5 Calibration of the Temperature Measurement System

All PRTs were calibrated in order to be able to accurately measure temperatures. Before calibration could take place, the complete measurement system was set up as described in section 3.4.1 so that the instrumentation used during the calibration process was the same as it was during experiments and additional errors due to changes in the system should not occur. After calibration had been completed, sensors were installed at their designated positions inside the cabin. The calibration process and resulting correction curves of the sensors are presented on the following pages.

For calibration, the sensors were immersed into a calibration thermostat bath of type *LAUDA ecoline RE 212* in which distilled water was used as bath liquid. The bath serves to provide a stable temperature during the calibration process. Expected temperatures in the experiments range from approximately 15 °C to 45 °C. Hence, sensors were calibrated in this temperature range using 5 K intervals. As particularly installed CPRTDs are not designed to be used in liquids but only in dry environment, they had to be protected from the water to guarantee an active data acquisition. Therefore, latex gloves were used as a sheath for the chip sensors. For optimal thermal coupling between sensors and water, sensors were grouped together with number of sensors in one sheath not exceeding six CPRTDs and with visibly good contact between sensor and sheath. Pt500s as well as foil sensors on the other hand were immersed directly into the fluid. Photographs taken during calibration can be found in the appendix on pages 242, 243 and 244.

For the calibration procedure, data of the sensors which have to be calibrated are compared to data from a measurement device of known accuracy which serves as a reference normal. In this case, a mercury-in-glass thermometer (MIGT) was applied as reference normal. A complete set of such thermometers is available at Biberach University of Applied Sciences with each thermometer covering a range of 10 K—for example from 20 °C to 30 °C. The scale graduation on each thermometer is 0.01 K. Thus, temperature can be read very precisely. Before calibration procedure of the installed PRTs was carried out, the necessary mercury-in-glass thermometers were shipped to a calibration laboratory which is accredited by the accreditation body of the Deutscher Kalibrierdienst (DKD) at the Physikalisch-

Technische Bundesanstalt (PTB) [1] where these thermometers themselves were calibrated as a first step. Mercury-in-glass thermometers were also calibrated in 5 K intervals and necessary corrections which have to be applied when using the thermometers can be found in the calibration certificates. In these certificates, uncertainty in temperature measurement with one of the mercury-in-glass thermometers is stated as 0.01 K with a level of confidence of 95 %.

During calibration, both PRTs and MIGT are immersed into the water of the calibration thermostat bath. As soon as stable conditions could be verified by both control software of the bath and readings of the sensors, the scale of the mercury-in-glass thermometer was read five times in 30 s intervals using a magnifying glass. Readings were taken simultaneously to the data acquisition of the installed temperature measurement system so that their values could be compared afterwards. For evaluation, recorded instantaneous values as well as calculated average values were used. Furthermore, each sensor was calibrated a second time at another day to gain information about the repeatability of this process.

An example of correction data derived for a chip sensor is presented in figure 3.10a. Figure 3.10b shows the results of a FPRTD. Both times, average temperature values are used. With the correction derived from the calibration measurements, the selected sensor will show the same temperature as the mercury-in-glass thermometer at each temperature at which it was calibrated. Corrections are displayed separately for the two calibration runs. It can be seen that repeatability is very high with deviations between the first and the second calibration run being in the range of only some hundredths of 1 K. Furthermore, derived linear correlations are shown for both calibration runs. Accordingly, linear calibration correlations have been used to correct collected raw data of each sensor. As the average of both calibrations must be seen as the best value available, the resulting correction curve is given by the average of the correction curves from the two separate calibrations. The accuracy of the chip sensor was found to be very high with a y-intercept of less than 0.1 K. Moreover, it can be seen that in the range from 0 °C to 50 °C, correction is practically independent of the prevalent temperature. On the

[1] The Physikalisch-Technische Bundesanstalt (PTB) is the German national metrology institute providing scientific and technical services. DKD is an association of calibration laboratories of industrial firms, research institutes, technical authorities etc. which are all accredited by the accreditation body of the DKD at the PTB.

other hand, the selected foil sensor needs a stronger correction as can be seen from the higher offset and steeper correction curve in figure 3.10b. Other foil sensors all show a similar behaviour and could be corrected in exactly the same manner.

Uncertainty in temperature measurement is treated in chapter 4.

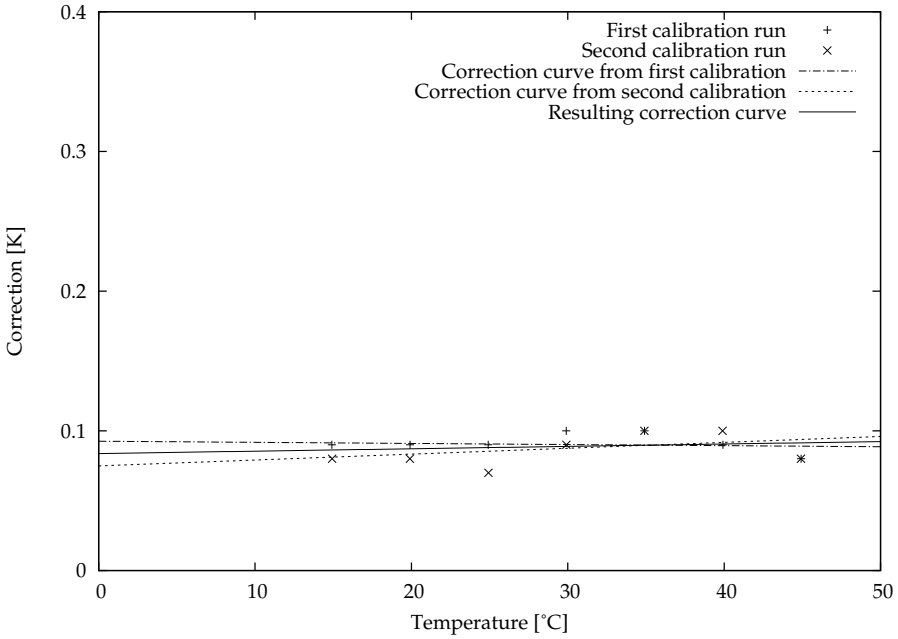

(a) Calibration results of sensor 2101 (CPRTD) and correction curve.

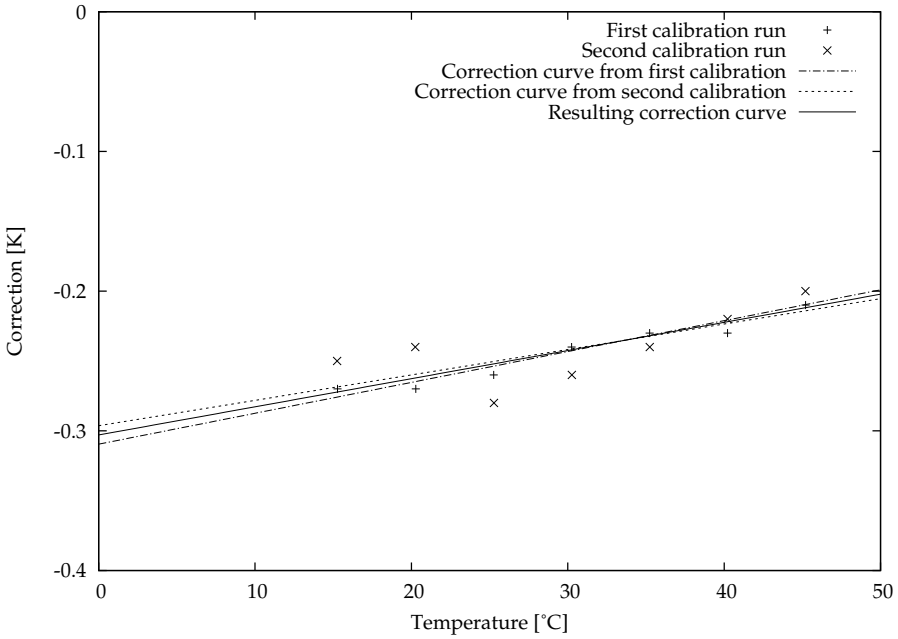

(b) Calibration results of sensor 2201 (FPRTD) and correction curve.

Figure 3.10: Calibration results of a chip and a foil sensor.

3.6 Experimental Conditions and Test Series

3.6.1 Unobstructed Ceiling without Ventilation

For the very first test series with an unobstructed ceiling in an unventilated chamber, the chamber and the associated instrumentation was prepared exactly as described in previous sections. The air inlet and outlet openings shown in figures 3.4 and 3.6 respectively were sealed with a metal plate to avoid any undesired leakage in this test series. A series of 17 experiments was carried out with total heat output of the hot plate ranging from approximately $15\,\mathrm{W\,m^{-2}}$ to $101\,\mathrm{W\,m^{-2}}$. The resulting temperature difference between the surface of the hot plate and mean air ranges from 2 K to 13 K. Eight omnidirectional velocity sensors were installed in the cabin in 8 of these 17 experiments. The sensors were mounted at position 1, 2, 4 and 5 in both the left row of sensors L and the right row R. The exact location of these sensor positions is given in figure 3.8 on page 80.

The correlation by Awbi and Hatton (1999)—which is recommended for use by several other researchers—has been derived from experiments in which only one experiment had a surface-to-air temperature difference of approximately 7 K. All other experiments of these authors had surface-to-air temperature differences between 10 K and 35 K. However, small temperature differences of even less than 7 K are very likely to occur with low energy cooling concepts like TABS. Therefore, the focus of the first test series of this work was set on experiments with low values of heat output which results in small temperature differences. One third of the experiments was carried out with a temperature difference between the surface of the hot plate and mean air of less than 5 K. Temperature difference did not exceed 9 K in two thirds of the experiments.

Changes made in the experimental conditions for subsequent test series are presented below.

3.6.2 Unobstructed Ceiling with Ventilation

Forced Convection

Forced convection was not the primary focus of this work as it is more likely that convective heat transfer in low energy buildings is governed by natural or mixed convection. However, a limited number of seven experiments has been carried out to investigate forced convection as it was shown in chapter 2 that forced convection correlations are used to describe mixed convection. For these experiments, the high-level air inlet in the rear wall was modified according to figure 3.11 to make sure that the incoming air remains attached to the ceiling when it reaches the hot plate installed at the centre of the ceiling. An additional polyurethane panel with a length of 80 cm was installed below the small slot in the air inlet opening which covers the whole width of the cabin and has a height of 5 cm. The polyurethane panel also covered the whole width of the cabin from the left to the right side wall. Incoming air was supplied to the cabin through the slot. This arrangement meant that the inlet was only 5 cm from the upstream edge of the heated plate. Thus, higher air velocities below the hot plate were achieved and convective heat transfer was increased.

The system air change rate was set to 10 ac/h during forced convection experiments with the result that the incoming air had a velocity of $0.29\,\mathrm{m\,s^{-1}}$ at the upstream edge of the hot plate. Air temperature below the hot plate was measured with sensor 2112 which is installed 6 cm below the centre of the hot plate as indicated in figure 3.7 on page 77. Heat output of the electrically heated plate ranged from $21\,\mathrm{W\,m^{-2}}$ to $107\,\mathrm{W\,m^{-2}}$ in this set of experiments. Eight flow sensors were installed in the cabin during five of the seven experiments. However, it was found out that the velocity sensors were placed outside of the flow after the completion of the test series. Thus, measured velocity data could not be used for further analysis. As a consequence, nominal inlet velocity was used for the evaluation of experimental data. Nominal inlet velocity is equivalent to the undisturbed upstream velocity which is for example used by Glück (2007), and is thus a good choice if results are compared to this existing correlation.

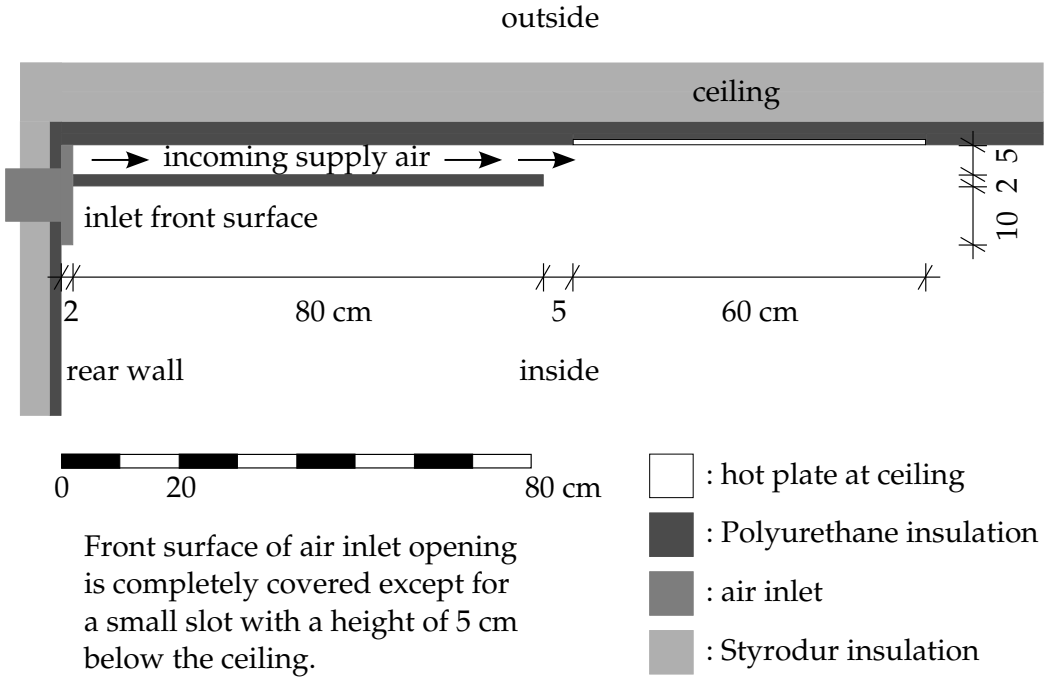

Figure 3.11: Section of the modified inlet geometry for forced convection experiments with an additional polyurethane insulation board below the ceiling in order to guide the incoming supply air to the hot plate.

Mixed Convection

24 experiments were carried out in the third test series to investigate mixed convection at an unobstructed ceiling. Eight velocity sensors were installed in each of these experiments. Mount positions are shown in figure 3.8 on page 80. The sensors were installed at positions 1, 3, 6 and 7 in both the left row L and the right row R.

The chamber was ventilated with an air change rate of $11\,h^{-1}$ using the regular high-level slot inlet in the rear wall below the ceiling. Therefore, the additional insulation panel shown in figure 3.11 which had been necessary for forced convection experiments was removed again.

Total heat output of the hot plate ranged from 16 W m^{-2} to 82 W m^{-2} which lead to temperature differences between the surface of the hot plate and mean air between 2 K and 10 K.

A further eight experiments were conducted to validate the limiting case of natural convection for large values of heat output. Therefore, total heat output was increased to a maximum value of more than 150 W m^{-2}. Ventilation rate was slightly reduced to 10 h^{-1} for these eight experiments. These additional experiments are denoted as test series 3b in table 3.2 on page 98.

3.6.3 Ceiling with Acoustic Baffles without Ventilation

Nineteen acoustic baffles were installed in the experimental chamber after the completion of the test series for investigation of heat transfer at an unobstructed ceiling. The installed baffles have the following properties:

- *OWA S12d baffle system*
  manufacturer : OWA Odenwald Faserplattenwerk GmbH
  product system : S12d acoustic baffle system
  baffle material : mineral wool
  baffle emissivity : 0.9
  baffle length : 150 cm
  baffle thickness : 2.5 cm
  baffle height : 15 cm
  Subsequently, the term *(acoustic) baffle* will be used for this material.

Hence, this work makes use of basically the same type of baffles which has already been used by Pfrommer and Zitzmann (2008) in their CFD model. There are only three differences:

1. A length of the baffles of 150 cm is used in this work while the baffles of Pfrommer and Zitzmann (2008) had a length of 120 cm.
2. The distance—measured from centre line to centre line—between the baffles is 10 cm in this work. Pfrommer and Zitzmann (2008) modelled the baffles with a distance of 20 cm. According to Uygun (2007), both values are recommended by the manufacturer. Since the smaller distance is expected to lead

to a more pronounced reduction in heat transfer from the ceiling and can thus be considered to be the worst case scenario, the small distance is used in this work.

3. The distance between the upper edge of the baffles and the ceiling is 12 cm in this work while a distance of only 7.5 cm is used by Pfrommer and Zitzmann (2008). It was not possible to achieve such a small distance in the experimental chamber due to technical reasons—for example there had to be enough space for installing the omnidirectional flow sensors.

A longitudinal section showing the ceiling of the experimental chamber and the installed acoustic baffles is given in figure 3.12. The baffle close to the front wall is labelled 01. The baffle close to the rear wall is labelled 19. Air temperature profiles—q.v. figure 3.7 on page 77—are measured between baffles 4 and 5 (front part of the cabin), between baffles 10 and 11 (below the hot plate at the centre of the cabin) and between baffles 16 and 17 (rear part of the cabin). For the sake of simplicity, only the three air temperature sensors at a height of 2.04 m—that is 19 cm below the ceiling and thus between the baffles—are shown in figure 3.12. The other air temperature sensors shown in figure 3.7 are, of course, still installed at the same positions and are also used for recording air temperature data.

Figure 3.12 also shows the positions of the installed flow sensors. These positions are (from right to left) identical to positions 1, 2, 4, 6 and 8 in figure 3.8 on page 80. One surface temperature is measured at each baffle. For baffles 1 to 10, the surface facing the rear wall is measured. For baffles 11 to 19, the surface facing the front wall is measured. Foil sensors are used for measuring these surface temperatures. Position of the foil sensor on the surface of the baffle can be taken from figure 3.13.

In total, a number of 16 experiments was carried out to investigate the influence of the acoustic baffles on natural convection in an unventilated chamber. The regular high-level slot inlet opening in the rear wall was covered during this test series 4. Eight flow sensors were installed in the cabin for 9 of the 16 experiments. Mount positions 1, 4, 6 and 8 were used in the left row (see figure 3.8). In the right row, flow sensors were installed at positions 1, 2, 6 and 8. Total heat output of the hot plate ranged from $16\,\mathrm{W\,m^{-2}}$ to $92\,\mathrm{W\,m^{-2}}$ which lead to temperature differences between the front surface of the hot plate and mean air from 3 K to 15 K.

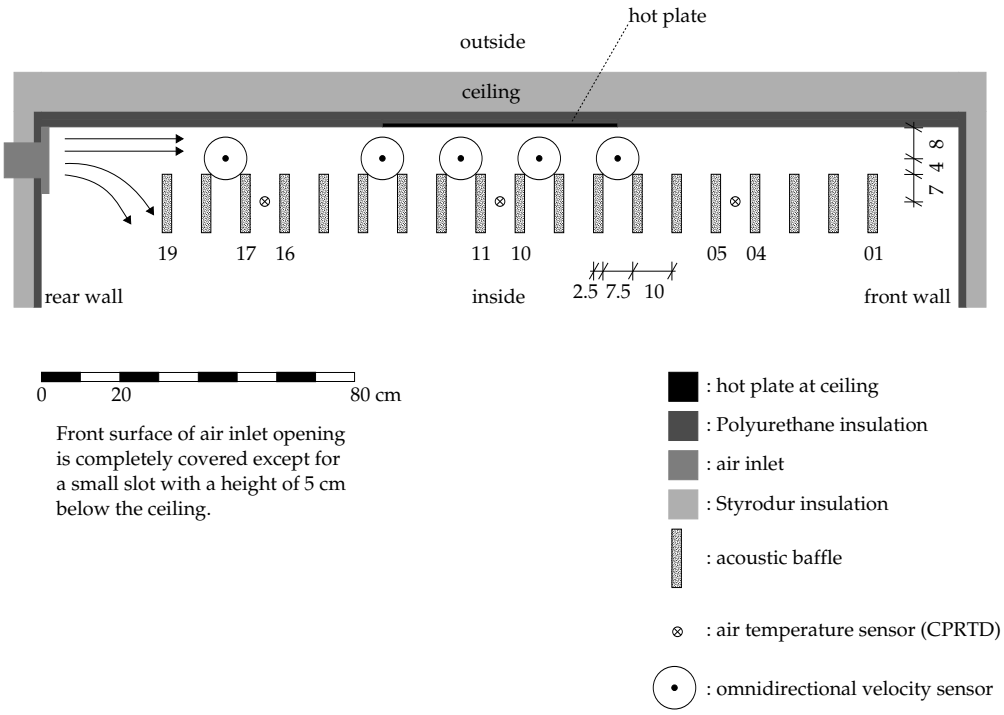

Figure 3.12: Longitudinal section of the cabin showing the hot plate at the ceiling, the acoustic baffles and the instrumentation.

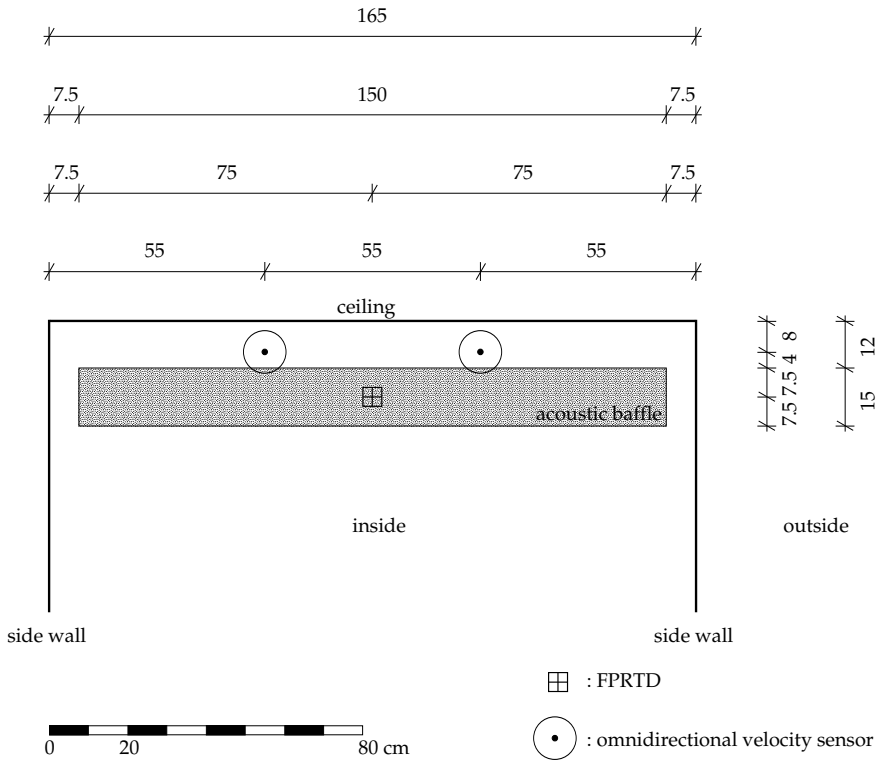

Figure 3.13: Cross section of the cabin showing the acoustic baffles, the velocity sensors and the foil sensor used for measuring the surface temperature of the baffle.

3.6.4 Ceiling with Acoustic Baffles with Ventilation

Last, experimental test series 5 was carried out to investigate the effect of the baffles on heat transfer at the ceiling in a ventilated cabin. Therefore, 18 experiments were conducted with an air change rate of $11\,h^{-1}$. Thus, air change rate is comparable to test series 3 which was used to investigate mixed convection at an unobstructed ceiling. The regular high-level slot inlet was used again to supply air to the experimental chamber. Only six flow sensors could be installed in 5 of the 18 experiments. Sensors were installed at the front and rear edge of the hot plate as well as 40 cm upstream of the hot plate. These locations correspond to positions 1, 6 and 8 for both L and R in figure 3.8. The values for total heat output of the hot plate are in a slightly smaller band than in the previous experimental test series ranging from $22\,W\,m^{-2}$ to $82\,W\,m^{-2}$. This leads to temperature differences between the front surface of the hot plate and mean air from 4 K to 13 K.

3.6.5 Evaluation Procedures

The primary experimental results derived from the measurements are presented in the form of convective heat transfer coefficients h_c which are calculated with equation (3.1). In test series 2 which was carried out to investigate forced convection, the local air temperature below the hot plate is used as reference temperature in the calculation of h_c so that experimental results can be compared to the correlation recommended by Glück (2007). Local air temperature is measured with sensor 2112. In the other experiments, the mean air temperature is used as reference temperature for the calculation of h_c. Mean air temperature is calculated as the volume-weighted average of the data recorded with the 18 air temperature sensors shown in figure 3.7.

For calculation of convection correlations and dimensionless numbers respectively, Glück (2007) evaluates fluid properties at an average temperature of the boundary layer $\vartheta_{bl} = 0.5\,(\vartheta_{surf} + \vartheta_{air})$ where ϑ_{surf} is the temperature of the heated plate and ϑ_{air} is the temperature of the undisturbed air. However, according to Oosthuizen and Naylor (1999), "it is usually adequate to evaluate the fluid properties at the bulk temperature" for internal flows. Therefore, a limited number of experiments from different setups have been investigated using both the more detailed

approach by Glück (2007) and the simpler approach by Oosthuizen and Naylor (1999) for determining fluid properties. It was found out that variation in resulting dimensionless numbers due to a slight deviation in the reference temperature chosen for calculating fluid properties such as conductivity or density can be neglected. Thus, the simplified approach recommended by Oosthuizen and Naylor (1999) is used for evaluation of all experiments and $\vartheta_{\text{meanair}}$ is used as reference temperature for calculating fluid properties in experiments where it is also used for calculation of convective heat transfer coefficients h_c—that is all mixed and natural convection experiments. For forced convection experiments on the other hand, local temperature below the hot plate is not only used for calculation of h_c but also for the calculation of fluid properties.

Furthermore, results are presented in the form of a heat transfer coefficient h^*. It has been shown in chapter 2 that h^* is used to describe the combination of both convective and radiant heat transfer. Therefore, h^* can be calculated from experimentally gained data as

$$h^* = \frac{\dot{q}_{\text{conv}} + \dot{q}_{\text{rad}}}{T_{\text{plate}} - T_{\text{ref}}} = \frac{\dot{q}_{\text{el}} - \dot{q}_{\text{cond}}}{T_{\text{plate}} - T_{\text{ref}}}. \tag{3.2}$$

In this case, operative room temperature is used as reference temperature. Operative room temperature is calculated using equation (2.77b). The necessary radiant temperature of the room's enclosing surface ϑ_{rad} is obtained from a detailed modelling of radiant heat transfer using the software RadTherm and the recorded temperature data as input for this model. Detailed modelling of radiant heat transfer is treated separately in chapter 5. The mean air temperature is used again for ϑ_{air} in equation (2.77b).

A presentation of dimensionless numbers including the equations necessary for their calculation can be found in appendix C. The dimensionless numbers in the plots shown in chapter 6 were calculated with these equations. Characteristic length L_c was set to 0.6 m—that is the short edge of the hot plate—in each experiment.

3.7 Summary

In this chapter,

- the experimental design has been explained,
- the experimental chamber has been presented, and associated measurement systems have been shown.
- An overview of the experimental conditions has been given.

Experiments were designed to investigate heat transfer at the ceiling and a new experimental chamber was built for this purpose. An electrically heated plate which served as a heat source was installed at the ceiling of the cabin and heat output of the hot plate measured with a high precision power meter. Convective heat flux is calculated according to equation (3.1) by subtracting conductive losses and radiation exchange inside the chamber from the measured total heat output. Dividing convective heat flux by a temperature difference between the surface of the hot plate and some appropriate reference temperature of the fluid results in a convective heat transfer coefficient which can be used to describe convection. For forced convection experiments, local air temperature is used as reference temperature. In the other experiments, mean air temperature is used as reference temperature. Total heat transfer by both convection and radiation is expressed in terms of the heat transfer coefficient h^* which was introduced in chapter 2.

The experimental chamber used for this investigation has been built at Biberach University of Applied Sciences, Germany. The cabin offers a length of 2.34 m, a width of 1.65 m, and a height of 2.23 m (internal dimensions). It is built of insulation materials to reduce unwanted conductive losses as much as possible. The chamber is equipped with a ventilation system that is capable of delivering up to approximately 18 ac/h. However, the maximum air change rate used in the experiments is $11\,h^{-1}$. The air inlet opening is positioned at high level, the outlet opening at low level at the rear wall of the chamber. Thus, single-sided ventilation can be examined. A small slot with a height of 5 cm covering the whole width of the cabin is used as inlet. Both flow rate measurements and a tracer gas test showed that the cabin and the ventilation system can be regarded as airtight.

Currently 112 PRTs are installed for measuring surface and air temperatures. All temperature sensors used for conducting experiments have been calibrated twice. Calibration results can be found in the comprehensive list of sensors given in appendix A.

Omnidirectional thermoelectric flow sensors with a symmetrical ball tip and with a protecting cage of ø110 mm have been installed temporarily inside the cabin for velocity measurements. Flow rate of the ventilation system is measured permanently with a rotating vane anemometer installed at the end of the return air duct.

Five different experimental configurations have been investigated in this work. An overview summarizing these test series can be found in table 3.2. An analysis of the uncertainty in calculation of resulting convective heat transfer coefficients is presented in the next chapter.

Table 3.2: Overview of experimental test series carried out for this work.

	experimental test series					
	1	2	3	3b	4	5
1. aim of experiment	natural convection	forced convection	mixed convection	limiting case	influence of baffles, unventilated	ventilated
2. number of installed baffles	0	0	0	0	19	19
3. air change rate in h^{-1}	0	10	11	10	0	11
4. number of experiments per test series (total)	17	7	24	8	16	18
5. number of experiments with velocity sensors	8	5	24	-	9	5
6. number of installed velocity sensors	8	8	8	-	8	6
7. mount positions of velocity sensors as given in figure 3.8 on page 80 for						
a. left row (L)	1, 2, 4, 6	1, 3, 5, 6	1, 3, 6, 7	-	1, 4, 6, 8	1, 6, 8
b. right row (R)	1, 2, 4, 6	1, 3, 5, 6	1, 3, 6, 7	-	1, 2, 6, 8	1, 6, 8
8. air inlet opening	covered	modified	regular	regular	covered	regular
9. total heat output in $W\,m^{-2}$	15 to 101	21 to 107	16 to 82	26 to 154	16 to 92	22 to 82
10. $\vartheta_{plate} - \vartheta_{meanair}$ in K	2 to 13	2 to 12	2 to 10	3 to 21	3 to 15	4 to 13

4 Error Analysis

4.1 Introduction

This chapter presents an analysis of the uncertainties in the experimental measurements and the corresponding uncertainty in the convection coefficient data derived from these measurements.

The analysis of uncertainties starts with the equation for the calculation of convective heat transfer coefficients h_c from experimental results and the general formula for propagation of errors. Using these equations, each occurring partial uncertainty in convective heat transfer coefficient h_c is identified and quantified. Each source of uncertainty is discussed in separate sections of this chapter.

Initial calculations have shown that uncertainty in h_c is strongly influenced by uncertainty in the emissivity of the hot plate $\delta\varepsilon_{plate}$. Consequently, emphasis has been put on an accurate determination of emissivity and on reduction of its uncertainty. An experiment devised specifically to quantify this value has been designed and constructed. Two test series were carried out for determination of ε_{plate}. Experimental design and results are presented in detail in section 4.5. Furthermore, results obtained from the calibration procedure of the temperature sensors are evaluated to determine uncertainty in temperature measurement. Values of each uncertainty component contributing to δh_c are summarized in table 4.5 at the end of the chapter.

4.2 Propagation of Errors

In chapter 3 it was shown that calculation of convective heat flux from the data in each experiment could be achieved by subtraction of radiation and conduction

fluxes from the total heat output of the electrically heated plate. For the calculation of a convective heat transfer coefficient h_c, convective heat flux is then divided by the temperature difference between the surface of the hot plate and an appropriate reference temperature of the fluid as shown in equation (4.1).

$$h_c = \frac{\dot{q}_{conv}}{T_{plate} - T_{fluid}} = \frac{\dot{q}_{el} - \dot{q}_{rad} - \dot{q}_{cond}}{T_{plate} - T_{fluid}} \tag{4.1}$$

where

$\dot{q}_{conv}$ is the convective heat flux in $W\,m^{-2}$,
$\dot{q}_{el}$ is the measured total heat output of the hot plate in $W\,m^{-2}$,
$\dot{q}_{rad}$ is the radiative heat flux in $W\,m^{-2}$,
$\dot{q}_{cond}$ is the conductive heat flux towards the back in $W\,m^{-2}$,
T_{plate} is the surface temperature of the hot plate in K, and
T_{fluid} is an appropriate reference temperature of the fluid in K.

Conductive losses towards the back $\dot{q}_{cond}$ can be written as

$$\dot{q}_{cond} = U^{\star}\left(T_{plate} - T_{back}\right) = \left(\sum \frac{d_i}{\lambda_i}\right)^{-1}\left(T_{plate} - T_{back}\right) \tag{4.2}$$

where $U^{\star}$ is the reciprocal value of the thermal resistance of the ceiling behind the hot plate and T_{back} is the backside temperature of the ceiling behind the hot plate. Using values for thickness d_i and conductivity λ_i of the installed materials as described in section 3.3, $U^{\star}$ was calculated to be $0.22\,W\,m^{-2}\,K^{-1}$.

In chapter 5, it will be shown that radiant heat transfer inside the experimental chamber can be calculated using equation (5.9) for simple configurations where acoustic baffles do not obstruct the view. Inserting this equation as well as equation (4.2) into equation (4.1) leads to

$$h_c = \frac{\dot{q}_{el} - \varepsilon_{plate} \cdot \sigma \cdot \left(T_{plate}^4 - T_{rad}^4\right) - U^{\star} \cdot \left(T_{plate} - T_{back}\right)}{T_{plate} - T_{fluid}} \tag{4.3}$$

and thus, h_c is a function of seven variables.

According to the general formula for error propagation in a function of several variables $q\,(x,\ldots,z)$, the uncertainty in q can be written as

$$\delta q = \sqrt{\left(\frac{\partial q}{\partial x}\delta x\right)^2 + \cdots + \left(\frac{\partial q}{\partial z}\delta z\right)^2} \tag{4.4}$$

with independent and random uncertainties $\delta x,\ldots,\delta z$ in its components $x,\ldots,z$.

Applying this approach on equation (4.3) leads to partial uncertainties in h_c due to its seven components as given by equations (4.5a) to (4.5g). Here, $\delta h_{\mathrm{c},\dot{q}_\mathrm{el}}$ is the uncertainty in calculated h_c due to the uncertainty in measurement of total heat output of the hot plate $\dot{q}_\mathrm{el}$. Equations (4.5b) to (4.5g) are analogs for the other components.

$$\delta h_{\mathrm{c},\dot{q}_\mathrm{el}} = \left|\frac{\partial h_\mathrm{c}}{\partial \dot{q}_\mathrm{el}}\right| \cdot \delta\dot{q}_\mathrm{el} = \left|\frac{1}{T_\mathrm{plate} - T_\mathrm{fluid}}\right| \cdot \delta\dot{q}_\mathrm{el} \tag{4.5a}$$

$$\delta h_{\mathrm{c},\varepsilon_\mathrm{plate}} = \left|\frac{\partial h_\mathrm{c}}{\partial \varepsilon_\mathrm{plate}}\right| \cdot \delta\varepsilon_\mathrm{plate} = \left|\frac{-\sigma\left(T_\mathrm{plate}^4 - T_\mathrm{rad}^4\right)}{T_\mathrm{plate} - T_\mathrm{fluid}}\right| \cdot \delta\varepsilon_\mathrm{plate} \tag{4.5b}$$

$$\delta h_{\mathrm{c},\mathrm{T_{plate}}} = \left|\frac{\partial h_\mathrm{c}}{\partial T_\mathrm{plate}}\right| \cdot \delta T_\mathrm{plate} = \left|\frac{U^\star\left(T_\mathrm{fluid} - T_\mathrm{back}\right) - \dot{q}_\mathrm{el} + \varepsilon_\mathrm{plate}\sigma\left[3T_\mathrm{plate}^3\left(\frac{4}{3}T_\mathrm{fluid} - T_\mathrm{plate}\right) - T_\mathrm{rad}^4\right]}{\left(T_\mathrm{plate} - T_\mathrm{fluid}\right)^2}\right| \cdot \delta T_\mathrm{plate} \tag{4.5c}$$

$$\delta h_{\mathrm{c},\mathrm{T_{rad}}} = \left|\frac{\partial h_\mathrm{c}}{\partial T_\mathrm{rad}}\right| \cdot \delta T_\mathrm{rad} = \left|\frac{4\varepsilon_\mathrm{plate}\sigma T_\mathrm{rad}^3}{T_\mathrm{plate} - T_\mathrm{fluid}}\right| \cdot \delta T_\mathrm{rad} \tag{4.5d}$$

$$\delta h_{\mathrm{c},\mathrm{U^\star}} = \left|\frac{\partial h_\mathrm{c}}{\partial U^\star}\right| \cdot \delta U^\star = \left|\frac{T_\mathrm{plate} - T_\mathrm{back}}{T_\mathrm{plate} - T_\mathrm{fluid}}\right| \cdot \delta U^\star \tag{4.5e}$$

$$\delta h_{\mathrm{c},\mathrm{T_{back}}} = \left|\frac{\partial h_\mathrm{c}}{\partial T_\mathrm{back}}\right| \cdot \delta T_\mathrm{back} = \left|\frac{U^\star}{T_\mathrm{plate} - T_\mathrm{fluid}}\right| \cdot \delta T_\mathrm{back} \tag{4.5f}$$

$$\delta h_{\mathrm{c,T_{fluid}}} = \left| \frac{\partial h_\mathrm{c}}{\partial T_\mathrm{fluid}} \right| \cdot \delta T_\mathrm{fluid} = \left| \frac{\dot{q}_\mathrm{el} - \varepsilon_\mathrm{plate}\sigma\left(T_\mathrm{plate}^4 - T_\mathrm{rad}^4\right) - U^\star\left(T_\mathrm{plate} - T_\mathrm{back}\right)}{\left(T_\mathrm{plate} - T_\mathrm{fluid}\right)^2} \right| \cdot \delta T_\mathrm{fluid} \quad (4.5g)$$

Combining the results from equations (4.5a) to (4.5g) in quadrature leads to total uncertainty in h_c as given by equation (4.4). Hence, values for uncertainty in

- heat output of the hot plate $\delta\dot{q}_\mathrm{el}$,
- U-factor of the ceiling behind the hot plate $\delta U^\star$,
- emissivity of the hot plate $\delta\varepsilon_\mathrm{plate}$, as well as
- temperature behind the hot plate δT_back,
- surface temperature of the hot plate δT_plate,
- radiation temperature of the other enclosing surfaces δT_rad, and
- the selected fluid (air) temperature δT_fluid

must be quantified. These uncertainties are presented in the following sections.

4.3 Uncertainty in Heat Output of the Hot Plate

Heat output of the electrically heated plate is measured with a new, calibrated *ZES LMG95* single-phase high-precision power meter described in section 3.4.4. It was noted that uncertainty in power measurement δP depends on the magnitude of the heat output but never exceeds 0.5 % for any given value of P. The largest absolute value of occurring uncertainty δP is 0.32 W for a maximum heat output P of 150 W. For simplicity, fractional uncertainty $\delta\dot{q}_\mathrm{el}/\dot{q}_\mathrm{el}$ is taken to be a constant value of 0.5 % for each experiment in further error analysis.

Table 4.1: Uncertainty in calculation of thermal resistance of the ceiling.

value	best "estimate"	uncertainty	fractional uncertainty
d_{PUR}	0.020 m	0.002 m	10 %
d_{Styrodur}	0.050 m	0.005 m	10 %
λ_{PUR}	0.025 W m^{-1} K^{-1}	0.005 W m^{-1} K^{-1}	20 %
$\lambda_{\mathrm{Styrodur}}$	0.035 W m^{-1} K^{-1}	0.005 W m^{-1} K^{-1}	14 %
$d_{\mathrm{PUR}}/\lambda_{\mathrm{PUR}}$	0.800 m^2 K W^{-1}	0.179 m^2 K W^{-1}	22 %
$d_{\mathrm{Styrodur}}/\lambda_{\mathrm{Styrodur}}$	1.429 m^2 K W^{-1}	0.249 m^2 K W^{-1}	17 %
R_{total}	4.457 m^2 K W^{-1}	0.434 m^2 K W^{-1}	10 %
$U^\star$	0.224 W m^{-2} K^{-1}	0.022 W m^{-2} K^{-1}	10 %

4.4 Uncertainty in Ceiling Thermal Resistance

The thermal resistance of the ceiling is calculated as

$$R^\star = \frac{2d_{\mathrm{PUR}}}{\lambda_{\mathrm{PUR}}} + \frac{2d_{\mathrm{Styrodur}}}{\lambda_{\mathrm{Styrodur}}} \tag{4.6}$$

and

$$U^\star = \frac{1}{R^\star} = \frac{1}{\frac{2d_{\mathrm{PUR}}}{\lambda_{\mathrm{PUR}}} + \frac{2d_{\mathrm{Styrodur}}}{\lambda_{\mathrm{Styrodur}}}} \tag{4.7}$$

with the manufacturers' stated values of the material properties as given in table 4.1. It is assumed that the thickness of the PUR panel does not vary more than ± 2 mm and that the thickness of the Styrodur panel does not vary more than ± 5 mm. Thus, fractional uncertainty of the thickness is 10 % for both materials. Furthermore, it is assumed that conductivity does not vary more than ± 0.005 W m^{-2} K^{-1} as manufacturer's classification of the insulation boards is given in steps of 0.01 W m^{-2} K^{-1}—that is a conductivity of 0.025 W m^{-2} K^{-1} is described by WLG 025, and WLG 035 means a conductivity of 0.035 W m^{-2} K^{-1}. Using the data in table 4.1, the thermal resistance of the ceiling and its uncertainty is estimated as (0.224 ± 0.022) W m^{-2} K^{-1}. These values have been used in further error analysis.

4.5 Uncertainty in Emissivity of the Hot Plate

4.5.1 Preamble

Emissivity of the hot plate used in the experiments was investigated at an early stage of the project while the chamber was being constructed and commissioned. An emissivity of 0.84 was measured by evaluating images from a thermographic camera. However, evaluation turned out to be more difficult than anticipated as there seems to be a problem in the evaluation software delivered with the camera which can result in values of emissivity larger than 1.00. An alternative evaluation method based on analysing colour values of each pixel of a thermal image was developed. This method led to the value of 0.84 but it was difficult to estimate the uncertainty of this result. Hence, a value of 0.02 for uncertainty in ε was used as an initial estimate in preliminary error analysis.

Preliminary error analysis showed that a value of 0.84 ± 0.02 for emissivity ε of the surface of the hot plate contributes approximately 70 % to the uncertainty in derived convective heat transfer coefficients. Hence, verifying the value of 0.84 for emissivity of the hot plate precisely and narrowing its uncertainty from 0.02 to a smaller value with an understandable, reproducible and comparably simple experiment was considered a worthwhile exercise. Accordingly, an experiment which could be used for measuring the emissivity of the hot plate was developed, constructed and commissioned. Two experimental test series were conducted to confirm the value of emissivity of the hot plate and to determine its uncertainty. The experiment and results from these two test series are presented below.

4.5.2 Experimental Design and Evaluation

The experiment consisted of two aluminium elements of which one is used for heating and one for cooling. The heating element consists of two aluminium plates in between which an *EB-Therm* electrical sheet heating element is embedded. For cooling purposes, a hydronic element is used. Photographs of both elements as well as of the experimental arrangement can be found in Appendix F.

The hot and cold plate were completely embedded into insulating material as shown in figure 4.1. Light grey areas in the figure indicate insulation panels of type *Styrodur 3035 CS*. Dark grey areas indicate polyurethane insulation panels of type *Korff Superwand DS*. These two insulating materials were the same as those used for construction of the experimental chamber. Black areas in figure 4.1 represent aluminium heating and cooling elements. The heating element has a width of 60 cm, a length of 161 cm and a height of 1 cm. The width of the cooling element is 64 cm, its length amounts to 170 cm and its height is 4.5 cm. The white area in the figure denotes the air gap in between the hot and the cold plate. The gap has a length of 157 cm and a width of 58 cm as the edges of the hot plate must lie on top of the insulation material. The height of the gap is equal to the thickness of the polyurethane panels and is 2 cm.

Surface temperatures of the two plates are measured with at least eight foil sensors on each plate as shown in figure 4.2. The centre of each element is indicated by $(x, y) = (0, 0)$. Sensor ID numbers used in the figure can also be found in the comprehensive list of sensors given in table A.1. Besides the surface temperatures of hot and cold plate, both surface temperatures of the four side walls forming the air gap between the two plates and rear temperatures behind the insulation were measured. Furthermore, the air temperature inside the cabin in which the experiment for determining emissivity ε was constructed, was also logged.

During experiments, the hydronic element at the bottom was cooled with distilled water supplied by the calibration thermostat bath illustrated in figure 3.4. The sole purpose of the hydronic element is to provide a cool surface with a temperature as uniform as possible. The amount of heat extracted by the hydronic element was of no interest in these experiments. Thus, the supply temperature was kept constant and close to room temperature for each experiment. Furthermore, the flow rate was maximized to achieve the desired uniform temperature distribution on the surface of the cold plate.

The heat output of the electrically heated plate was also kept constant and measured with the high-precision power meter described earlier. For the test series carried out, heat output ranged from approximately 160 W to 230 W in order to achieve large temperature differences between hot and cold plate.

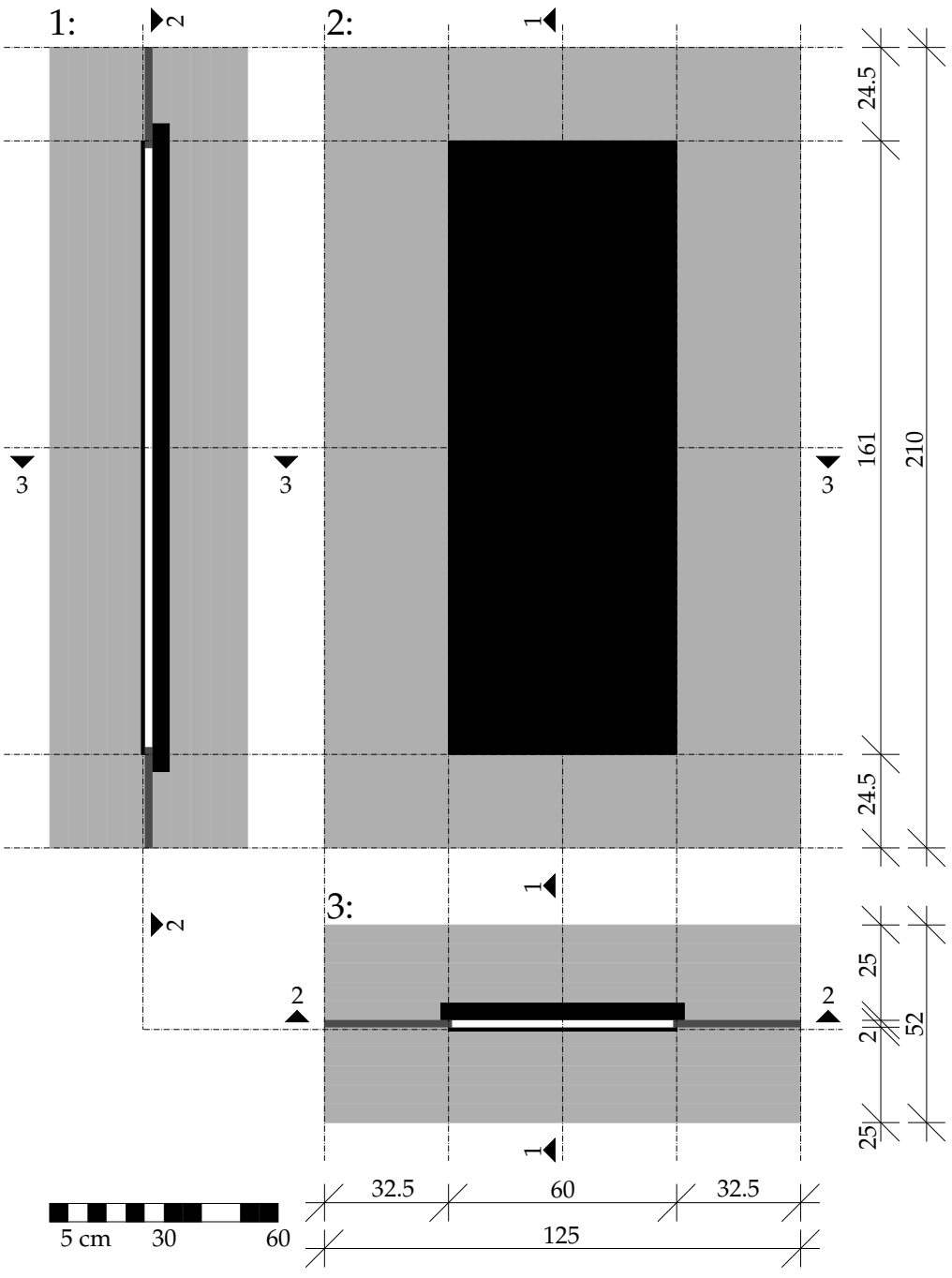

Figure 4.1: Arrangement of the ε-experiment.

hot plate, rear surface:

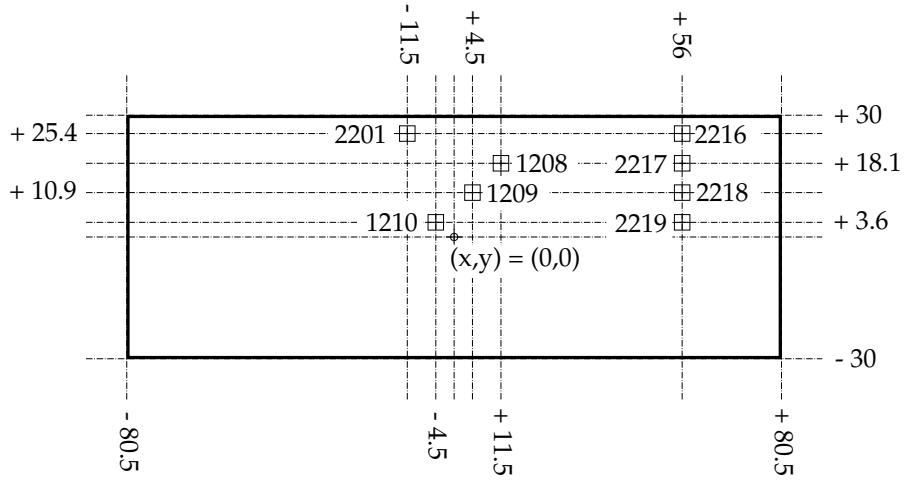

cold plate, front surface:

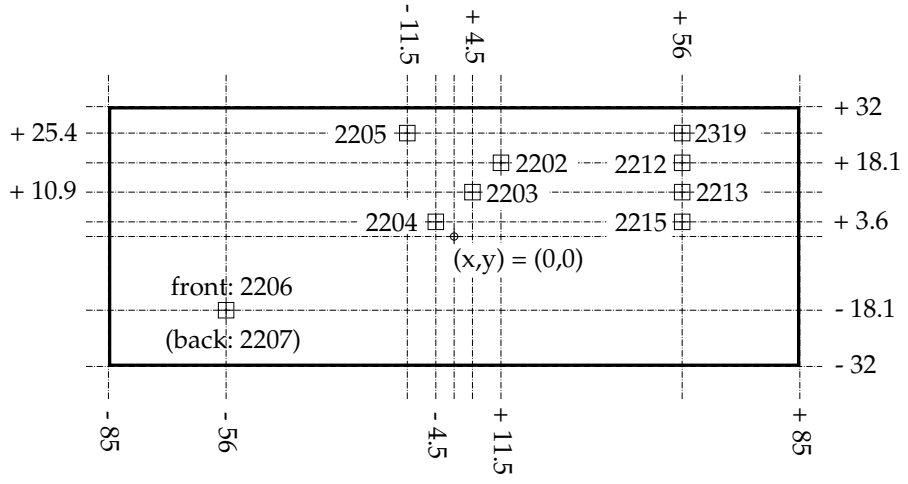

Figure 4.2: Sensor positions on hot and cold plate in an ε-experiment.

In order to determine emissivity ε, measured total heat output must be separated into its conductive, convective and radiative components so that the radiative part can be used to solve for ε. Conductive losses can take two paths. The first path is from the hot plate towards the cooler environment at the back. These losses are minimized due to the thick layer of insulation on top of the hot plate and could be calculated as conduction could be assumed to be one-dimensional with all variables needed for calculation known. The second path—which cannot be inhibited—is the heat bridge between hot and cold plate along the edges of the plate. As this path cannot be calculated as easily as the losses towards the back, a simulation-based evaluation had to be applied. Therefore, a model of the experiment was created in *THERM* - a finite element simulator developed at Lawrence Berkeley National Laboratory LBNL (2003) for modelling heat transfer effects in building components. The model is shown in figure 4.3 and is a section of the experimental arrangement from the outer edge (left) to the symmetry plane along the metal plates (right). The black arrows in the figure show resulting flux vectors. Measured temperatures are used as input for the model and heat fluxes were calculated. Total conductive losses along the edges of the hot plate were the main outputs of interest. These losses were inserted into the energy balance and subtracted from the total heat output of the hot plate to find the convective and radiative components.

As $Nu = 1$ (CIBSE, 2007) for such a configuration of a cavity with heated top and cooled bottom, convection can be treated as conduction-like using properties of air of the given temperature. Thus, convection could be readily calculated and subtracted from the total heat output to derive an accurate value of radiant heat flux.

It can be shown that for the chosen geometric configuration with a distance of only 2 cm between the two parallel flat plates, radiation exchange is largely limited to the surfaces of the hot and cold plate as their view factor gets close to 1.00 (q.v. table 5.1). Thus, the influence of the four side walls on radiative transfer is nearly negligible. The radiation heat flux—together with measured temperatures—was inserted into the "shoe box" radiation model (to be presented in chapter 5) and emissivity ε calculated.

Two test series were conducted. For the first test series, which was used to test the

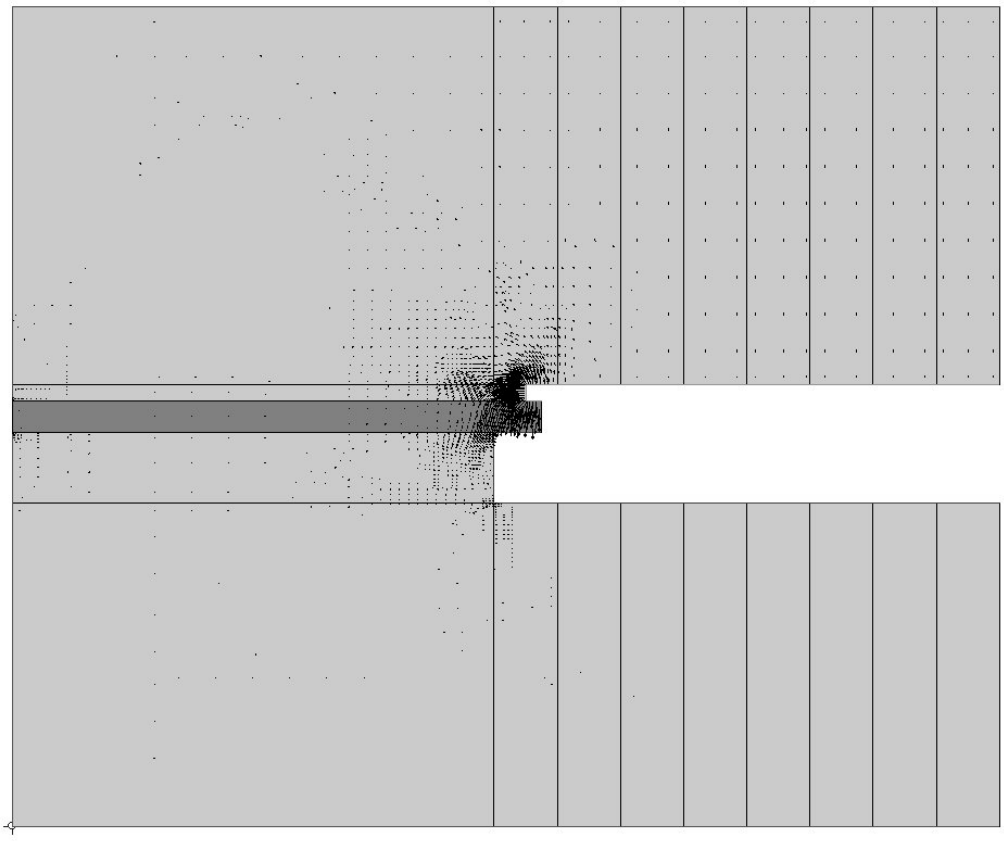

Figure 4.3: *Therm* model of the experiment showing a section from the outer edge (left) to the symmetry plane along the metal plates (right).

experiment, flat black lacquer was applied to both hot and cold plate. During the second test series, the cold plate is the same as in the first test series. However, a white lacquer is applied to the front surface of the hot plate. This white lacquer was used in all experiments for investigation of convection heat transfer inside the experimental chamber.

The two lacquers used are:

1. Flat black lacquer: *Tetenal Camera Varnish* (Art.-Nr. 105202)
2. White lacquer: *OBI Classic Thermolack* (Art.-Nr. 340105)

4.5.3 Experimental Results for a Flat Black Lacquer

In the first test series, *Tetenal Kameralack* (a flat black lacquer) was applied to both the hot and the cold plate. The emissivity of this lacquer was investigated in an earlier work by Haussecker (1996). He reports emissivity to be 0.97. Hence, this first test series could be used to check the applicability of experiment and evaluation method. Three experiments with different settings of heat output of the hot plate were conducted and the emissivity of the flat black lacquer was calculated. Radiative heat transfer ranged from 120 W to 155 W. Results are given in table 4.2. Values of emissivity differ only slightly varying in the third digit. Rounding mean emissivity from these three experiments to two digits leads to $\varepsilon = 0.97$ which is exactly the value given by Haussecker (1996). Thus, even with a limited number of only three experiments it was shown that experiment and evaluation method could deliver reliable results.

Table 4.2: Resulting emissivity for *Tetenal Kameralack* from three experiments. In addition to the calculated emissivities, radiative heat transfer as well as average temperatures of hot and cold plate are given.

Experiment	$\dot{q}_{\mathrm{rad}}$	$\bar{\vartheta}_{\mathrm{hotplate}}$	$\bar{\vartheta}_{\mathrm{coldplate}}$	ε
-	W	°C	°C	-
1	120.4	41.38	18.83	0.972
2	155.0	47.42	19.16	0.970
3	138.9	44.50	18.99	0.974
mean				0.972

4.5.4 Experimental Results for a White Lacquer

For the second test series, *OBI classic Thermolack* (a white lacquer) was applied to the surface of the hot plate. Six experiments were carried out where radiative heat transfer covered an even wider range than during the first experimental setup with values between 121 W and 165 W. These experiments included two repetitions with nearly identical radiative heat rates. The resulting emissivity of the hot plate for each of the six experiments is shown in figure 4.4 together with the calculated

mean emissivity of 0.838 which is represented by the dashed line and was taken to be the best estimate. The added error bars span two sample standard deviations and can be used to indicate the uncertainty in a single measurement.

For expressing final uncertainty of a series of experiments, normally standard deviation of the mean (SDOM or σ_{m}) is used as one can assume that a combination of n measurements is more reliable than any one measurement taken alone. However, for a small number of measurements even this approach is regarded as unreliable (see Holman, 2001, page 99ff.) and confidence intervals should be estimated using Student's t.

Therefore, standard deviation of the mean

$$\sigma_{\mathrm{m}} = \frac{\sigma}{\sqrt{n}} \tag{4.8}$$

is replaced by

$$\Delta = \frac{t\sigma}{\sqrt{n}} \tag{4.9}$$

where values of Student's t are tabulated in many textbooks (e.g. Papula, 1999; Holman, 2001) for different confidence levels and different degrees of freedom. A table showing these values can also be found in the appendix of this document on page 215.

Using a confidence level of 99 % leads to an uncertainty as indicated by the grey band in figure 4.4, that is emissivity of the hot plate with the white lacquer can be stated as 0.838 ± 0.003 with a confidence level of 99 %.

Rounding this value to two digits leads to a value of 0.84 which is exactly the value that was obtained from evaluation of thermal images at the very beginning of this work. Herewith, the old value could be confirmed by this experimental test series which was carried out at the very end of the experimental programme. Consequently, variation in ε with time could be excluded—a fact also observed by Awbi and Hatton (1999) in their work. Furthermore, uncertainty in the obtained value—which was only guessed in a first step—could be significantly reduced.

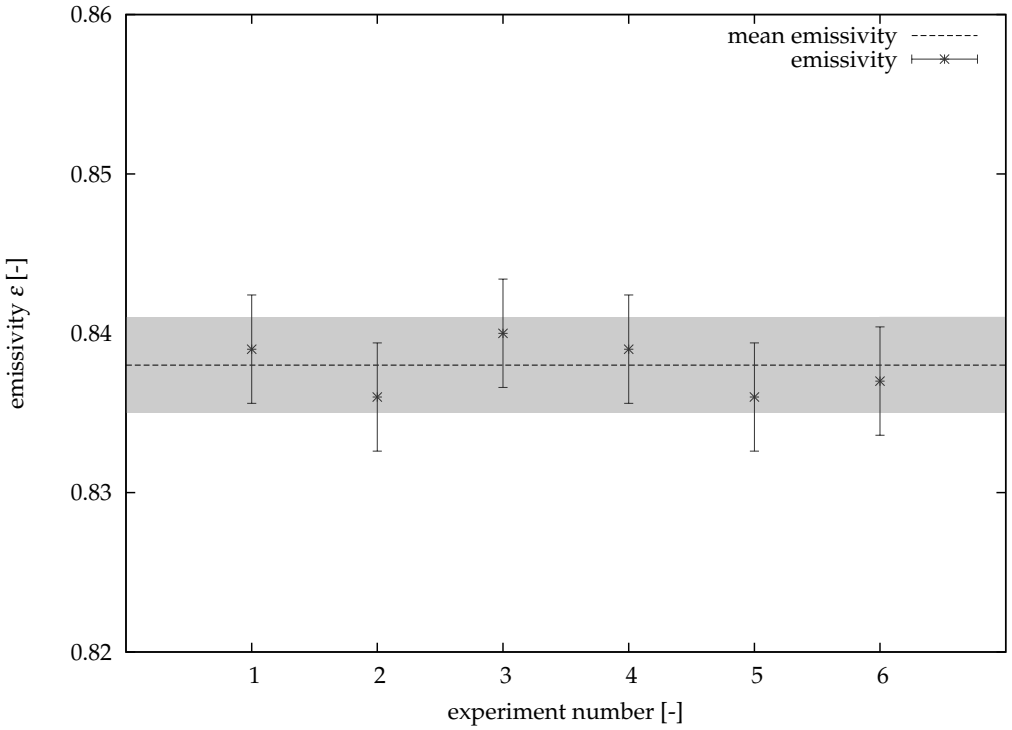

Figure 4.4: Resulting emissivity of the white lacquer from a set of six experiments.

Now, an error analysis can be carried out using the obtained value for emissivity of the hot plate and the high confidence associated with it.

4.6 Uncertainty in Temperature Measurement

4.6.1 Uncertainty in Temperature Measurement with a Single Sensor

Uncertainty in temperature measurement has been quantified using the results obtained from the calibration procedure.

For an experimentally measured quantity x—in this case temperature—there will be a discrepancy $\Delta\bar{x}_i$ between the average measured value $\bar{x}_i$ and the true value x_{true} which is assumed to be known from an instrument with a high level of precision—in this case the mean value of the mercury-in-glass thermometers used

for calibration. However, even using the mercury-in-glass thermometer leads to some small random error which is expressed by the bell-shaped standard distribution curve around x_{true} as indicated in figure 4.5 a). Hence, read single values of the reference device x_{ref} will be distributed normally around x_{true}. Furthermore, recorded values—for example $x_{\text{i,rec}}$—will also be distributed normally around some average measured value $\bar{x}_{\text{i}}$ as they, too, are subject to random uncertainties. This is indicated by the other bell-shaped curves.

It should be noted that $\bar{x}_{\text{i}}$ and $\bar{x}_{\text{j}}$ could either be measurements made at the same temperature with two different sensors or two measurements using the same sensor but at different temperatures. Installed foil sensors for example show a larger discrepancy from the MIGT at higher temperatures. The discrepancies $\Delta\bar{x}_{\text{i}}$ or $\Delta\bar{x}_{\text{j}}$ between the average recorded values and the corresponding true values have been determined in the calibration process for finding correction of the PRTs and were shown in figure 3.10 for two sensors. In order to estimate the overall uncertainty in temperature measurement, other random uncertainties must be statistically evaluated. Therefore, two assumptions are made:

1. All sensors of one type show the same characteristic behaviour.
   Chip sensors for example could lead to a narrow bell curve shown in figure 4.5 b) as they are specified to have a higher accuracy class than the foil sensors which in turn would show a wider distribution. This assumption seems reasonable as each sensor of one specific type is from the same manufacturer, offers the same accuracy class and thus should have passed the same quality management system. Furthermore, each sensor of one type was assembled and installed in the same manner as the other sensors of this type.

2. Dispersion of the measured values does not depend on temperature, that is a sensor shows the same behaviour at 20 °C as it does at 40 °C.
   This assumption also seems reasonable as each possibly occurring temperature is within a small temperature range from approximately 15 °C to 45 °C whereas the manufacturer states an operating range from −80 °C to 180 °C for the foil sensors (JUMO GmbH & Co. KG, Data sheet 90.6023), and one from −50 °C to 200 °C for the chip sensors (JUMO GmbH & Co. KG, Data sheet 90.6121) in which they guarantee an accuracy of class 1/3 DIN B.

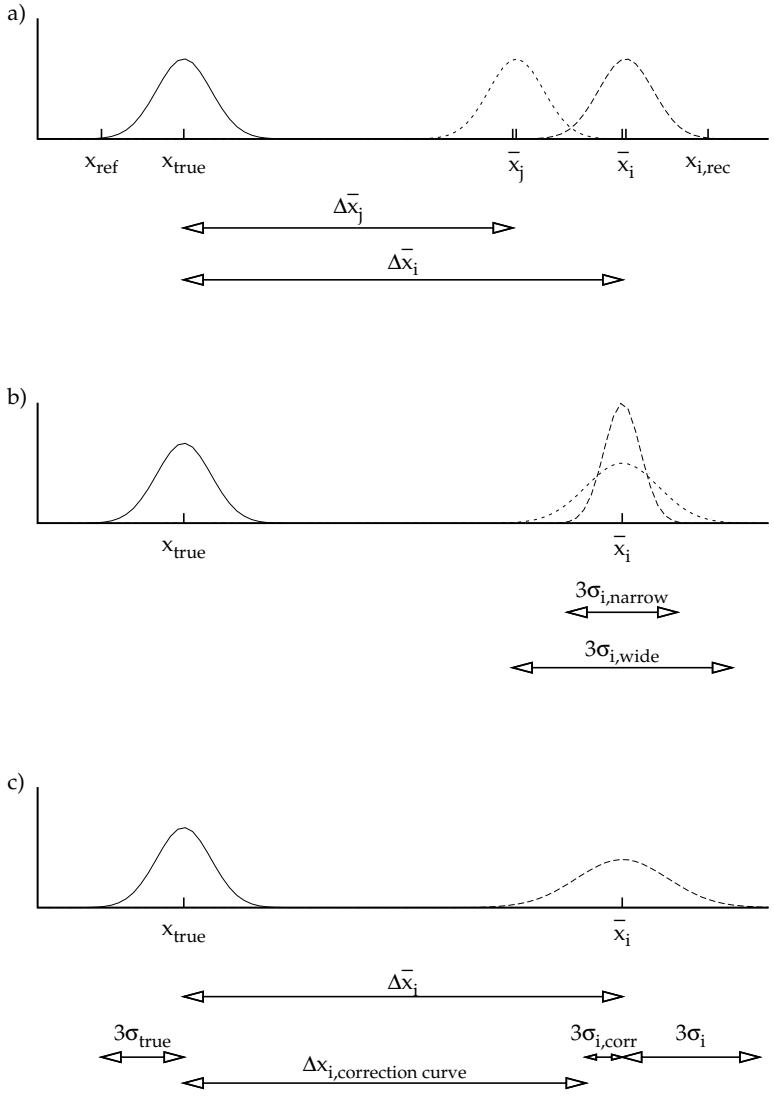

Figure 4.5: Uncertainties occurring during calibration of temperature sensors.

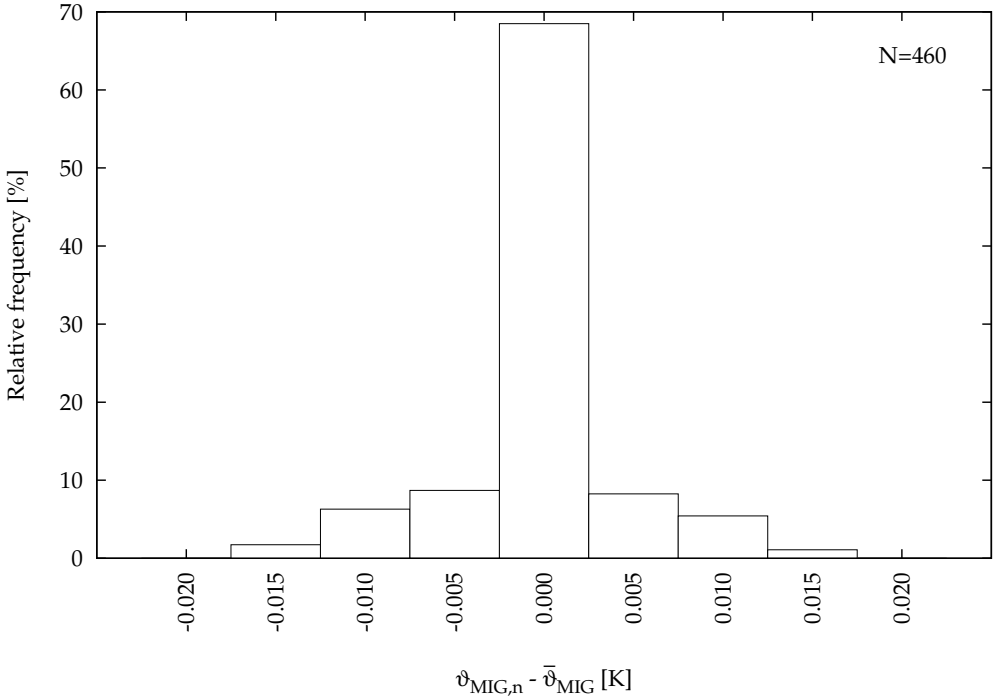

Figure 4.6: Dispersion of mercury-in-glass thermometers during calibration.

Thus, all calibration data of one type of sensors can be considered to be one population for the purposes of statistical analysis. This leads to a total number of 5080 values for the foil sensors and a slightly smaller number of values for the chip sensors. Moreover, above assumptions are also applied to the mercury-in-glass thermometers so that their behaviour can also be statistically evaluated.

The abscissa in figure 4.6 shows the difference between a single temperature value read from the MIGT $\vartheta_{MIG,n}$ and its corresponding average value $\bar{\vartheta}_{MIG}$ which was used for calculating the correction correlations in section 3.5. The ordinate of the graph shows the relative frequency. More than two thirds of the recorded values do not deviate more than 0.005 K from the average value which is equal to one half of the scale graduation of the thermometer. The mean value and standard deviation characterizing the frequency distribution and thus the bell curve around x_{true} can be found in table 4.3 on page 118.

The behaviour of chip and foil sensors has been investigated in a similar manner. The resulting histograms for both types of sensors are presented in figure 4.7. One can see that the chip sensors show a distribution which is very similar to the one already known from the MIGT although the peak around 0.00 K is not quite as pronounced. Thus, the distribution gets closer to the expected normal distribution with a better defined bell curve. This is also shown in figure 4.7a for comparison. Nearly half of all values lie in a small band of 0.005 K. For the foil sensors, the range of observed dispersion is slightly wider than that of the CPRTDs ranging from -0.08 K to 0.08 K. However, more than 98 % of the observed deviations still do not exceed a band of ± 0.025 K and so the outer bins of the histogram are hardly visible.

It can be assumed that (see figure 4.5) for every reading x_{ref} from the reference MIGT a single corresponding reading $x_{\mathrm{i,rec}}$ has been recorded by one of the chip sensors. The probability that a measurement will fall within three standard deviations is already more than 99 %. Hence, three standard deviations has been used in estimates of the uncertainty in temperature measurement. In the worst case, x_{ref} and $x_{\mathrm{i,rec}}$ have values such as those indicated in figure 4.5. Then, $3\sigma_{\mathrm{i}}$ from the measurement of the PRT can simply be added to $3\sigma_{\mathrm{true}}$ from the mercury-in-glass thermometer for calculation of worst-case uncertainty.

It is important to note that the difference $\Delta\bar{x}_{\mathrm{i}}$ in figure 4.5 a) is only known for distinct temperatures prevalent during calibration. For correction of the sensor, not the differences at discrete temperature points are used but a linear correlation which allows correction at an arbitrary temperature within a defined range. As was shown in figure 3.10, the single calibration points do not necessarily lie on the correction curve but are spread around it. This effect is illustrated in figure 4.5 c) and must also be taken into consideration. Only a part of $\Delta\bar{x}_{\mathrm{i}}$ is adjusted by applying $\Delta x_{\mathrm{i,correctioncurve}}$ to the raw data of a sensor. The remaining deviation becomes a third source of uncertainty and was named $3\sigma_{\mathrm{i,corr}}$ and also statistically evaluated. Results are shown in figure 4.8. More than 70 % of the mean values of the chip sensors from the calibration do not deviate more than ± 0.01 K from the value obtained from the correction curve. However, the range of values which can be observed with the foil sensors is considerably larger starting at -0.09 K and reaching 0.13 K. Thus, neglecting this effect would lead to underestimates of the

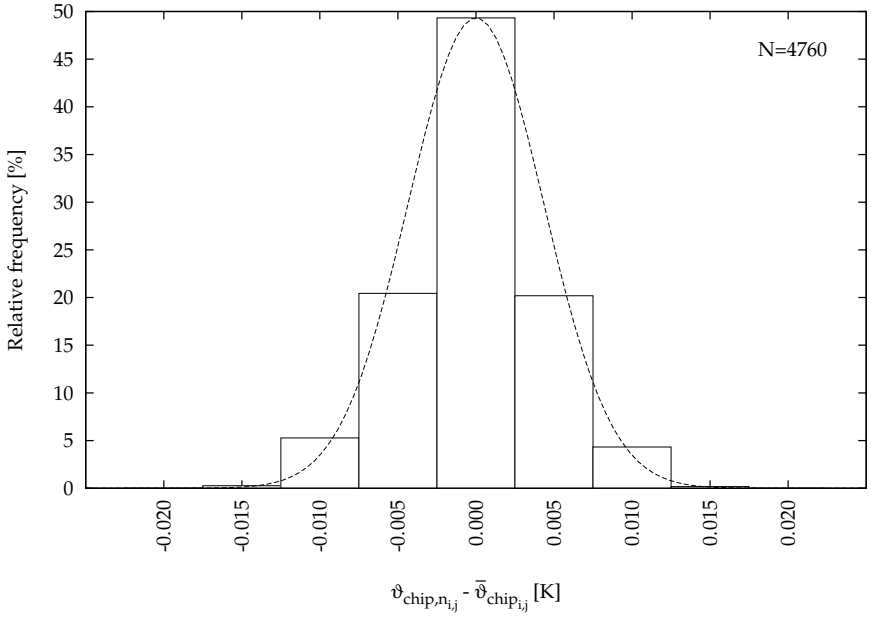

(a) for all chip sensor measurements at all investigated temperatures.

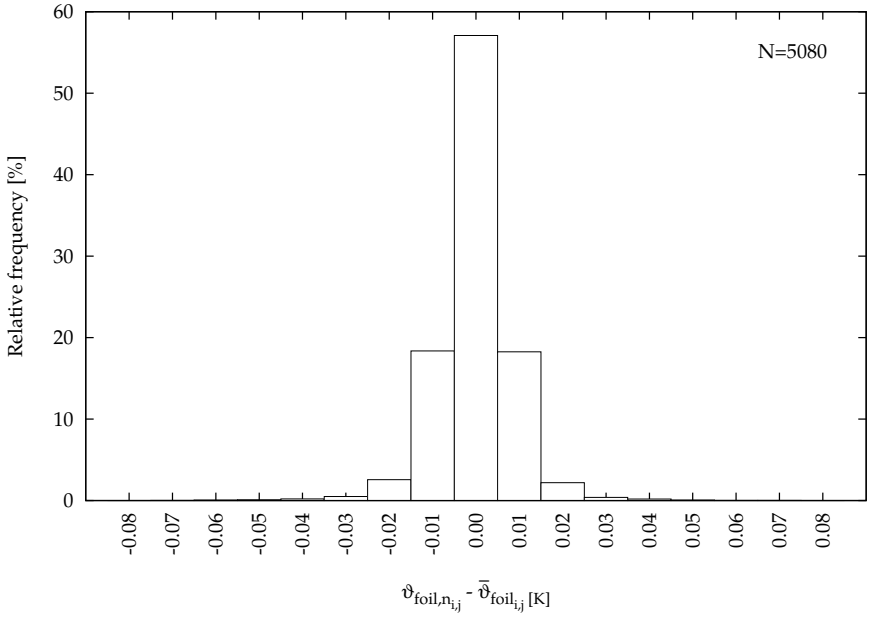

(b) for all foil sensor measurements at all investigated temperatures.

Figure 4.7: Dispersion of single measured values around the corresponding mean temperature.

Table 4.3: Worst-case and final total uncertainty in temperature measurement with both chip and foil PRTs.

	CPRTDs		FPRTDs	
	mean	3σ	mean	3σ
	K	K	K	K
dispersion of MIGTs	0.000	0.013	0.000	0.013
dispersion of PRTs	0.000	0.013	0.000	0.027
dispersion of correction curve	−0.001	0.029	0.000	0.124
worst-case total uncertainty		0.055		0.164
final total uncertainty		0.034		0.127

overall uncertainty.

Having estimated individual sources of uncertainty, total uncertainty in temperature measurement can be calculated. For the worst-case, uncertainty can be written as

$$\delta\vartheta_{\mathrm{worst-case}} = 3\sigma_{\mathrm{true}} + 3\sigma_{\mathrm{i,corr}} + 3\sigma_{\mathrm{i}} \tag{4.10}$$

Worst-case and final total uncertainty in temperature measurement with both chip and foil PRTs are tabulated in table 4.3.

However, as contributing factors can be assumed to be random and independent, final uncertainty in temperature measurement with installed PRTs can be stated as the quadratic sum of the three uncertainties identified in the calibration process as follows,

$$\delta\vartheta = \sqrt{(3\sigma_{\mathrm{true}})^2 + (3\sigma_{\mathrm{i,corr}})^2 + (3\sigma_{\mathrm{i}})^2} \tag{4.11}$$

Final uncertainty in temperature measurement can be stated as $\pm 0.04\,\mathrm{K}$ for the CPRTDs and $\pm 0.13\,\mathrm{K}$ for the FPRTDs. As the backside temperature of the ceiling is measured with a single FPRTD, uncertainty δT_{back} is $\pm 0.13\,\mathrm{K}$.

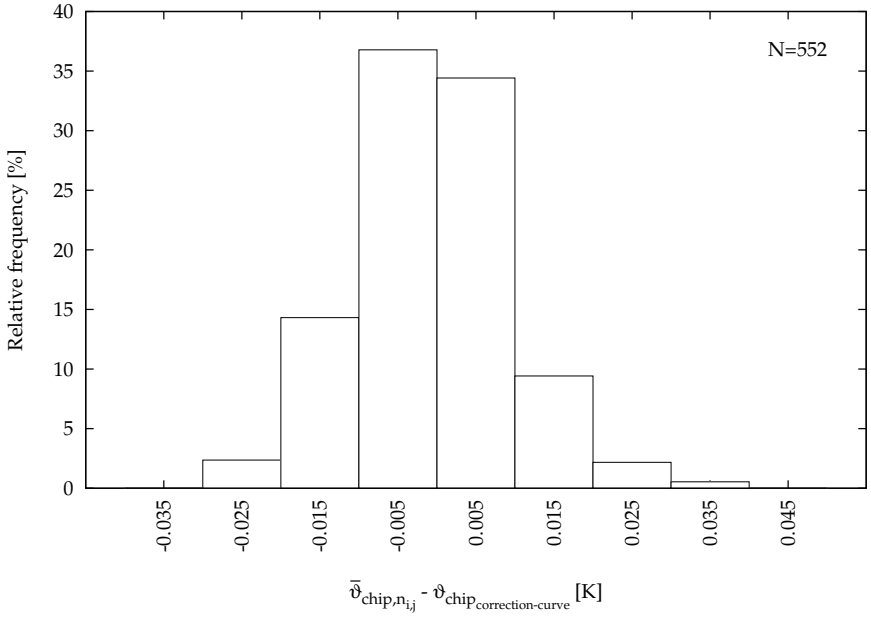

(a) for all chip sensors at all investigated temperatures.

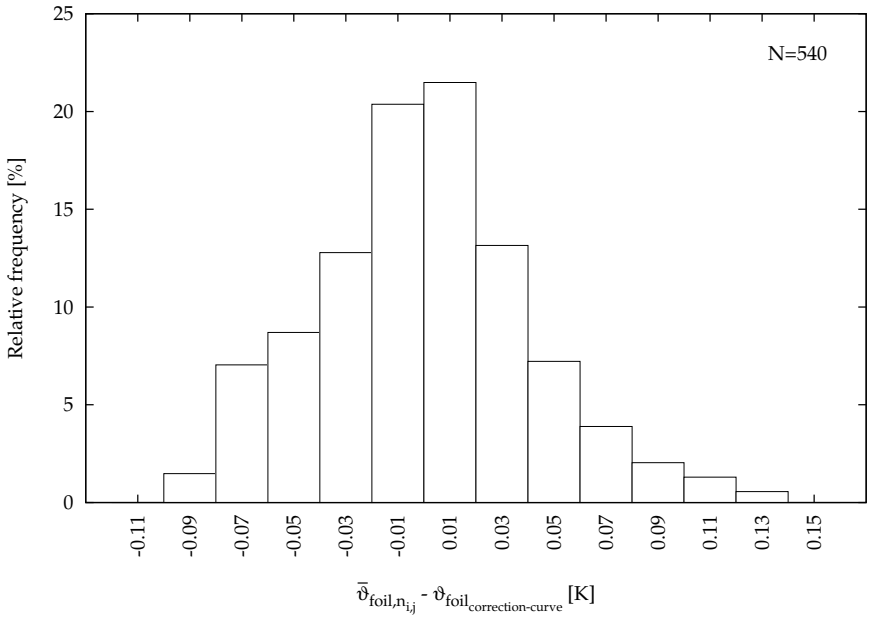

(b) for all foil sensors at all investigated temperatures.

Figure 4.8: Dispersion of mean value from evaluation of calibration data around the corresponding value calculated from correction curve.

4.6.2 Uncertainty in Average Surface Temperatures

Uncertainty in Average Surface Temperature of the Hot Plate

It was noted earlier that three foil sensors are used to measure temperatures on the front surface of the hot plate. The average value from these three sensors is used as the value of the front surface temperature. Thermal images from multiple experiments with different heat output of the hot plate were used to show that averaging the values of the three sensors gives a good representation of the actual average surface temperature—independent of the heat output. In a preliminary test, temperature values of the three sensors were used to calculate the average value and compared with average surface temperatures obtained from evaluating thermal images. Results are summarized in table 4.4. The deviation between the two methods is shown in the last column. As there is no significant difference between the two values, the method of averaging the three sensors' readings seems justified and gives a good representation of the true average surface temperature. Hence, uncertainty in surface temperature of the hot plate δT_{plate} can be stated as a function of uncertainties of the three sensors and is given as

$$\delta T_{\text{plate}} = \frac{1}{\sqrt{3}} \delta T_{\text{FPRTD}} \approx \pm 0.1\,\text{K} \tag{4.12}$$

Uncertainty in Radiation Temperature of the Enclosing Surfaces

The radiation temperature of the enclosing surfaces T_{rad} in equation (4.3) is the area weighted average temperature of the surfaces which can be "seen" by the hot plate. This can be written,

$$T_{\text{rad}} = \frac{\sum \bar{T}_{\text{i}} A_{\text{i}}}{\sum A_{\text{i}}} \tag{4.13}$$

with $\bar{T}_{\text{i}}$ being the average surface temperature of an enclosing surface i—for example a side wall—and A_{i} being the surface area. Neglecting any error in calculation

Table 4.4: Surface temperatures of the hot plate from the evaluation of thermal images for different values of heat output. The table shows surface temperatures of the three sensors (left, middle, right) and the average value.The overall value is that found from analysis of the corresponding thermal images. The last column shows the error between the two methods of defining surface temperature of the hot plate.

$\dot{q}_{el}$	T_{left}	T_{middle}	T_{right}	$T_{average}$	$T_{overall}$	dT
W	°C	°C	°C	°C	°C	K
(1)	(2)	(3)	(4)	(5)	(6)	(5) − (6)
30	24.5	25.4	25.2	25.0	25.0	0.0
40	26.2	27.3	27.0	26.8	26.9	-0.1
50	28.7	30.2	29.8	29.6	29.6	0.0
80	31.7	34.1	33.5	33.1	33.1	0.0

of surface areas A_i and setting $\delta\bar{T}_i = \pm 0.3\,\mathrm{K}$ for each surface, uncertainty in radiation temperature of the enclosing surfaces can be expressed as

$$\delta T_{rad} = \delta\bar{T}_i \frac{\sqrt{\sum A_i^2}}{\sum A_i} = 0.45\delta\bar{T}_i \approx \pm 0.14\,\mathrm{K}. \tag{4.14}$$

4.6.3 Uncertainty in Reference Temperature of the Fluid

In chapter 2, it was noted that different fluid reference temperatures can be used for calculation of convective heat transfer coefficients. Among them are

- local air temperature below the hot plate,
- air temperature at the inlet opening of the ventilation system,
- air temperature at the outlet opening of the ventilation system, as well as
- mean air temperature inside the cabin.

The first three possibilities for an appropriate reference temperature are measured with a single CPRTD. Thus, uncertainty in reference temperature is given by the uncertainty in temperature measurement using a single CPRTD. However, mean air temperature inside the cabin—the last possibility listed above—is expressed as

the volume weighted average of 18 CPRTDs shown in figure 3.7. Hence, uncertainty in mean air temperature can be written as

$$\delta T_{\text{meanair}} = \delta T_{\text{sensor}} \frac{\sqrt{\sum_{j=2101}^{2118} V_{\text{j}}^2}}{\sum_{j=2101}^{2118} V_{\text{j}}} = 0.2948 \cdot \delta T_{\text{sensor}} \tag{4.15}$$

where $j = 2101...2118$ is the sensor ID number according to table A.1.

As it cannot be guaranteed that the temperature measured with a single sensor is always identical to the mean air temperature of the volume it represents, an enhanced value of $\pm 0.5\,\text{K}$ is used for uncertainty δT_{sensor} instead of the regular uncertainty in measurement with a single sensor obtained from the calibration results δT_{CPRTD} which is only $\pm 0.04\,\text{K}$. Inserting this value into equation (4.15) finally leads to an uncertainty in mean air temperature $\delta T_{\text{meanair}}$ of $\pm 0.147\,\text{K}$.

4.7 Summary

At the beginning of chapter 4, the equation for the calculation of convective heat transfer coefficients h_{c} from experimental results is presented. Subsequently, partial uncertainties of the seven variables contributing to uncertainty in h_{c} are introduced and calculated. Emphasis has been put on an accurate determination of the emissivity of the hot plate and on reduction of uncertainty in the obtained value as initial calculations have shown that uncertainty in h_{c} is strongly influenced by uncertainty in $\varepsilon_{\text{plate}}$ for larger values of $\delta\varepsilon_{\text{plate}}$. Thus, the design of the experiment for determination of $\varepsilon_{\text{plate}}$ and the results have been presented in detail. The uncertainty in emissivity could be reduced to a value of ± 0.003. Furthermore, uncertainty in temperature measurement is quantified using the results of the calibration procedure. Values of each partial uncertainty contributing to δh_{c} are summarized in table 4.5. These uncertainties have been used with equations (4.5) to establish the upper and lower bounds of each convection coefficient value derived from a particular experiment. These data are shown in the form of error bars in the results presented in chapter 6.

Table 4.5: Summary of uncertainties contributing to total uncertainty in convective heat transfer coefficient δh_c.

source of uncertainty	sign		value
heat output of the hot plate	$\delta\dot{q}_{el}/\dot{q}_{el}$	=	$\pm 0.5\,\%$
U-factor of the ceiling behind the hot plate	$\delta U^{\star}$	=	$\pm 0.022\,\mathrm{W\,m^{-2}\,K^{-1}}$
emissivity of the hot plate	$\delta\varepsilon_{plate}$	=	± 0.003
temperature behind the hot plate	δT_{back}	=	$\pm 0.13\,\mathrm{K}$
surface temperature of the hot plate	δT_{plate}	=	$\pm 0.1\,\mathrm{K}$
radiation temperature of enclosing surfaces	δT_{rad}	=	$\pm 0.14\,\mathrm{K}$
fluid temperature (if set to $T_{meanair}$)	δT_{fluid}	=	$\pm 0.147\,\mathrm{K}$

5 Radiant Heat Transfer Modelling

5.1 Introduction

For experimental investigation of heat transfer from a heated plate to the indoor environment, the total heat output—which under steady-state conditions equals the measured heat input—of the plate has to be separated into its conductive, convective and radiative components using the measured temperature data. Conductive losses towards the back of the plate can easily be calculated using the temperature difference between inside and outside and the conductivities of the materials used. The convective part is obtained by subtracting conduction and radiation from the total heat output of the plate. Thus, radiation exchange between the heated plate and the indoor environment must also be determined. As it has been shown in chapter 2, an approach using simply a radiative heat transfer coefficient is far too inaccurate for this purpose. Therefore, a suitable method had to be found that was both accurate enough and not too consuming with regard to time and effort.

The first method presented in this chapter is the solution of the integral equation for radiative exchange between grey, diffuse surfaces of an arbitrary enclosure. Solving this equation can be simplified to solving a set of algebraic equations for idealized enclosures. However, the number of equations and thus the effort necessary for solving them increases with the number of surfaces participating in heat transfer. Thus, for determining radiant heat transfer in the experimental programme this approach is too intricate. However, the exact solution from this method can be used to validate a more flexible approach with a numerical solution.

RadTherm, a software specifically designed for investigation of heat transfer prob-

lems involving radiation, was used for calculating radiant heat transfer numerically. A description of the capabilities and features of the software can be found on the web site http://www.thermoanalytics.com as well as in the brochure and user manual (ThermoAnalytics, Inc., 2006). Several validation examples are given in the latter where the numerical solution of the software is compared to an analytical solution. RadTherm is written in C++ and solves radiation exchange using the view factor method. View factors are generated with a integrated ray tracer. The accuracy of the view factor calculation and the effects of different solver settings on the resulting radiant heat flux have been tested and are presented below. Once a RadTherm model has been set up and tested, only temperature data from the experiments has to be fed to the model and radiant energy fluxes will be calculated.

In a first step, the accuracy of the program was tested using a simple shoe box test model with a length of 5 m, a width of 4 m and a variable height of 0.3 m, 3 m and 15 m respectively as shown in figure 5.1. Radiation exchange was calculated using both methods and results were compared to find out whether RadTherm was a suitable tool for evaluating radiant heat transfer in the experimental chamber. This comparison can be found in the following section.

Additionally, an even simpler method was searched for which could easily be implemented into the experimental analysis for a first guess of radiation. Section 5.2.4 will show that this simplified calculation delivers pretty accurate results. However, it is only valid for investigation of radiant heat transfer if there are no additional objects obstructing the view between the hot plate and the other surfaces like the acoustic baffles that were installed in several sets of experiments.

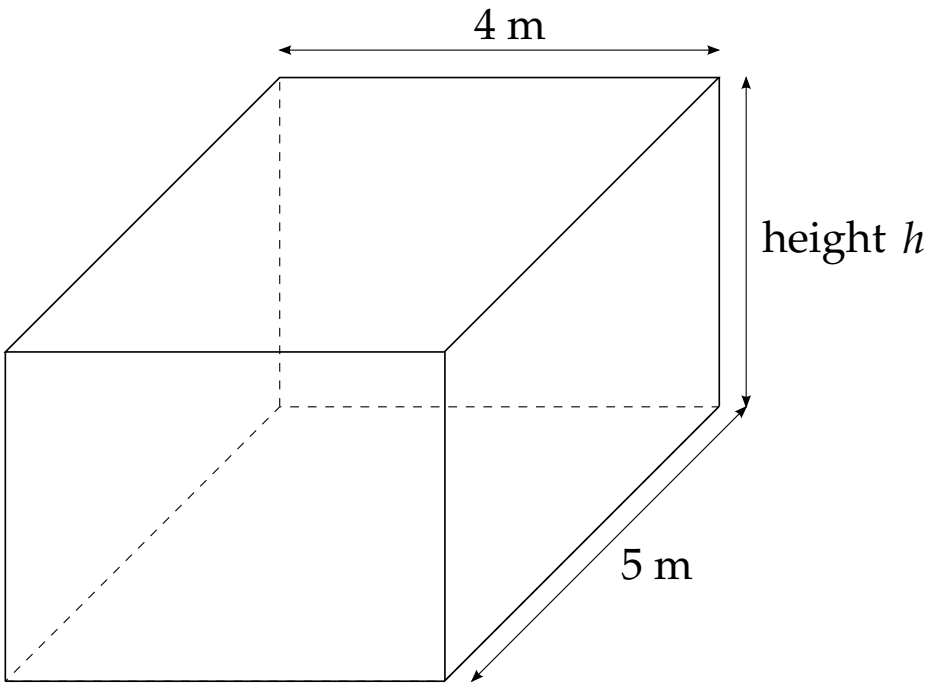

Figure 5.1: Shoe box test model.

5.2 Shoebox Test Model

5.2.1 Analytical Solution

For an exact analytical solution the net radiation method by Poljak was applied. This method can be used to analyse radiative heat transfer in enclosures of N discrete internal surfaces taking into account all reflections and re-reflections. It is presented in many textbooks on radiation exchange, for example in the book by Siegel and Howell (2002, ch. 6-3) and can be summarized as follows.

Starting with an energy balance for the kth internal surface of an enclosure, one can write

$$\dot{Q}_k = \dot{q}_k A_k = \left(\dot{q}_{o,k} - \dot{q}_{i,k}\right) A_k \tag{5.1}$$

with $\dot{q}_{o,k}$ being the outgoing rate of radiant energy per unit area of surface A_k and $\dot{q}_{i,k}$ being the incident rate of radiant energy per unit area of surface A_k. Then, $\dot{q}_k$ is the heat flux which is necessary to make up for the net radiative loss so that the temperature of the surface does not change.

The outgoing radiant heat flux is often called radiosity and consists of an emitted and a reflected part. For diffuse-grey surfaces $\alpha_k = \varepsilon_k$ (absorptivity equals emissivity) and $\dot{q}_{o,k}$ can thus be written as

$$\dot{q}_{o,k} = \varepsilon_k \sigma T_k^4 + (1 - \varepsilon_k)\, \dot{q}_{i,k}. \tag{5.2}$$

The incoming flux is the sum of all radiant fluxes from the remaining inside surfaces incident on the kth surface and is characterized by

$$\dot{q}_{i,k} = \sum_{j=1}^{N} F_{k-j} \dot{q}_{o,j} \tag{5.3}$$

where F_{k-j} is the view factor between surface k and surface j.

Substituting either equation (5.2) or (5.3) into equation (5.1) leads to the two energy balance equations (5.4) and (5.5).

$$\dot{q}_k = \frac{\varepsilon_k}{1 - \varepsilon_k} \left(\sigma T_k^4 - \dot{q}_{o.k} \right) \tag{5.4}$$

$$\dot{q}_k = \sum_{j=1}^{N} F_{k-j} \left(\dot{q}_{o,k} - \dot{q}_{o,j} \right) \tag{5.5}$$

These last two equations are written for each of the N surfaces and lead to a set of $2N$ simultaneous equations with $2N$ unknowns which can finally be solved for unknown $\dot{q}$ and T by eliminating $\dot{q}_o$. In case of the shoe box test model, $N = 6$. Before these equations can finally be solved, the necessary view factors must be calculated .

View factors for different geometric configurations can for example be found in (Modest, 2003, App. D). For the simple shoe box geometry, the two configurations shown in figure 5.2 are sufficient. For calculating the view factor between two

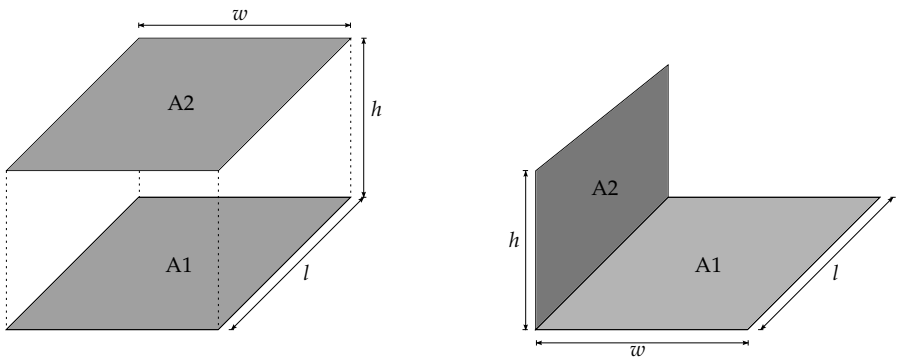

(a) Identical, parallel, and directly opposed.

(b) Two finite rectangles of same length, having one common edge, and at an angle of 90° to each other.

Figure 5.2: View factor relations for two rectangles.

identical, parallel and directly opposed rectangles, equations (5.6) can be used. Equations (5.7) give the view factor for two finite rectangles which have the same length and one common edge, and which are at an angle of 90° to each other.

After having calculated the view factors and having assigned surface temperatures and emissivities, net radiation inside the model can be calculated. Results are presented in section 5.2.3.

$$F_{1-2} = \frac{2}{\pi XY}\left\{ \ln\left[\frac{\left(1+X^2\right)\left(1+Y^2\right)}{1+X^2+Y^2}\right]^{0.5} + X\sqrt{1+Y^2}\tan^{-1}\frac{X}{\sqrt{1+Y^2}} + Y\sqrt{1+X^2}\tan^{-1}\frac{Y}{\sqrt{1+X^2}} - X\tan^{-1}X - Y\tan^{-1}Y\right\} \tag{5.6a}$$

$$X = \frac{w}{h} \tag{5.6b}$$

$$Y = \frac{l}{h} \tag{5.6c}$$

$$F_{1-2} = \frac{1}{\pi W}\left(W \tan^{-1}\frac{1}{W} + H \tan^{-1}\frac{1}{H} - \sqrt{H^2+W^2}\tan^{-1}\frac{1}{\sqrt{H^2+W^2}} + \frac{1}{4}\ln\left\{ \frac{\left(1+W^2\right)\left(1+H^2\right)}{1+W^2+H^2} \cdot \left[\frac{W^2\left(1+W^2+H^2\right)}{\left(1+W^2\right)\left(W^2+H^2\right)}\right]^{W^2} \left[\frac{H^2\left(1+H^2+W^2\right)}{\left(1+H^2\right)\left(H^2+W^2\right)}\right]^{H^2} \right\} \right) \tag{5.7a}$$

$$H = \frac{h}{l} \tag{5.7b}$$

$$W = \frac{w}{l} \tag{5.7c}$$

5.2.2 Numerical Solution

For obtaining a numerical solution of radiant heat transfer in the shoe box model, its geometry was modelled in RadTherm using the software's built-in geometry primitives. Therefore, six *plates* representing the six surfaces were created with dimensions as mentioned above. RadTherm creates a mesh for each part with mesh size depending on the number of elements specified along the length and the width of a *plate* respectively. The number of elements was set in such a way that the elements on each surface have a length of 10 cm. Temperatures were assigned to the surfaces according to table 5.2 on page 132. RadTherm's built-in surface conditions were assigned to the front side of each surface for setting the appropriate emissivities, for example *black body* for an emissivity of 1.00. Convection was set to *none* as only radiant heat transfer was investigated and all surface temperatures were assumed constant and known. Each back side was set to *insulated* because no conductive losses to the outside were considered. The results of the test cases calculated with this model are summarized and compared to analytical calculations in the next section.

Table 5.1: Calculated view factors for the three different shoe box models.

Size Method	small A	small R	medium A	medium R	large A	large R
$F_{1\text{-}2}$	0.88	0.88	0.32	0.32	0.03	0.02
$F_{1\text{-}3}$	0.03	0.03	0.19	0.19	0.27	0.27
$F_{1\text{-}4}$	0.03	0.03	0.19	0.19	0.27	0.27
$F_{1\text{-}5}$	0.03	0.03	0.15	0.15	0.22	0.22
$F_{1\text{-}6}$	0.03	0.03	0.15	0.15	0.22	0.22
Sum	1.00	1.00	1.00	1.00	1.00	0.99

5.2.3 Comparison of Results

In a first step, view factors from RadTherm are compared to those obtained from equations (5.6) and (5.7). As view factors in RadTherm are not directly accessible as output, a workaround had to be found for extracting these values from the software. First, all back surfaces were set to *insulated* to eliminate heat loss to the bounding box RadTherm draws around a model. Then, each emissivity of the front surfaces was set to 1.00. The surface temperature of the ceiling was set to 1 K and the surface temperatures of the other enclosing surfaces were set to 0 K so that the ceiling was the only surface of the model emitting heat. Thus, the magnitude of its heat flux $\dot{q}$ becomes equal to the Stefan–Boltzmann constant σ. Now, the amount of heat which is absorbed by an other surface than the ceiling depends on how well this surface is "seen" by the ceiling. By dividing the absorbed heat flux of each surface by the Stefan–Boltzmann constant (that is the emitted heat flux), the view factors shown in table 5.1 were found. In table 5.1, the model with dimensions of 5 m x 4 m x 0.3 m is labelled *small*. *Medium* denotes the model of 5 m x 4 m x 3 m. The model with dimensions of 5 m x 4 m x 15 m is labelled *large*. View factors for each model were both calculated analytically and obtained from a simulation in RadTherm. *A* denotes view factors from the analytical solution. *R* denotes view factors obtained from the simulation. $F_{1\text{-}2}$ is the view factor between ceiling and floor. $F_{1\text{-}3}$ and $F_{1\text{-}4}$ are the view factors between ceiling and sidewalls. $F_{1\text{-}5}$ and $F_{1\text{-}6}$ are the view factors between ceiling and front and rear respectively.

The table shows that view factors from RadTherm are equal to the ones found when applying the above equations. Varying the size of the shoe box model lead to a range of view factors, for example the view factor between ceiling and floor F_{12} varies between 0.88 and 0.03. The very small deviation between the analytical result and RadTherm for F_{12} of the large shoe box model with a height of 15 m may be explained by both the very small values for emitted and absorbed heat and possibly an error due to rounding. Overall, the agreement between both view factor calculations is very good.

In a second step, temperatures and emissivities were assigned to the surfaces of the three shoe box test models and net heat rates were calculated. Calculations were done for all three different shoe box geometries using values of 1.00 for emissivity. The medium size model was also solved for an emissivity of 0.84. Table 5.2 shows the assigned temperatures as well as net heat rates from the analytical solution and from RadTherm together with the deviation between the two calculation methods. The maximum deviation in the table is 0.68 % for the net heat rate of the rear wall of the medium size model using emissivities of 0.84. Results could lead to the conclusion that deviation increases for lower values of emissivity. However, a further test calculation with $\varepsilon = 0.05$ which is not shown here revealed that discrepancies between RadTherm and the analytical solution do not exceed 0.88 %.

Hence, both view factors and heat rates calculated with RadTherm can be regarded as very accurate and the software is a reliable method to determine radiant heat transfer in this work.

Table 5.2: Assigned temperatures and net heat rates for each surface from the analytical solution and a RadTherm simulation. The right column shows the deviation between the two calculation methods.

surface	temperature	net heat rate analytical solution	net heat rate RadTherm	deviation
	°C	W	W	%
geometry: 5.0 m x 4.0 m x 0.3 m, emissivity: 1.00				
ceiling	20.0	1018.80	1021.37	0.25
floor	10.0	−1020.32	−1022.52	0.22
first side wall	17.0	16.20	16.18	−0.13
second side wall	16.0	7.76	7.76	−0.02
front wall	14.0	−7.97	−7.98	0.08
rear wall	13.0	−14.47	−14.46	−0.10
geometry: 5.0 m x 4.0 m x 3.0 m, emissivity: 1.00				
ceiling	20.0	710.10	710.44	0.05
floor	10.0	−718.87	−718.92	0.01
first side wall	17.0	180.68	180.82	0.08
second side wall	16.0	82.60	82.70	0.12
front wall	14.0	−91.46	−91.66	0.22
rear wall	13.0	−163.05	−163.25	0.12
geometry: 5.0 m x 4.0 m x 3.0 m, emissivity: 0.84				
ceiling	20.0	567.78	564.30	−0.61
floor	10.0	−574.72	−571.43	−0.57
first side wall	17.0	147.25	146.45	−0.54
second side wall	16.0	67.25	67.45	0.30
front wall	14.0	−74.26	−74.45	0.26
rear wall	13.0	−133.30	−132.39	−0.68
geometry: 5.0 m x 4.0 m x 15.0 m, emissivity: 1.00				
ceiling	20.0	553.71	552.96	−0.14
floor	10.0	−560.85	−559.78	−0.19
first side wall	17.0	933.20	933.56	0.04
second side wall	16.0	356.65	356.54	−0.03
front wall	14.0	−436.84	−437.36	0.12
rear wall	13.0	−845.86	−846.24	0.04

5.2.4 Simplified Calculation

So far, it could be shown that RadTherm is a suitable tool for analysis of radiation exchange in this work. However, each time an experiment is evaluated the collected data has to be fed into RadTherm. After calculating the radiant heat fluxes from the hot plate to the other enclosing surfaces of the chamber in RadTherm, these heat fluxes have to be reinserted into a spreadsheet application for further analysis. Thus, a simplified, more straight-forward calculation method which can be used for checking experimental results at an early stage of the evaluation process is desirable.

For any surface A_1 with $F_{1-1} = 0$ which radiates only to surface A_2, net radiative heat flux of A_1 is given by equation (5.8) according to Modest (2003, ch. 5.3).

$$\dot{q}_1 = \frac{\sigma \left(T_{A1}^4 - T_{A2}^4 \right)}{\frac{1}{\varepsilon_1} + \frac{A_1}{A_2} \left(\frac{1}{\varepsilon_2} + 1 \right)} \tag{5.8}$$

For a convex surface placed into a large isothermal environment—that is $A_1 << A_2$—equation (5.8) may be further simplified to

$$\dot{q}_1 = \varepsilon_1 \sigma \left(T_{A1}^4 - T_{A2}^4 \right) \tag{5.9}$$

where radiant flux only depends on the emissivity of surface A_1 and the temperatures of the two surfaces.

This condition can be regarded as fulfilled for the experimental chamber as the surface area of the heated plate is considerably smaller than the sum of the surface areas of the other enclosing surfaces (4 %) and as both air temperature gradients inside the cabin and temperature variations between the enclosing surfaces are expected to be quite small. Hence, equation (5.9) offers a simplified calculation method which can easily be implemented in a spreadsheet application. Consequently, it was also compared to the analytical solution presented above using the medium sized shoe box model with emissivities set to 1.00 and temperatures of floor and wall surfaces as given in table 5.2. The five values of floor and wall surface temperatures are inserted into equation (5.10) to calculate a resulting temperature of surface A_2 which is called T_{A2}.

$$T_{A2} = \frac{\sum_{N=1}^{5} T_i A_i}{\sum_{N=1}^{5} A_i} \tag{5.10}$$

The temperature of the ceiling was varied to achieve a range of temperature differences between ceiling and surface A_2. For each temperature of the ceiling, radiative net heat loss of the ceiling was calculated using both the simplified method from equation (5.9) and the analytical solution method. The ratio of simplified to analytical radiant flux is plotted versus the temperature difference in figure 5.3. The diagram shows that the result from the simplified calculation tends to be closer to the analytical solution for larger temperature differences between the ceiling and the other enclosing surfaces. This behaviour was expected as temperature variation between the single sub-surfaces which make surface A_2 become more negligible the higher the difference between ceiling and A_2 gets. Thus, the validity criteria of equation (5.9) (isothermal surface A_2) is better fulfilled.

From equation (5.10) it can be seen that temperature T_{A2} does not only depend on the temperatures of the single surfaces but also on the surface areas of its components. As geometry plays a role, it was adapted to the dimensions of the experimental chamber for testing the simplified calculation method. Temperatures are kept the same as for the shoe box model and emissivities were set to 1.00 and 0.84 respectively. Figure 5.3 shows that for the geometry of the chamber results are even better than results for the shoe box model with deviation between simplified and exact method of less than 3 % for temperature differences between 4 K and 8 K and less than 1 % for temperature differences above 8 K. Furthermore, the diagram shows that emissivity has only a small effect on the accuracy of the solution.

Hence, equation (5.9) offers a very good first guess of resulting radiation which is already very close to the exact radiant heat flux and can thus be used for checking experimental results before doing any detailed analysis. However, this method is limited to configurations where the hot plate only radiates towards the other enclosing surfaces. As soon as additional acoustic baffles are installed beneath the ceiling, this simplified calculation no longer delivers reliable results as the baffles act like a heat shield of a different temperature and thus the conditions for validity of equation (5.9) are no longer fulfilled.

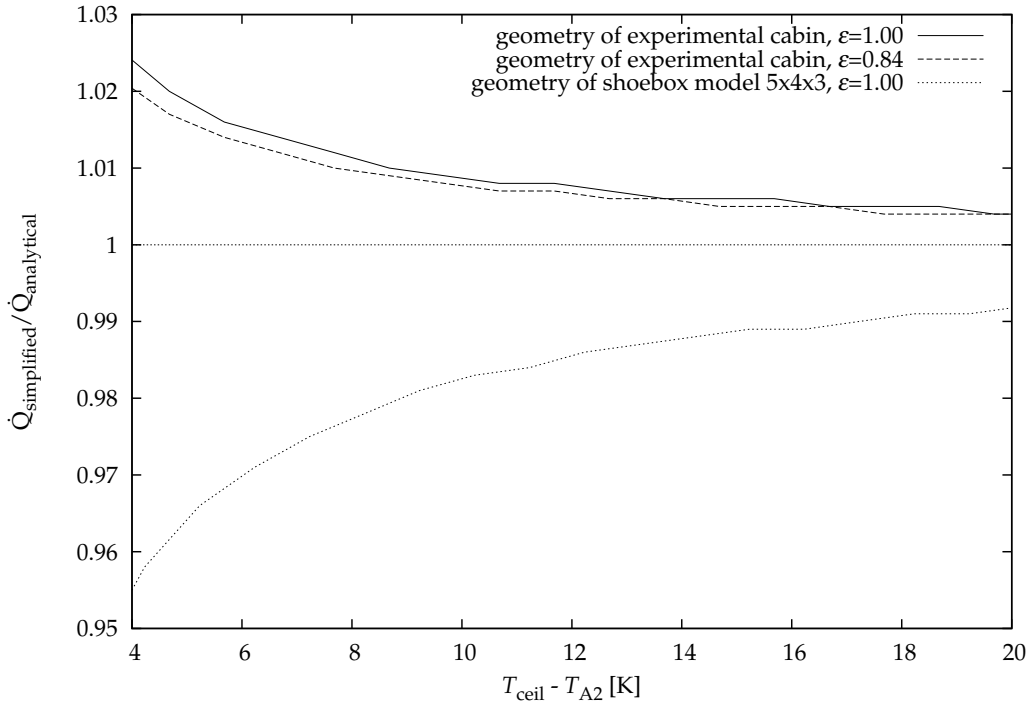

Figure 5.3: Accuracy of a simplified calculation of radiative heat transfer for both the shoe box test model and the geometry of the experimental cabin over a range of excess temperatures of the hot ceiling.

5.3 Models of the Experimental Chamber

Having shown that RadTherm is an appropriate tool for calculating radiant exchange, two models of the experimental chamber were created in the same manner as described in section 5.2.2 with specifications of the chamber as presented in chapter 3. The first model is one of the cabin with the hot plate at the ceiling and without any obstacles beneath it. In the second model, additional surfaces representing the 19 baffles have been included. Specifications of the baffles are also given in chapter 3.

Finally, the parameters of the RadTherm solver have been tested with measured data from an experiment where the hot plate was placed at the ceiling, its heat output was set to approximately 60 W and the ventilation system was turned off

Table 5.3: Tested settings of view factor configuration and convergence criteria in RadTherm. The leftmost column shows the resulting number of rays cast from each element for the selected settings. Calculated radiant heat rates from the hot plate to the other surfaces are displayed in the rightmost column.

Number of rays	View factor settings		Convergence criteria		$\dot{Q}_{rad}$
	Rays	Subdivision	Tolerance slope °C	Maximum iterations	W
8192	3	2	5E-15	1000	−49.63
8192	3	2	5E-07	500	−49.63
1152	2	1	5E-07	500	−49.63
512	1	1	5E-07	500	−49.63

to investigate natural convection in the unventilated chamber. Then, the solver was run with four different combinations of settings for view factor accuracy and convergence criteria as shown in table 5.3. As radiation emitted by the hot plate is the target value of interest, it is displayed together with the settings. Table 5.3 shows clearly that already the setting with the lowest number of rays cast from each element to its surrounding is sufficient for an accurate calculation of radiant heat transfer as the created mesh is already very dense. Thus, a further increase in either view factor accuracy or the convergence criteria does not lead to improved results but only boosts computational time.

5.4 Summary

This chapter has shown that RadTherm is a suitable and accurate enough tool to calculate radiant exchange inside the experimental chamber by comparing results obtained from RadTherm to a well-known analytical solution of radiation exchange given in literature. The deviation between RadTherm and the analytical solution was less than $\pm 1\%$ for all investigated cases. As a consequence, two RadTherm models have been set up. The first one is for evaluating experiments with the hot plate installed at the ceiling and no further obstacles beneath the plate. The second one is for the experimental test series with additional acoustic

baffles installed below the ceiling where geometry is too complex to be treated otherwise. For the basic geometry without further obstacles, a simplified calculation method was presented which can be used for an immediate first guess and which delivers results that differ from the analytical solution by less than 2 % in most cases.

6 Experimental Results

6.1 Introduction

In this chapter, experimental results of the carried out test series are presented. As previously mentioned, the hot plate has been installed at the centre of the ceiling for each test series.

First, outcomes for an unobstructed ceiling are presented in section 6.2. These are divided into

- results from an unventilated chamber for investigation of natural convection which are shown in section 6.2.1. The test series consists of 17 experiments and covers a range of total heat output of the hot plate from approximately $15\,\mathrm{W\,m^{-2}}$ to $101\,\mathrm{W\,m^{-2}}$. Results from repeated experiments are also included in this set of experiments. Outcomes from this test series are compared to correlations known from literature in order to assure the quality of the experimental method.
- results for a chamber ventilated at a rate of approximately 10 ac/h via a modified high-level air inlet for investigation of forced convection. This test series consists of only seven experiments as forced convection is not in the focus of this work but results are needed for a detailed analysis of mixed convection conditions. Total heat output of the hot plate ranged from $21\,\mathrm{W\,m^{-2}}$ to $107\,\mathrm{W\,m^{-2}}$. In these experiments, *Re* numbers are approximately 11000 so that the inlet jet is fully turbulent. When "forced convection" or "high *Re* numbers" are mentioned in later discussions, these are the experiments referred to. The experimental arrangements have been presented on page 88 in chapter 3.6.2. Results are shown on pages 149ff. in section 6.2.2.

- results for a chamber ventilated at a rate of 11 ac/h via the regular high-level inlet opening, which are shown on pages 151ff. in section 6.2.2. This test series was used for investigation of mixed convection in the experimental chamber. It consists of 24 experiments with total heat output of the hot plate varying from approximately $16\,W\,m^{-2}$ to $82\,W\,m^{-2}$. Velocities below the heated plate were measured in each experiment. Resulting *Re* numbers lay between 1800 and 8100 and so encompassed the transitional turbulence range.
- results for an additional set of mixed convection experiments which was used to study the limiting case given by the natural convection correlation. Eight experiments were carried out in this test series. Heat output of the hot plate was nearly doubled with a maximum value of more than $150\,W\,m^{-2}$ and the ventilation rate was slightly reduced to 10 ac/h. A temperature difference between hot plate and mean air of more than 20 K was achieved in these conditions.

Outcomes of the test series with acoustic baffles are shown in section 6.3. These are divided into

- results from an unventilated chamber for investigating the influence of the baffles on natural convection. For this test series which is presented in section 6.3.1, 16 experiments were carried out where total heat output of the hot plate ranged from $16\,W\,m^{-2}$ to $92\,W\,m^{-2}$. In 9 of these 16 experiments, hotwire sensors were installed below the hot plate for measuring velocities.
- results for a chamber ventilated with 11 ac/h via the regular high-level inlet opening as shown in section 3.6. These experiments have been carried out analogous to the third test series without baffles above. The aim of this test series was to investigate the influence of the baffles on mixed convection. Its 18 experiments cover a total heat output from $22\,W\,m^{-2}$ to $82\,W\,m^{-2}$. Velocities below the heated plate were measured in 5 of these 18 experiments.

The experimental results are summarized in section 6.4.

Additional experimental results which are supplementary to those in the main text of this document can be found in appendix D which begins on page 218.

6.2 Unobstructed Ceiling

6.2.1 Results without Ventilation

For investigation of natural convection in the experimental chamber, a series of 17 experiments has been carried out with an unventilated chamber and the hot plate at the ceiling. A detailed description of the experimental method and an error analysis has been given in chapters 3 and 4. Total heat output of the hot plate ranged between approximately $15\,W\,m^{-2}$ and $101\,W\,m^{-2}$ in the 17 experiments. The test series also includes repetitions of experiments—for example with a heat output of $20\,W\,m^{-2}$—for checking the quality of the experimental method. Thus, the typical range of heat transfer rates expected at ceilings of buildings with low energy cooling concepts has been fully covered.

Resulting temperature differences between the heated plate and mean air range from slightly more than 2 K to nearly 14 K. As heat fluxes in low energy cooling concepts are rather low—typical values for TABS range between $30\,W\,m^{-2}$ and $40\,W\,m^{-2}$, emphasis has been put on experiments with small values of heat output and temperature differences of 5 K or less. One third of the conducted experiments fall in this range whereas measured temperature differences were rather large in previous works. The correlation by Awbi and Hatton (1999) is derived from five experiments with temperature differences between 7 K and 34 K of which only the smallest value was below 10 K.

Convective heat transfer coefficients have been calculated using the mean air temperature in the chamber as reference temperature for the reasons given in chapter 2. The obtained convective heat transfer coefficients are shown in figure 6.1.

In general, resulting CHTCs are quite low with values reaching only slightly above $1\,W\,m^{-2}\,K^{-1}$ for the largest temperature differences. Repetitions of experiments with the same temperature difference lead to nearly identical values for h_c even for experiments with low values of heat output where uncertainty in a single experiment—indicated by the error bars—reaches up to $\pm 0.41\,W\,m^{-2}\,K^{-1}$. For large temperature differences, uncertainty in a single experiment decreases to a value of only $\pm 0.1\,W\,m^{-2}\,K^{-1}$. This uncertainty is similar to the one given by Awbi

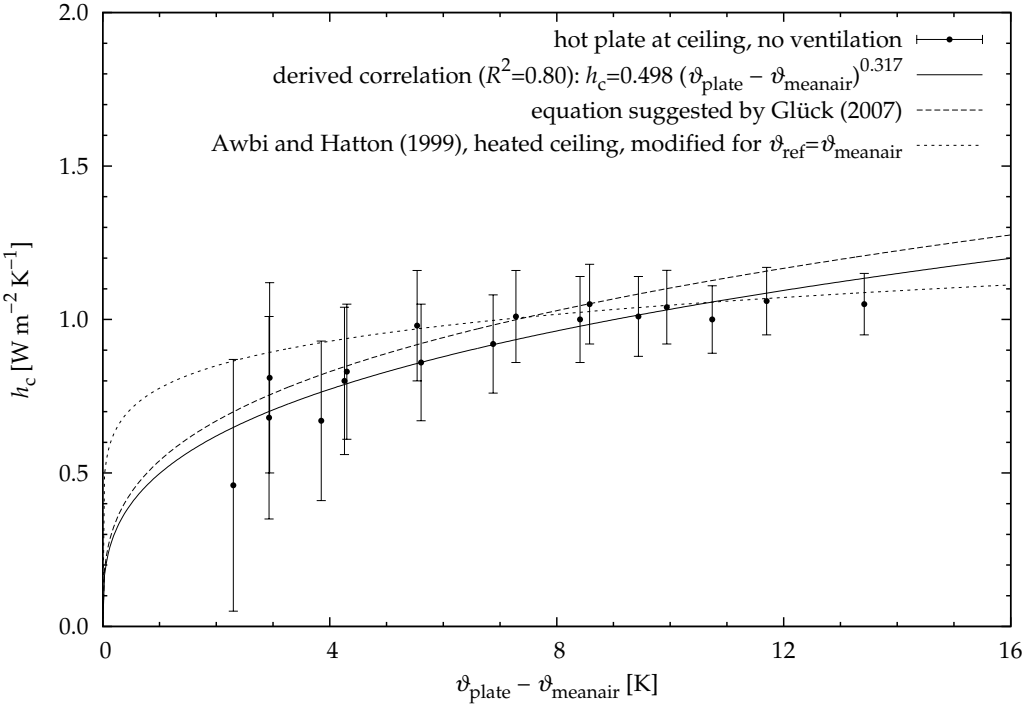

Figure 6.1: Convective heat transfer coefficients from the first test series and the derived correlation as well as existing natural convection correlations suggested by Glück (2007) and by Awbi and Hatton (1999).

(1998) for his ceiling experiments. Hence, the expected quality and repeatability of experiments was confirmed. The resulting correlation for h_c from these results is

$$h_c = 0.498 \left(\vartheta_{plate} - \vartheta_{meanair}\right)^{0.317} . \tag{6.1}$$

According to Stahel (2002), the coefficient of determination R^2 is given as

$$R^2 = \frac{SS_R}{SS_Y} \tag{6.2}$$

with SS_R being the regression sum of squares and SS_Y being the total sum of squares. Furthermore, Stahel (2002) states that the total sum of squares can be

written as

$$SS_{\mathrm{Y}} = SS_{\mathrm{R}} + SS_{\mathrm{E}} \tag{6.3}$$

with SS_{E} being the residual sum of squares. Combining equations (6.2) and (6.3) and rewriting SS_{E} as $\sum (y_{\mathrm{i}} - f(x_{\mathrm{i}}))^2$ and SS_{Y} as $\sum (y_{\mathrm{i}} - \bar{y})^2$ leads to

$$R^2 = 1 - \frac{\sum (y_{\mathrm{i}} - f(x_{\mathrm{i}}))^2}{\sum (y_{\mathrm{i}} - \bar{y})^2} \tag{6.4}$$

which is used as an indicator for the goodness of fit of the derived correlation. For equation (6.1), R^2 is 0.80.

For comparison, the experimental results of this work have been plotted together with an existing correlation suggested by Glück (2007) and a further correlation recommended by Awbi and Hatton (1999) which have all been presented in chapter 2 and which are given in equation (2.25) and (2.39) respectively. The correlation suggested by Glück is,

$$h_{\mathrm{c}} \leq 0.54 \Delta\vartheta^{0.31}. \tag{6.5}$$

With the geometry of the hot plate in the experimental chamber, the correlation suggested by Awbi and Hatton can be written as

$$h_{\mathrm{c}} = 0.76 \Delta\vartheta^{0.133}. \tag{6.6}$$

As the correlation of Awbi and Hatton (1999) uses air temperature at the centre of the cabin as a reference temperature instead of the mean air temperature, a temperature correction obtained from the measurements of temperature gradients in each experiment was applied to their equation. These temperature gradients are shown in appendix D.1.1 on page 219ff. The modified correlation for a temperature difference based on the mean air temperature as reference temperature is plotted in figure 6.1. It should be noted that the error in h_{c} due to an erroneous reference temperature would have been negligibly small with a discrepancy of less than $0.02\,\mathrm{W\,m^{-2}\,K^{-1}}$ as air temperature at the centre of the cabin is very close to the mean air temperature.

For small values of $\Delta\vartheta$, the new correlation delivers the lowest values although it shows very good agreement with the one given by Glück (2007). The correlation

by Awbi and Hatton (1999) does not fit the new correlation for $\Delta\vartheta < 5\,\mathrm{K}$. However, a closer look at the publication by Awbi and Hatton reveals that their correlation has been derived from a set of five experiments where only one single experiment was conducted at a temperature difference of 7 K. Awbi and Hatton's remaining results were obtained from experiments with temperature differences between 14 K and 34 K. Thus, the applicability of their correlation for temperature differences of 5 K and less must be questioned. For this range, either the new correlation or the one by Glück seems more appropriate. On the other hand, the results of this work are closer to Awbi and Hatton's values than the ones by Glück for large temperature differences. The correlation suggested by Glück delivers the largest values of all three correlations shown in figure 6.1 for large values of $\Delta\vartheta$. Glück (1997) already states that his correlation for h_c above is based on the Nusselt correlations of Michejew (1964) which were obtained from various experiments with heated wires, ducts, plates and spheres. He does not explicitly state a temperature range for which his correlation is valid but from a graphical representation he gave, it can be concluded that his correlation is valid for temperature differences between hot plate and air of up to 100 K with air temperatures between 0 °C and 20 °C. It is questionable if a correlation obtained from experiments with isolated plates which is valid for such a wide range of values gives a good representation of the conditions that might be expected in a room with low energy heating or cooling concepts. The new correlation is a little bit closer to the values obtained by Awbi and Hatton (1999) in an experimental cabin.

Hence, the new correlation could be regarded as the best choice for describing natural convection over the whole range of $\Delta\vartheta$ which are of interest for low energy cooling concepts.

Furthermore, this test series is considered as a base case

- which demonstrates the quality of the built experimental chamber, and
- which confirms recent outcomes of other scientists' works that convective heat transfer coefficients for natural convection at a heated ceiling are around $1\,\mathrm{W\,m^{-2}\,K^{-1}}$ instead of the significantly larger or smaller values shown in chapter 2 which can be found in older correlations and which were often obtained from experiments with isolated flat plates.

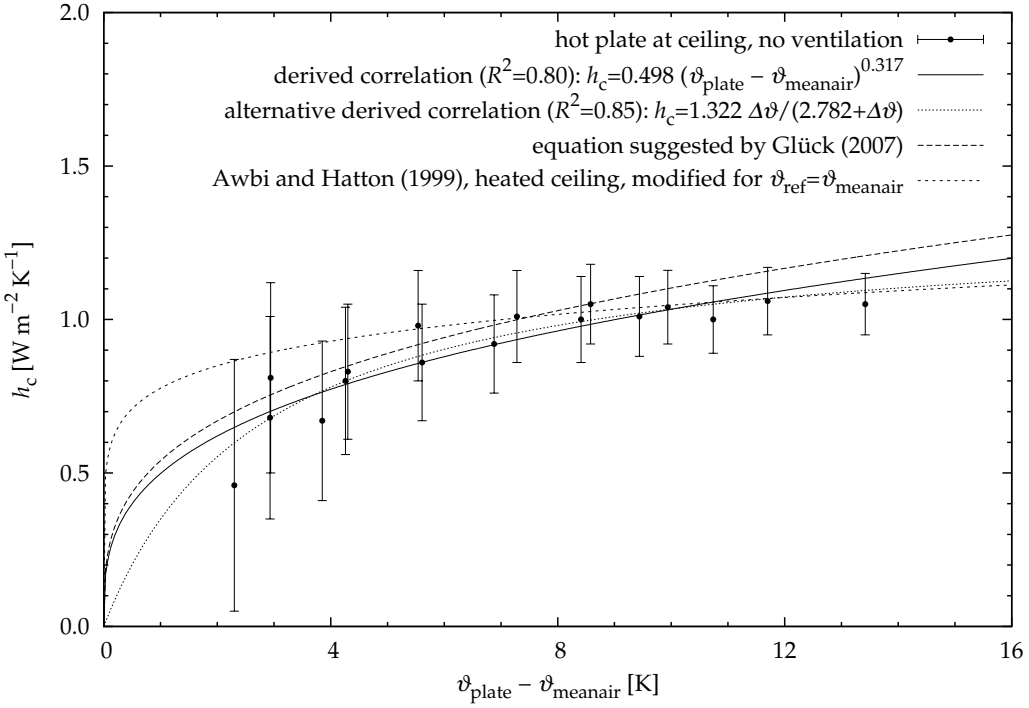

Figure 6.2: Alternative correlation for the natural convection experiments.

So far, the classical, well-known form of $h_c = C\ (\Delta\vartheta)^n$ has been used to provide a correlation for natural convection at an unobstructed ceiling derived from the experiments of this first test series. The advantage of the chosen form is that results of this work can easily be compared to existing correlations and can also be easily implemented into existing building simulation codes such as TRNSYS as these codes often make use of the same form for the correlation. This was shown in chapter 2. However, further analysis of the experimental data showed that an alternative form of the equation leads to a correlation which fits the experimental results better. For the experiments of this first test series, this is shown in figure 6.2.

The derived alternative correlation is

$$h_c = \frac{1.322\ \left(\vartheta_{plate} - \vartheta_{meanair}\right)}{2.782 + \left(\vartheta_{plate} - \vartheta_{meanair}\right)}. \tag{6.7}$$

With $R^2 = 0.85$, the alternative correlation of equation (6.7) fits the experimental results better than the correlation given in equation (6.1) in the classical form which only led to $R^2 = 0.80$. Figure 6.2 provides the visual confirmation that the alternative correlation offers a good representation of the experimental results at the lower end of observed temperature differences. For larger temperature differences, the alternative correlation leads to values which are very close to those of Awbi and Hatton (1999) who conducted experiments between 7 K and 35 K. Their correlation was also obtained from experiments in an experimental chamber while the correlation by Glück (2007) is based on experiments with isolated plates. An alternative form of the correlation might be a suitable solution if its application is limited to heat transfer in closed indoor environments. Further tests and additional analysis would be necessary to verify such an approach.

A dimensionless representation of results in the form of Nu versus Ra is presented in figure 6.3. The obtained Nusselt numbers are plotted versus Rayleigh numbers for each experiment. Rayleigh numbers range from approximately 4.7×10^7 to 2.6×10^8. Nusselt numbers start at approximately 10 for the lowest value of Ra and slowly increase up to 25 with increasing Ra. The correlation for natural convection in the unventilated chamber with a hot plate at the ceiling has a value of 0.81 for R^2 and is given as

$$Nu = 0.04 Ra^{0.335}. \tag{6.8}$$

For building design purposes both radiation and convection must be taken into consideration. Thus, the approach elaborated by Glück (2007) which has been also thoroughly discussed in chapter 2 has been pursued in the evaluation of experimental results. Glück (2007) suggested to describe heat transfer by both convection and radiation with the heat transfer coefficient according to characteristic base curve h^*. The correlation for a heated ceiling has been given in equation (2.85). For convenience, it is shown again.

$$h^*_{\text{hori,down}} = 0.54 \left| \vartheta_{\text{surf}} - \vartheta_{\text{operative}} \right|^{0.31} \left(1 + 0.4\,\text{m}^{-1} \left(1.1\,\text{m} - H \right) \right)^{1.31} + 6.12 \tag{6.9}$$

The resulting heat transfer coefficient according to characteristic base curve h^* is plotted in figure 6.4 together with the experimental results of this work. As expected after the previously shown very good agreement for the convective heat

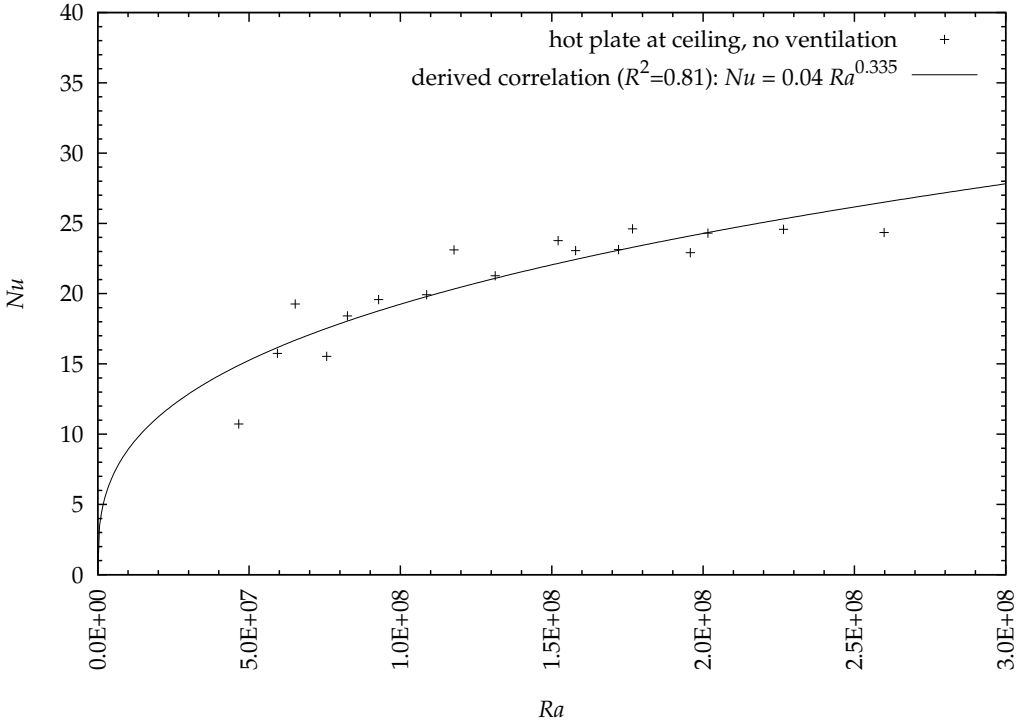

Figure 6.3: *Nu* number versus *Ra* number for experiments with the hot plate installed at an unobstructed ceiling and with an unventilated cabin.

transfer coefficients, experimental results for heat transfer by both convection and radiation are of the same magnitude as the correlation for h^* given by Glück (2007) in equation (2.85) and (6.9) respectively. Largest discrepancies occur for low values of $\Delta\vartheta$. A closer look at equation (2.85) reveals the reason for this discrepancy. Glück uses a constant value—the last summand with a value of 6.12—for radiant heat transfer whereas the correlation from this work is based on the experimental results and the chosen form of the equation of the derived correlation. For intermediate values of $\Delta\vartheta$, there again is a very good agreement between the experimental results of this work and the correlation given by Glück. Finally, for large temperature differences the new correlation delivers larger values for h^* than Glück's equation as radiation will increase with higher temperature differences. While radiation will be underestimated by the simplified approach of Glück with a constant value of $6.12\,\mathrm{W\,m^{-2}\,K^{-4}}$, these results are based on a detailed treat-

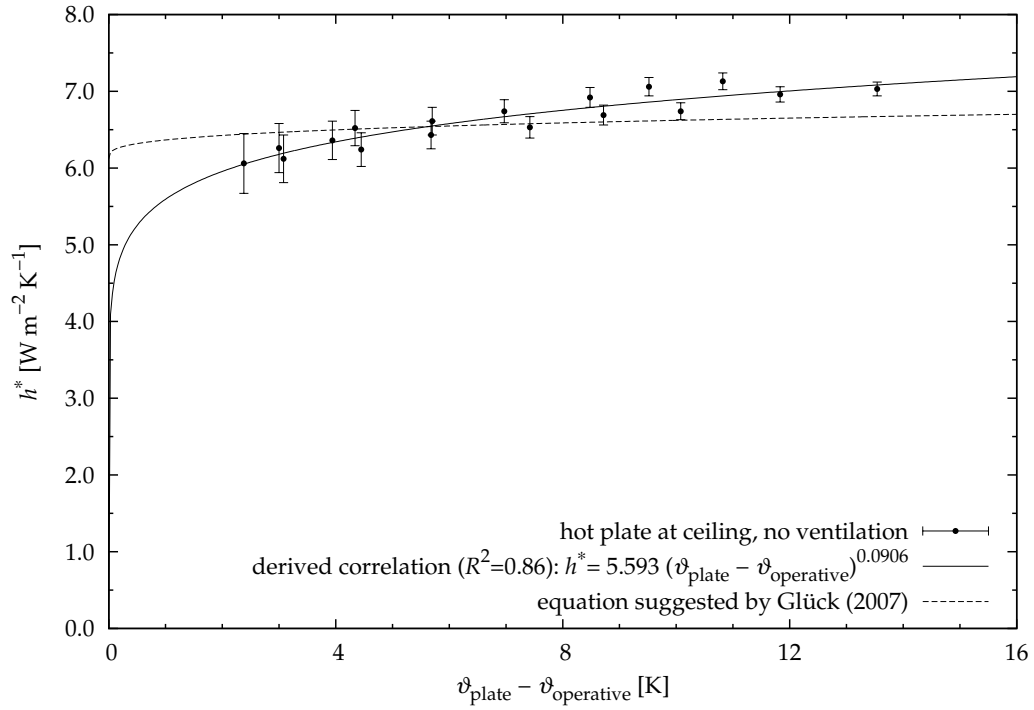

Figure 6.4: Heat transfer coefficient according to characteristic base curve h^* from experiments with the hot plate at the ceiling of an unventilated cabin.

ment of both convection and radiation. Thus, a possible source of inaccuracy is eliminated.

Hence, the derived correlation

$$h^* = 5.593 \left(\vartheta_{plate} - \vartheta_{operative}\right)^{0.0906} \tag{6.10}$$

with a coefficient of determination of 0.86 could be regarded as a suitable approach for the calculation of h^* in case of a heated ceiling in an unventilated chamber, which takes into consideration an increased radiant heat transfer at larger temperature differences whereas the existing correlation of Glück uses a constant value for radiation.

The correlation of Glück (2007) does provide physical meaningful values for very small temperature differences. The correlation derived in this work does not do

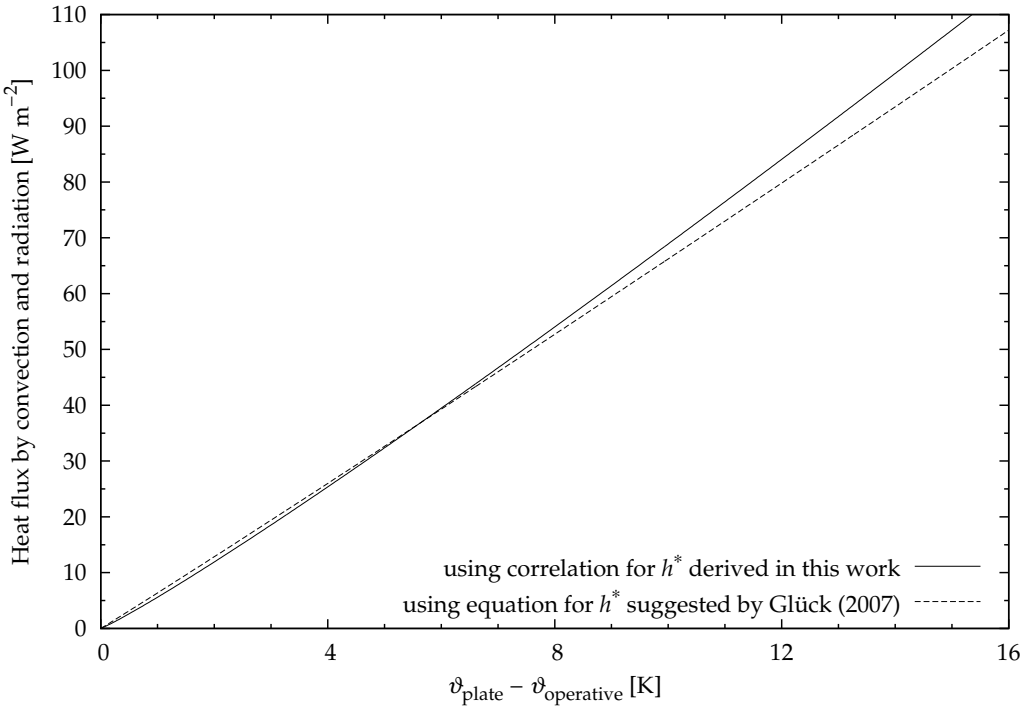

Figure 6.5: Resulting heat fluxes from the correlation for h^* of this work and the correlation suggested by Glück.

this for such values due to the chosen form of the equation. However, from a practical point of view, this does not lead to disadvantage. In figure 6.5, the heat fluxes from both correlations are compared. It can be seen that on the one hand similar results are obtained for small temperatures differences. On the other hand, larger deviations are achieved at larger temperature differences. For such values, the correlation of this work could be regarded as more accurate due to the detailed treatment of radiation although only given implicitly in the chosen form of the equation. Consequently, the new correlation could be regarded as the best choice for describing total heat transfer by both convection and radiation in the experimental chamber over the whole range of observed temperature differences.

6.2.2 Results with Ventilation

After natural convection in an unventilated chamber had been determined, effect of ventilation on convective heat transfer is examined. In a first step, forced convection is investigated. Afterwards, results for mixed convection will be presented. Ventilation cases can be compared to literature only partially as the experimental configuration is slightly different from previously published investigations (high-level slot inlet in this case, different nozzles or low-level inlet in other researchers' work).

Forced Convection

As the main interest of this work lies on heat transfer at the ceiling of low energy buildings using either TABS or night-time ventilation, and as forced convection is unlikely to occur in the majority of such situations, results from this test series are only needed for a detailed analysis of mixed convection results which will be presented later. Consequently, only a limited number of seven experiments has been conducted for investigation of forced convection. Ventilation rates in these experiments were in a narrow range of 9.8 ac/h to 10.4 ac/h with corresponding Reynolds numbers in the range of 10 600 to 11 300. Thus, the inlet jet is fully turbulent. The velocity used to calculate *Re* is the inlet velocity according to equation (2.58) at the end of the modified air inlet opening which is described in figure 3.11 on page 89. The length of the hot plate in direction of the flow—that is 0.6 m—is used as characteristic length L_c. Varying the heat output of the hot plate from 21 $W\,m^{-2}$ to 107 $W\,m^{-2}$ in these experiments resulted in surface-to-air temperature differences of 1.8 K to 11.9 K. Air temperature measured 6 cm below the centre of the hot plate (q.v. sensor 2112 in figure 3.7) is used as reference temperature for the evaluation. Fluid properties like conductivity or viscosity have been taken at the reference temperature.

Figure 6.6 in which calculated h_c is plotted versus $\vartheta_{plate} - \vartheta_{air}$ shows that h_c has a constant value of approximately 3.7 $W\,m^{-2}\,K$ for $\Delta\vartheta \leq 7\,K$. In this range, the CHTC does not depend on heat output of the hot plate or temperature difference between hot plate and air. There is good agreement between the experimental results and

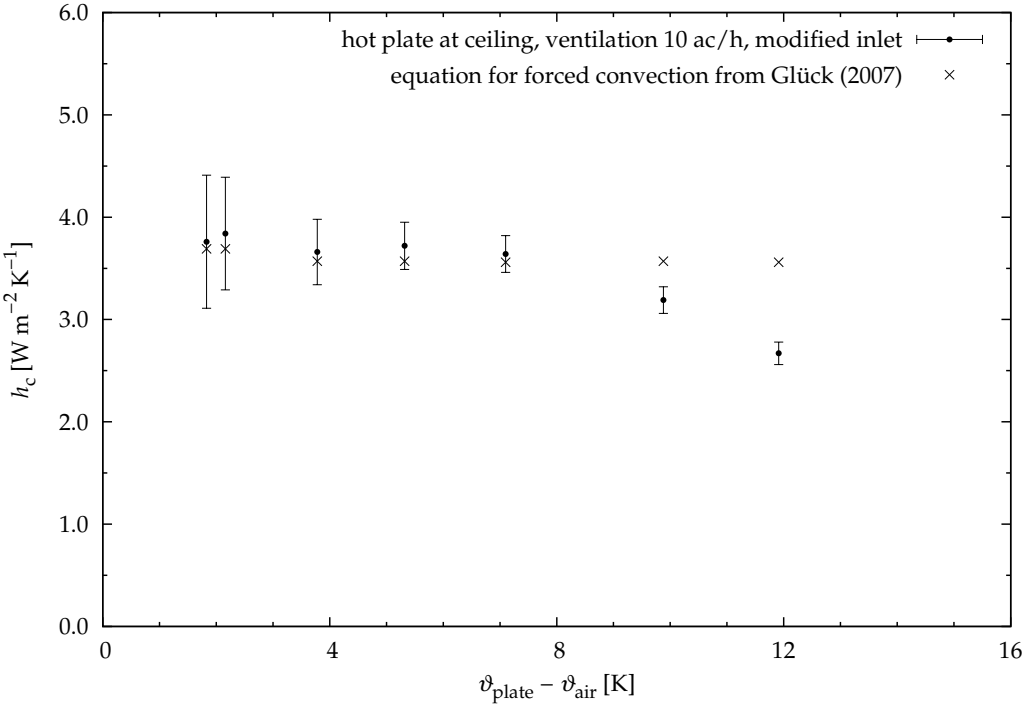

Figure 6.6: Convective heat transfer coefficients h_c from the second test series and results from an existing correlation for forced convection recommended by Glück (2007).

values from the correlation for forced convection presented by Glück (2007) in equation (2.51) which is repeated in equation (6.11). Values from this equation are also shown in figure 6.6. For forced convection, Glück (2007) suggested to use

$$Nu = \left[0.441\, Re\, Pr^{0.667} + \frac{Re^{1.6}\, Pr^2}{\left[27.027 + 66.027\, Re^{-0.1} \left(Pr^{0.667} - 1 \right) \right]^2} \right]^{0.5} . \qquad (6.11)$$

Up to $\Delta\vartheta = 7\,\mathrm{K}$, the experimental results can be perfectly explained with this forced convection correlation when taking into consideration the uncertainty of the experimental results—again expressed by the error bars.

Only two experiments with larger temperature differences were found to have

significantly smaller values for h_c (figure 6.6) and these values decrease with increasing temperature difference. As *Re* numbers of these two experiments are comparable to the values from other experiments and as *Re* is calculated using the nominal inlet velocity at the end of the supply air duct, it is suggested that at some point between $7\,\mathrm{K} < \Delta\vartheta < 9\,\mathrm{K}$ air flow pattern below the hot plate changes. For smaller temperature differences, the incoming air passes the hot plate and the situation can be described precisely using the velocity at the end of the modified inlet and equation (2.51). It is hypothesized that the incoming jet no longer remains attached to the hot plate but that the jet falls away from the ceiling for large temperature differences. Thus, velocity under the hot plate can no longer be expressed by the velocity upstream of the hot plate and equation (2.51) overestimates the occurring convective heat flux.

To test this hypothesis, the experimental conditions were changed and an extensive set of experiments was carried out to investigate mixed convection. For these experiments, velocity sensors were installed below the hot plate to investigate the behaviour of the passing air. Results of this test series are presented below.

Mixed Convection

In order to investigate mixed convection and to test the hypothesis of a change in air flow pattern beneath the hot plate, 24 experiments with heat output between approximately $16\,\mathrm{W\,m^{-2}}$ and $82\,\mathrm{W\,m^{-2}}$ have been carried out using the regular high-level slot inlet described in chapter 3. Both air change rate was measured at the end of the return air duct using the rotating vane anemometer and velocities beneath the hot plate using the hotwire sensors. The observed air change rate is 11 ac/h. Resulting *Nu* numbers range from 27 to 61, *Re* numbers (calculated using the measured average velocity below the hot plate) lie between 1800 and 8100. Thus, *Re* encompasses the transitional turbulence range. *Nu* starts at the upper end of observed values for natural convection but does not reach the values which occurred during forced convection experiments.

In figure 6.7, resulting convective heat transfer coefficients are plotted versus temperature difference between hot plate and mean air. As previous experimental setups for natural and forced convection showed a very good agreement with

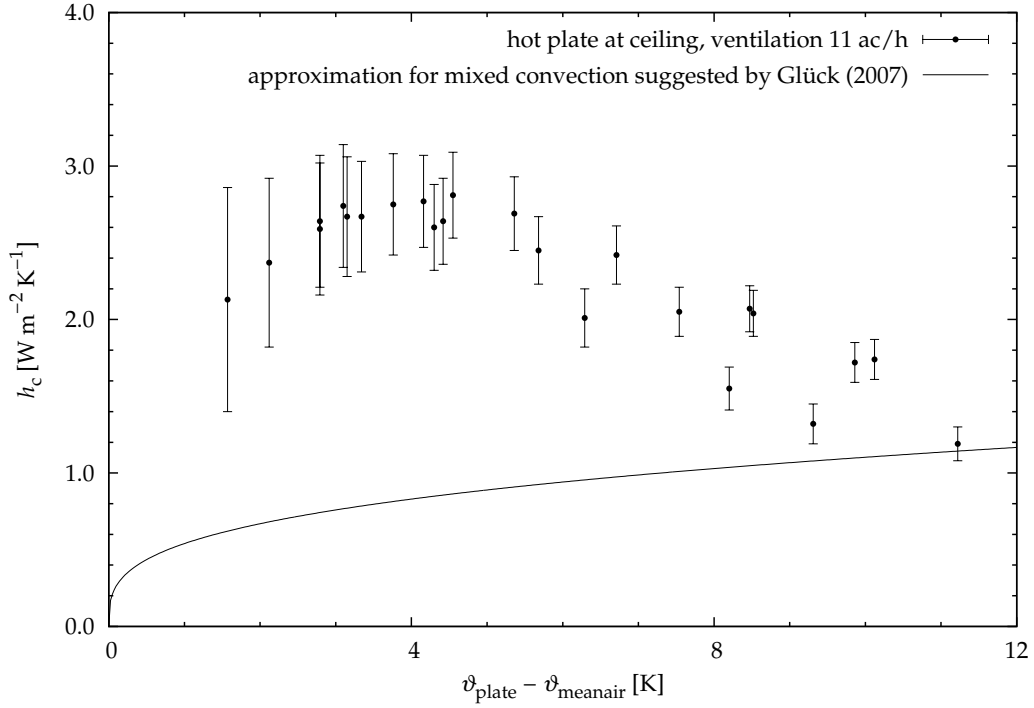

Figure 6.7: Convective heat transfer coefficients h_c of the third test series as well as an approximation for mixed convection suggested by Glück (2007).

correlations given by Glück (2007), results from this test series are also plotted together with an existing approximation for mixed convection which is suggested by the same author and which is given in equation (2.76).

It is obvious that the experimental results no longer match Glück's equation. Apart from the two experiments conducted at the smallest temperature differences which lead to convective heat transfer coefficients of approximately 2.2 W m^{-2} K^{-1} and 2.4 W m^{-2} K^{-1} respectively, a large number of experiments lead to nearly constant values for h_c which all lie in the range of 2.6 W m^{-2} K^{-1} to 2.8 W m^{-2} K^{-1} for temperature differences between 2 K and 5 K. The deviation of the experimental results from values calculated with Glück's equation is significant with convective heat transfer coefficients that are three times as large as expected. A further increase in temperature difference results in a decrease of h_c towards the approximation suggested by Glück. However, only the experiment with the largest tem-

perature difference between hot plate and mean air shows a good agreement with Glück's equation. This behaviour is similar to the one already observed in the forced convection experiments. Those lead to values for h_c which were generally larger and the decrease could only be observed for $\Delta\vartheta > 8\,\mathrm{K}$. With the new experimental arrangement and boundary conditions, the decrease of convective heat transfer coefficients can already be observed at $\Delta\vartheta = 5\,\mathrm{K}$.

Hence, three questions arise:

1. Can the drop in convective heat transfer coefficients be explained from the velocity measurements below the hot plate?
2. Is there a reasonable explanation for the difference between experimental results and the equation suggested by Glück?
3. Is there a better representation than the one by Glück which describes the behaviour observed in the chamber more accurately?

The answer to the first question is given by figures 6.8 and 6.9. In figure 6.8, velocities U measured at the rear, upstream edge of the hot plate and at the front, downstream edge are plotted versus temperature difference between the hot plate and mean air. At the low end of observed temperature differences, the measurements yield values slightly above $0.2\,\mathrm{m\,s^{-1}}$ for upstream velocity at the rear edge. With increasing temperature difference, the upstream velocity slowly decreases but does not fall below $0.15\,\mathrm{m\,s^{-1}}$ except for the one experiment with the largest temperature difference. In this case, measured upstream velocity differs significantly from all other experiments with a value of less than $0.1\,\mathrm{m\,s^{-1}}$. The downstream velocities which are measured at the front edge of the hot plate also start at approximately $0.2\,\mathrm{m\,s^{-1}}$. However, the correlation between decrease in velocity and increase in temperature is much more pronounced than for the upstream velocity. For temperature differences above 6 K, each downstream velocity is less than $0.1\,\mathrm{m\,s^{-1}}$. While there are only minor deviations between upstream and downstream velocities for small values of $\Delta\vartheta$, deviations become significant for higher heat output and the larger temperature differences accompanied by it.

A more detailed investigation of the air flow pattern below the hot plate is shown in figure 6.9. There, U is plotted versus the distance d from the rear wall in which

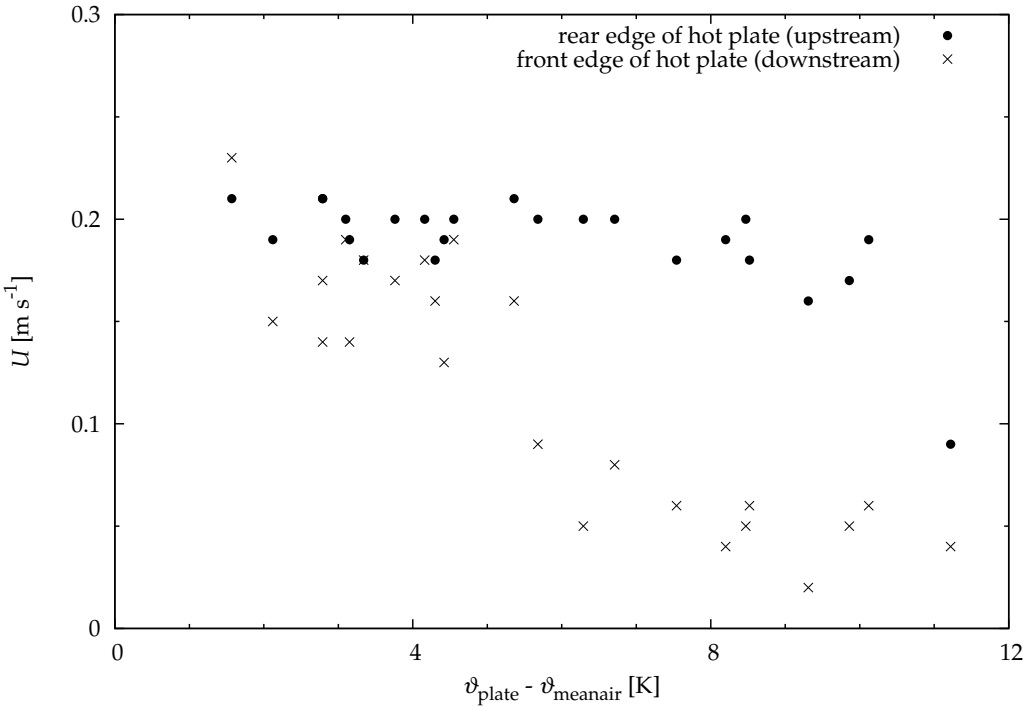

Figure 6.8: Velocities measured below the rear (upstream) and front (downstream) edge of the hot plate versus $\Delta\vartheta$ between hot plate and mean air.

the air inlet and outlet openings are located. For a better comprehension, direction of the flow and position of the hot plate are also drawn in the figure. Velocities are measured at the rear and front edge of the hot plate. Furthermore, velocities in the rear part of the cabin and below the centre of the hot plate have been recorded. The velocity profile is plotted for different values of total heat output of the hot plate $\dot{Q}_{el}$ starting at 30 W and reaching up to more than 80 W.

These measurements confirm the trend already observed in figure 6.8. In the rear part of the cabin, U ranges from 0.15 m s^{-1} to 0.2 m s^{-1}. Highest velocities could be observed for intermediate values of heat output. For low values of heat output, U at the front (downstream) edge is comparable to U in the rear part. With an increase in heat output to 50.6 W, the velocity at the front edge has dropped significantly to 0.05 m s^{-1} while U at the remaining points remains around 0.2 m s^{-1}. As heat output is further increased, the point at which a reduced velocity is measured

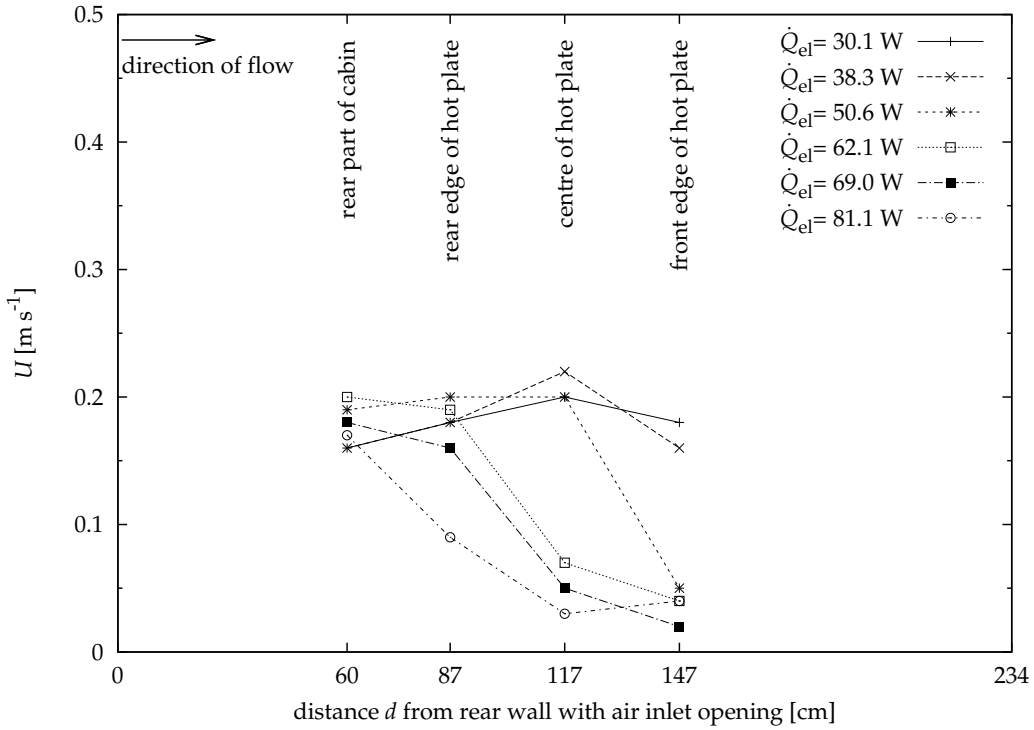

Figure 6.9: Velocities measured below the hot plate for different values of heat output. For better comprehension, direction of flow and position of the hot plate is also included in the figure.

moves upstream from the front edge of the hot plate towards the rear edge. For the maximum heat output of 81.1 W, U is below 0.1 m s^{-1} even at the rear (upstream) edge of the hot plate.

Hence, the drop in convective heat transfer coefficients can be explained using the velocity measurements. With increasing heat transfer, air movement below the hot plate is reduced. The air jet no longer remains attached to the ceiling but drops towards the floor. Thus, air movement under the plate is reduced and with increasing temperature differences conditions tend to become similar to the stably stratified conditions in an unventilated chamber. Due to the reduced air movement convective heat transfer is also reduced.

The second question stated above can be easily answered with a closer look at the

publication in which the approximation suggested by Glück was found. Glück (2007) mentions in the text that this approximation for mixed convection represents the upper end of natural convection and the lower end of mixed convection. From the experimental results it must be concluded that this approximation should be used only for very large temperature differences or low air change rates when the influence of natural convection dominates convective heat transfer and when forced convection can be mostly neglected.

Therefore, a better existing representation of mixed convection than the one given by Glück (2007) in equation (2.76) is sought.

In chapter 2, it was shown that convective heat transfer coefficients and Nu numbers for mixed convection can be expressed as a combination of the two terms which are valid for natural and forced convection. Therefore, equation (2.75) was used to obtain the convective heat transfer coefficient for mixed convection $h_{\mathrm{c,mixed}}$ by blending $h_{\mathrm{c,forced}}$ and $h_{\mathrm{c,natural}}$. The Nusselt number of the forced convection component is calculated from equation (6.11) which has already been used in the previous test series. CHTC for forced convection can then be calculated as $h_{\mathrm{c,forced}} = Nu \cdot \lambda / L_{\mathrm{c}}$. Fluid properties are evaluated at the temperature measured 6 cm below the hot plate again—that is just like in the previous experiments for investigation of forced convection. The local average velocity below the hot plate which was measured with the installed velocity sensors, was used to calculate Re. Characteristic length L_c is again set to 0.6 m. The natural convection component in equation (2.75) is calculated from the new correlation derived from the first experimental test series which is given in equation (6.1). This blending method has been described by multiple authors and relies on correlations for the forced and natural components. Primary inputs for this calculation are the velocities measured below the hot plate. (Some temperature data such as mean air temperature is still needed, but the detailed evaluation of temperatures is not necessary.)

In figure 6.10, the results from the blending method are shown together with the results which have been obtained from the experimental method presented in chapter 3. Now, experimental results match the method known from literature very closely again.

While figure 6.10 displays the actual values for convective heat transfer coeffi-

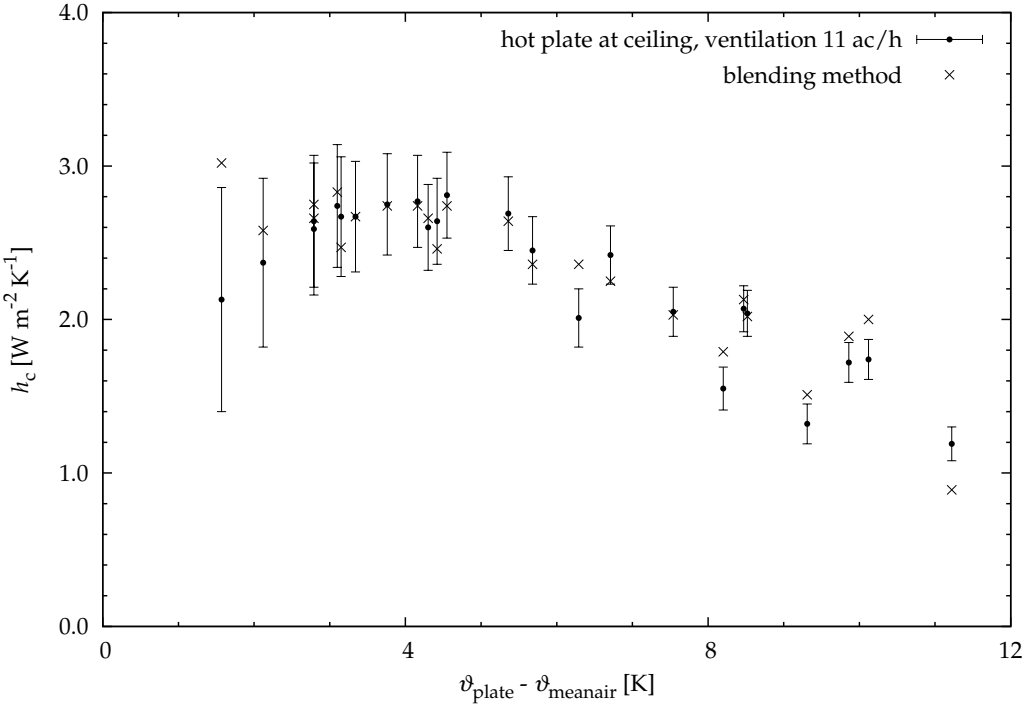

Figure 6.10: Convective heat transfer coefficients h_c calculated with data recorded in the third test series and corresponding values from the blending method presented in the literature review.

cients, the discrepancy Δh_c between the value obtained for h_c from the experimental results of this work and the value obtained using equation (2.75) for the blending method is shown in figure 6.11 in order to investigate the applicability of the blending method known from literature to the experimental results of this work. Therefore, the uncertainty in the experimental results is shown by the error bars around $\Delta h_c = 0$.

Seven experiments show a discrepancy Δh_c which exceeds the uncertainty of the experimental results. In six out of this seven experiments, the blending method leads to convective heat transfer coefficients which are larger than h_c from the experimental results. Only one experiment—the one with the largest temperature difference between hot plate and mean air—leads to a h_c from the blending method which is significantly smaller than the experimental result.

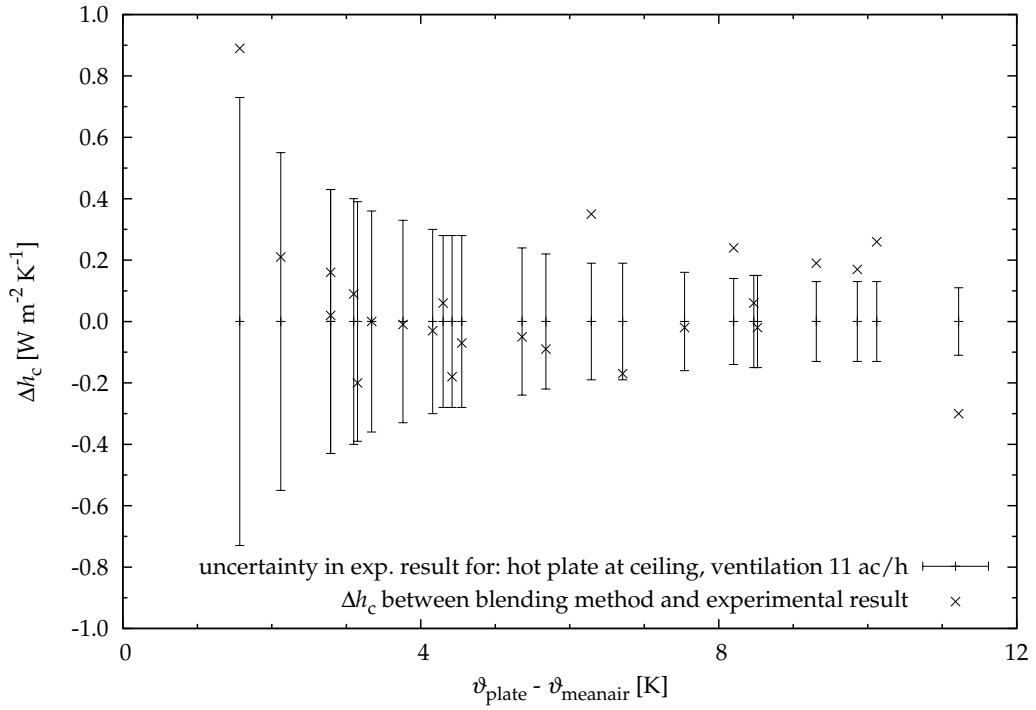

Figure 6.11: Difference Δh_c between convective heat transfer coefficients calculated with the blending method and the ones calculated with the experimental method described in chapter 3.

The deviation in this very experiment can be explained by the velocity measurements shown in figure 6.8. It was already noted that—while the downstream velocity is comparable to other experiments' results—upstream velocity of this experiment is considerably smaller than upstream velocities measured in all other experiments. This small value for upstream velocity leads to a smaller value for average velocity which is used to calculate h_c from the blending method. The deviation is most likely due to this outlier in velocity as a larger value for U would lead to a larger h_c comparable to the experimental result. The fact that h_c from this experiment is close to the approximation which is suggested by Glück as valid for the lower end of mixed convection and the upper end of natural convection further supports the theory that this discrepancy is rather caused by a wrong velocity measurement than by a wrongly calculated experimental result.

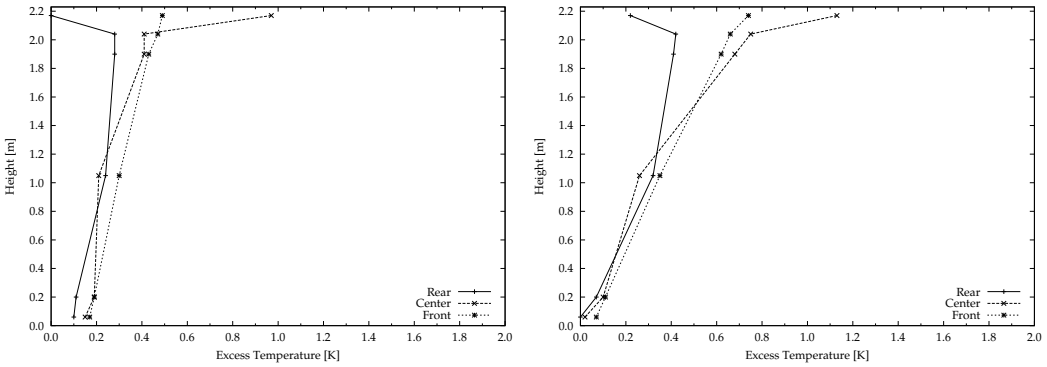

(a) $\vartheta_{\text{plate}} - \vartheta_{\text{meanair}} = 6.29\,\text{K}^{\star}$ (b) $\vartheta_{\text{plate}} - \vartheta_{\text{meanair}} = 6.71\,\text{K}$

Figure 6.12: Temperature gradients measured in the chamber during two mixed convection experiments. The one that leads to an outlier in figure 6.11 is indicated by a * in the caption.

The remaining six experiments for which the blending method delivers values larger than the experimental results offer no obvious outliers in velocity measurement. Thus, another reason for the deviation must be found.

The cause for this remaining discrepancy is revealed by a look at the measured temperature gradients. Two of these temperature gradient plots are shown in figure 6.12. A collection of temperature gradient plots from all mixed convection experiments can be found in appendix D.1.2 on page 223ff. Experiments with a deviation Δh_{c} larger than the experimental uncertainty from figure 6.11 are marked with a * in the caption of the temperature gradient plots.

It is obvious that in the experiments of interest, air temperature measured in the rear part close to the ceiling and the inlet opening shows a different behaviour than in the other experiments—that is air temperature measured in the rear part close to the ceiling and the inlet opening is colder than the one measured close to the floor. Thus, in figure 6.13 the difference between the air temperature measured in the rear part of the cabin close to the ceiling and the inlet opening at a height of 2.17 m and the air temperature measured close to the floor at a height of 0.06 m—for exact sensors positions q.v. figure 3.7—is plotted versus the temperature difference between hot plate and mean air for all mixed convection experiments. The outliers in figure 6.11 are also marked separately in figure 6.13. The latter figure shows

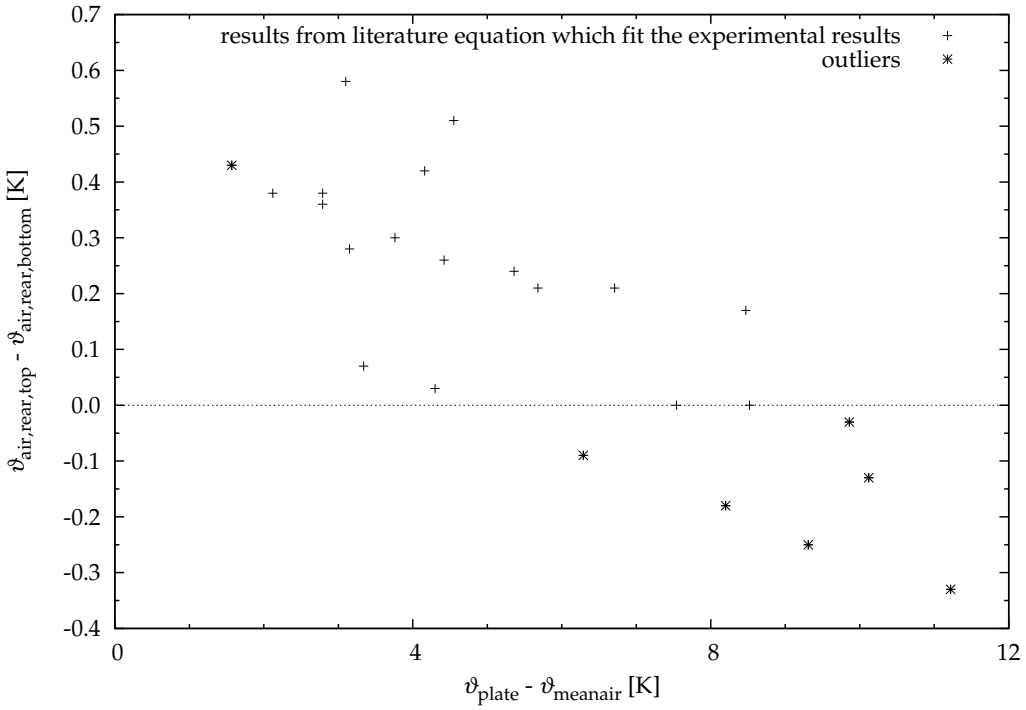

Figure 6.13: Air temperature difference between rear top and rear bottom for different temperature differences between hot plate and mean air.

that—except for the experiment with the lowest temperature difference between hot plate and mean air—only experiments with a Δh_c larger than the experimental uncertainty offer a $\vartheta_{air,rear,top} - \vartheta_{air,rear,bottom} < 0$. Experiments in which a good agreement between experimental results and the blending method is reached offer a $\vartheta_{air,rear,top} - \vartheta_{air,rear,bottom} \geq 0$.

Obviously, the blending method only delivers results which match the results from the experimental evaluation as long as a certain flow pattern governs the heat transfer in the cabin. This flow pattern does no longer exist as soon as the air temperature in the rear part of the cabin close to the ceiling gets colder than the air close to the floor. A schematic representation of three different flow patterns which might occur in the experimental chamber are shown in figure 6.14. With flow pattern A, the incoming air fully passes along the hot plate at the ceiling. This was for example achieved with the modified inlet opening in most of the

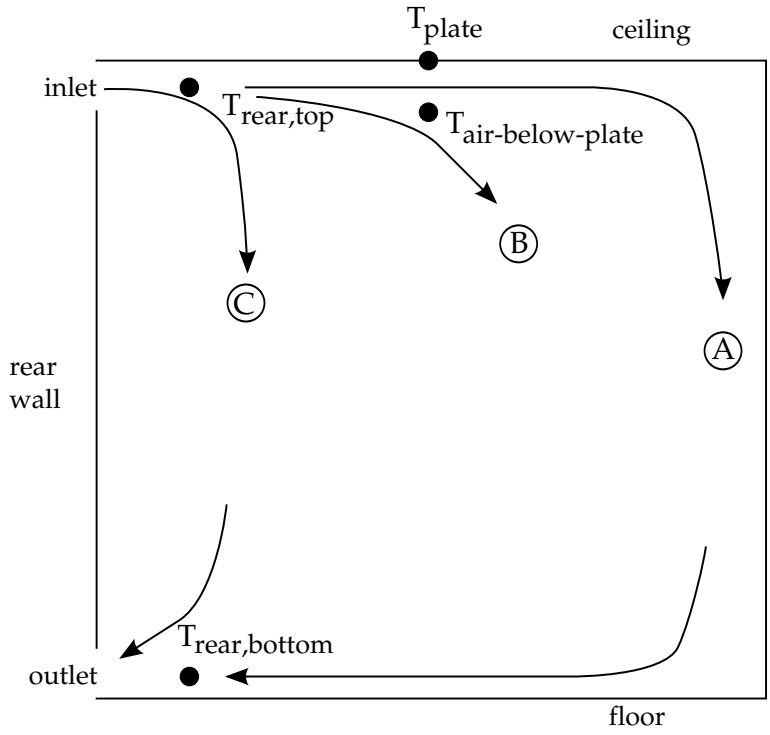

Figure 6.14: Schematic representation of three different possible air flow patterns (A, B and C) in the chamber.

forced convection experiments. Using the regular high-level inlet opening of this test series, the jet does not remain fully attached to the ceiling but drops to the floor. This is indicated by flow pattern B and has been confirmed by the velocity measurements described above. For $\vartheta_{\text{air,rear,top}} - \vartheta_{\text{air,rear,bottom}} < 0$, the incoming air seems to pour to the floor immediately and air movement below the hot plate is no longer directly influenced by the jet (flow pattern C in figure 6.14). As a consequence, the blending method overestimates the resulting convective heat transfer coefficient in such a case.

Thus, by now all discrepancies between the experimental results and the values for h_c from the blending method could be explained except for the experiment with the smallest heat output and thus the smallest temperature difference between hot

plate and mean air. As there is neither an anomaly in the velocity measurement nor a distinct difference in the temperature profile recorded during this experiment, it must be concluded that this experimental result for h_c is an outlier whose cause could not be detected. The only solution to find out whether convective heat transfer coefficients at this temperature difference are normally larger would be additional experiments with a very low heat output. These additional measurements could be part of a future project.

Figure 6.15 shows a plot of CHTCs over the recorded average velocities below the hot plate U. It can be seen that all experiments except for the one with the largest velocity are close to the resulting correlation which has a R^2 of 0.91 if the outlier is excluded from the fitting of the correlation. This outlier with the largest velocity is the experiment with the minimum heat output which has already been identified above. The derived correlation is

$$h_c = 9.291 U^{0.739}. \tag{6.12}$$

The same behaviour and the same outlier can be observed in a dimensionless plot of the form Nu versus Re which is given in figure 6.16.

The dimensionless correlation for this plot is

$$Nu = 0.093 Re^{0.736} \tag{6.13}$$

with an R^2 value of 0.91.

Finally, total heat transfer by both convection and radiation has also been investigated for this experimental test series. The resulting convective heat transfer coefficients according to characteristic base curve h^* are displayed in figure 6.17 together with the correlation given by Glück (2007). Experimental results differ from the values suggested by Glück over the whole range of observed temperature differences. Values for h^* start between $8\,\mathrm{W\,m^{-2}\,K}$ and $9\,\mathrm{W\,m^{-2}\,K}$ and slowly decrease to $7\,\mathrm{W\,m^{-2}\,K}$ for larger temperature differences $\vartheta_{\mathrm{plate}} - \vartheta_{\mathrm{operative}}$.

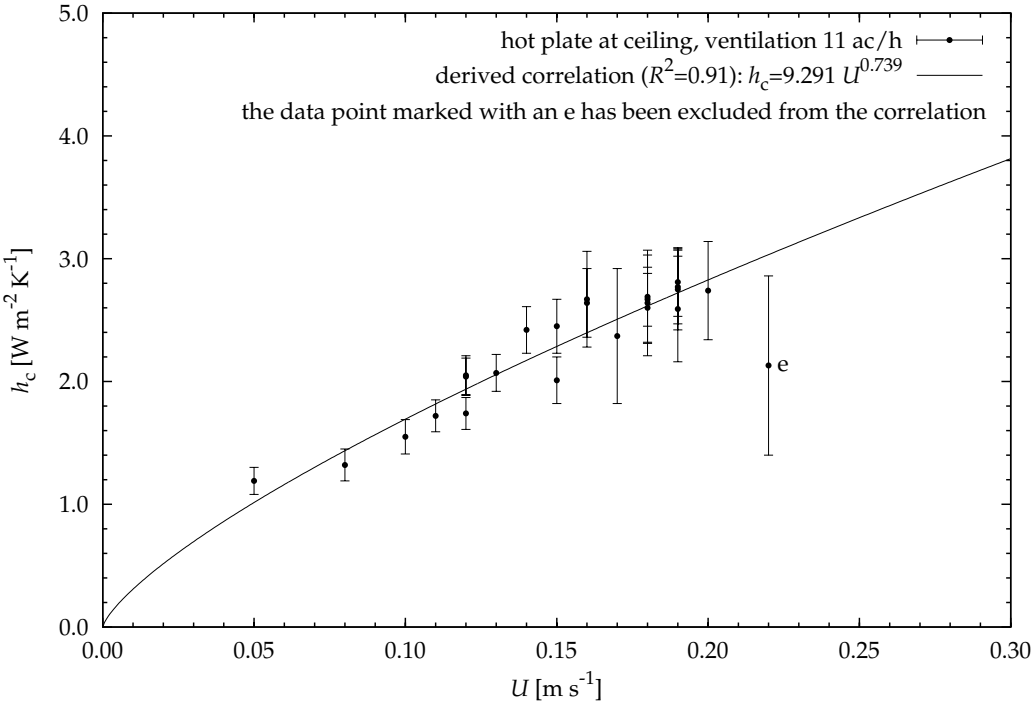

Figure 6.15: Convective heat transfer coefficient h_c versus average velocity below the hot plate U for experiments with the hot plate at an unobstructed ceiling, ventilation 11 ac/h.

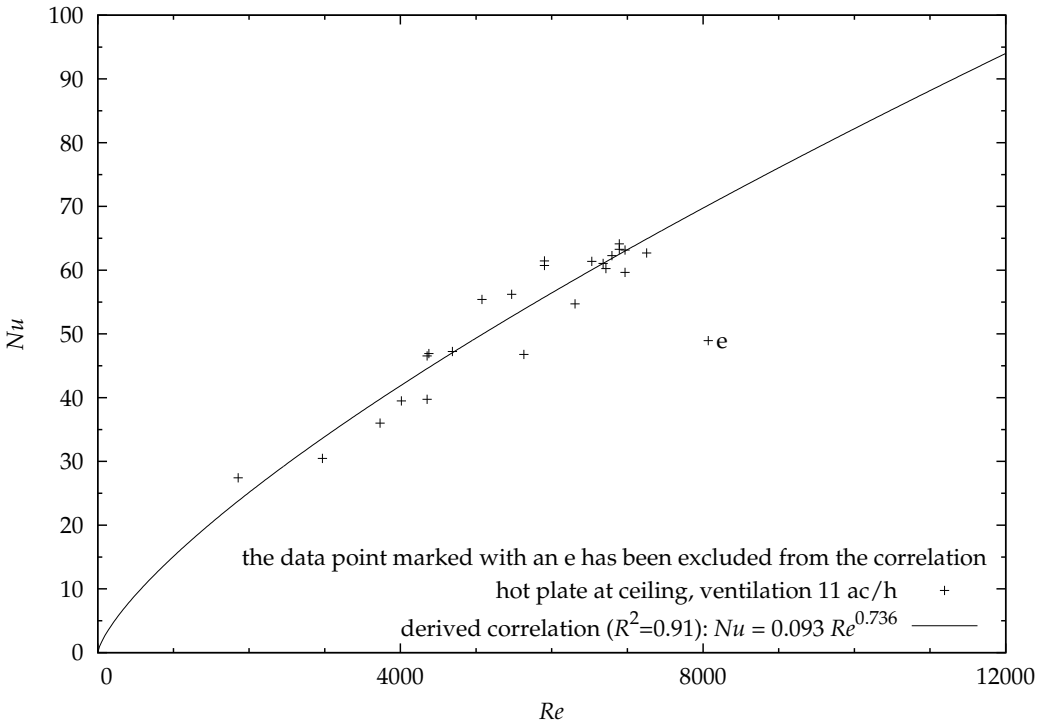

Figure 6.16: *Nu* versus *Re* for experiments with the hot plate at an unobstructed ceiling, ventilation 11 ac/h.

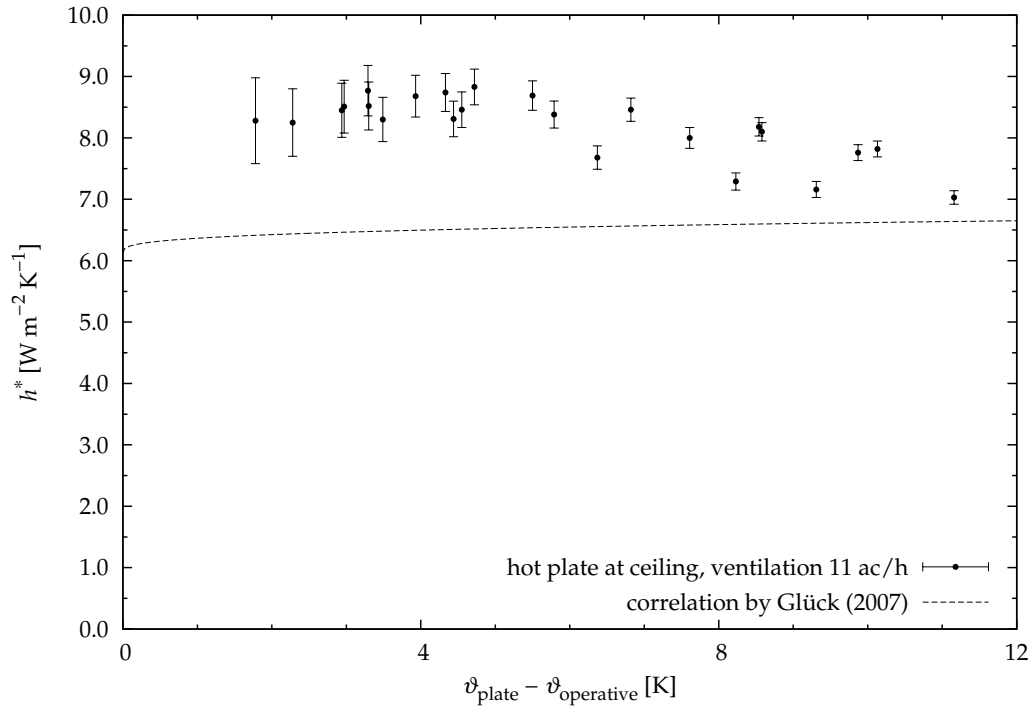

Figure 6.17: Heat transfer coefficient according to characteristic base curve h^* for experiments of the third test series as well as the correlation given by Glück (2007).

Additional Mixed Convection Experiments

As there was only one experiment which was close to the anticipated limiting case given by the natural convection correlation in the original set of experiments for investigation of mixed convection, an additional set of experiments has been carried out. This test series consists of eight experiments. Lowest value of heat output of the hot plate is approximately $26\,\mathrm{W\,m^{-2}}$. Hence, the lower end of observed heat output is comparable to the previous experiments. However, the upper end of heat output of the hot plate could be moved drastically with a maximum heat output of more than $150\,\mathrm{W\,m^{-2}}$. Thus, temperature difference between hot plate and mean air could be nearly doubled and more than 20 K could be observed in one experiment. The reduced air change rate of only 10 ac/h leads to a slightly smaller forced convection component. Therefore, resulting convective heat transfer coefficients for mixed convection from experiments with low values of $\Delta\vartheta$ are slightly smaller than the ones from the original set of experiments.

Resulting CHTCs are presented in figure 6.18. The correlation for natural convection from the very first test series which has been given in equation (6.1) represents the limiting case and is also plotted in the figure. It can be seen that now two additional experiments are very close to the natural convection correlation. Convective heat transfer coefficients follow the limiting case of natural convection and can be described by the natural convection correlation if the heat output and the corresponding temperature difference becomes large. Thus, the aim of this additional experimental test series—that is studying the limiting case—is regarded as achieved. Remaining experimental results show a similar behaviour as the previous results although values are slightly smaller due to the changed ventilative flow rate.

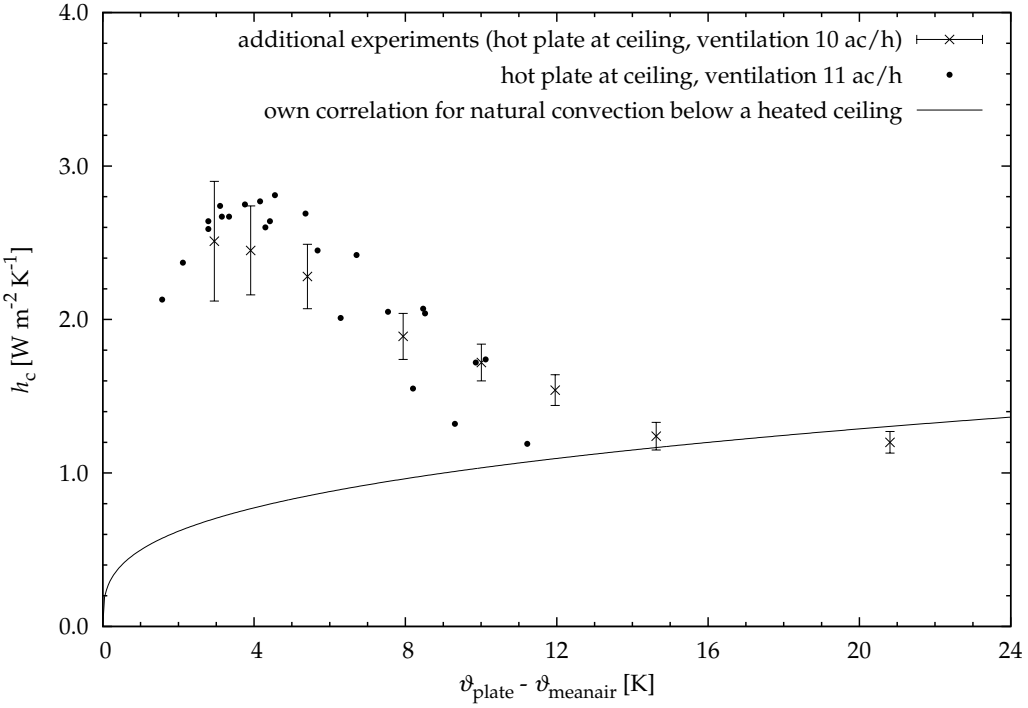

Figure 6.18: Convective heat transfer coefficients h_c from the additional experiments of test series 3b and original mixed convection results as well as the natural convection correlation derived from the first test series.

6.3 Ceiling with Acoustic Baffles

After the completion of the experimental test series with an unobstructed ceiling, acoustic baffles have been installed in the experimental chamber as shown in chapter 3. All relevant details such as baffle spacing and geometry can be found there. Results from a set of 16 experiments in an unventilated chamber are described in the following subsection to disclose the effect of acoustic baffles on natural convection. Afterwards, results for a cabin ventilated with 11 ac/h are presented. The outcomes of this last test series highlight the influence of the baffles on mixed convection. In all experiments with acoustic baffles, characteristic length L_c is again set to 0.6 m. Furthermore, mean air temperature is selected as reference temperature and average velocity below the hot plate is used in the evaluation.

6.3.1 Results without Ventilation

Resulting convective heat transfer coefficients for the baffle experiments are shown in figure 6.19 together with the correlation for natural convection at an unobstructed ceiling which has been obtained in the very first experimental test series and which is given in equation (6.1). Temperature differences between the surface of the hot plate and mean air range from 3 K to 16 K. These values are comparable to the ones obtained for the unobstructed ceiling. However, resulting CHTCs differ significantly. Measured values for h_c do not exceed 0.4 $W\,m^{-2}\,K^{-1}$ for experiments with installed baffles while in the experiments without baffles, h_c reached up to 1.2 $W\,m^{-2}\,K^{-1}$. Thus, the obtained convective heat transfer coefficient with baffles is only 40 % of the convective heat transfer coefficient of an unobstructed ceiling for the highest temperature difference displayed in figure 6.19. For smaller temperature difference, the ratio of convective heat transfer coefficient with baffles to convective heat transfer coefficient at an unobstructed ceiling also becomes smaller. For $4\,K < \Delta\vartheta < 8\,K$, this ratio ranges from 15 % to 25 %. The three experiments at the smallest observed temperature differences—that is at 4 K—lead to significantly smaller values for h_c. It will be shown below that the lower end of natural convection where convection is described by the conductivity of the fluid ($Nu = 1$), is reached under these conditions. Therefore, these three experiments are not included in the derived correlation. The resulting correlation (R^2=0.88) which is valid for $\vartheta_{plate} - \vartheta_{meanair}$ between 5 K and 16 K for the experiments with acoustic baffles is

$$h_c = 0.07 \left(\vartheta_{plate} - \vartheta_{meanair}\right)^{0.655}. \tag{6.14}$$

A dimensionless representation of results is again given in the form of a *Nu* versus *Ra* plot. The resulting graph is shown in figure 6.20. *Ra* ranges from slightly above 6.0×10^7 to approximately 2.8×10^8 and is thus comparable to the range observed in the first test series with an unobstructed ceiling. However, values for *Nu* are considerably smaller. At the low end of *Ra* numbers, *Nu* is around 1. Hence, convection is governed by the conductivity of the fluid. *Nu* does not exceed a value of 10 in any of the 16 experiments and is therefore smaller than the lowest value observed in the test series with an unobstructed ceiling. The resulting correlation

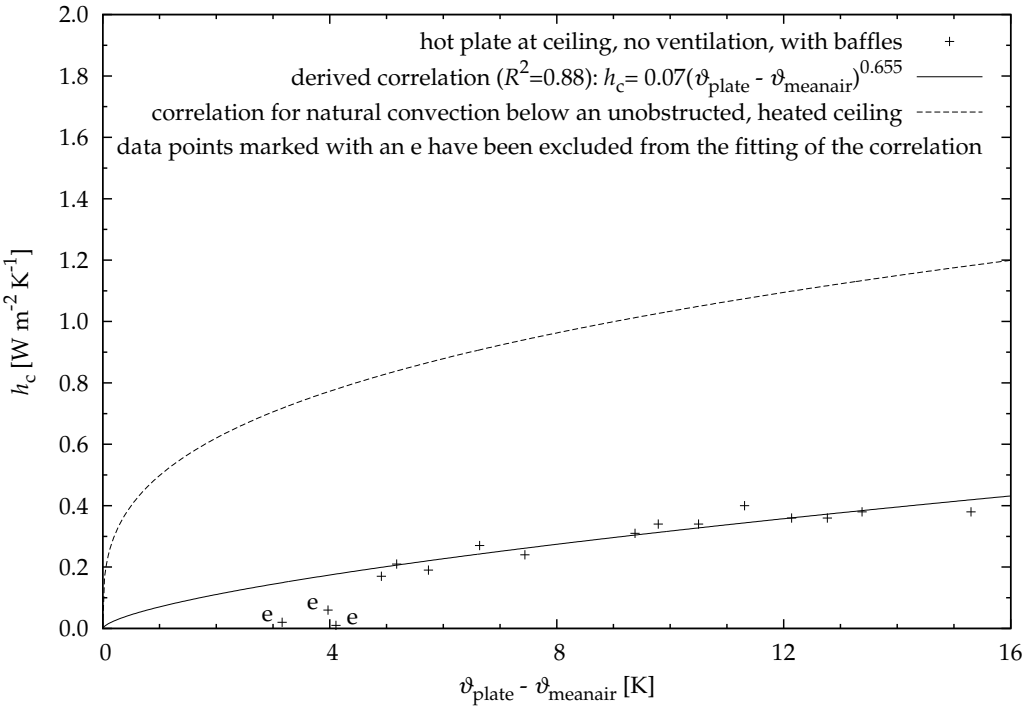

Figure 6.19: Convective heat transfer coefficients from the test series with baffles in an unventilated experimental chamber. For comparison, the natural convection correlation for an unobstructed ceiling is also shown.

for the experiments with acoustic baffles in an unventilated chamber is

$$Nu = 9.97 \times 10^{-6} Ra^{0.708} \tag{6.15}$$

with a value of 0.87 for R^2 if the three experiments with lowest Nusselt numbers are again excluded from the correlation.

It must be concluded from these experiments that convective heat transfer is reduced significantly by the acoustic baffles. This outcome is slightly unexpected as Pfrommer and Zitzmann (2008) report a heat shield effect of the acoustic baffles of only 10 % on nightly discharge of a thermal slab during summer—that is the situation at a hot ceiling. However, the authors also state that heat transfer is dominated by radiation and that convection is negligible. Hence, total heat transfer by

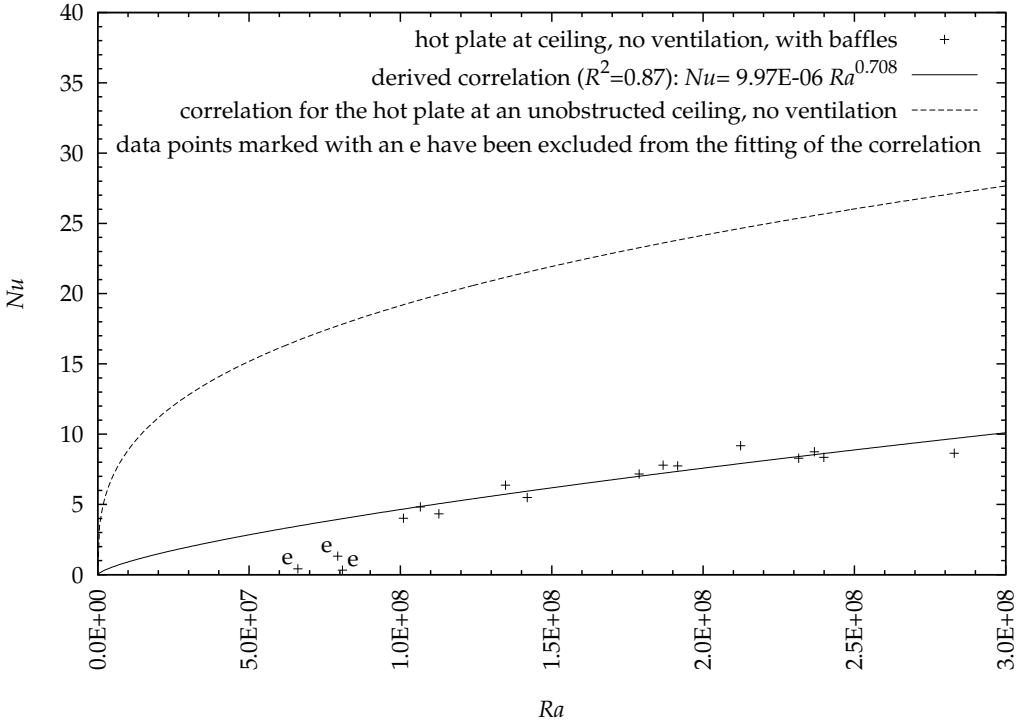

Figure 6.20: Nu versus Ra for experiments with baffles in an unventilated experimental facility. For comparison, the correlation for an unobstructed ceiling without ventilation is also shown.

both convection and radiation must be evaluated.

Figure 6.21 shows the heat transfer coefficient according to characteristic base curve h^* for different values of $\vartheta_{\text{plate}} - \vartheta_{\text{operative}}$. The resulting correlation from the experimental data ($R^2 = 0.98$) is

$$h^* = 3.767 \left(\vartheta_{\text{plate}} - \vartheta_{\text{operative}}\right)^{0.15}. \tag{6.16}$$

Furthermore, the correlation for h^* at an unobstructed ceiling is also plotted in the figure. At $\Delta\vartheta = 2\,\text{K}$, there is a 30 % reduction in heat transfer by convection and radiation due to installation of the acoustic baffles. At $\Delta\vartheta = 16\,\text{K}$, observed reduction is only 20 %.

Hence, reduction in total heat transfer is still two to three times larger than the

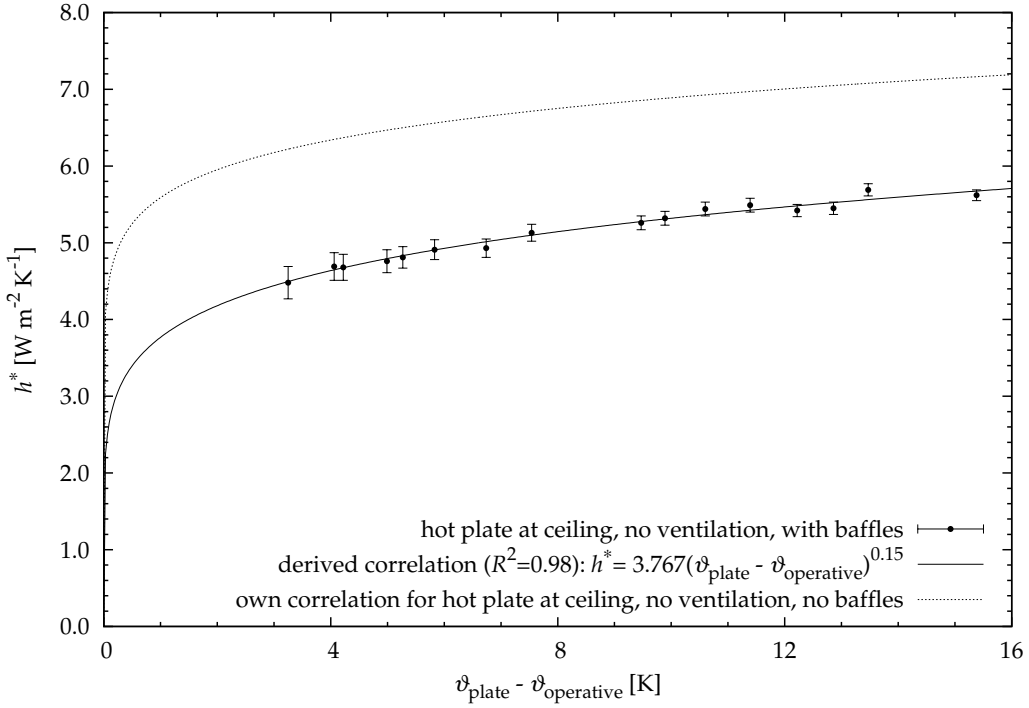

Figure 6.21: Heat transfer coefficient according to characteristic base curve h^* for experiments with baffles in an unventilated experimental chamber as well as the previously derived correlation for an unobstructed ceiling.

10 % shielding effect of the baffles reported by Pfrommer and Zitzmann (2008). The remaining discrepancy is most likely caused by different boundary conditions in the experimental arrangement and boundary conditions used for this work and the simulation model of the previously mentioned authors. According to Uygun (2007), the acoustic baffles may be mounted with a distance of either 10 cm or 20 cm between the baffles (measured from centre of baffle to centre of baffle). For the experiments conducted in this work, the baffles were mounted with a horizontal distance of 10 cm while Pfrommer and Zitzmann (2008) used a distance of 20 cm in their model. The most simple assumption one could make is that there is an inversely proportional relationship between baffle distance and shielding effect. Thus, doubling the distance between the baffles would lead to half the value in shielding effect. If this assumption was valid, reduction in h^* would be

between 10 % and 15 % for experiments with a distance of 20 cm. Hence, there is the need for further experiments to investigate the influence of baffle distance on heat transfer. Such experiments were not conducted within this work but could be part of a future research project.

6.3.2 Results with Ventilation

The final test series consists of 18 experiments which have been carried out with acoustic baffles installed in the chamber. Ventilation of the experimental chamber was set to 11 ac/h. Supply air was delivered via the regular high-level slot inlet which had already been used for mixed convection experiments without baffles. Total heat output covered with this set of 18 experiments ranges from 22 $\mathrm{W\,m^{-2}}$ to 82 $\mathrm{W\,m^{-2}}$. This leads to temperature differences between hot plate and mean air from approximately 4 K to 13 K.

In figure 6.22, resulting convective heat transfer coefficients from this test series are plotted versus $\Delta\vartheta$. For comparison, the natural convection correlation for an unobstructed heated ceiling which has been obtained in the first test series is also shown in the figure. Furthermore, the correlation from the experiments with acoustic baffles in an unventilated chamber is also displayed. The results show that values for h_c from the test series with acoustic baffles and a ventilation rate of 11 ac/h are larger than the ones obtained in an unventilated chamber. However, CHTCs are still smaller than the values valid for natural convection at an unobstructed ceiling albeit the high ventilative flow rate.

Lowest values for h_c start at 0.3 $\mathrm{W\,m^{-2}\,K^{-1}}$ for a $\Delta\vartheta$ of 4 K. Then, convection coefficients increase with increasing temperature difference. The maximum value obtained in the experiments is a h_c of 0.98 $\mathrm{W\,m^{-2}\,K^{-1}}$. The resulting correlation ($R^2 = 0.73$) from the experimental data is

$$h_c = 0.132 \left(\vartheta_{\mathrm{plate}} - \vartheta_{\mathrm{meanair}}\right)^{0.733} . \tag{6.17}$$

Figure 6.23 shows the corresponding dimensionless plot. Ra ranges from 9.0×10^7 to 2.9×10^8 and Nu ranges from 7 to 23. Thus, Ra numbers are again comparable to other test series while Nu numbers for the experiments with baffles in a ventilated

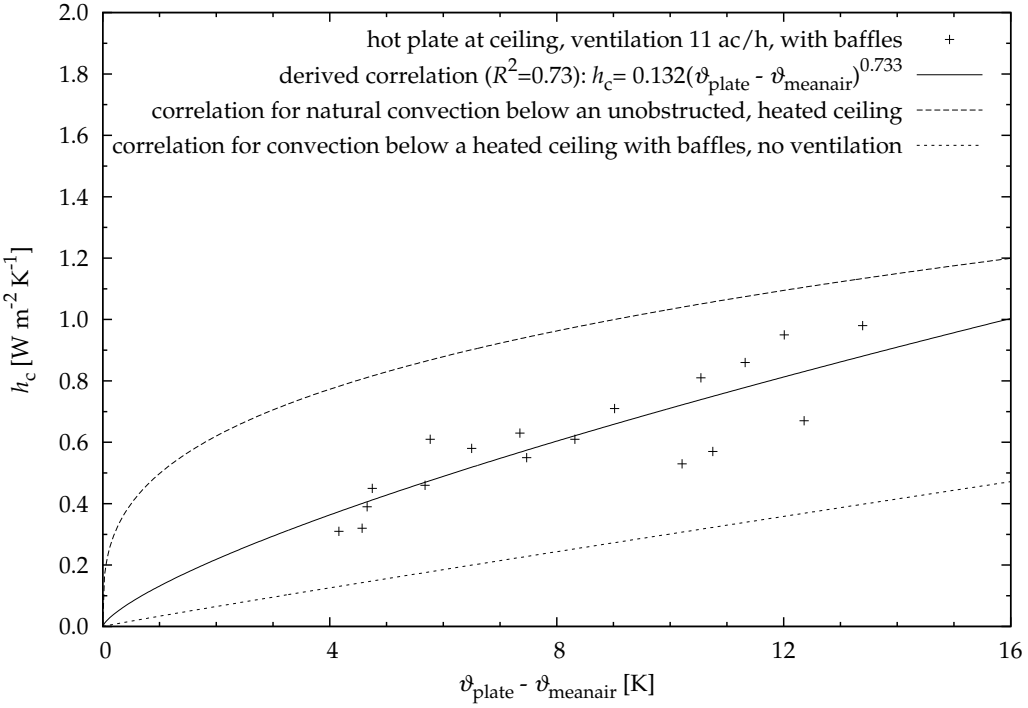

Figure 6.22: Convective heat transfer coefficients for experiments with baffles in a ventilated chamber as well as the previously derived correlations for an unventilated chamber both with and without baffles.

chamber are larger than the ones obtained in an unventilated chamber but still smaller than the ones from the very first test series with an unobstructed ceiling. The resulting correlation for the experiments with acoustic baffles in the ventilated chamber is

$$Nu = 8.75 \times 10^{-6} Ra^{0.754} \tag{6.18}$$

with a value of 0.72 for R^2.

In figure 6.24, heat transfer coefficients according to characteristic base curve h^* are displayed. For comparison, the correlations derived from the previous test series and the test series with an unobstructed ceiling are also plotted in this figure again. The experimental results clearly show that there is nearly no change in h^* although ventilation has been increased from 0 ac/h to 11 ac/h. The derived

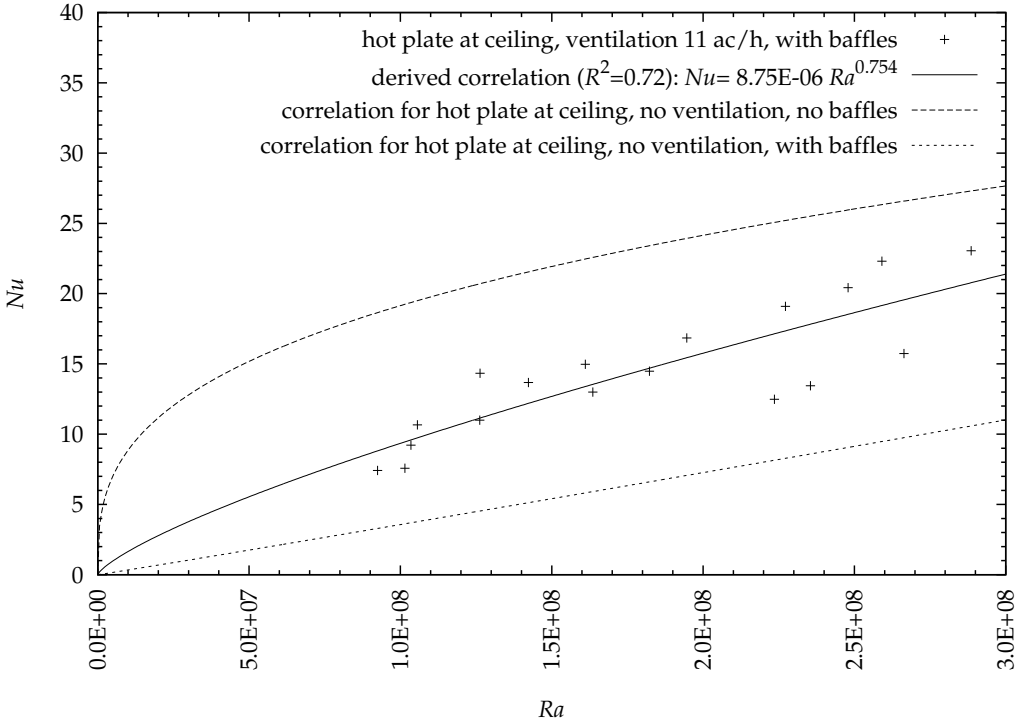

Figure 6.23: *Nu* versus *Ra* for experiments with baffles in a ventilated experimental facility. For comparison, correlations from two previous experimental setups are also shown.

correlation ($R^2 = 0.89$) for h^* from the experimental data of this last test series is

$$h^* = 3.87 \left(\vartheta_{\text{plate}} - \vartheta_{\text{operative}}\right)^{0.15}. \tag{6.19}$$

This result is coincident with the statement by Pfrommer and Zitzmann (2008) that a change in ventilative flow rate in their CFD model had no detectable influence on the shielding effect of the baffles and the amount of transferred heat.

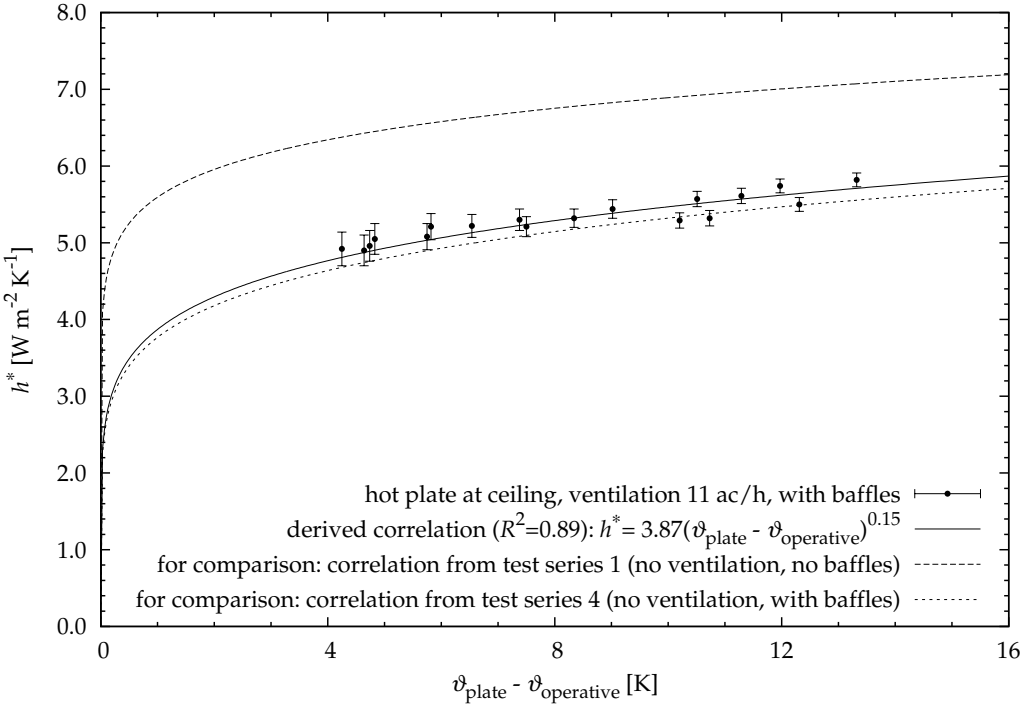

Figure 6.24: Heat transfer coefficient according to characteristic base curve h^* for experiments with baffles in a ventilated chamber as well as the correlations for an unventilated chamber both with and without baffles.

6.4 Summary

Experimental results obtained in the chamber have been presented in this chapter. The hot plate has been installed at the centre of the ceiling in each experiment. The experimental programme has been divided into five different test series. Three test series were used to investigate natural, forced and mixed convection at an unobstructed ceiling. For mixed convection, additional data has been collected from a set of experiments with reduced air change rate and increased heat output of the hot plate in order to study the limiting case given by natural convection. The last two test series were used to experimentally determine the influence of acoustic baffles on heat transfer in the chamber. Combined heat transfer by both radiation and convection has been investigated in all test series except for the

forced convection experiments.

The test series with an unventilated chamber for investigation of natural convection at an unobstructed ceiling showed a very good agreement between the experimental results and existing correlations by Glück (2007) and Awbi and Hatton (1999) for a heated ceiling. The obtained correlation is given in equation (6.1). For small temperature differences, the new correlation shows a very good agreement with the one by Glück (2007) while results from Awbi and Hatton (1999) differ from both correlations. However, the latter correlation was obtained from experiments with larger temperature differences. Thus, the applicability of this equation to such small temperature differences as the ones investigated in this work is questionable. For large temperature differences, the new correlation obtained in this work delivers values between the ones by Awbi and Hatton (1999) and the ones by Glück (2007) which offers the largest values at large temperature differences. Glück's correlation is derived from experiments with mainly isolated plates. Hence, it is regarded as possible that restrictions on heat transfer which are expected to occur in a three-dimensional enclosure are not taken into consideration when using Glück's correlation. Therefore, the correlation obtained from this experimental programme could be regarded as the best choice for describing natural convection over the whole range of temperature differences which are of interest for low energy cooling concepts. Furthermore, the quality of the built experimental chamber and the chosen experimental method could be demonstrated. With increasing temperature differences, resulting uncertainty in h_c from a single experiment decreases to $\pm 0.1\,\mathrm{W\,m^{-2}\,K^{-1}}$. Hence, uncertainty is comparable to the one Awbi (1998) achieved in his ceiling experiments.

In addition to convective heat transfer, combined heat transfer by both radiation and convection has been investigated. The heat transfer coefficient according to characteristic base curve h^* is given in equation (6.10). An existing correlation given by Glück (2007) already delivers good results. However, the new correlation is better insofar as it (implicitly) contains a more accurate treatment of radiant heat transfer while Glück (2007) uses a constant value for radiation.

The second test series in which the chamber was ventilated with 10 ac/h via a modified high-level air inlet, was used to investigate forced convection. Only a limited number of experiments has been carried out since forced convection is

not in the focus of this work. Again, a very good agreement with a correlation from literature could be achieved. Deviations only occurred at larger temperature differences. These deviations lead to the hypothesis of a change in air flow pattern beneath the hot plate for larger values of total heat output. For verification of this hypothesis, mixed convection was investigated in an extensive set of experiments.

24 experiments were conducted to investigate mixed convection at the ceiling of the experimental chamber. Therefore, the chamber was ventilated with 11 ac/h via the regular high-level inlet opening. Results showed that convective heat transfer coefficients decrease with increasing temperature differences between the surface of the hot plate and the mean air temperature. Hotwire measurements confirmed that there is reduced air movement below the hot plate for larger values of heat output of the hot plate. The point where the incoming jet is deflected from the ceiling and air movement is reduced wanders upstreams with increasing heat output. Furthermore, it could be shown that an existing approximative correlation does not give an accurate representation of the situation at a heated ceiling. However, most experiments still showed a very good agreement with the blending method, which is also known from literature, as long as temperature of the incoming air in the rear part of the cabin close to the ceiling did not become too cold. Otherwise, even the blending method will lead to erroneous values for CHTCs. Combined heat transfer by both radiation and convection was again expressed by h^*. Values for h^* range between $7\,\mathrm{W\,m^{-2}\,K^{-1}}$ and $9\,\mathrm{W\,m^{-2}\,K^{-1}}$.

In an additional set of mixed convection experiments, it could be shown that convective heat transfer coefficients drop to the limiting case which is given by the natural convection correlation for (very) large values of heat output. For this test, eight experiments were conducted with a slightly reduced air change rate and values for total heat output of the hot plate of up to more than $150\,\mathrm{W\,m^{-2}}$.

Finally, the influence of acoustic baffles has been investigated. Since there is practically no published experimentally derived data available, obtained values have been compared to results from Pfrommer and Zitzmann (2008) who used CFD to investigate the reduction in heat transfer due to the installation of acoustic baffles.

16 experiments were carried out in an unventilated chamber to disclose the effect of acoustic baffles on natural convection. It could be shown that convective heat

transfer is significantly reduced. At the low end of observed temperature differences, Nusselt numbers of approximately 1 are achieved—that is convection becomes conduction-like. The obtained convective heat transfer with baffles is only 40 % of the CHTC for an unobstructed ceiling for large temperature differences. As Pfrommer and Zitzmann (2008) only reported a shielding effect of approximately 10 %, combined heat transfer by both radiation and convection was investigated. The experimentally identified reduction in combined heat transfer is between 20 % and 30 % when compared to the no-baffle case. Hence, it is still two to three times larger than the value obtained by Pfrommer and Zitzmann (2008) from their CFD model. The remaining discrepancy is most likely due to the different arrangement of the baffles. In the CFD model, baffles were modelled with a distance of 20 cm while the baffles were installed with a distance of only 10 cm in the experimental chamber. According to the manufacturer, both distances are common for the installation of such baffles. For a verification of the assumption that the remaining discrepancy is due to the different distances, additional experiments are necessary.

The last test series consists of 18 experiments. For this set of experiments, the experimental chamber was ventilated with 11 ac/h. It could be shown that convective heat transfer coefficients for the series with baffles in a ventilated chamber are still smaller than convective heat transfer coefficients for natural convection at an unobstructed ceiling. Furthermore, heat transfer coefficients according to characteristic base curve h^* from these experiments are only marginally larger than the ones obtained in an unventilated chamber. These results confirm the statement by Pfrommer and Zitzmann (2008) who found out that a change in ventilative flow rate had no observable influence on the shielding effect of the acoustic baffles in the CFD model.

A summary of experimental results which contains the derived correlations for h_c and h^* as well as the dimensionless representation in the form of a Nusselt correlation is given in table 6.1 together with the range of observed temperature differences and dimensionless numbers. The table also contains information about the boundary conditions of the conducted test series.

Table 6.1: Experimental results and derived correlations for the various test series.

experimental test series	1	2	3	4	5
1. aim of experiment	natural convection	forced convection	mixed convection	influence of baffles, cabin unventilated	influence of baffles, cabin ventilated
2. number of installed baffles	0	0	0	19[A)]	19[A)]
3. air change rate in h^{-1}	0	10	11	0	11
4. velocity[B)] in $m\,s^{-1}$	≤ 0.02	-	0.05 to 0.22	≤ 0.02	0.04
5. number of experiments per test series (total)	17	7	24	16	18
6. air inlet opening	covered	modified	regular	covered	regular
7. total heat output in $W\,m^{-2}$	15 to 101	21 to 107	16 to 82	16 to 92	22 to 82
8. $\vartheta_{plate} - \vartheta_{meanair}$ in K	2 to 13	2 to 12	2 to 10	3 to 15	4 to 13
9. range of *Ra* numbers	4.7×10^7 to 2.6×10^8	-	-	6.6×10^7 to 2.8×10^8	9.2×10^7 to 2.9×10^8
10. range of *Re* numbers	-	1.06×10^4 to 1.13×10^4	1.9×10^3 to 8.1×10^3	-	-
11. range of *Nu* numbers	11 to 24	62 to 89	27 to 64	1 to 9	7 to 23
12. $Nu =$ (derived correlation)	$0.04Ra^{0.335}$ $R^2 = 0.81$	-	$0.093Re^{0.736}$ $R^2 = 0.91$	$9.97 \times 10^{-6}Ra^{0.708}$ $R^2 = 0.87$	$8.75 \times 10^{-6}Ra^{0.754}$ $R^2 = 0.72$
13. $h_c =$ (derived correlation)[C)]	$0.498\Delta\vartheta^{0.317}$ $R^2 = 0.80$	-	$9.291U^{0.739}$ $R^2 = 0.91$	$0.07\Delta\vartheta^{0.665}$ $R^2 = 0.88$	$0.132\Delta\vartheta^{0.733}$ $R^2 = 0.73$
14. $h^* =$ (derived correlation)[D)]	$5.593\Delta\vartheta^{0.091}$ $R^2 = 0.86$	-	-	$3.767\Delta\vartheta^{0.15}$ $R^2 = 0.98$	$3.87\Delta\vartheta^{0.15}$ $R^2 = 0.89$

[A)]: horizontal distance between baffles: 10 cm; vertical distance from baffle to ceiling: 12 cm; air movement primarily below baffles. [B)]: measured average velocities below hot plate (if available).
[C)]: with $\Delta\vartheta = (\vartheta_{plate} - \vartheta_{meanair})$ [D)]: with $\Delta\vartheta = (\vartheta_{plate} - \vartheta_{operative})$

7 Conclusions and Recommendations for Further Work

7.1 Summary

The overall aim of the work presented in this thesis was to investigate heat transfer at the ceiling of an experimental chamber in conditions representative of passive cooling by ventilation or TABS. One of the primary aims was to experimentally determine the influence of acoustic baffles on heat transfer at the ceiling as publications on this topic (experimental investigation with acoustic baffles) are not known to exist. Pfrommer and Zitzmann (2008) seem to be first who quantified the shielding effect of such baffles using a CFD model of an office room. The authors concluded that their simulation results should be verified by an experimental investigation. Additionally, several experimental test series with an unobstructed ceiling have been made prior to the baffle experiments to investigate natural, forced and mixed convection.

In this work, a new experimental facility was built at Biberach University of Applied Sciences in order to be able to carry out the programme of experiments. The experimental design which has been presented in detail in chapter 3, makes use of an electrically heated plate at the ceiling of the chamber. Information about the instrumentation can also be found there. Experiments were run until steady-state conditions were achieved. Convective heat transfer could be quantified by subtracting conductive losses and radiation from the total heat output of the hot plate measured with a high-precision power meter. Radiant heat transfer was calculated using a detailed view factor model as radiation contributes significantly to total heat transfer in the chamber. Radiation modelling has been treated in detail in chapter 5.

Experimental results are primarily given in the form of convective heat transfer coefficients h_c. Furthermore, total heat transfer coefficients and dimensionless representations have been derived. The partial uncertainties contributing to the overall uncertainty in the values for h_c have been identified in a detailed error analysis which is presented in chapter 4. Initial calculations showed that the uncertainty in h_c is strongly influenced by the uncertainty in the emissivity of the hot plate. Consequently, emissivity of the hot plate ε and its uncertainty $\delta\varepsilon$ were measured accurately in a separate experiment which has been devised specifically to quantify these values.

In the first test series, a maximum value of $\pm 0.41\,\mathrm{W\,m^{-2}\,K^{-1}}$ was achieved for the uncertainty in the convective heat transfer coefficient h_c at low temperature differences slightly above 2 K. For larger temperature differences, uncertainty in h_c reduces to a value of $\pm 0.1\,\mathrm{W\,m^{-2}\,K^{-1}}$ which is comparable to the uncertainty stated by Awbi (1998) for his ceiling experiments.

Five different test series have been carried out which can be characterized as follows:

- Heat source at an unobstructed ceiling with an unventilated chamber. Objective of this test series was to investigate natural convection below the heat source. The results of these tests served as a base case to which other conditions could be compared.
- Heat source at an unobstructed ceiling with a chamber ventilated via a modified air inlet opening at high level. This arrangement was used to investigate forced convection.
- Heat source at an unobstructed ceiling with a ventilated chamber. Air was supplied with the regular high-level inlet in the rear wall. This test series was used to investigate the effect of ventilation on heat transfer below the ceiling and to study mixed convection.
- Heat source at the ceiling with acoustic baffles installed below. Again, the chamber was unventilated. The objective of these experiments was to investigate the influence of acoustic baffles on natural convection below the heat source.

- Heat source at the ceiling with acoustic baffles installed below and with ventilation. This arrangement was used to investigate the effect of acoustic baffles in the ventilated case.

7.2 Conclusions

Table 7.2 on page 187 at the end of this section contains a summary with the observed range of dimensionless numbers and the resulting Nusselt correlations for all conducted test series. A more detailed table which also contains the main boundary conditions as well as the derived correlations for h_c and h^* can be found at the end of chapter 6 on page 179. The most important outcomes of each test series are given below:

1. Obtained convective heat transfer coefficients for natural convection at an unobstructed ceiling show a good agreement with two existing correlations. The first correlation is recommended by Glück (2007) and was obtained from experiments with isolated plates. The second correlation was derived from experiments in a test chamber and is recommended by Awbi and Hatton (1999). At the lower end of observed temperature differences, the largest discrepancies are between the results of this work—which are very close to the values from Glück (2007)—and the values of Awbi and Hatton (1999). However, the latter correlation is based on experiments with temperature differences between 7 K and 35 K while more than one third of the experiments of this work had temperature differences below 5 K. Thus, it is questionable if the correlation of Awbi and Hatton (1999) can be used under these conditions. At the upper end of observed temperature differences, results of this work are in between the values from the correlation of Glück (2007), which delivers the largest values, and the values from the correlation of Awbi and Hatton (1999), which results in the lowest values. As there are restrictions on air flow pattern in indoor environments that can only be observed with experiments in a chamber and not in experiments with an isolated plate, the results of this work could be regarded as the best choice for describing natural convection over the whole range of temperature differences which are of interest for low energy cooling concepts.

Total heat transfer in the chamber by both convection and radiation has been described in the form of h^*. Again, there is a good agreement with a correlation recommended by Glück (2007)—especially for experiments with intermediate values for the observed temperature difference. At large temperature differences, experiments of this work lead to values for h^* that are larger than the values from Glück (2007). The deviation could be explained with a simplified, constant value for radiant heat transfer used by Glück (2007) while radiation is calculated in detail in this work. Consequently, the new correlation could be regarded as the best choice for describing total heat transfer by both convection and radiation in the experimental chamber over the whole range of observed temperature differences.

2. The small number of forced convection experiments showed that there is a good agreement with an existing correlation recommended by Glück (2007). Only two experiments led to significantly smaller values than this correlation. It was hypothesized that this is due to a change in air flow pattern below the hot plate. This hypothesis was verified in a subsequent test series for investigation of mixed convection.

3. It can be concluded from the third test series that simplified approximations which make solely use of equations known from natural convection, are a poor choice for describing mixed convection in the chamber ventilated with an air change rate of $11\,\mathrm{h}^{-1}$ via a high-level inlet. At low temperature differences, convective heat transfer coefficients tend to be dominated by the forced convection component and, consequently, large values for h_c are achieved. For larger temperature differences between hot plate and mean air, CHTCs tend to decrease due to increased negative buoyancy of the incoming jet. The lower limit is given by the natural convection correlation from the first test series. A suitable solution for describing mixed convection in the experimental chamber is the blending method introduced in chapter 2. This approach shows a good overall agreement with a detailed calculation of h_c using the experimental data.

4. Experimental results with acoustic baffles in an unventilated chamber differ significantly from the results of the first tests series used for investigation of natural convection at an unobstructed ceiling. Measured CHTCs

did not exceed $0.4\,\mathrm{W\,m^{-2}\,K^{-1}}$ for the temperature range investigated while values above $1.0\,\mathrm{W\,m^{-2}\,K^{-1}}$ were achieved for natural convection at an unobstructed ceiling. At the lower end of investigated heat output, Nusselt numbers of approximately 1 were obtained. In this case, magnitude of convection is calculated using the conductivity of the fluid. Consequently, the three experiments concerned were not included in the derived correlation for h_c with baffles in an unventilated chamber. The derived correlation given in equation (6.14) is valid for $5\,\mathrm{K} < \vartheta_{plate} - \vartheta_{meanair} < 16\,\mathrm{K}$.

Reduction in total heat transfer by both convection and radiation was between 20 % and 30 % for $2\,\mathrm{K} < \vartheta_{plate} - \vartheta_{operative} < 16\,\mathrm{K}$ when compared to experiments without baffles. Pfrommer and Zitzmann (2008) reported a heat shield effect of the baffles of approximately 10 % to 14 % when compared to an unobstructed ceiling. However, a distance of 20 cm between the baffles was used in their simulation while experiments of this work were carried out with a distance of 10 cm between the baffles. Thus, a more pronounced reduction in total heat transfer seems reasonable.

5. Experimental results with acoustic baffles in a ventilated chamber showed that there is slightly more convection than in the test series with baffles in an unventilated chamber. However, values of h_c from this last test series are still smaller than the values for natural convection at a unobstructed ceiling. Consequently, total heat transfer by both convection and radiation is also only slightly (approximately 3 %) increased when compared to the test series with baffles in an unventilated chamber. Changing the ventilative flow rate from $0\,\mathrm{h^{-1}}$ in the fourth test series to a value of $11\,\mathrm{h^{-1}}$ in this last test series only lead to the 3 % increase in heat transfer by both convection and radiation. Within the investigated range of air change rates, these results confirm the statement by Pfrommer and Zitzmann (2008) who found out that a change in ventilative flow rate in their CFD model had no significant influence on the shielding effect of the baffles and the amount of heat transferred from the ceiling.

6. The main boundary conditions and parameters as well as the results of the two experimental test series with acoustic baffles are given in table 7.1 on page 186. In addition to the outcomes of this work, the results of the CFD

simulations of Pfrommer and Zitzmann (2008) (printed in grey) are also shown. Thus, table 7.1 could be used by practitioners in the field of building services engineering for a design of indoor environments with acoustic baffles which does not neglect the effects of the acoustic baffles on indoor heat transfer. For more advanced installation guidelines, further investigations are necessary. The recommendations for further work are given in the next section.

Table 7.1: Summary of boundary conditions used (top) and resulting influence of acoustic baffles on ceiling heat transfer for both unventilated conditions (centre) and ventilated conditions (bottom) based on experimental results of this work as well as on existing CFD results of Pfrommer and Zitzmann.

Source	results of this work	results of Pfrommer and Zitzmann (2008)
Boundary conditions valid for both unventilated and ventilated conditions:		
1. type of investigation	experimental	CFD
2. distance between baffles	10 cm	20 cm
3. distance from baffle to ceiling	12 cm	7.5 cm
4. baffle length	150 cm	120 cm
5. baffle height	15 cm	15 cm
6. baffle width	2.5 cm	2.5 cm
7. room length	2.34 m	5 m
8. room width	1.65 m	3.5 m
9. room height	2.23 m	3 m
Results of test series without ventilation:		
10. Reduction in total heat transfer	20 % to 30 %[A)]	not available
11. Correlation for h_c [B)]	$0.07\Delta\vartheta^{0.665}$	not available
12. Correlation for h^* [C)]	$3.767\Delta\vartheta^{0.15}$	not available
Additional boundary conditions and results of test series with ventilation:		
13. air change rate	11 h^{-1}	2 h^{-1} and 6 h^{-1}
14. orientation of baffles[D)]	$\perp$	$\perp$ and $\parallel$
15. ventilation regime	single-sided	single-sided
16. air inlet opening	high-level	low-level
17. Reduction in total heat transfer	19 % to 28 %[A)]	10 % to 14 %[E)]
18. Correlation for h_c [B)]	$0.132\Delta\vartheta^{0.733}$	not available
19. Correlation for h^* [C)]	$3.87\Delta\vartheta^{0.15}$	not available

[A)]: when compared to the first test series with an unobstructed ceiling.
[B)]: with $\Delta\vartheta = \left(\vartheta_{\text{plate}} - \vartheta_{\text{meanair}}\right)$.
[C)]: with $\Delta\vartheta = \left(\vartheta_{\text{plate}} - \vartheta_{\text{operative}}\right)$.
[D)]: with regard to direction of flow. $\perp$ is perpendicular and $\parallel$ is parallel.
[E)]: when compared to an unobstructed ceiling without baffles.

Table 7.2: Summary of observed range of dimensionless numbers and resulting Nusselt correlations.

experimental test series	1	2	3	4	5
1. aim of experiment	natural convection	forced convection	mixed convection	influence of baffles[A)], cabin unventilated	cabin ventilated
2. range of Ra numbers	4.7×10^7 to 2.6×10^8	-	-	6.6×10^7 to 2.8×10^8	9.2×10^7 to 2.9×10^8
3. range of Re numbers	-	1.06×10^4 to 1.13×10^4	1.9×10^3 to 8.1×10^3	-	-
4. range of Nu numbers	11 to 24	62 to 89	27 to 64	1 to 9	7 to 23
5. $Nu =$ (derived correlation)	$0.04Ra^{0.335}$ $R^2 = 0.81$	-	$0.093Re^{0.736}$ $R^2 = 0.91$	$9.97 \times 10^{-6}Ra^{0.708}$ $R^2 = 0.87$	$8.75 \times 10^{-6}Ra^{0.754}$ $R^2 = 0.72$

[A)]: horizontal distance between baffles: 10 cm; vertical distance from baffle to ceiling: 12 cm; air movement primarily below baffles.

7.3 Recommendations for Further Work

Several new and interesting questions arise from the outcomes of this work. Further experiments should be carried out or alternative ways of analysis should be taken into consideration for answering these questions. Recommendations for further work to obtain answers to these questions are given below.

1. The classical, well-known form of $h_c = C\ (\Delta\vartheta)^n$ has been used to provide a correlation for natural convection at an unobstructed ceiling derived from the experiments of the first test series. The advantage of the chosen form is that results of this work can easily be compared to existing correlations and can also be easily implemented into existing building simulation codes. Furthermore, an alternative form of the equation was presented which fits the experimental results better. Such an alternative form of the correlation might be a suitable solution if its application is limited to heat transfer in closed indoor environments. However, further tests and additional analysis would be necessary to verify such an approach.

   Another topic which could not be investigated in this work is the influence of geometry of the hot plate on heat transfer. Will a different geometry—for example a fully heated ceiling instead of only one hot plate—lead to a different correlation as previously observed by other researchers? Currently, this question cannot be answered as all experiments were carried out with the one available hot plate at the ceiling. Further experimental tests with a different geometric situation would be necessary to find an answer.

2. The results from the forced convection experiments agree closely with an existing correlation recommended by Glück (2007). However, flow rate was set to a constant value in these experiments and nominal inlet velocity was used in the evaluation. For a confirmation that the existing correlation can indeed be used for a wider range of velocities and Reynolds numbers respectively, additional experiments with variation in ventilative flow rate would be necessary.

3. It was shown that the blending method delivered good results for mixed convection. There were only some experiments where the results did not match

the blending method exactly. These small deviations could be explained with air temperature gradients in the cabin. For further investigation of this effect, additional experiments—for example with heated or cooled supply air—would be necessary. In addition to the blending method, a correlation based solely on local velocity below the hot plate could be derived. This correlation also showed a very good agreement with the experimental results. These results could be used to derive a correlation in dimensionless form based on a combination of *Re* and *Gr* numbers. One possibility would be to derive a correlation where Nusselt number is correlated with Richardson number as the latter is based on Reynolds and Grashof numbers.

Furthermore, a CFD model of the experimental chamber should be created. Such a model could help to define boundary conditions of future experimental test series so that less time must be spent on preliminary experiments. The CFD model could be calibrated with the existing experimental data presented in this work.

4. With the experiments of this work, the heat shield effect of acoustic baffles in an unventilated chamber could be quantified as between 20 % and 30 % while Pfrommer and Zitzmann (2008) obtained values between 10 % and 14 % in their CFD simulation. However, different distances between the baffles were used in the experiments and in the CFD model. Therefore, at least one additional test series with acoustic baffles in an unventilated chamber should be made where the baffles are mounted at a horizontal distance of 20 cm (centre of baffle to centre of baffle) so that the significance of baffle spacing and the CFD results of Pfrommer and Zitzmann (2008) could be verified.

5. Pfrommer and Zitzmann (2008) stated that they had to coarsen their mesh in some regions in order to achieve a reasonable number of cells and an acceptable computational time in the simulations with acoustic baffles. With cheaper and better hardware available by now, it might be interesting to create a model with a larger number of cells and a denser mesh. Thus, additional experiments could be supported with additional high resolution CFD simulations. Air movement in the space between the baffles themselves and between baffles and ceiling could be investigated much better with such a model than with an experiment as the space available for sensors above

and between the baffles is very limited.

Both the experiments of this work and the CFD results of Pfrommer and Zitzmann (2008) showed that ventilation has little influence on the amount of heat transferred from the ceiling if acoustic baffles are installed. Thus, another parameter which might be interesting to vary is the vertical distance between the top edge of the baffle and the surface of the ceiling to find out if there is a critical distance which leads to local convection cells below the ceiling that are responsible for the fact that convection with baffles in a ventilated chamber is smaller than natural convection at an unobstructed ceiling but still larger than pure conduction.

Bibliography

M. Aghajani, H. Müller-Steinhagen, and M. Jamialahmadi. New design equations for liquid/solid fluidized bed heat exchangers. *International Journal of Heat and Mass Transfer*, 48:317–329, 2005.

M. Al-Arabi and B. Sakr. Natural convection heat transfer from inclined isothermal plates. *International Journal of Heat and Mass Transfer*, 31:559–566, 1988.

F. Alamdari and G. P. Hammond. Improved data correlations for buoyancy-driven convection in rooms. *Building Services Engineering Research and Technology*, 4: 106–112, 1983.

N. Artmann, R. L. Jensen, H. Manz, and P. Heiselberg. Experimental investigation of heat transfer during night-time ventilation. *Energy and Buildings*, 42:366–374, 2010.

ASHRAE. *Handbook Fundamentals*. 1981.

ASR6. Arbeitsstätten-Richtlinie ASR 6. Raumtemperatur. Ausgabe: Mai 2001. URL `http://www.gaa.baden-wuerttemberg.de/servlet/is/16486/5_006.pdf`.

Hazim B. Awbi. Calculation of convective heat transfer coefficients of room surfaces for natural convection. *Energy and Buildings*, 28:219–227, 1998.

Hazim B. Awbi and A. Hatton. Natural convection from heated room surfaces. *Energy and Buildings*, 30:233–244, 1999.

Hazim B. Awbi and A. Hatton. Mixed convection from heated room surfaces. *Energy and Buildings*, 32:153–166, 2000.

Ian Beausoleil-Morrison. *The adaptive coupling of heat and air flow modelling within dynamic whole-building simulation*. PhD thesis, University of Strathclyde, Glasgow, UK, 2000.

Ian Beausoleil-Morrison. An algorithm for calculating convection coefficients for internal building surfaces for the case of mixed flow in rooms. *Energy and Buildings*, 33:351–361, 2001.

Ian Beausoleil-Morrison. The adaptive simulation of convective heat transfer at internal building surfaces. *Building and Environment*, 37:791–806, 2002.

Christoph Beck. Einfluss akustisch wirksamer Elemente auf die Leistung thermisch aktiver Decken (TAB). *Ingenieurspiegel*, 4:84–85, 2008.

Francesco Causone, Stefano P. Corgnati, Marco Filippi, and Bjarne W. Olesen. Experimental evaluation of heat transfer coefficients between radiant ceiling and room. *Energy and Buildings*, 41:622–628, 2009.

S.W. Churchill and R. Usagi. A general expression for the correlation of rates of transfer and other phenomena. *AIChE Journal*, 18:1121–1128, 1972.

CIBSE. *CIBSE Guide C. 3. Heat Transfer.* The Chartered Institution of Building Services Engineers London, 1976.

CIBSE. *CIBSE Guide C*. The Chartered Institution of Building Services Engineers London, 2007.

A. P. Colburn. Heat Transfer by Natural and Forced Convection. Eng. Bull., Purdue University, 26, No. 1, Bull. No. 84, 1942.

Malcolm J. Cook. *An Evaluation of Computational Fluid Dynamics for Modelling Buoyancy-Driven Displacement Ventilation*. PhD thesis, De Montfort University, Leicester, August 1998.

DIN 4108-2:2003-07. Wärmeschutz und Energie-Einsparung in Gebäuden; Teil 2: Mindestanforderungen an den Wärmeschutz. Beuth Verlag, Berlin, Germany.

DIN EN 1264-2:1997-11. Fußboden-Heizung, Systeme und Komponenten – Teil 2: Bestimmung der Wärmeleistung, Deutsche Fassung EN 1264-2:1997. floor heating, systems and components – Part 2: Determination of the thermal output, German version EN 1264-2:1997. Beuth Verlag, Berlin, Germany.

DIN EN 12831:2003-08. Heizungsanlagen in Gebäuden. Verfahren zur Berechnung der Norm-Heizlast. Beuth Verlag, Berlin, Germany.

DIN EN ISO 7730:1995-09. Gemäßigtes Umgebungsklima – Ermittlung des PMV und des PPD und Beschreibung der Bedingungen für thermische Behaglichkeit (ISO 7730:1994); Deutsche Fassung EN ISO 7730:1995. Moderate thermal environments – Determination of the PMV and PPD indices and specification of the conditions for thermal comfort (ISO 7730:1994); German version EN ISO 7730:1995. Beuth Verlag, Berlin, Germany.

DIN EN ISO 7730:2006-05. Ergonomie der thermischen Umgebung – Analytische Bestimmung und Interpretation der thermischen Behaglichkeit durch Berechnung der PMV- und des PPD-Indexes und Kriterien der lokalen thermischen Behaglichkeit (ISO 7730:2005); Deutsche Fassung EN ISO 7730:2005. Ergonomics of the thermal environment – Analytical determination and interpretation of thermal comfort using calculation of the PMV and PPD indices and local thermal comfort criteria (ISO 7730:2005); German version EN ISO 7730:2005. Beuth Verlag, Berlin, Germany.

DIN V 18599:2007-02. Energetische Bewertung von Gebäuden - Berechnung des Nutz-, End- und Primärenergiebedarfs für Heizung, Kühlung, Lüftung, Trinkwasser und Beleuchtung. Beuth Verlag, Berlin, Germany.

Norbert Elsner, Siegfried Fischer, and Jörg Huhn. *Grundlagen der Technischen Thermodynamik, Band 2: Wärmeübertragung*. Akademie Verlag, 8th edition, 1993.

EnEV2002. Verordnung über energiesparenden Wärmeschutz und energiesparende Anlagentechnik bei Gebäuden (Energieeinsparverordnung - EnEV) vom 16. November 2001.

EPBD2003. Directive on the energy performance of buildings (EPBD). Directive 2002/91/EC of the European Parliament and of the Council of 16 December 2002 on the energy performance of buildings. Official Journal of the European Communities.

A. Fage and V. M. Faulkner. On the Relation between Heat Transfer and Surface Friction for Laminar Flow. A.R.C.T. 3060, F.M. 31. See also A.R.C.T. 2997, F.M. 16 (1930); Brit. Adv. Committee Aero. Rep. and Mem. No. 1408, 1931.

M. Fishenden and O. A. Saunders. *An Introduction to Heat Transfer*. Oxford: Clarendon Press, 1950.

D.E. Fisher. *An experimental investigation of mixed convection heat transfer in a rectangular enclosure*. PhD thesis, University of Illinois, Urbana, USA, 1995.

Stéphane Fohanno and Guillaume Polidori. Modelling of natural convective heat transfer at an internal surface. *Energy and Buildings*, 38:548–553, 2006.

A. Frank. Gesundheitsingenieur Jg. 52, S. 541, 1929.

Bernd Glück. *Wärmetechnisches Raummodell. Gekoppelte Berechnungen und wärmephysiologische Untersuchungen*. C.F. Müller Verlag, Heidelberg, 1997.

Bernd Glück. Ein Vorschlag zur verbesserten Darstellung und Messung der operativen Raumtemperatur. *Gesundheitsingenieur*, 127:76–82, 2006.

Bernd Glück. Wärmeübergangskoeffizienten an thermisch aktiven Bauteiloberflächen und der Übergang zu Basiskennlinien für die Wärmestromdichte. *Gesundheitsingenieur*, 128:1–10, 2007.

Kate Goldstein and Atila Novoselac. Convective Heat Transfer in Rooms with Ceiling Slot Diffusers (RP-1416). *HVAC&R Research*, 16:629–655, 2010.

E. Griffiths and A. H. Davis. The Transmission of Heat by Radiation and Convection. DSIR Food Investigation Board. Special Report No 9. *HMSO*, 1922.

Horst Haussecker. *Messung und Simulation von kleinskaligen Austauschvorgängen an der Ozeanoberfläche mittels Thermographie*. PhD thesis, Ruprecht-Karls-Universität Heidelberg, 1996.

R. H. Heilman. Surface Heat Transmission. *ASME Transactions*, 51:6–11, 1929.

J. P. Holman. *Experimental Methods for Engineers*. McGraw-Hill, seventh edition, 2001.

Robert Huhn. *Beitrag zur thermodynamischen Analyse und Bewertung von Wasserwärmespeichern in Energieumwandlungsketten*. PhD thesis, Fakultät für Maschinenwesen, Technische Universität Dresden, 2007.

IEA. Review of Low Energy Cooling Technologies. Subtask 1 Report. Technical report, International Energy Agency, Energy Conservation in Buildings and Community Systems Programme: Annex 28 - Low Energy Cooling, 1995.

IPCC. Summary for Policymakers. In S. Solomon, D. Qin, M. Manning, Z. Chen, M. Marquis, K.B. Averyt, M. Tignor, and H.L. Miller, editors, *Climate Change 2007: The Physical Science Basis. Contribution of Working Group I to the Fourth Assessment Report of the Intergovernmental Panel on Climate Change*. Cambridge University Press, 2007.

M. Jakob and W. M. Dow. Heat Transfer from a Cylindrical Surface to Air in Parallel Flow etc.. Trans. Am. Soc. Mech. Eng., 68, 123, 1946.

JUMO GmbH & Co. KG, Data sheet 90.6023. Platinum-foil temperature sensors to EN 60751. 01.05/00311574. pages 1–3.

JUMO GmbH & Co. KG, Data sheet 90.6121. Platinum Chip Temperature Sensors with Connection Wires to EN 60751. 2009-05-15/00311575. pages 8–10.

W. Jürges. Gesundheitsingenieur, Reihe 1, Beiheft 19, 1924.

Abdul-Jabbar N. Khalifa. Natural convective heat transfer coefficient – a review I. Isolated vertical and horizontal surfaces. *Energy Conversion and Management*, 42:491–504, 2001a.

Abdul-Jabbar N. Khalifa. Natural convective heat transfer coefficient – a review II. Surfaces in two- and three-dimensional enclosures. *Energy Conversion and Management*, 42:505–517, 2001b.

W. J. King. The Basic Laws and Data of Heat Transmission. *Mechanical Engineering*, 54:347–353, 1932.

Roland Koenigsdorff. Status und Perspektiven thermischer Bauteilaktivierung. In *Tagungsband zum Bauphysikertreffen, Stuttgart*, volume 64, pages 57–67. Fachhochschule Stuttgart - Hochschule für Technik, 2003.

Roland Koenigsdorff and Martina Sedlak. Digitales Gebäude- und Lernmodell des Technikums Gebäudeklimatik der Hochschule Biberach (Digitales Modell Technikum G - DIMOTE). *Beiträge zum 6. Tag der Lehre, 24.11.2005, Fachhochschule Ulm, Studienkommission für Hochschuldidaktik an Fachhochschulen in Baden-Württemberg*, pages 62–65, 2005.

B.G. Lakatos, Z. Süle, and Cs. Mihálykó. Population balance model of heat transfer in gas–solid particulate systems. *International Journal of Heat and Mass Transfer*, 51:1633–1645, 2008.

Lawrence Berkeley National Laboratory LBNL. THERM Finite Element Simulator. Version 5.2. 2003.

LG Bielefeld. Az 3 O 411/01, April 2003. Judgement of the LG (Regional Court) Bielefeld, 16.04.2003.

Martin W Liddament. A Guide to Energy Efficient Ventilation. Technical Report AIC-TN-VENTGUIDE-1996, IEA Energy Conservation in Buildings and Community Systems Programme, Annex V Air Infiltration and Ventilation Centre, March 1996.

W. H. McAdams. *Heat Transmission*. New York: McGraw-Hill, 1954.

M. A. Michejew. *Grundlagen der Wärmeübertragung*. VEB Verlag Technik Berlin, second edition, 1964.

T. C. Min, L. F. Schutrum, G. V. Parmelee, and J. D. Vouris. Natural convection and radiation in a panel-heated room. *ASHRAE Transactions*, 62:337–358, 1956.

Michael F. Modest. *Radiative Heat Transfer*. Academic Press, second edition, 2003.

L. Neiswanger, G.A. Johnson, and V.P. Carey. An experimental study of high Rayleigh number mixed convection in a rectangular enclosure with restricted inlet and outlet openings. *Journal of Heat Transfer*, 109:446–453, 1987.

Atila Novoselac, Brendon J. Burley, and Jelena Srebric. Development of new and validation of existing convection correlations for rooms with displacement ventilation systems. *Energy and Buildings*, 38:163–173, 2006.

OLG Rostock. Az 3 U 83/98, December 2000. Judgement of the OLG (Higher Regional Court) Rostock, 29.12.2000.

Patrick H. Oosthuizen and David Naylor. *Introduction to Convective Heat Transfer Analysis*. McGraw-Hill, 1999.

Lothar Papula. *Mathematik für Ingenieure und Naturwissenschaftler Band 3*. Vieweg, third edition, 1999.

Luis Pérez-Lombard, José Ortiz, and Christine Pout. A review on buildings energy consumption information. *Energy and Buildings*, 40:394–398, 2008.

B. S. Petuchov, A. A. Detlaf, and W. W. Kirillow. Shurnal technitscheskoi fisiki (Zeitschrift für technische Physik), Jg. 24, H. 10, 1954.

Jens Pfafferott. *BINE Informationsdienst 2003: Passive Kühlung durch Nachtlüftung. Themeninfo I/03*. Fachinformationszentrum Karlsruhe, Gesellschaft für wissenschaftlich-technische Information mbH; 76344 Eggenstein-Leopoldshafen, 2003.

Jens Pfafferott and Doreen Kalz. *BINE Informationsdienst 2007: Thermoactive building systems. High-comfort, energy-efficient heating and cooling of non-residential buildings. Themeninfo I/07*. Fachinformationszentrum Karlsruhe, Gesellschaft für wissenschaftlich-technische Information mbH; 76344 Eggenstein-Leopoldshafen, 2007.

Jens Pfafferott, Sara Schiel, and Sebastian Herkel. Bauteilkühlung. Messungen und modellbasierte Auswertung. *Tagungsband 15. Symposium Thermische Solarenergie, OTTI-Energie-Kolleg, Staffelstein*, 2005.

Peter Pfrommer and Tobias Zitzmann. Dynamische Simulation des sommerlichen Temperaturverhaltens eines Büroraumes mit einer modifizierten CFD-Technik. *Bauphysik*, 30:163–173, 2008.

Simon J. Rees. *Modelling of Displacement Ventilation and Chilled Ceiling Systems Using Nodal Models*. PhD thesis, Loughborough University, March 1998.

Wolfgang Richter. *Handbuch der thermischen Behaglichkeit -Heizperiode-*. Wirtschaftsverlag NW Verlag für neue Wissenschaft GmbH, Bremerhaven, 2003.

Solar Energy Laboratory at the University of Wisconsin-Madison SEL. Trnsys 17, a TRaNsient SYstem Simulation program, Volume 5, Multizone Building modeling with Type 56 and TRNBuild, For TRNSYS 17.01.0006, 02 2012.

A. A. Shukauskas. Dissertation. MEI Moskauer Energetisches Institut 1953. Teploenergetika (Wärmeenergetik) 4, 1955.

Robert Siegel and John R. Howell. *Thermal Radiation Heat Transfer*. Taylor & Francis, fourth edition, 2002.

J. D. Spitler, C. O. Pedersen, and D. E. Fisher. Interior Convective Heat Transfer in Buildings with Large Ventilative Flow Rates. *ASHRAE Transactions*, 97(1): 505–515, 1991a.

J. D. Spitler, C. O. Pedersen, D. E. Fisher, P. F. Menne, and J. Cantillo. An Experimental Facility for Investigation of Interior Convective Heat Transfer. *ASHRAE Transactions*, 97(1):497–504, 1991b.

Werner A. Stahel. *Statistische Datenanalyse. Eine Einführung für Naturwissenschaftler*. Vieweg, 2002.

John R. Taylor. *An Introduction to Error Analysis. The Study of Uncertainties in Physical Measurements*. University Science Books, Sausalito, California, second edition, 1997.

ThermoAnalytics, Inc. *RadTherm. Thermal Analysis Software. User Manual for RadTherm Version 8*. 2006.

Abidin Uygun. Recommendations for installation of acoustic baffles. face-to-face discussion during a visit at OWA headquarters, Amorbach, 24. September 2007.

J. van der Maas. Air Flow through Large Openings in Buildings. Technical report, International Energy Agency, Energy Conservation in Buildings and Community Systems Programme, Annex 20: Air Flow Patterns within Buildings, Subtask 2: Air Flows between Zones, 1992.

VDI 2078. Berechnung der Kühllast klimatisierter Räume (VDI-Kühllastregeln); Cooling Load Calculation of Air-conditioned Rooms (VDI Cooling Load Regulations). Verein Deutscher Ingenieure, July 1996.

VDI 6020 Blatt 1 / Part 1. Anforderungen an Rechenverfahren zur Gebäude- und Anlagensimulation, Gebäudesimulation; Requirements on methods of calculation to thermal and energy simulation of buildings and plants, Buildings. Verein Deutscher Ingenieure, May 2001.

WSVO95. Verordnung über einen energiesparenden Wärmeschutz bei Gebäuden (Wärmeschutzverordnung - WärmeschutzV) vom 16. August 1994.

ZES. *Benutzerhandbuch LMG95 1-Phasen-Präzisionsleistungsmessgerät. Stand: 15. Juni 2007*. Zimmer Electronic Systems, 2007.

Glossary

ac/h air changes per hour. 43, 44, 60, 61, 71, 87, 95, 137, 138, 148, 150, 163, 164, 169, 170, 173–175
ASCII American Standard Code for Information Interchange. 73, 81
AUST Average Unheated Surface Temperature. 10, 24, 53

CFD Computational Fluid Dynamics. 28, 29, 59, 61, 64, 89, 171, 174, 175, 177, 181, 183, 184
CHTC convective heat transfer coefficient. 14, 18, 27, 41, 47, 50–52, 63, 139, 148, 155, 159, 163, 165, 169, 174, 175, 180
CPRTD chip platinum resistance temperature detector. 74, 77, 83, 114, 117, 120, 121

DAQ data acquisition and switch unit. 74, 77, 78, 193
DKD Deutscher Kalibrierdienst. 83

EIB European Installation Bus. 71

FPRTD foil platinum resistance temperature detector. 74, 77, 84, 117

HVAC heating, ventilation and air conditioning. 1, 3

ICT information and communications technology. 3
IEA International Energy Agency. 2
IPCC Intergovernmental Panel on Climate Change. 1

MIGT mercury-in-glass thermometer. 83, 112, 114, 117

PC Personal Computer. 78
PCBA printed circuit board assembly. 77, 233
PRT platinum resistance thermometer. 76, 77, 82, 83, 96, 112, 114, 117

PTB Physikalisch-Technische Bundesanstalt. 83

RTD resistance temperature detector. 77
RVA rotating vane anemometer. 79

SD standard deviation. 206
SDOM standard deviation of the mean. 110, 206

TABS thermo-active building systems. 2, 3, 5, 18, 19, 36, 48, 58, 60, 65, 86, 139, 148, 177

WLG WärmeLeitGruppe WLG, a classification system for insulation materials which is used in Germany. WLG 025 means that the material has a conductivity of 0.025 $\mathrm{W\,m^{-2}\,K}$ and WLG 035 means a conductivity of 0.035 $\mathrm{W\,m^{-2}\,K}$. 73, 102

A Information on Temperature Sensors

Table A.1 is a comprehensive list of temperature sensors installed in the experimental chamber. The sensors' ID number and type, their location, as well as calibration results and sensor labels (written on the cable) are shown. The first digit of the sensor ID indicates the DAQ and thus the file in which the measured value is saved (q.v. figure A.1). The second digit represents the device's plug-in module to which the sensor is connected. The used channel is expressed by the last two digits. With the temperature measurement system, measured raw data is saved. To obtain an accurate temperature value T, raw data from each sensor must be corrected as shown in equation (A.1).

$$T = T_{\text{raw}} + (\text{slope} \cdot T_{\text{raw}} + \text{intercept}) \tag{A.1}$$

The values given in table A.1 must be inserted for slope and intercept.

Sensors 1101 to 2211 are the original sensors installed during the construction phase of the cabin by the author of this work for the experimental programme. These sensors are described in detail in chapter 3. Sensors 2210 and 2211 are two Pt500 screw-in temperature probes for measuring supply and return fluid temperature of an optional hydronic heating and cooling element which could possibly be installed in the cabin in future. These two sensors are the only sensors which are not of type Pt100. Temperature sensors with ID 2212 and higher are additional sensors which were installed by a student towards the end of this work. For these additional sensors, calibration data is only available for the foil sensors.

After the schematic representation of the measurement system in figure A.1, technical drawings in figures A.2 to A.4 show the position of sensors used for measuring surface temperatures. Furthermore, position of additional sensors are shown in figures A.5 and A.6 at the end of this appendix.

Table A.1: List of sensors installed in the experimental chamber.

Sensor ID	Type	Correction Curve Slope	Intercept	Label	Location
1101	Chip	−0.00140	0.01720	I 1	Outside
1102	Chip	−0.00155	−2.49255	I 2	Outside
1103	Chip	−0.00055	0.12690	I 3	Ceiling Inside
1104	Chip	0.00005	0.05215	I 4	Ceiling Inside
1105	Chip	−0.00070	0.08515	I 5	Ceiling Inside
1106	Chip	0.00015	0.13620	I 6	Ceiling Inside
1107	Chip	0.00057	0.03690	I 7	Ceiling Inside
1108	Chip	−0.00035	0.11460	I 8	Ceiling Inside
1109	Chip	0.00010	0.00075	I 9	Front Wall Inside
1110	Chip	0.00035	0.07525	I 10	Front Wall Inside
1111	Chip	0.00050	0.06795	I 11	Front Wall Inside
1112	Chip	−0.00010	0.12550	I 12	Right Side Wall Inside
1113	Chip	0.00050	0.14545	II 1	Right Side Wall Inside
1114	Chip	0.00020	0.13710	II 2	Right Side Wall Inside
1115	Chip	0.00085	0.10520	II 3	Rear Wall Inside
1116	Chip	0.00070	0.16355	II 4	Rear Wall Inside
1117	Chip	−0.00095	0.10470	II 5	Rear Wall Inside

(continued)

Table A.1: List of sensors installed in the experimental chamber. (Continued)

Sensor ID	Type	Correction Curve Slope	Intercept	Label	Location
1118	Chip	0.00105	0.03925	II 6	Left Side Wall Inside
1119	Chip	−0.00050	0.13840	II 7	Left Side Wall Inside
1201	Chip	−0.00125	0.06665	II 8	Left Side Wall Inside
1202	Chip	−0.00070	−0.00830	II 9	Ceiling Internal
1203	Chip	−0.00085	0.09595	II 10	Ceiling Internal
1204	Chip	0.00130	−0.00200	II 11	Ceiling Internal
1205	Chip	−0.00005	0.07990	II 12	Ceiling Internal
1206	Chip	−0.00060	0.08740	III 1	Ceiling Internal
1207	Chip	−0.00120	0.10270	III 2	Ceiling Internal
1208	Foil	0.01130	−0.34545	III 3	Hot Plate Front
1209	Foil	0.00895	−0.39380	III 4	Hot Plate Front
1210	Foil	0.00195	−0.22880	III 5	Hot Plate Front
1211	Foil	0.00610	−0.55225	III 6	Floor Inside
1212	Foil	0.00795	−0.69835	III 7	Hot Plate Back
1213	Foil	0.00965	−0.52510	III 8	Hot Plate Back
1214	Foil	0.00160	−0.54220	III 9	Front Wall Inside
1215	Foil	0.00415	−0.46610	III 10	Front Wall Inside
1216	Foil	0.00750	−0.08180	III 11	Front Wall Inside
1217	Foil	0.00345	−0.37760	III 12	Right Side Wall Inside
1218	Foil	0.00190	−0.50530	IV 1	Right Side Wall Inside
1219	Foil	0.00430	−0.40485	IV 2	Right Side Wall Inside
1301	Foil	0.00705	−0.41495	IV 3	Rear Wall Inside
1302	Foil	0.00405	−0.49775	IV 4	Rear Wall Inside
1303	Foil	0.00175	−0.40290	IV 5	Rear Wall Inside
1304	Foil	0.00430	−0.44695	IV 6	Left Side Wall Inside
1305	Foil	0.00390	−0.46690	IV 7	Left Side Wall Inside
1306	Foil	0.00075	−0.37610	IV 8	Left Side Wall Inside
1307	Foil	0.00570	−0.54415	IV 9	Floor Internal
1308	Foil	0.00820	−0.58735	IV 10	Floor Internal
1309	Foil	0.00630	−0.33910	IV 11	Floor Internal
1310	Foil	0.00300	−0.41185	IV 12	Floor Internal
1311	Foil	0.00775	−0.64605	V 1	Floor Internal
1312	Foil	0.00645	−0.45455	V 2	Floor Internal
1313	Foil	0.00790	−0.48800	V 3	Right Side Wall Inside
1314	Foil	0.00285	−0.40330	V 4	Right Side Wall Internal

(continued)

Table A.1: List of sensors installed in the experimental chamber. (Continued)

Sensor ID	Type	Correction Curve Slope	Intercept	Label	Location
1315	Foil	0.00290	−0.39275	V 5	Outside
1316	Foil	0.00625	−0.58460	V 6	Ceiling Internal
1317	Foil	0.00260	−0.52275	V 7	Ceiling Internal
1318	Foil	0.00495	−0.47380	V 8	Outside
1319	not occupied				
2101	Chip	0.00017	0.08371	ACS 1	Indoor Air
2102	Chip	−0.00065	0.04914	ACS 2	Indoor Air
2103	Chip	0.00099	0.05643	ACS 3	Indoor Air
2104	Chip	0.00051	0.06100	ACS 4	Indoor Air
2105	Chip	−0.00031	0.15457	ACS 5	Indoor Air
2106	Chip	−0.00099	0.07264	ACS 6	Indoor Air
2107	Chip	−0.00074	0.08593	ACS 7	Indoor Air
2108	Chip	0.00119	0.01393	ACS 8	Indoor Air
2109	Chip	0.00018	0.16964	ACS 9	Indoor Air
2110	Chip	0.00156	0.11814	ACS 10	Indoor Air
2111	Chip	−0.00192	0.10850	ACS 11	Indoor Air
2112	Chip	−0.00146	0.06000	ACS 12	Indoor Air
2113	Chip	0.00074	0.05257	ACS 13	Indoor Air
2114	Chip	−0.00067	0.08671	ACS 14	Indoor Air
2115	Chip	0.00126	0.08207	ACS 15	Indoor Air
2116	Chip	0.00266	−0.02050	ACS 16	Indoor Air
2117	Chip	0.00166	0.11528	ACS 17	Indoor Air
2118	Chip	−0.00004	0.06364	ACS 18	Indoor Air
2119	Chip	0.00222	−0.00629	ACS 19	Indoor Air
2201	Foil	0.00201	−0.30239	AFS 1	Baffles Surface
2202	Foil	0.00205	−0.41085	AFS 2	Baffles Surface
2203	Foil	0.00422	−0.50472	AFS 3	Baffles Surface
2204	Foil	0.00646	−0.44461	AFS 4	Baffles Surface
2205	Foil	0.00439	−0.49733	AFS 5	Floor Inside
2206	Foil	0.00609	−0.46792	AFS 6	Floor Inside
2207	Foil	0.00675	−0.52795	AFS 7	Floor Inside
2208	Foil	0.00265	−0.39337	AFS 8	Floor Inside
2209	not occupied				
2210	DS500	−0.00058	0.12393	red	for future hydronic element
2211	DS500	−0.00088	0.14250	blue	for future hydronic element

(continued)

Table A.1: List of sensors installed in the experimental chamber. (Continued)

Sensor ID	Type	Correction Curve Slope	Intercept	Label	Location
2212	Foil	0.00759	−0.365272	KAF 2	External
2213	Foil	0.00853	−0.383485	KAF 3	External
2214	Foil	0.00733	−0.362316	KAF 4	External
2215	Foil	0.00429	−0.524965	KAF 5	External
2216	Foil	0.00673	−0.472705	KAF 6	External
2217	Foil	0.00557	−0.410837	KAF 7	External
2218	Foil	−0.00088	−0.880937	KAF 8	External
2219	Foil	0.00700	−0.332434	KAF 9	External
2301	Chip	not calibrated		KAC 1	External
2302	Chip	not calibrated		KAC 2	External
2303	Chip	not calibrated		KAC 3	External
2304	Chip	not calibrated		KAC 4	External
2305	Chip	not calibrated		KAC 5	External
2306	Chip	not calibrated		KAC 6	External
2307	Chip	not calibrated		KAC 7	External
2308	Chip	not calibrated		KAC 8	External
2309	Chip	not calibrated		KAC 9	External
2310	Chip	not calibrated		KAC 10	External
2311	Chip	not calibrated		KAC 11	External
2312	Chip	not calibrated		KAC 12	External
2313	Chip	not calibrated		KAC 13	External
2314	Chip	not calibrated		KAC 14	External
2315	Chip	not calibrated		KAC 15	External
2316	Chip	not calibrated		KAC 16	External
2317	Chip	not calibrated		KAC 17	External
2318	Chip	not calibrated		KAC 18	External
2319	Foil	0.00621	−0.607613	KAF 1	External

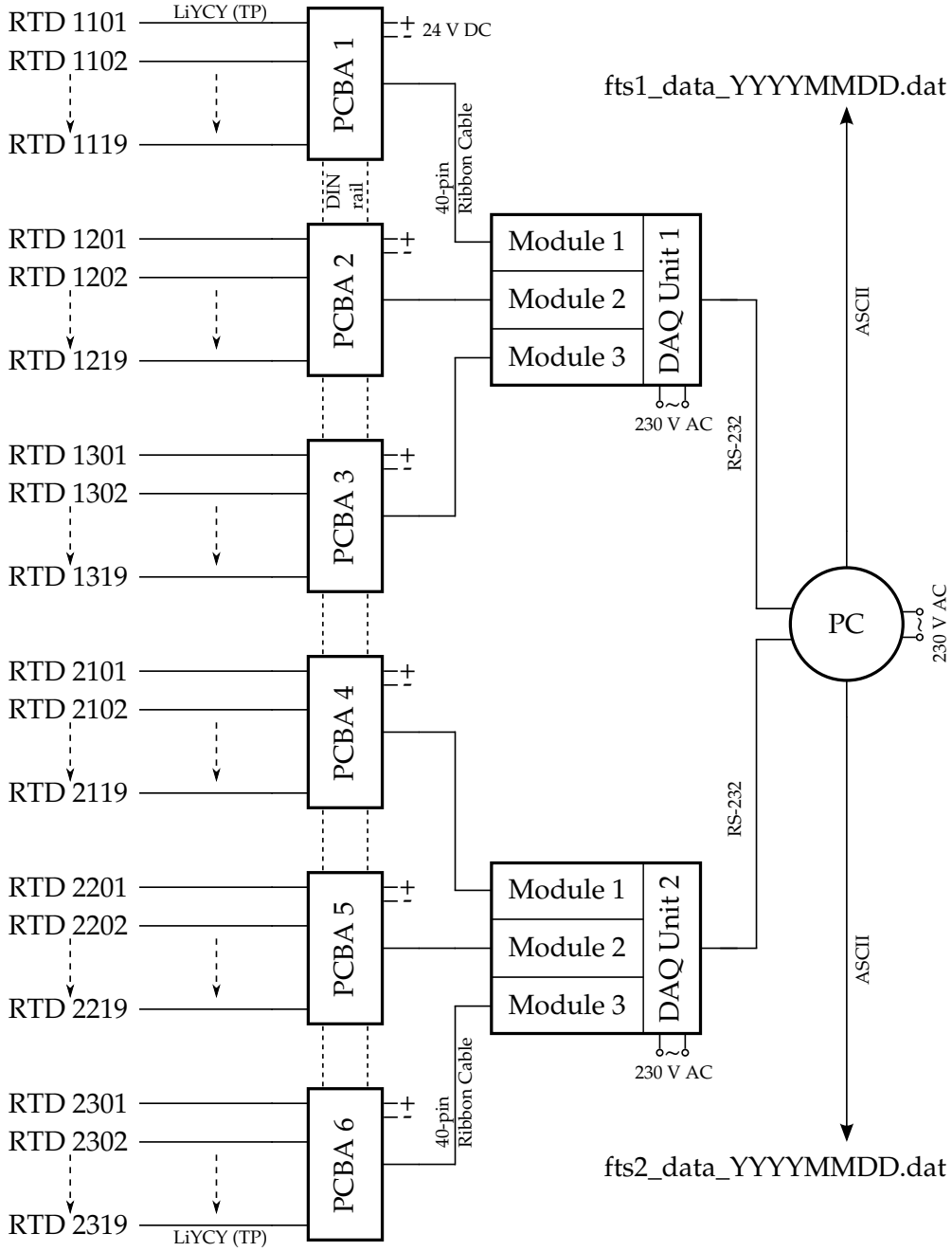

Figure A.1: Schematic of the temperature measurement system.

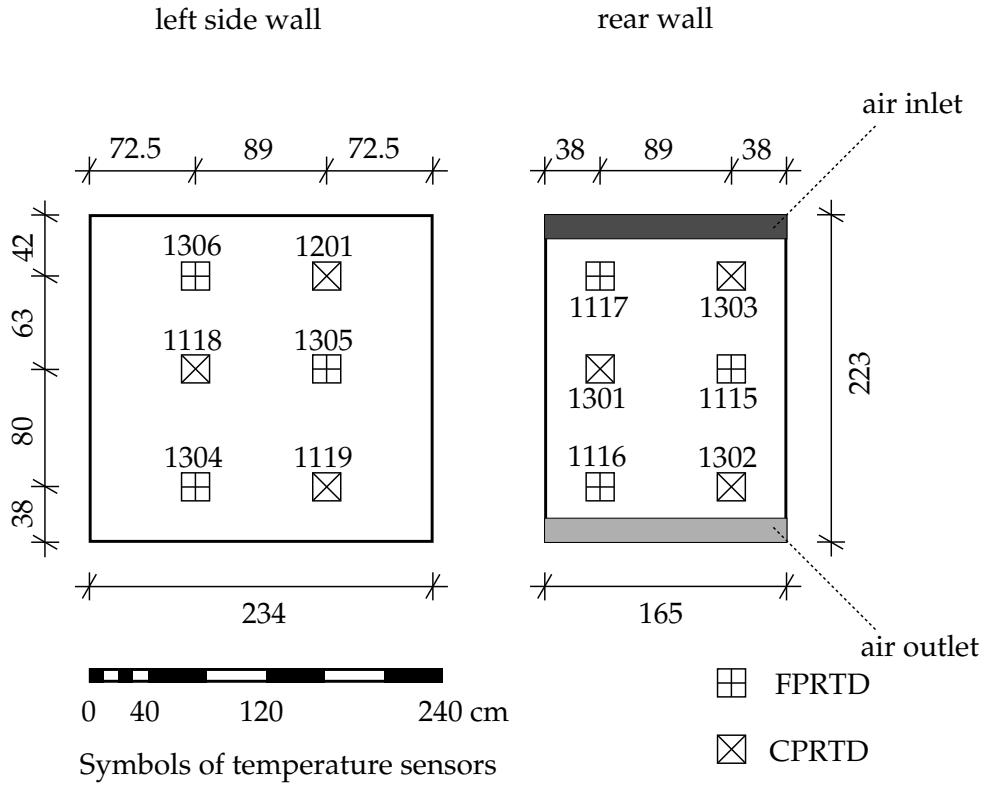

Figure A.2: View of the left side wall and the rear wall showing the positions of surface temperature sensors and the sensors' ID numbers.

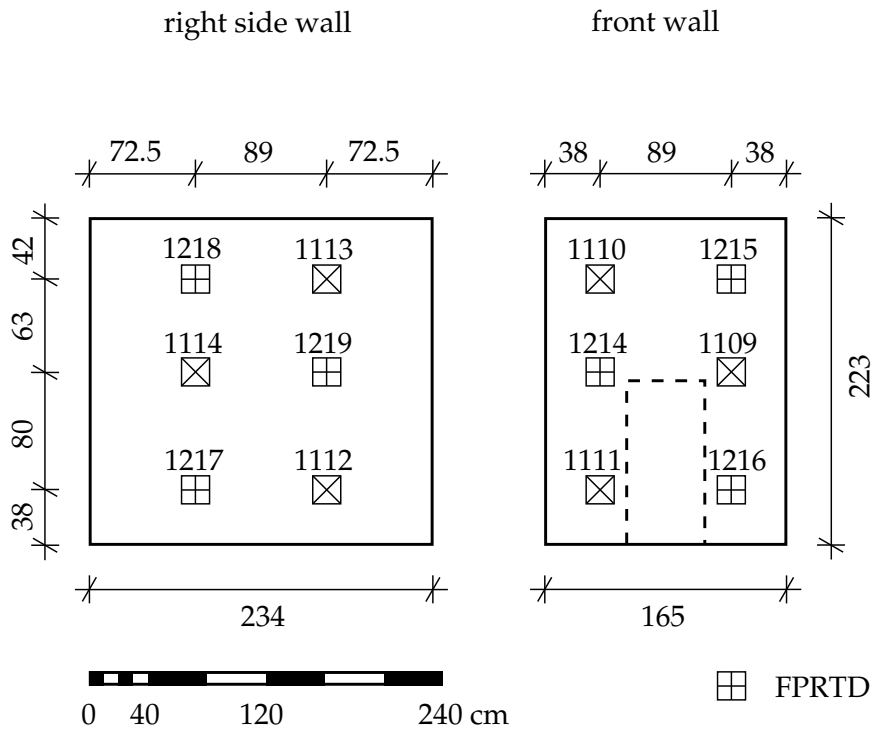

Figure A.3: View of the right side wall and the front wall showing the positions of surface temperature sensors and the sensors' ID numbers.

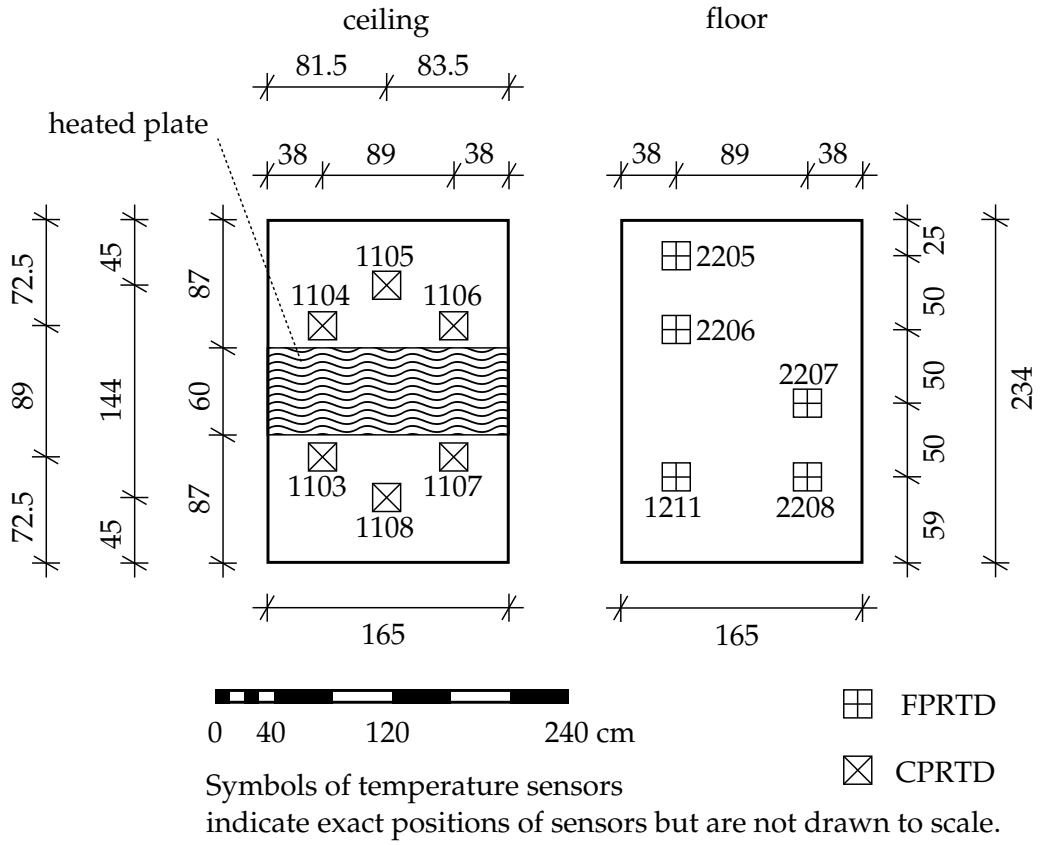

Figure A.4: View of the ceiling and the floor showing the positions of surface temperature sensors and the sensors' ID numbers.

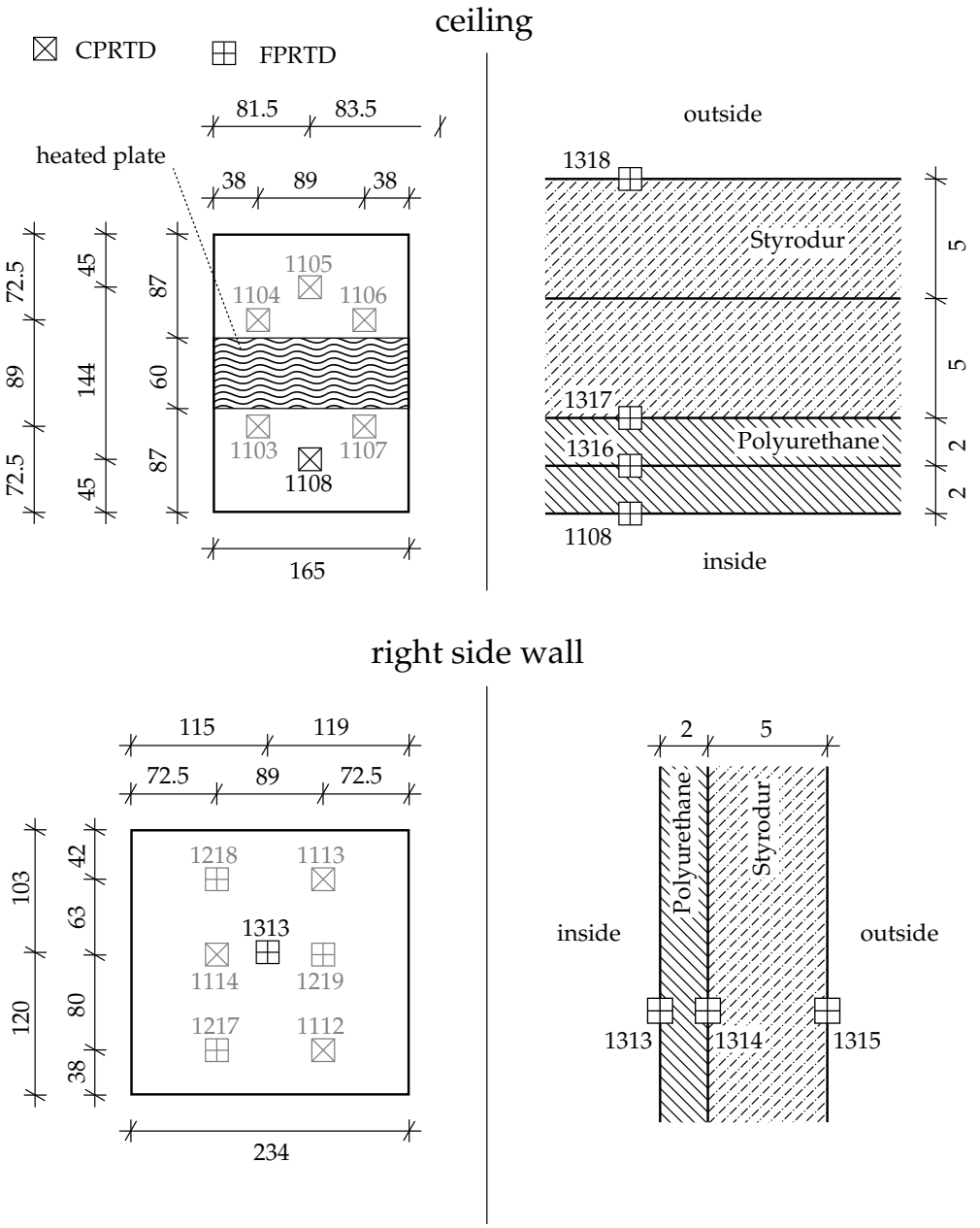

Symbols of temperature sensors indicate exact positions of sensors but are not drawn to scale.

Figure A.5: View (left) and section (right) of the ceiling (top) and the right side wall (bottom) showing positions of additional foil sensors which can be used to determine conduction losses of the cabin.

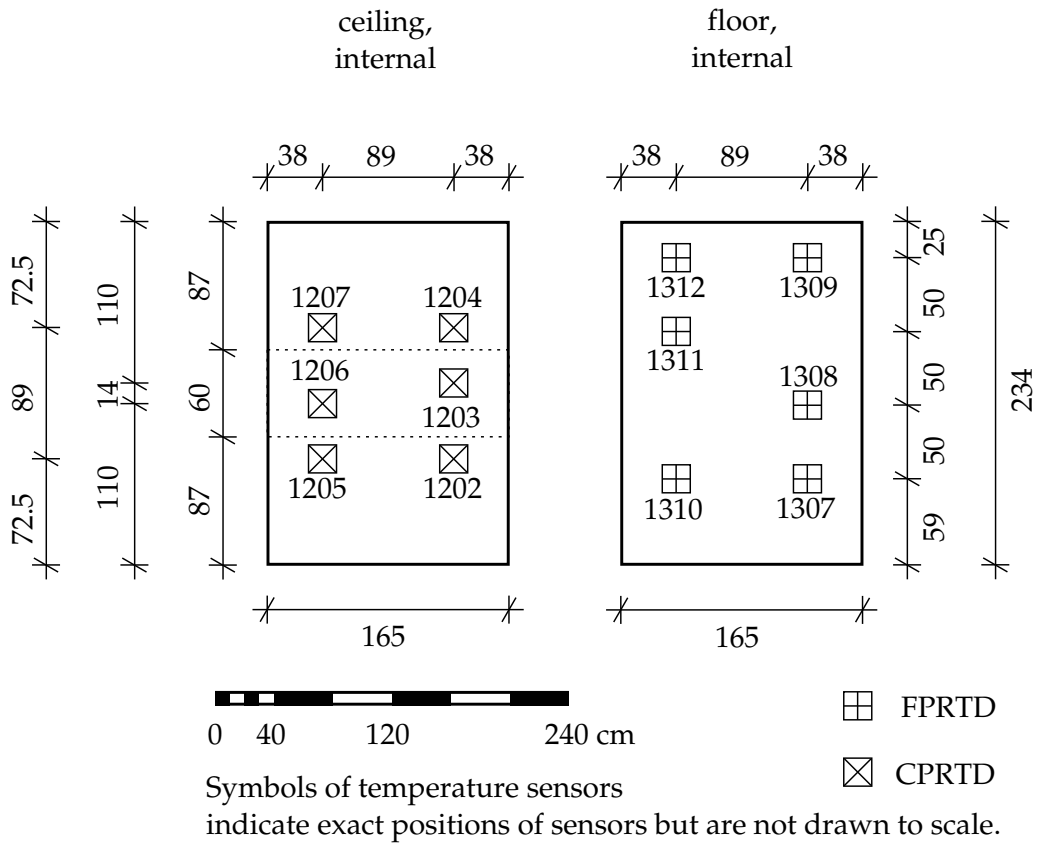

Figure A.6: Positions of temperature sensors which are installed in the ceiling and floor for measuring internal temperatures behind the first layer of insulation.

B Additional Error Analysis

In chapter 4, the partial uncertainties which contribute to the overall uncertainty in h_c were determined. These relevant values were uncertainty in

- heat output of the hot plate $\delta\dot{q}_{el}$,
- U-factor of the ceiling behind the hot plate $\delta U^{\star}$,
- emissivity of the hot plate $\delta\varepsilon_{plate}$, as well as
- temperature behind the hot plate δT_{back},
- surface temperature of the hot plate δT_{plate},
- radiation temperature of the other enclosing surfaces δT_{rad}, and
- the selected air temperature δT_{fluid}.

For further analysis of the experimental data, other uncertainties might also be of interest. The uncertainty in surface-to-air temperature difference between hot plate and mean air is for example given as

$$\delta\left(T_{plate} - T_{air,mean}\right) = \pm 0.18\,\mathrm{K}. \tag{B.1}$$

Other values of interest can be calculated using the equations given below. All of these equations can also be found in Taylor (1997)—or most likely any other textbook on error analysis. Furthermore, a table with values of Student's t is given which is based on the one by Holman (2001).

Uncertainty δq in a quantity q which is calculated from several quantities $x, \ldots, w$ with small uncertainties $\delta x, \ldots, \delta w$ is given by:

1. If $q = x + \cdots + z - (u + \cdots + w)$, then

$$\delta q = \sqrt{(\delta x)^2 + \cdots + (\delta z)^2 + (\delta u)^2 + \cdots + (\delta w)^2} \tag{B.2a}$$

for independent random errors,

$$\delta q \leq \delta x + \cdots + \delta z + \delta u + \cdots + \delta w \tag{B.2b}$$

always.

2. If $q = \frac{x \times \cdots \times z}{u \times \cdots \times w}$, then

$$\frac{\delta q}{|q|} = \sqrt{\left(\frac{\delta x}{x}\right)^2 + \cdots + \left(\frac{\delta z}{z}\right)^2 + \left(\frac{\delta u}{u}\right)^2 + \cdots + \left(\frac{\delta w}{w}\right)^2} \tag{B.3a}$$

for independent random errors,

$$\frac{\delta q}{|q|} \leq \frac{\delta x}{|x|} + \cdots + \frac{\delta z}{|z|} + \frac{\delta u}{|u|} + \cdots + \frac{\delta w}{|w|} \tag{B.3b}$$

always.

3. If $q = Bx$ (with known B), then

$$\delta q = |B| \delta x. \tag{B.4}$$

4. If $q = q\,(x)$, then

$$\delta q = \left|\frac{dq}{dx}\right| \delta x. \tag{B.5}$$

5. If $q = x^n$, then

$$\frac{\delta q}{|q|} = |n| \frac{\delta x}{|x|}. \tag{B.6}$$

For N separate measurements $x_1, \ldots, x_N$ of a quantity x

$$\bar{x} = \frac{1}{N} \sum_{i=1}^{N} x_i \tag{B.7}$$

is the mean,

$$\sigma_x = \sqrt{\frac{1}{N-1}\sum (x_i - \bar{x})^2} \tag{B.8}$$

is the standard deviation (SD), and

$$\sigma_{\bar{x}} = \frac{\sigma_x}{\sqrt{N}} \tag{B.9}$$

is the standard deviation of the mean (SDOM).

Table B.1: Values of Student's t for use in equation (4.9) based on Holman (2001). Subscript in t indicates percent confidence level.

Degrees of freedom ν	t_{50}	t_{80}	t_{90}	t_{95}	t_{99}	$t_{99.9}$
1	1.000	3.078	6.314	12.706	63.657	636.619
2	0.816	1.886	2.920	4.303	9.925	31.598
3	0.765	1.638	2.353	3.182	5.841	12.941
4	0.741	1.533	2.132	2.776	4.604	8.610
5	0.727	1.476	2.015	2.571	4.032	6.859
6	0.718	1.440	1.943	2.447	3.707	5.959
7	0.711	1.415	1.895	2.365	3.499	5.405
8	0.706	1.397	1.860	2.306	3.355	5.041
9	0.703	1.383	1.833	2.262	3.250	4.781
10	0.700	1.372	1.812	2.228	3.169	4.587
11	0.697	1.363	1.796	2.201	3.106	4.437
12	0.695	1.356	1.782	2.179	3.055	4.318
13	0.694	1.350	1.771	2.160	3.012	4.221
14	0.692	1.345	1.761	2.145	2.977	4.140
15	0.691	1.341	1.753	2.131	2.947	4.073
16	0.690	1.337	1.746	2.120	2.921	4.015
17	0.689	1.333	1.740	2.110	2.898	3.965
18	0.688	1.330	1.734	2.101	2.878	3.922
19	0.688	1.328	1.729	2.093	2.861	3.883
20	0.687	1.325	1.725	2.086	2.845	3.850
40	0.681	1.303	1.684	2.021	2.704	3.551
60	0.679	1.296	1.671	2.000	2.660	3.460
120	0.677	1.289	1.658	1.980	2.617	3.373
∞	0.674	1.282	1.645	1.960	2.576	3.291

C Dimensionless Numbers

Experimental results have also been presented in dimensionless form. The necessary dimensionless numbers and their definitions are summarized below.

1. Reynolds number,

$$Re = \frac{U\,L_c}{\nu} \tag{C.1}$$

where U is the velocity of the flow in $\mathrm{m\,s^{-1}}$ and L_c is the characteristic length in m. ν is the kinematic viscosity in $\mathrm{m^2\,s^{-1}}$. The various suggestions for the characteristic length are discussed in chapter 2. For the evaluation of each experiment of this work, $L_c = 0.6\,\mathrm{m}$. The measured average velocity below the hot plate has been used for U in each set of experiments except for the forced convection experiments (test series 2) where the nominal inlet velocity has been used instead. The Reynolds number is used to characterize the flow regime of the fluid with forced convection. If $Re < Re_{\mathrm{critical}}$, the flow is laminar. If $Re > Re_{\mathrm{critical}}$, the flow is turbulent. The critical Reynolds number Re_{critical} depends on the geometric situation at hand. According to Elsner et al. (1993), Re_{critical} is between 3×10^5 and 5×10^5 for flows along walls or plates.

2. Grashof number,

$$Gr = \frac{\beta\, g\, (T_{\mathrm{surf}} - T_{\mathrm{fluid}})\, L_c^3}{\nu^2} \tag{C.2}$$

where β is the volumetric thermal expansion coefficient in $\mathrm{K^{-1}}$, g is the acceleration due to earth's gravity, T_{surf} is the surface temperature and T_{fluid} is the temperature of the fluid (both in K).

3. Prandtl number,

$$Pr = \frac{\nu}{\alpha} = \frac{c_p \mu}{\lambda} \tag{C.3}$$

where ν is the kinematic viscosity and α is the thermal diffusivity (both in $m^2\,s^{-1}$). Alternatively, c_p is the specific heat in $J\,kg^{-1}\,K^{-1}$, μ is the dynamic viscosity in $N\,s\,m^{-2}$ and λ is the thermal conductivity in $W\,m^{-1}\,K^{-1}$. In the present case (indoor air in the experimental chamber), $Pr \approx 0.73$.

4. Rayleigh number,

$$Ra = Gr \cdot Pr \tag{C.4}$$

is used to characterize the flow regime with natural convection. According to Elsner et al. (1993), Ra ranges from 5×10^2 to 2×10^7 for laminar flow. If the Rayleigh number is between 2×10^7 and 1×10^{13}, the flow regime is turbulent. Transition from laminar to turbulent flow typically takes place between 1×10^7 and 1×10^{10} but also depends on the geometric situation.

5. Nusselt number,

$$Nu = \frac{h_c\, L_c}{\lambda} \tag{C.5}$$

where h_c is the convective heat transfer coefficient in $W\,m^{-2}\,K^{-1}$. The Nusselt number describes the ratio of convectively transferred heat to heat transfer due to conduction. For $Nu = 1$, convective heat transfer is described by the conductivity of the fluid.

6. Richardson number,

$$Ri = \frac{Gr}{Re^2} = \frac{\beta\, g\, L_c\, (T_{surf} - T_{fluid})}{\nu^2} \tag{C.6}$$

and can be used to determine if either forced or natural convection are dominant in convective heat transfer or if both phenomena must be taken into consideration. For $Ri << 1$, forced convection is dominant. For $Ri >> 1$, natural convection is dominant. If $Ri \approx 1$, both natural and forced convection is present.

D Additional Experimental Results

Experimental results have been presented in chapter 6. Additional experimental results which are supplementary to those in the main text are shown below.

Section D.1 contains additional results for an unobstructed ceiling, in section D.2 supplementary material for the experimental test series with baffles is shown.

D.1 Unobstructed Ceiling

Ancillary information for the natural convection experiments is presented in section D.1.1. As forced convection experiments were not in the main focus of this work, there are no further plots for the forced convection experiments. All relevant information for this test series is already given in the main text. Section D.1.2 contains a collection of plots for the mixed convection experiments.

D.1.1 Natural Convection

Figures D.1, D.2 and D.3 show the temperature gradients measured inside the chamber during natural convection experiments. The temperature gradient plots are sorted in ascending order by the temperature difference between the surface of the hot plate and mean air. Each temperature difference is given in the caption so that the plots can be allocated to the results given in the main text. The position of the temperature sensors can be found in figure 3.7.

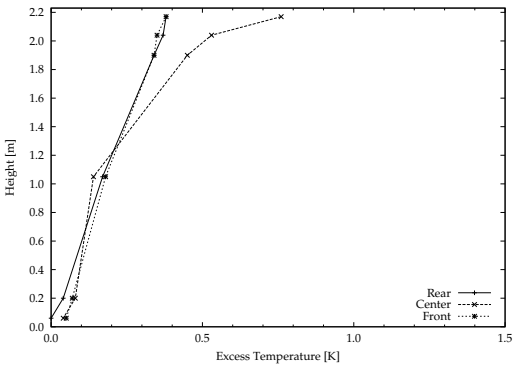

(a) $\vartheta_{\text{plate}} - \vartheta_{\text{meanair}} = 2.30\,\text{K}$

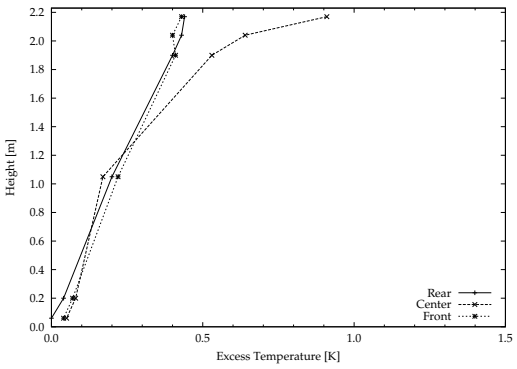

(b) $\vartheta_{\text{plate}} - \vartheta_{\text{meanair}} = 2.93\,\text{K}$

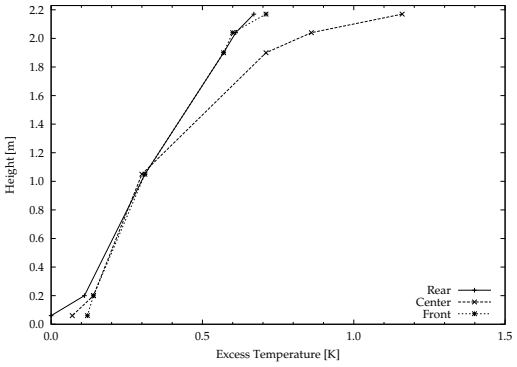

(c) $\vartheta_{\text{plate}} - \vartheta_{\text{meanair}} = 2.94\,\text{K}$

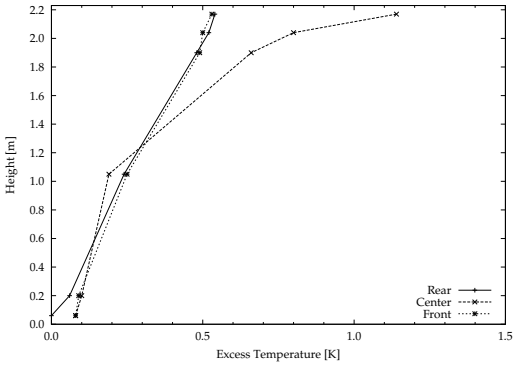

(d) $\vartheta_{\text{plate}} - \vartheta_{\text{meanair}} = 3.85\,\text{K}$

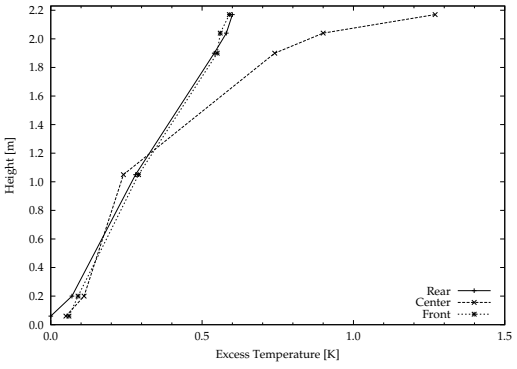

(e) $\vartheta_{\text{plate}} - \vartheta_{\text{meanair}} = 4.26\,\text{K}$

Figure D.1: Temperature gradients measured in the cabin for natural convection experiments with an unobstructed ceiling, $\vartheta_{\text{plate}} - \vartheta_{\text{meanair}} < 4.3\,\text{K}$.

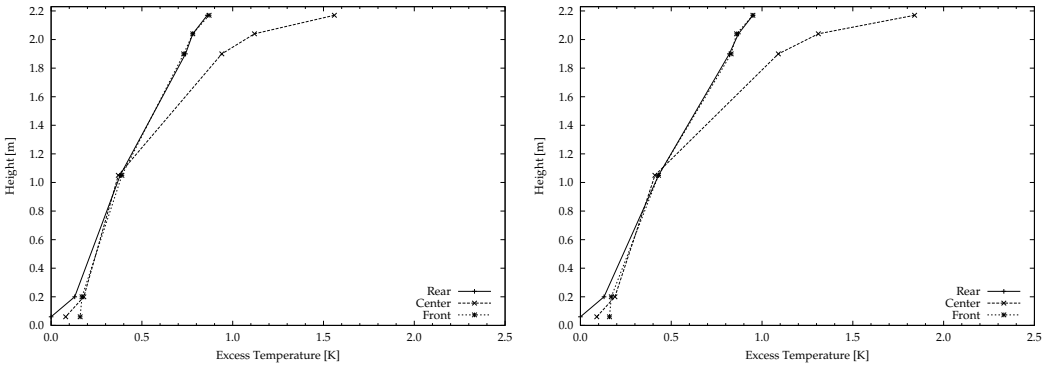

(a) $\vartheta_{\text{plate}} - \vartheta_{\text{meanair}} = 4.30\,\text{K}$ (b) $\vartheta_{\text{plate}} - \vartheta_{\text{meanair}} = 5.54\,\text{K}$

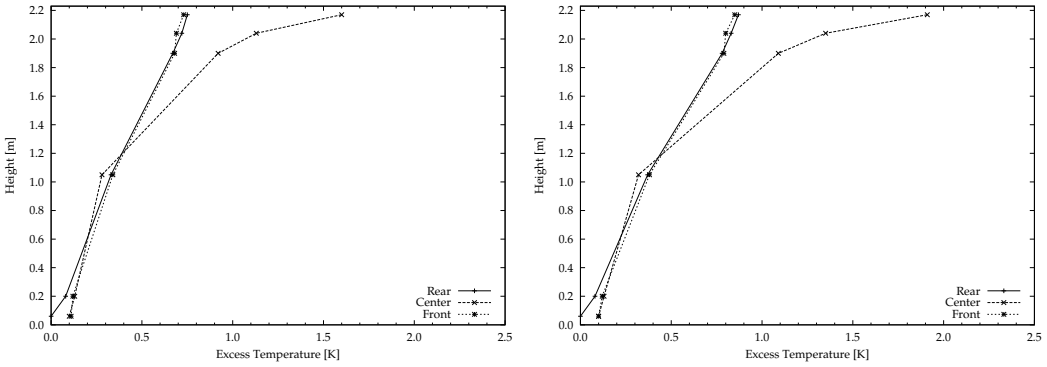

(c) $\vartheta_{\text{plate}} - \vartheta_{\text{meanair}} = 5.61\,\text{K}$ (d) $\vartheta_{\text{plate}} - \vartheta_{\text{meanair}} = 6.88\,\text{K}$

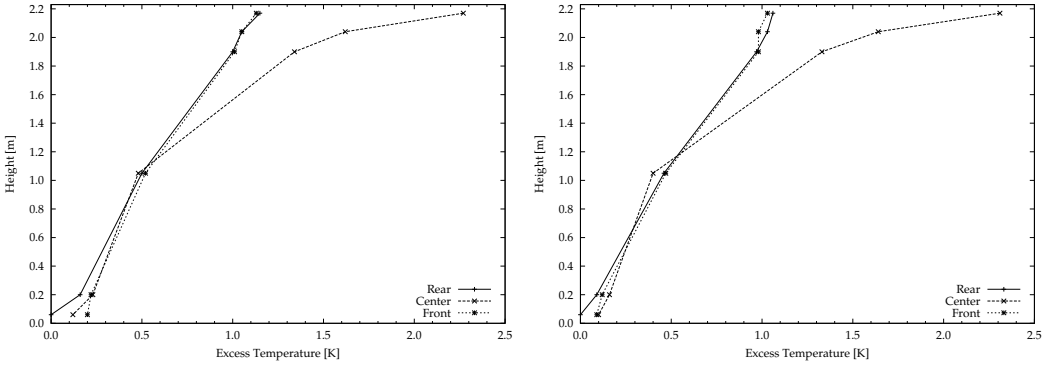

(e) $\vartheta_{\text{plate}} - \vartheta_{\text{meanair}} = 7.28\,\text{K}$ (f) $\vartheta_{\text{plate}} - \vartheta_{\text{meanair}} = 8.41\,\text{K}$

Figure D.2: Temperature gradients measured in the cabin for natural convection experiments with an unobstructed ceiling, $4.3\,\text{K} \leq \vartheta_{\text{plate}} - \vartheta_{\text{meanair}} < 8.5\,\text{K}$.

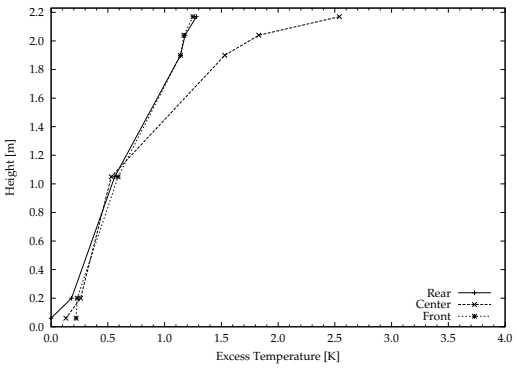

(a) $\vartheta_{\text{plate}} - \vartheta_{\text{meanair}} = 8.58\,\text{K}$

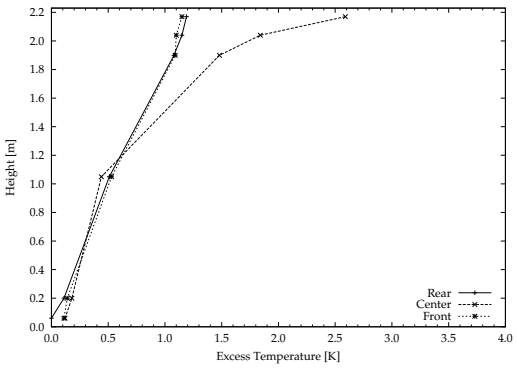

(b) $\vartheta_{\text{plate}} - \vartheta_{\text{meanair}} = 9.44\,\text{K}$

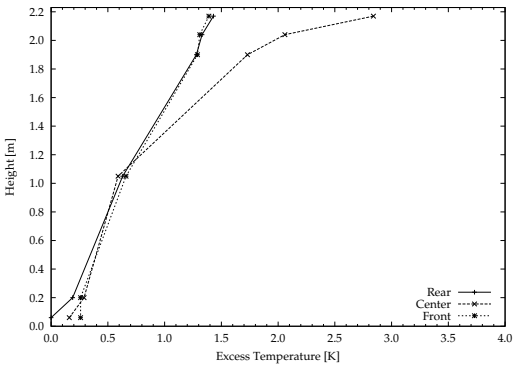

(c) $\vartheta_{\text{plate}} - \vartheta_{\text{meanair}} = 9.94\,\text{K}$

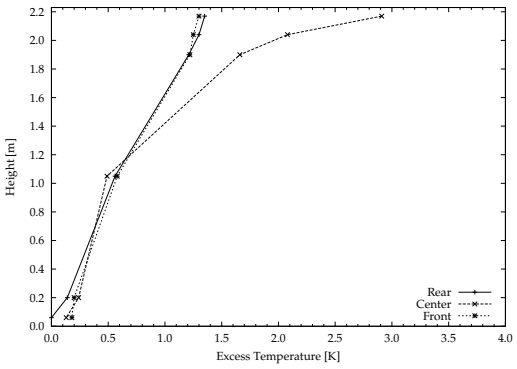

(d) $\vartheta_{\text{plate}} - \vartheta_{\text{meanair}} = 10.74\,\text{K}$

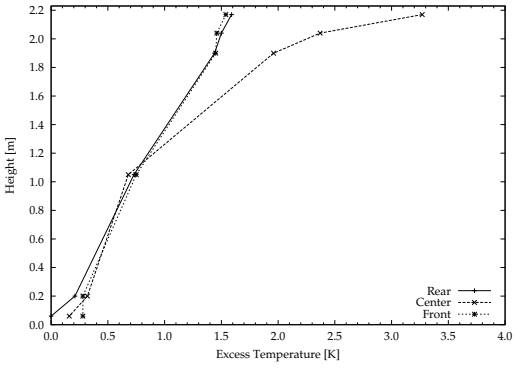

(e) $\vartheta_{\text{plate}} - \vartheta_{\text{meanair}} = 11.70\,\text{K}$

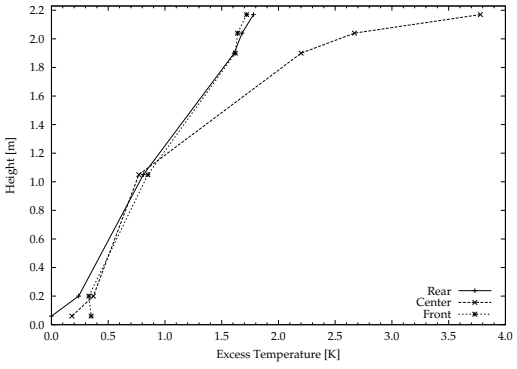

(f) $\vartheta_{\text{plate}} - \vartheta_{\text{meanair}} = 13.42\,\text{K}$

Figure D.3: Temperature gradients measured in the cabin for natural convection experiments with an unobstructed ceiling, $\vartheta_{\text{plate}} - \vartheta_{\text{meanair}} > 8.5\,\text{K}$.

D.1.2 Mixed Convection

Figures D.4, D.5, D.6 and D.7 show the temperature gradient plots for the mixed convection experiments. The graphs are anew grouped by temperature difference between surface of the hot plate and mean air. Outliers in figure 6.11 for which the experimental results do not fit the blending method from literature are marked with a *. It is obvious that the outliers show a behaviour for air temperature in the rear half of the cabin (i.e. close to the ceiling and the air inlet opening in the rear wall) which is different from the other experiments. Air temperature measured close to the ceiling in the rear is colder in these experiments.

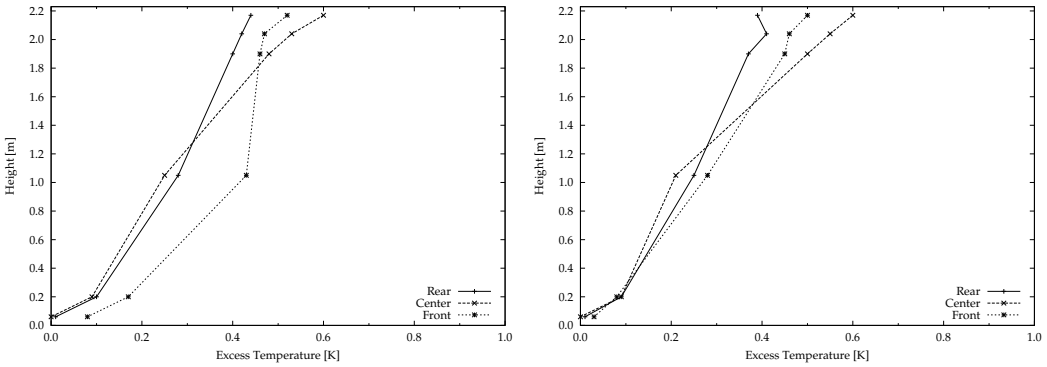

(a) $\vartheta_{\text{plate}} - \vartheta_{\text{meanair}} = 1.57\,\text{K}^{\star}$ (b) $\vartheta_{\text{plate}} - \vartheta_{\text{meanair}} = 2.12\,\text{K}$

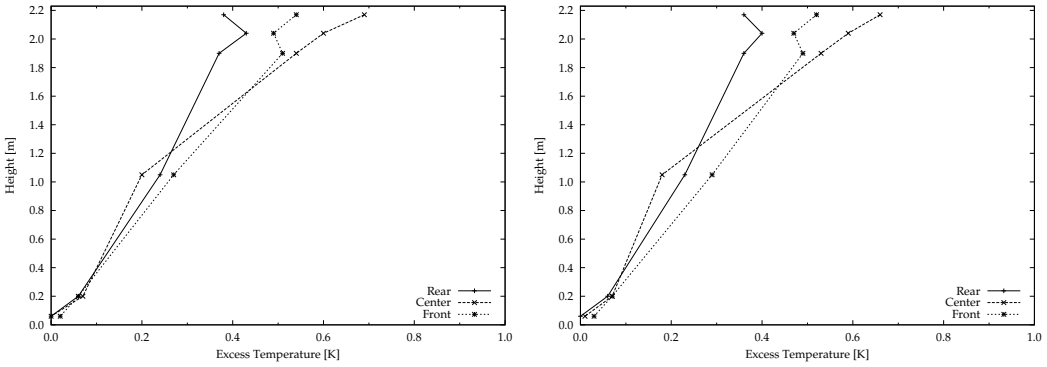

(c) $\vartheta_{\text{plate}} - \vartheta_{\text{meanair}} = 2.79\,\text{K}$ (d) $\vartheta_{\text{plate}} - \vartheta_{\text{meanair}} = 2.79\,\text{K}$

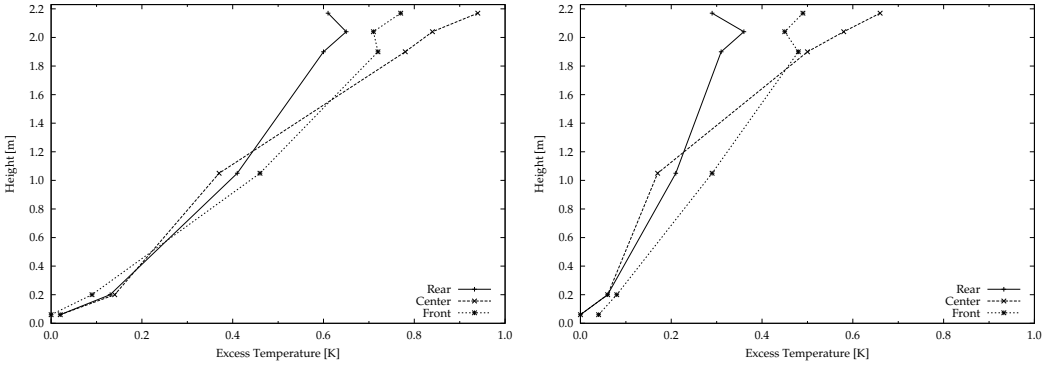

(e) $\vartheta_{\text{plate}} - \vartheta_{\text{meanair}} = 3.10\,\text{K}$ (f) $\vartheta_{\text{plate}} - \vartheta_{\text{meanair}} = 3.15\,\text{K}$

Figure D.4: Temperature gradients measured in the cabin for mixed convection experiments with $\vartheta_{\text{plate}} - \vartheta_{\text{meanair}} < 3.2\,\text{K}$. Outliers from figure 6.11 are indicated by a * in the caption.

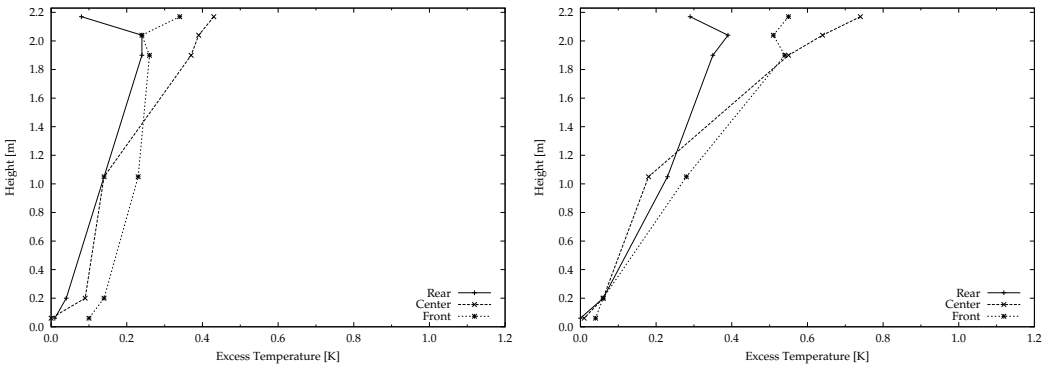

(a) $\vartheta_{\text{plate}} - \vartheta_{\text{meanair}} = 3.34\,\text{K}$

(b) $\vartheta_{\text{plate}} - \vartheta_{\text{meanair}} = 3.76\,\text{K}$

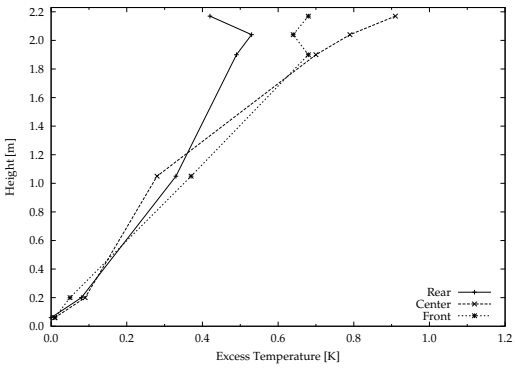

(c) $\vartheta_{\text{plate}} - \vartheta_{\text{meanair}} = 4.16\,\text{K}$

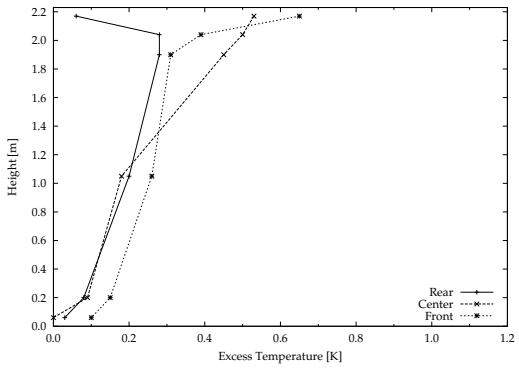

(d) $\vartheta_{\text{plate}} - \vartheta_{\text{meanair}} = 4.30\,\text{K}$

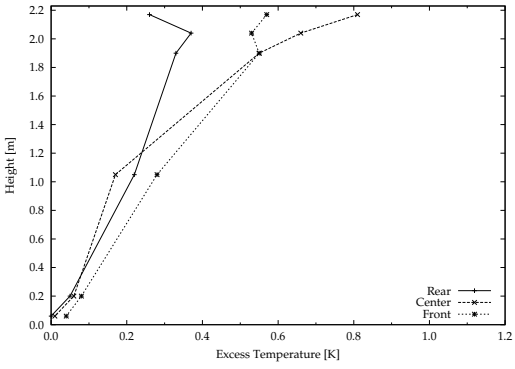

(e) $\vartheta_{\text{plate}} - \vartheta_{\text{meanair}} = 4.42\,\text{K}$

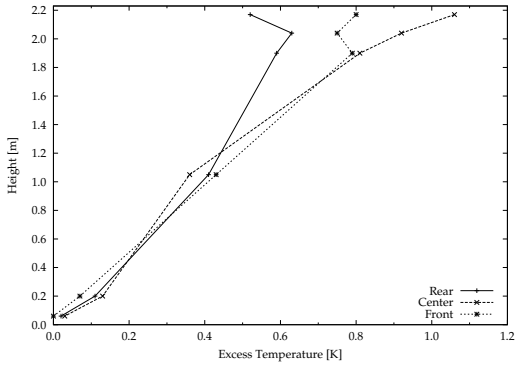

(f) $\vartheta_{\text{plate}} - \vartheta_{\text{meanair}} = 4.55\,\text{K}$

Figure D.5: Temperature gradients measured in the cabin for mixed convection experiments with $3.3\,\text{K} < \vartheta_{\text{plate}} - \vartheta_{\text{meanair}} < 4.6\,\text{K}$.

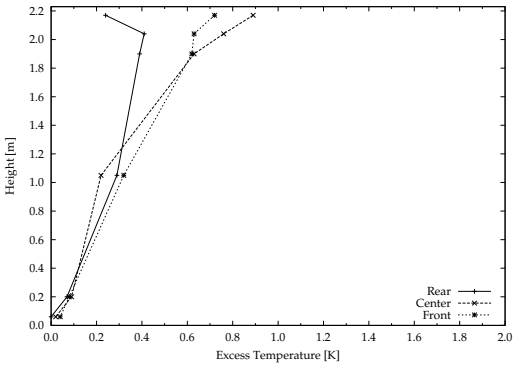

(a) $\vartheta_{\text{plate}} - \vartheta_{\text{meanair}} = 5.36\,\text{K}$

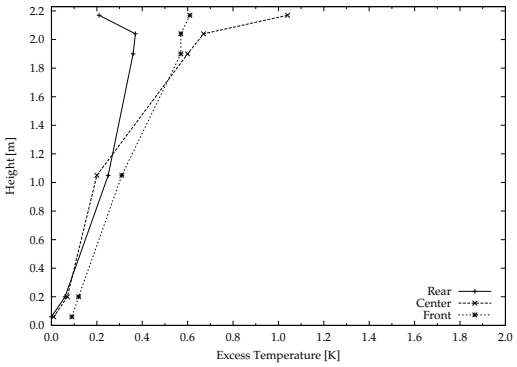

(b) $\vartheta_{\text{plate}} - \vartheta_{\text{meanair}} = 5.68\,\text{K}$

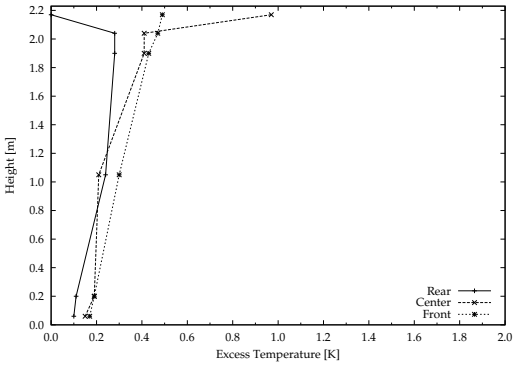

(c) $\vartheta_{\text{plate}} - \vartheta_{\text{meanair}} = 6.29\,\text{K}^{\star}$

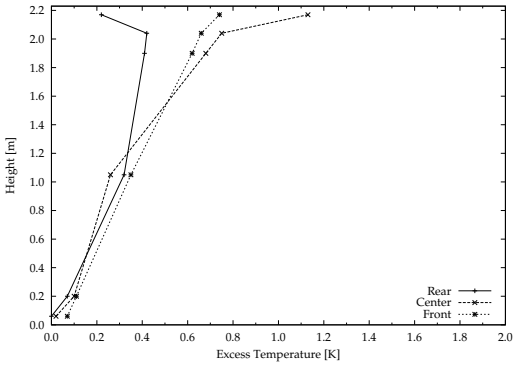

(d) $\vartheta_{\text{plate}} - \vartheta_{\text{meanair}} = 6.71\,\text{K}$

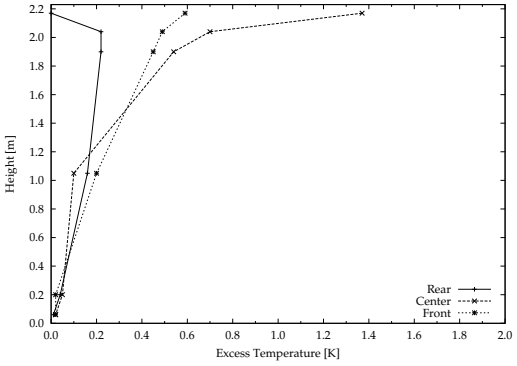

(e) $\vartheta_{\text{plate}} - \vartheta_{\text{meanair}} = 7.54\,\text{K}$

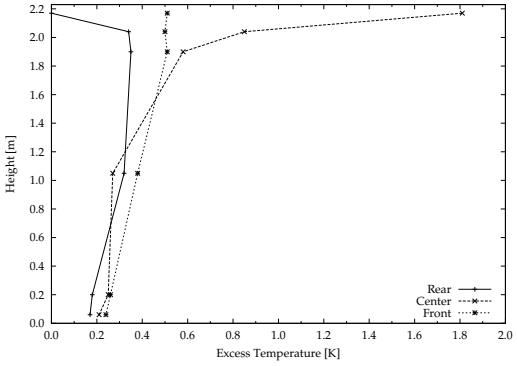

(f) $\vartheta_{\text{plate}} - \vartheta_{\text{meanair}} = 8.20\,\text{K}^{\star}$

Figure D.6: Temperature gradients measured in the cabin for mixed convection experiments with $5.3\,\text{K} < \vartheta_{\text{plate}} - \vartheta_{\text{meanair}} < 8.3\,\text{K}$. Outliers from figure 6.11 are indicated by a * in the caption.

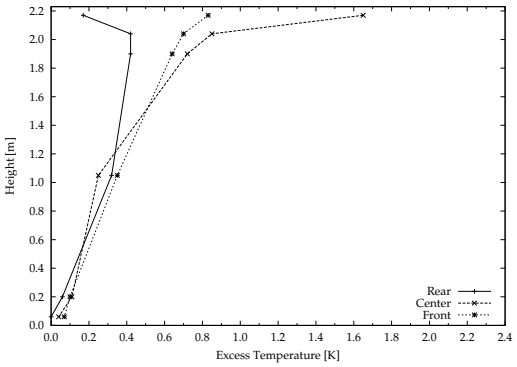

(a) $\vartheta_{\text{plate}} - \vartheta_{\text{meanair}} = 8.47\,\text{K}$

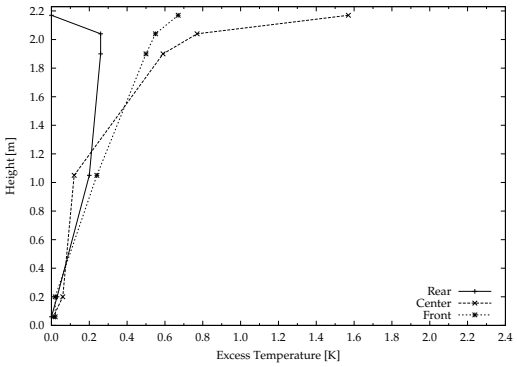

(b) $\vartheta_{\text{plate}} - \vartheta_{\text{meanair}} = 8.52\,\text{K}$

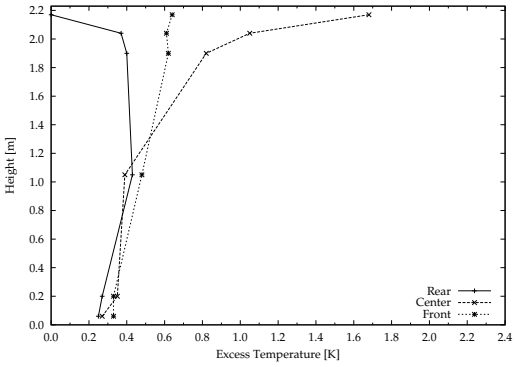

(c) $\vartheta_{\text{plate}} - \vartheta_{\text{meanair}} = 9.31\,\text{K}^{\star}$

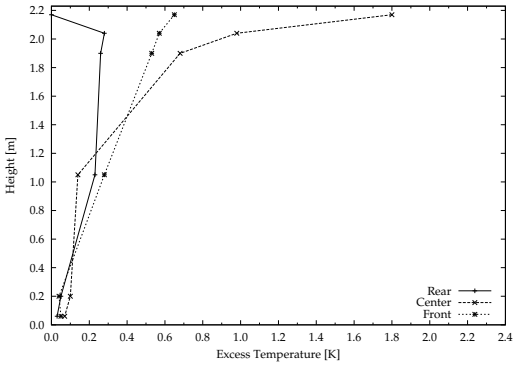

(d) $\vartheta_{\text{plate}} - \vartheta_{\text{meanair}} = 9.86\,\text{K}^{\star}$

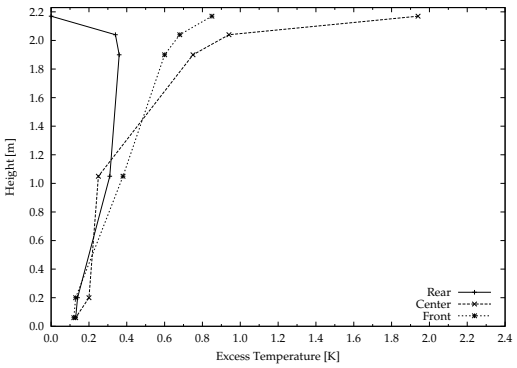

(e) $\vartheta_{\text{plate}} - \vartheta_{\text{meanair}} = 10.12\,\text{K}^{\star}$

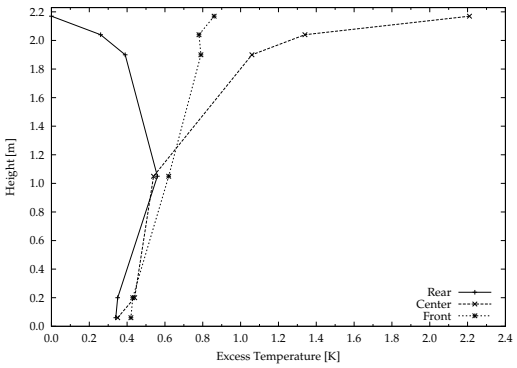

(f) $\vartheta_{\text{plate}} - \vartheta_{\text{meanair}} = 11.22\,\text{K}^{\star}$

Figure D.7: Temperature gradients measured in the cabin for mixed convection experiments with $\vartheta_{\text{plate}} - \vartheta_{\text{meanair}} > 8.4\,\text{K}$. Outliers from figure 6.11 are indicated by a * in the caption.

D.2 Ceiling with Acoustic Baffles

First, additional results from the experimental tests with baffles in an unventilated chamber are shown in section D.2.1. Then, results with ventilation are shown in section D.2.2.

D.2.1 Results Without Ventilation

Figure D.8 shows results for the total heat transfer coefficient h_{total} for different values of surface-to-air temperature difference. The derived correlation is also given in the figure and has a coefficient of determination R^2 of 0.97.

Figures D.9, D.10 and D.11 show the temperature gradient plots for the experiments with acoustic baffles and no ventilation. The position of the baffles is indicated by the grey band in the plots. The figures show that temperature gradients are much more pronounced with baffles than during the natural convection experiments at an unobstructed ceiling which have been presented above. Now, an excess temperature of more than 7 K can be observed below the hot plate at the centre of the ceiling while the excess temperature did not exceed 4 K during the natural convection experiments. However, the more pronounced rise in temperature is limited to the top part of the chamber where the baffles are installed.

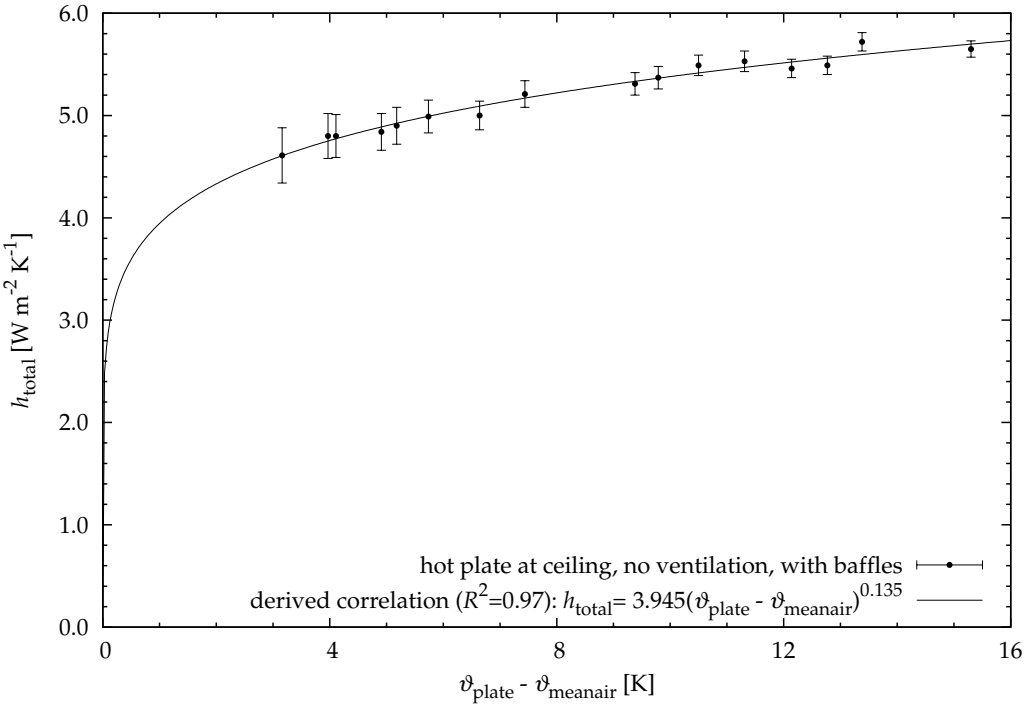

Figure D.8: Total heat transfer coefficients for the test series with acoustic baffles in an unventilated chamber.

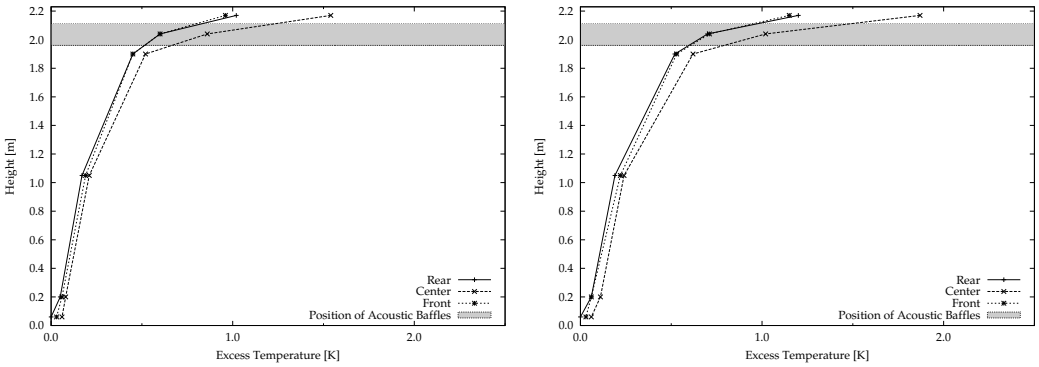

(a) $\vartheta_{\text{plate}} - \vartheta_{\text{meanair}} = 3.16\,\text{K}$

(b) $\vartheta_{\text{plate}} - \vartheta_{\text{meanair}} = 3.97\,\text{K}$

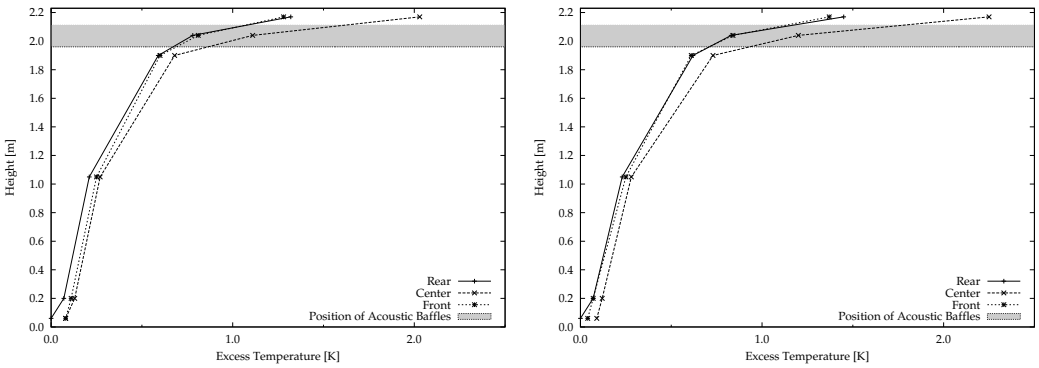

(c) $\vartheta_{\text{plate}} - \vartheta_{\text{meanair}} = 4.11\,\text{K}$

(d) $\vartheta_{\text{plate}} - \vartheta_{\text{meanair}} = 4.91\,\text{K}$

Figure D.9: Temperature gradients measured in the cabin for experiments with acoustic baffles, no ventilation, $\vartheta_{\text{plate}} - \vartheta_{\text{meanair}} < 5\,\text{K}$.

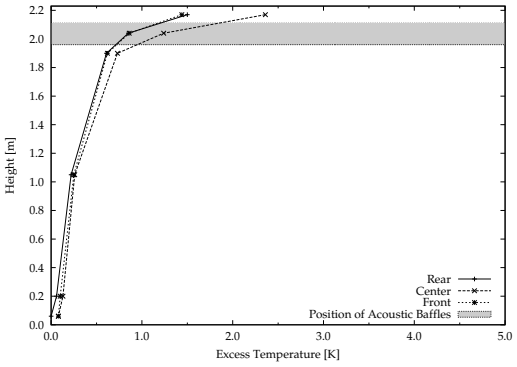

(a) $\vartheta_{\text{plate}} - \vartheta_{\text{meanair}} = 5.18\,\text{K}$

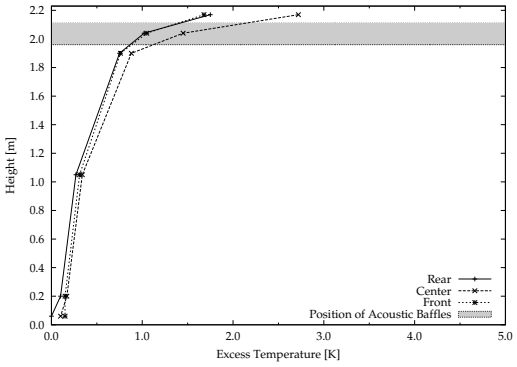

(b) $\vartheta_{\text{plate}} - \vartheta_{\text{meanair}} = 5.74\,\text{K}$

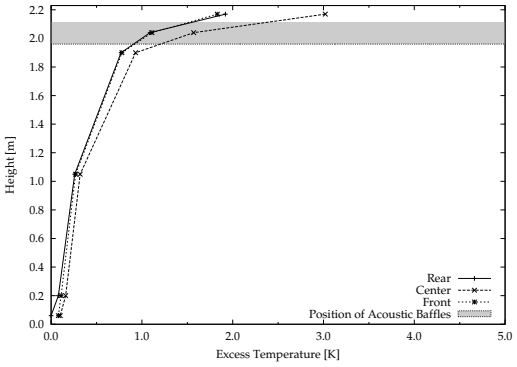

(c) $\vartheta_{\text{plate}} - \vartheta_{\text{meanair}} = 6.64\,\text{K}$

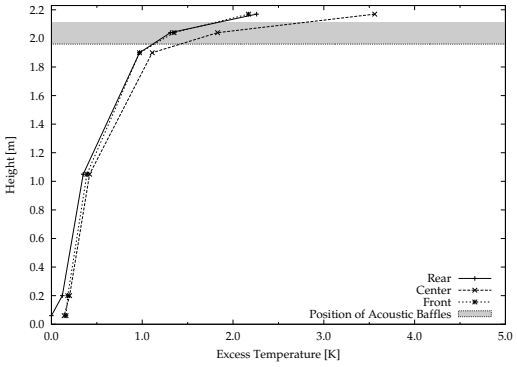

(d) $\vartheta_{\text{plate}} - \vartheta_{\text{meanair}} = 7.44\,\text{K}$

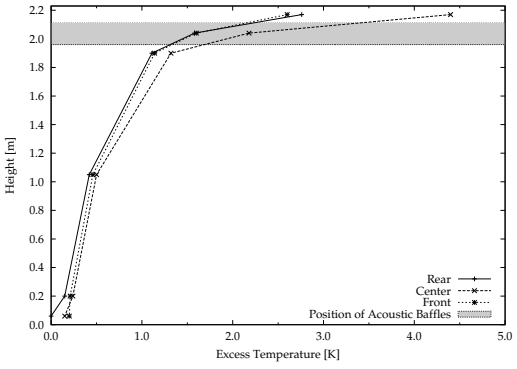

(e) $\vartheta_{\text{plate}} - \vartheta_{\text{meanair}} = 9.38\,\text{K}$

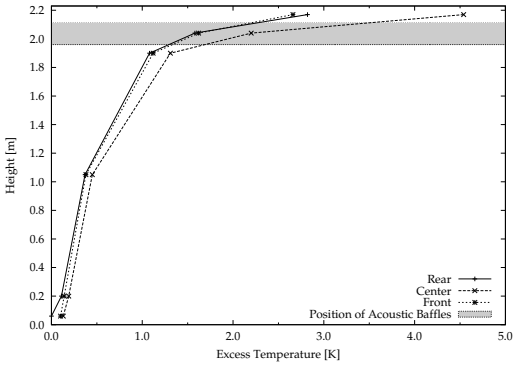

(f) $\vartheta_{\text{plate}} - \vartheta_{\text{meanair}} = 9.79\,\text{K}$

Figure D.10: Temperature gradients measured in the cabin for experiments with acoustic baffles, no ventilation, $5\,\text{K} < \vartheta_{\text{plate}} - \vartheta_{\text{meanair}} < 10\,\text{K}$.

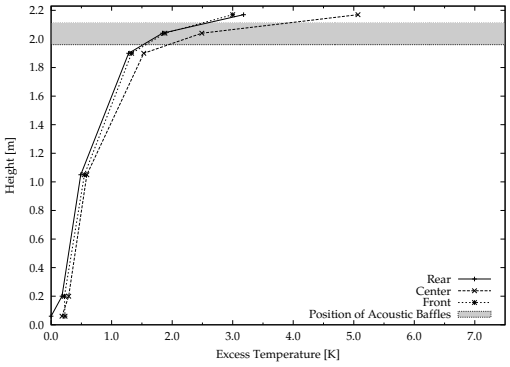

(a) $\vartheta_{\text{plate}} - \vartheta_{\text{meanair}} = 10.50\,\text{K}$

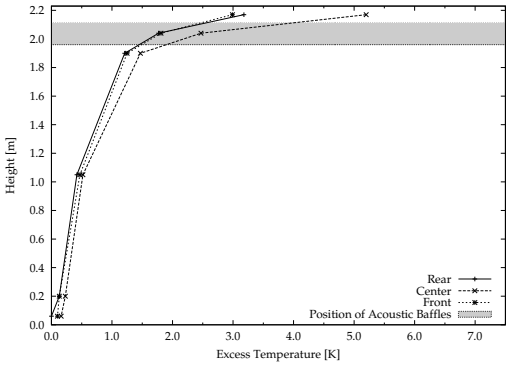

(b) $\vartheta_{\text{plate}} - \vartheta_{\text{meanair}} = 11.31\,\text{K}$

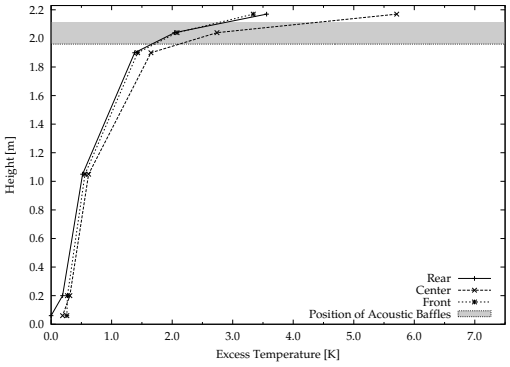

(c) $\vartheta_{\text{plate}} - \vartheta_{\text{meanair}} = 12.14\,\text{K}$

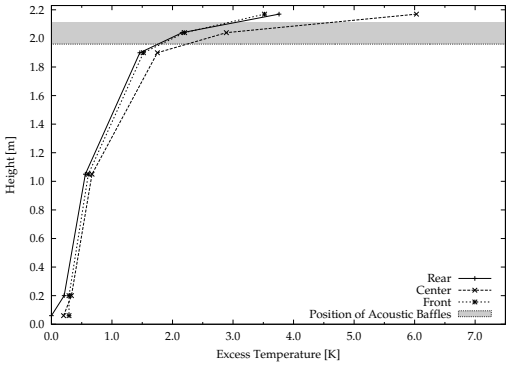

(d) $\vartheta_{\text{plate}} - \vartheta_{\text{meanair}} = 12.77\,\text{K}$

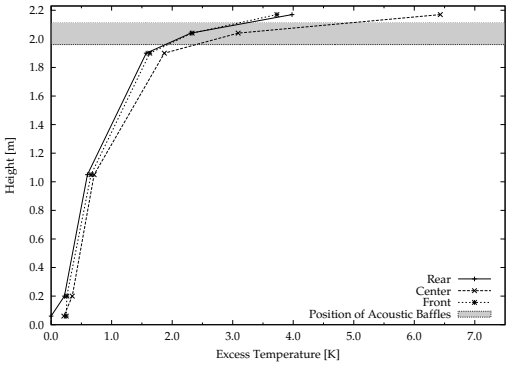

(e) $\vartheta_{\text{plate}} - \vartheta_{\text{meanair}} = 13.38\,\text{K}$

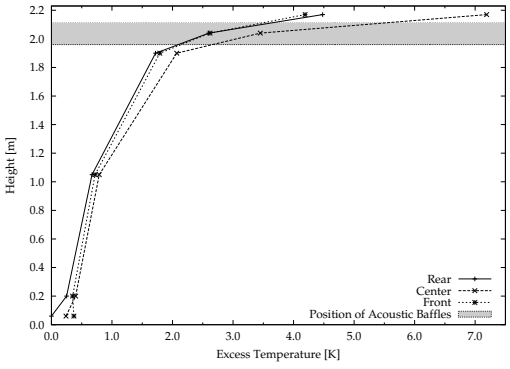

(f) $\vartheta_{\text{plate}} - \vartheta_{\text{meanair}} = 15.30\,\text{K}$

Figure D.11: Temperature gradients measured in the cabin for experiments with acoustic baffles, no ventilation, $\vartheta_{\text{plate}} - \vartheta_{\text{meanair}} > 10\,\text{K}$.

D.2.2 Results With Ventilation

Figure D.12 shows the resulting total heat transfer coefficients h_{total} for different values of surface-to-air temperature difference. The derived correlation is also given in the figure again and has a coefficient of determination R^2 of 0.86.

The temperature gradient plots for the experiments with both acoustic baffles and ventilation can be found in figures D.13, D.14 and D.15

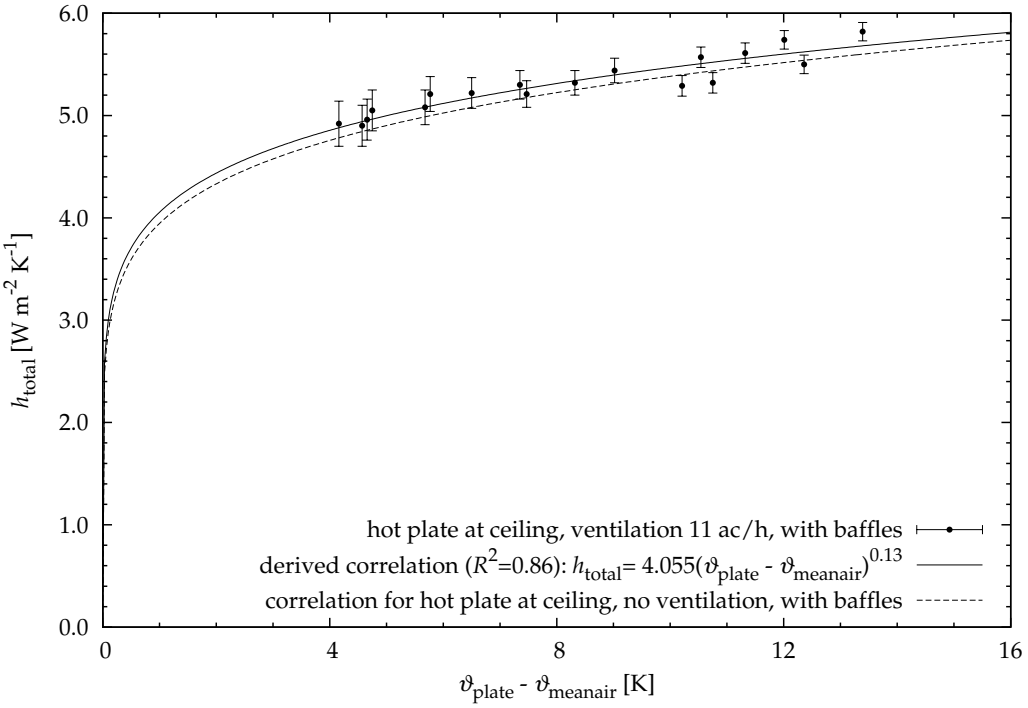

Figure D.12: Total heat transfer coefficients for the test series with acoustic baffles in a ventilated chamber.

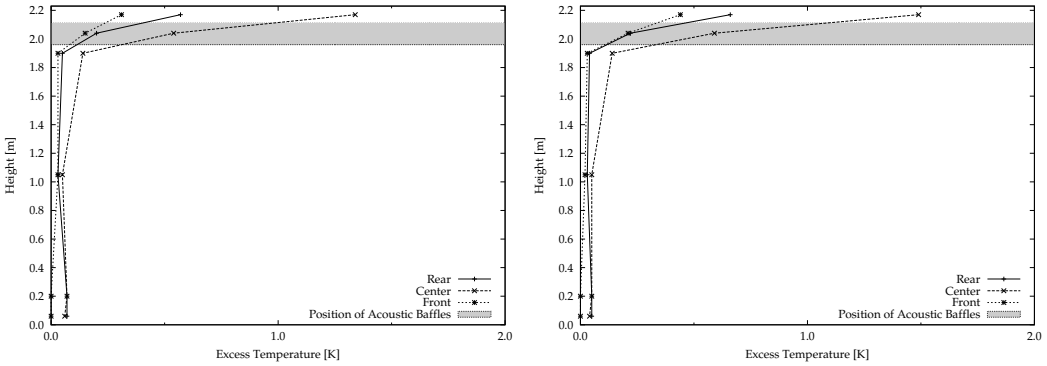

(a) $\vartheta_{\text{plate}} - \vartheta_{\text{meanair}} = 4.16\,\text{K}$

(b) $\vartheta_{\text{plate}} - \vartheta_{\text{meanair}} = 4.57\,\text{K}$

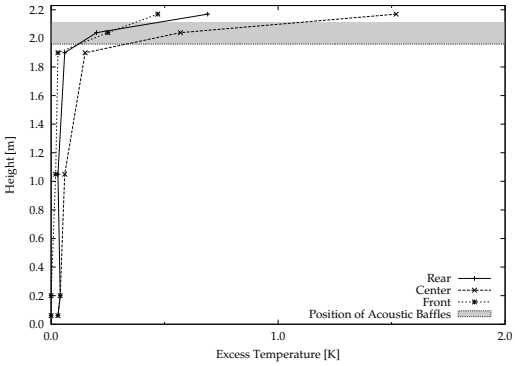

(c) $\vartheta_{\text{plate}} - \vartheta_{\text{meanair}} = 4.66\,\text{K}$

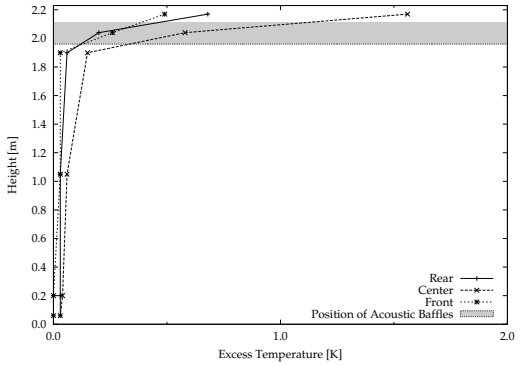

(d) $\vartheta_{\text{plate}} - \vartheta_{\text{meanair}} = 4.75\,\text{K}$

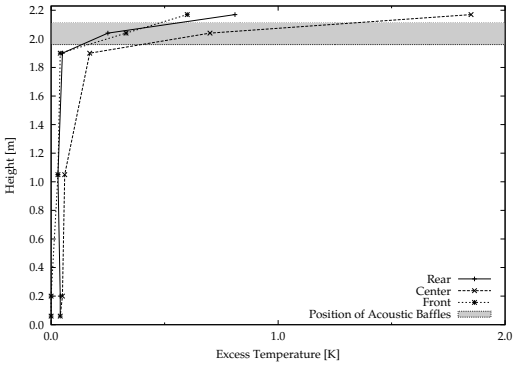

(e) $\vartheta_{\text{plate}} - \vartheta_{\text{meanair}} = 5.68\,\text{K}$

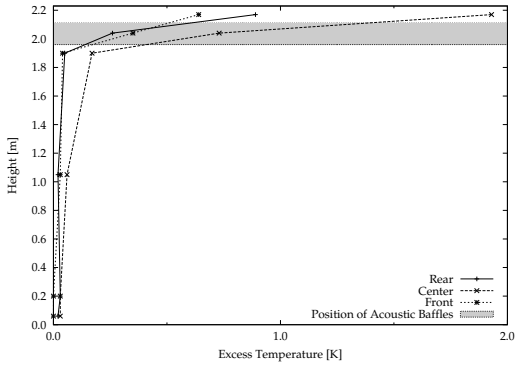

(f) $\vartheta_{\text{plate}} - \vartheta_{\text{meanair}} = 5.77\,\text{K}$

Figure D.13: Temperature gradients measured in the cabin for experiments with acoustic baffles, with ventilation, $\vartheta_{\text{plate}} - \vartheta_{\text{meanair}} < 6\,\text{K}$.

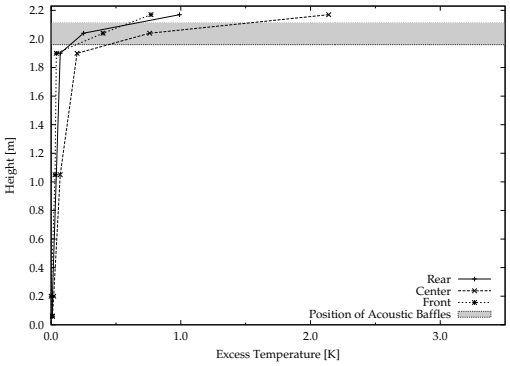

(a) $\vartheta_{\text{plate}} - \vartheta_{\text{meanair}} = 6.50\,\text{K}$

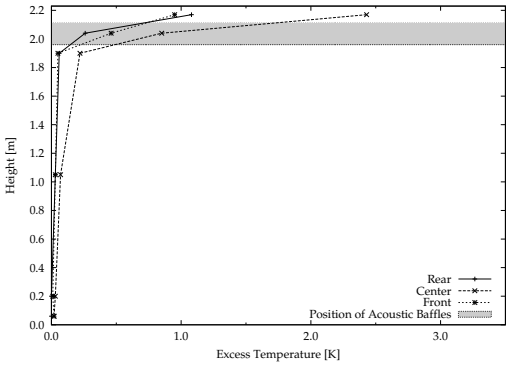

(b) $\vartheta_{\text{plate}} - \vartheta_{\text{meanair}} = 7.35\,\text{K}$

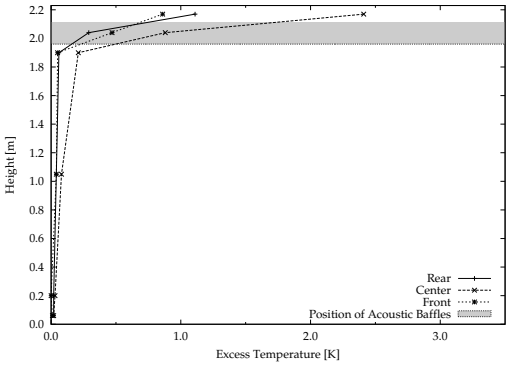

(c) $\vartheta_{\text{plate}} - \vartheta_{\text{meanair}} = 7.47\,\text{K}$

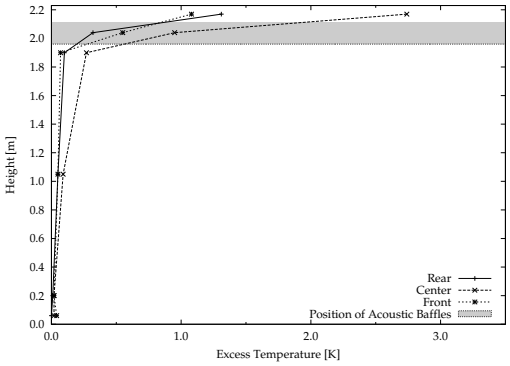

(d) $\vartheta_{\text{plate}} - \vartheta_{\text{meanair}} = 8.32\,\text{K}$

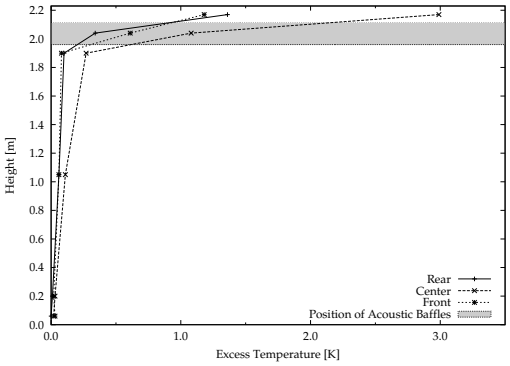

(e) $\vartheta_{\text{plate}} - \vartheta_{\text{meanair}} = 9.02\,\text{K}$

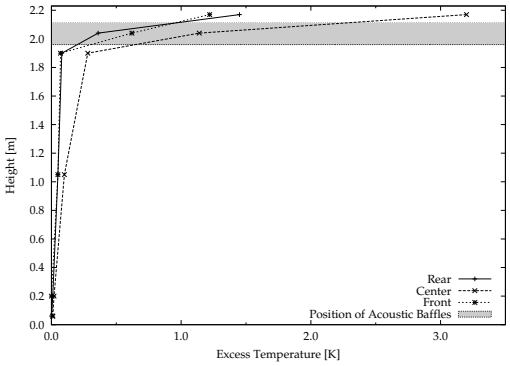

(f) $\vartheta_{\text{plate}} - \vartheta_{\text{meanair}} = 10.21\,\text{K}$

Figure D.14: Temperature gradients measured in the cabin for experiments with acoustic baffles, with ventilation, $6\,\text{K} < \vartheta_{\text{plate}} - \vartheta_{\text{meanair}} < 10.5\,\text{K}$.

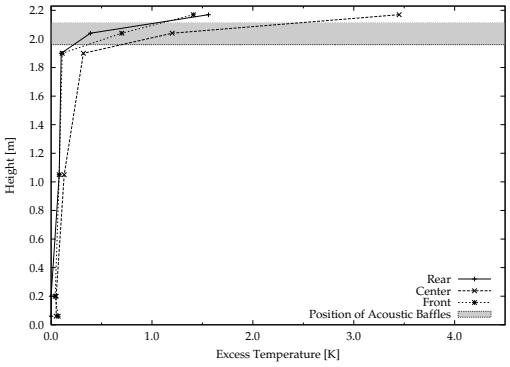

(a) $\vartheta_{\text{plate}} - \vartheta_{\text{meanair}} = 10.54\,\text{K}$

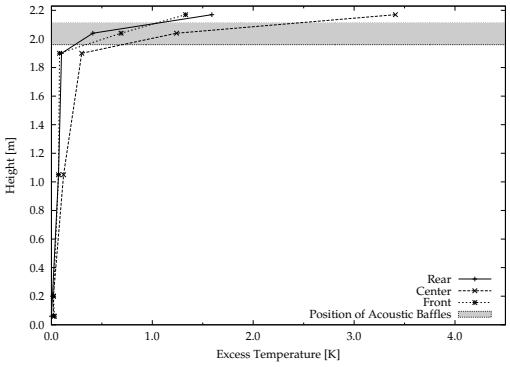

(b) $\vartheta_{\text{plate}} - \vartheta_{\text{meanair}} = 10.75\,\text{K}$

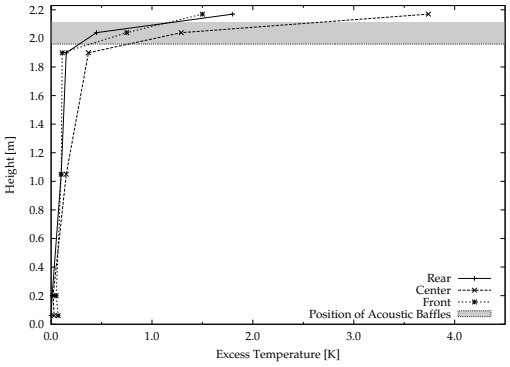

(c) $\vartheta_{\text{plate}} - \vartheta_{\text{meanair}} = 11.32\,\text{K}$

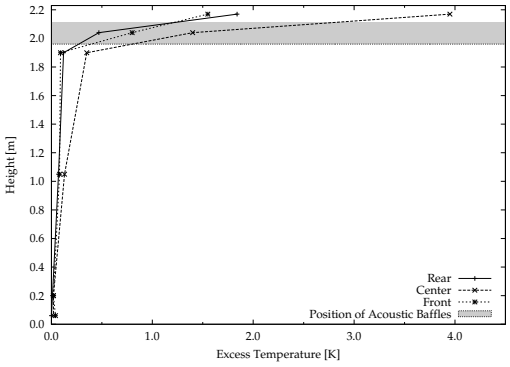

(d) $\vartheta_{\text{plate}} - \vartheta_{\text{meanair}} = 12.01\,\text{K}$

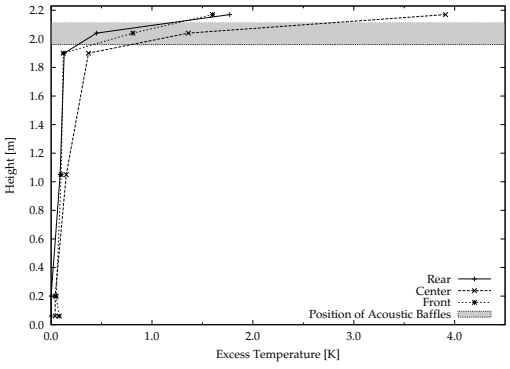

(e) $\vartheta_{\text{plate}} - \vartheta_{\text{meanair}} = 12.36\,\text{K}$

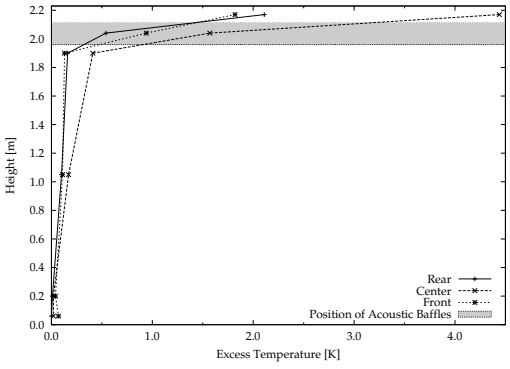

(f) $\vartheta_{\text{plate}} - \vartheta_{\text{meanair}} = 13.39\,\text{K}$

Figure D.15: Temperature gradients measured in the cabin for experiments with acoustic baffles, with ventilation, $\vartheta_{\text{plate}} - \vartheta_{\text{meanair}} > 10.5\,\text{K}$.

E Photos of the Experimental Facility

Figure E.1: Photograph showing the *Labor für Gebäudesimulation G1.02* (laboratory room) with the glass compartment in the corner of the room at the beginning of the project. Originally, the glass compartment was intended to be used as a test facility for façade elements. Then, the experimental chamber for this work was constructed within this glass compartment as can be seen in subsequent photographs.

Figure E.2: Inside of the glass compartment. First insulation panels are laid out on the floor, first lumber is installed for construction of the side wall.

Figure E.3: Outer layer of insulation is installed at rear and side walls. The shown opening was insulated and sealed at the end of construction.

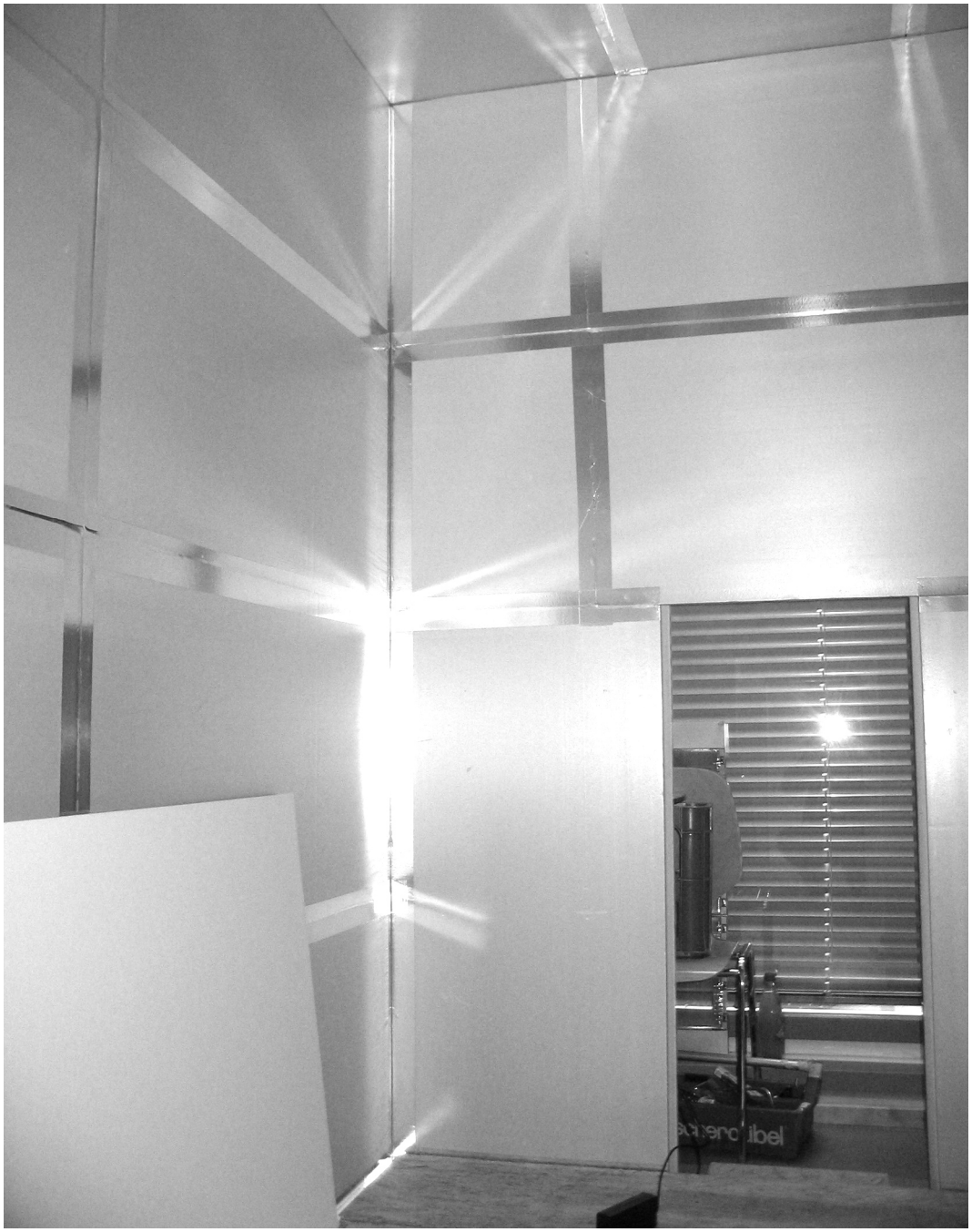

Figure E.4: All joints are sealed with aluminium tape to ensure that leakage is reduced as much as possible.

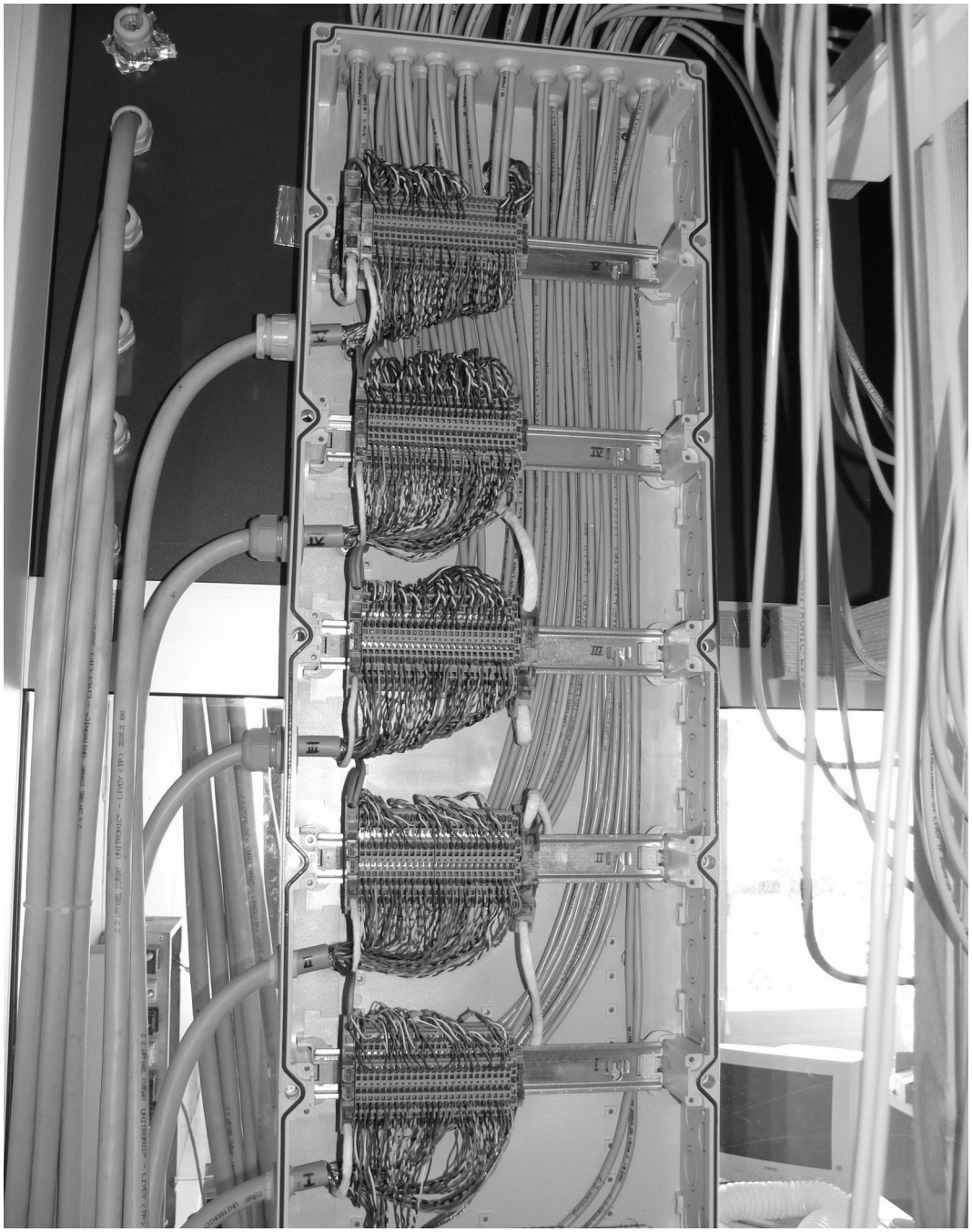

Figure E.5: Enclosure for the wiring of the temperature measurement system. Here, sensors are connected to the PCBAs shown in figure A.1.

Figure E.6: Photograph showing the newly built chamber inside the glass compartment. In the front, temperature sensors are being calibrated before getting installed inside the chamber.

Figure E.7: Close-up view of some foil sensors being immersed in the fluid of the calibration thermostat bath.

Figure E.8: Close-up view of some chip sensors protected from the water by latex gloves. Furthermore, the two Pt500s have also just been calibrated.

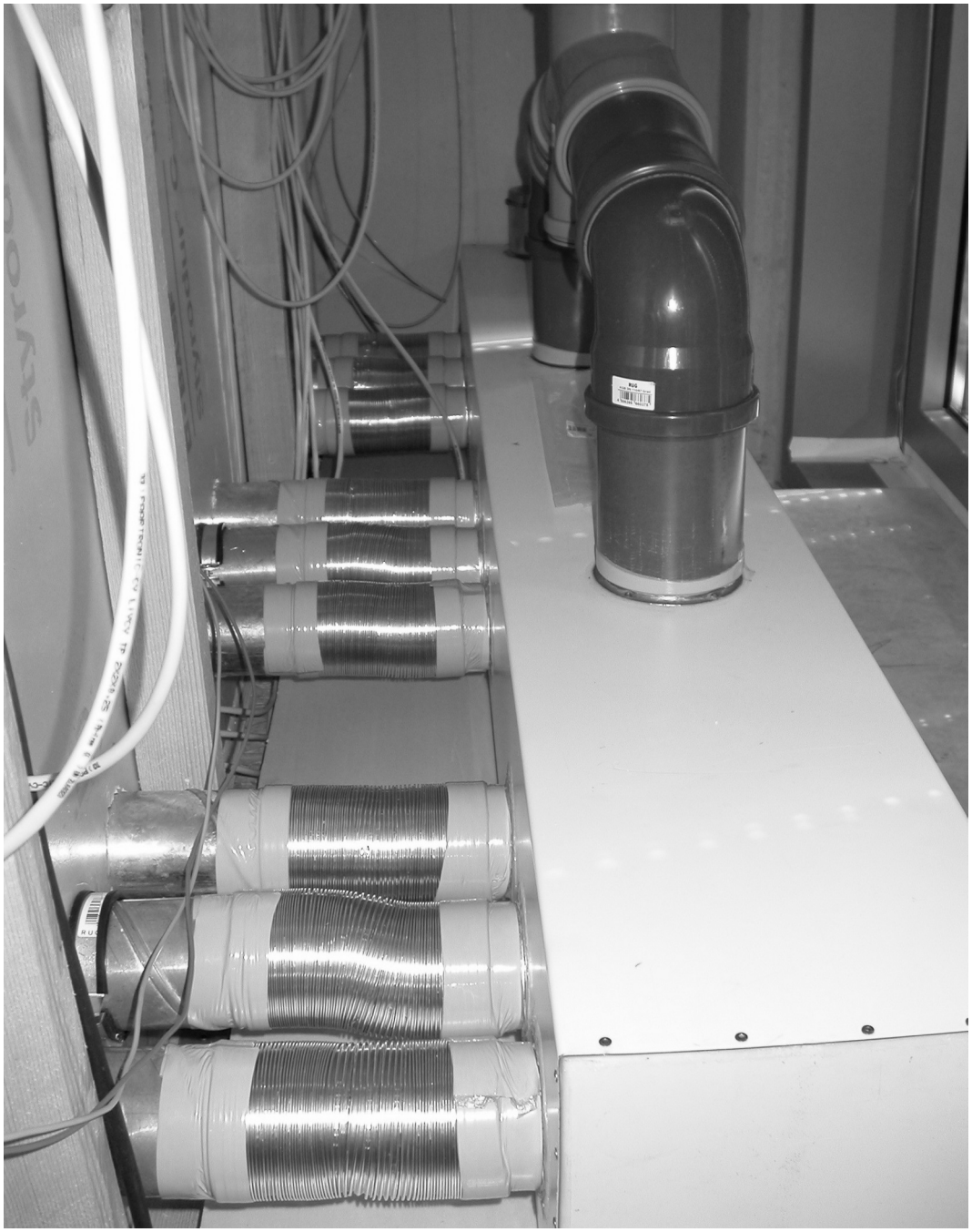

Figure E.9: Return air box behind the chamber. Air can leave the chamber through nine parallel openings at low level and is collected in the box.

Figure E.10: Inside view of the experimental chamber. The heating element is installed at the centre of ceiling.

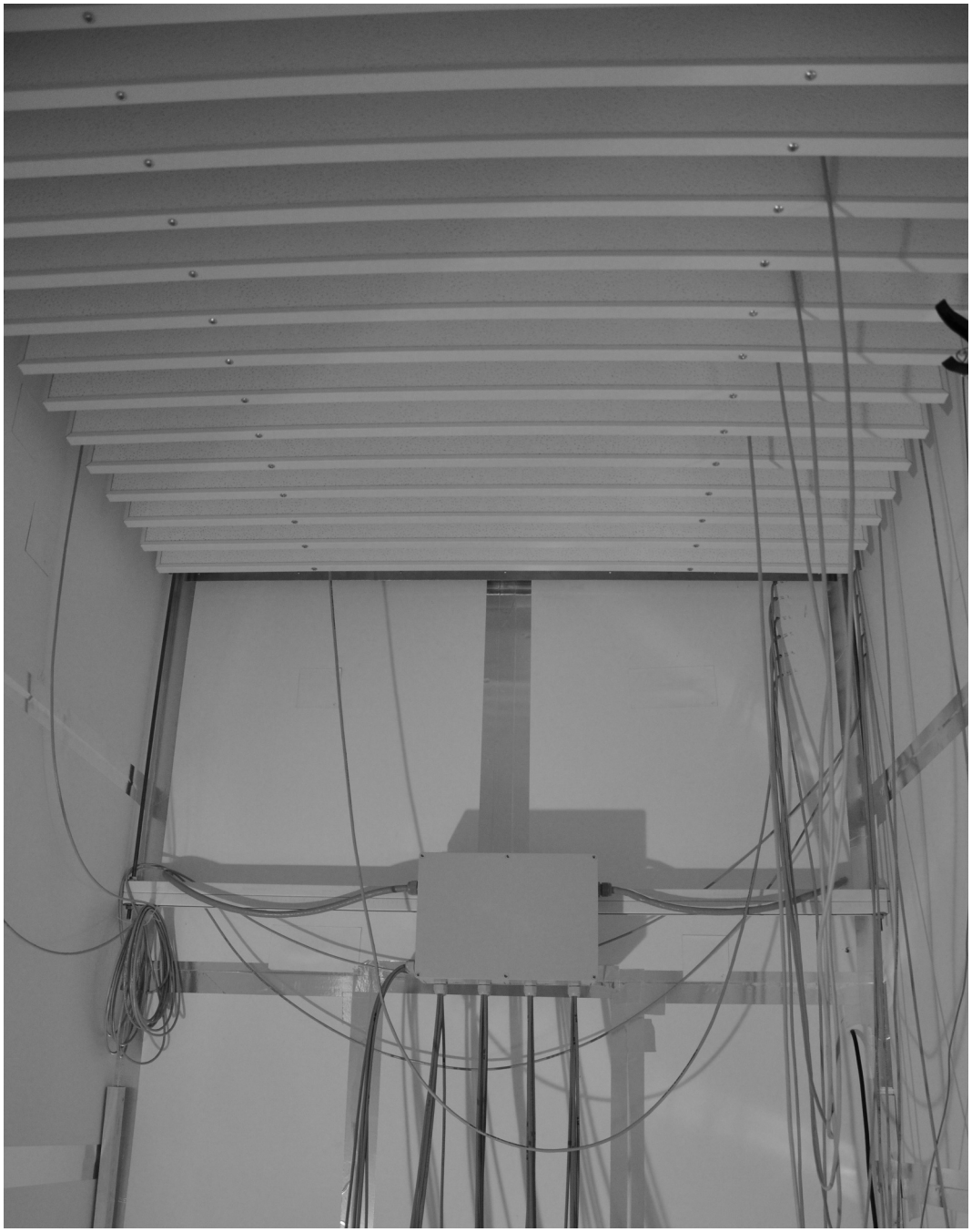

Figure E.11: Inside view of the experimental chamber, this time shot from the front with acoustic baffles installed below the ceiling.

Figure E.12: Rectangular lattice used for installing air temperature sensors and flow sensors in the chamber.

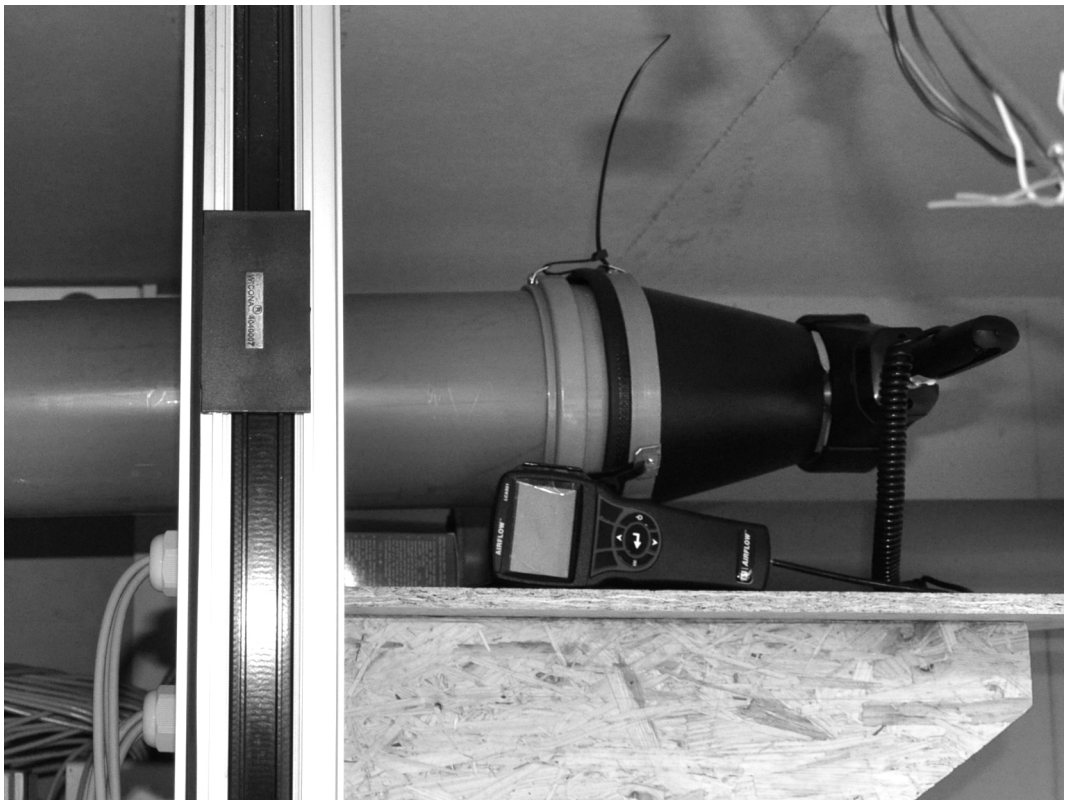

Figure E.13: Return air duct from the cabin (left, not shown) ending at the aircone flow hood (right) in the laboratory room with a permanently attached rotating vane anemometer at the end of the duct.

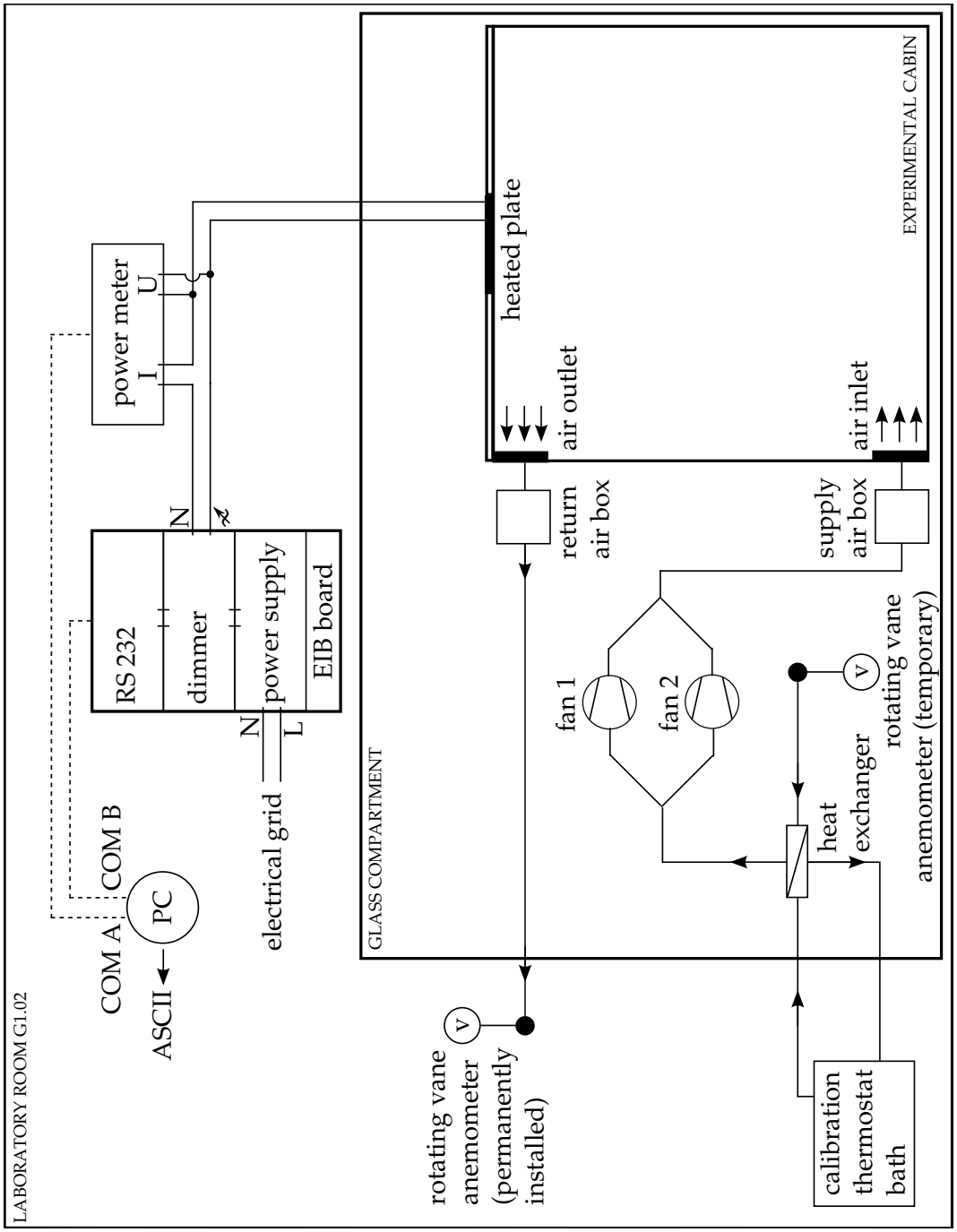

Figure E.14: Schematic of the experimental facility with an alternative configuration (not used in this work) of the air ducts for an inlet at low level.

F Photos of the Experiment for Determining Emissivity

Figure F.1: Photos taken during the construction phase of the "ε-experiment".
top left: assembled hydronic cooling element,
top right: black surface of the hydronic cooling element,
bottom left: electrical heating element,
bottom right: wooden bounding box construction of the experiment.

Figure F.2: More photos from the construction of the "ε-experiment".
top left: sizing the insulation layer surrounding the cold plate,
top right: tubing on one end of the hydronic element,
middle left: temperature sensors on the cold plate,
middle right: hot plate installed on top,
bottom left: last layer of insulation installed,
bottom right: view from the outside of the chamber showing the experimental arrangement, tubing and sensor wiring.